

Oxygen Crossover in Solid-Solid Heat Exchangers for Solar Thermochemical Redox Cycles

Sauerstoffübergang in Feststoffwärmetauschern für solarthermochemische Redoxkreisprozesse

Von der Fakultät für Maschinenwesen der Rheinisch-Westfälischen Technischen Hochschule
Aachen zur Erlangung des akademischen Grades eines Doktors der Ingenieurwissenschaften
genehmigte Dissertation

vorgelegt von

Philipp Holzemer-Zerhusen

Berichter: Univ.-Prof. Dr. rer. nat. Christian Sattler
Univ.-Prof. Dr.-Ing. Thomas Wetzel

Tag der mündlichen Prüfung: 15. Januar 2024

Diese Dissertation ist auf den Internetseiten der Universitätsbibliothek online verfügbar.

Acknowledgements

This dissertation was written during my time as a doctoral student at the Institute of Future Fuels of the German Aerospace Center (DLR) – a time marked by many challenges but also by the support of many people to whom I would like to express my sincere gratitude.

First and foremost, I would like to thank Prof. Dr. Christian Sattler, my doctoral advisor, for asking critical questions and providing helpful advice throughout the whole doctoral project. In addition, I thank Prof. Dr. Thomas Wetzel for offering his time and expertise to act as a second reviewer for this thesis.

Special thanks go to Dr. Stefan Brendelberger, who patiently supervised my work professionally, for taking time for me so often, for many interesting and sometimes lively scientific discussions, and for much helpful feedback.

Furthermore, I thank Dr. Martin Roeb, our department head, who also gave me important feedback at important points and provided the necessary framework that enabled me to carry out my work. I would also like to thank Prof. Dr. Robert Pitz-Paal and Prof. Dr. Bernhard Hoffschmidt for valuable comments and discussions during progress talks.

The whole team at the Institute of Future Fuels and our friends from the Institute of Solar Research deserve my thanks for creating a motivating and friendly working atmosphere. In particular I thank Mathias Pein and Lena Klaas for the time spent together in laboratory and office and for letting me share my worries with them, Andreas Rosenstiel for many exciting scientific debates, Dr. Alon Lidor, Dr. Luke Venstrom, and Dr. Silvan Siegrist for many fruitful discussions that helped me to move this work forward, especially at an early stage and Dr. Henrik von Storch for acting as a mentor and for his interest in my work.

I am grateful to Dr. Gözde Alkan for sharing her skill and expertise in analytic methods. Furthermore, I thank Luca Matzel and Hannes Brudi, whose theses I had the honor of supervising and who not only presented me with unexpected challenges, but from whom I was also privileged to learn a great deal.

Moritz Becker I would like to thank for proofreading parts of this work and for being a great friend, as well as all my other friends for being there when I need them.

I am also very grateful to Dr. Thomas Droß, who awakened my passion for science and technology and thus had a great influence on my decision to pursue the path that ultimately led to this dissertation.

My parents I want to thank for their unconditional and selfless love and support, which made my path and this work possible in the first place.

I am incredibly grateful to Marinara for a support beyond words that got me through even the hardest times. I would not have made it to this point without you.

Abstract

Two-step solar thermochemical redox cycles represent a promising path to carbon-neutral fuels. In this process, solar radiation is concentrated to release oxygen from a redox material at high temperatures. This material can then split H_2O and/or CO_2 at lower temperatures, producing renewable H_2 or synthesis gas. The latter can be further processed into a liquid fuel, for example. A crucial factor for an efficient and competitive process is heat recovery between oxygen release and the splitting step. It is expected that an undesired crossover of oxygen from the oxidised to the reduced redox material may occur in a corresponding heat exchanger if this is not prevented by separating the two material flows. However, physical separation could limit the effectiveness of heat recovery. This oxygen transport would oxidise reduced redox material prior to the splitting reaction, reducing its ability to split H_2O or CO_2 . The consequence would be a lower process efficiency. The present work is dedicated to the investigation of said oxygen transfer, which is referred to as recombination.

The effect of recombination on the process efficiency is investigated with simulations assuming chemical equilibria or given reaction rates. The results are examined for compliance with the second law of thermodynamics. The kinetics of the re-oxidation of ceria, a common redox material, is investigated experimentally. A test rig was designed and built for this purpose. In these experiments, the addition of an inert gas as a mass transport resistor to the gas phase of the heat exchanger and its influence on the re-oxidation kinetics is investigated. Furthermore, a one-dimensionally resolved numerical model of indirect heat recovery via a heat storage unit is developed. Finally, based on all results, different options for heat recovery in solar redox cycles are compared.

The simulations show a correlation between heat recovery and recombination. At high heat recovery, recombination lowers the overall efficiency more than it is increased by heat recovery. At low heat recovery, recombination is reversed so that the reduced material is further reduced. This effect is caused by the oxygen partial pressure in the heat exchanger. Experimental results show that the addition of an inert gas actually decelerates the re-oxidation of the ceria sample. If this finding is considered in simulations, it seems realistic that heat recovery can increase the efficiency of the process despite recombination. For the indirect heat exchanger concept, which can be a technically easier-to-implement alternative to counter current heat exchangers, calculations yield promising heat recovery ratios.

Zusammenfassung

Zweistufige solarthermochemische Redoxkreisprozesse stellen einen vielversprechenden Weg zu CO₂-neutralen Kraftstoffen dar. Dabei wird Solarstrahlung konzentriert, um bei hohen Temperaturen Sauerstoff aus einem Redoxmaterial freizusetzen. Dieses Material kann dann bei niedrigeren Temperaturen H₂O und/oder CO₂ spalten, wobei erneuerbarer H₂ oder Synthesegas entsteht. Letzteres kann beispielsweise zu einem flüssigen Kraftstoff weiterverarbeitet werden. Ein entscheidender Faktor für einen effizienten und wettbewerbsfähigen Prozess ist die Wärmerückgewinnung zwischen Sauerstofffreisetzung und Spaltschritt. Es ist zu erwarten, dass es in einem entsprechenden Wärmetauscher zu einem unerwünschten Übergang von Sauerstoff vom oxidierten zum reduzierten Redoxmaterial kommen kann, wenn dies nicht durch eine Trennung der beiden Materialströme verhindert wird. Eine Trennung könnte allerdings die Effektivität der Wärmerückgewinnung einschränken. Dieser Sauerstofftransport würde reduziertes Redoxmaterial vor der Spaltreaktion oxidieren, wobei die Fähigkeit des Materials H₂O oder CO₂ zu spalten verringert wird. Die Folge wäre ein geringerer Prozesswirkungsgrad. Die vorliegende Arbeit widmet sich der Untersuchung dieses Sauerstofftransfers, der im Folgenden als Rekombination bezeichnet wird.

Die Auswirkung der Rekombination auf den Wirkungsgrad wird mit Simulationen unter Annahme chemischer Gleichgewichte oder gegebener Reaktionsraten untersucht. Die Ergebnisse werden auf Einhaltung des zweiten Hauptsatzes der Thermodynamik untersucht. Die Kinetik der Reoxidation von Ceroxid, einem gängigen Redoxmaterial, wird experimentell untersucht. Zu diesem Zweck wurde ein Versuchstand konstruiert und gebaut. In diesen Experimenten wird auch die Zugabe eines Inertgases als Massentransportwiderstand in die Gasphase des Wärmetauschers und ihr Einfluss auf die Reoxidationskinetik untersucht. Darüber hinaus wird ein ein-dimensionales aufgelöstes numerisches Modell von indirekter Wärmerückgewinnung über einen Wärmespeicher aufgestellt. Auf Grundlage aller Ergebnisse werden abschließend verschiedene Optionen zur Wärmerückgewinnung in solaren Redoxkreisprozessen verglichen.

Die Simulationen zeigen eine Korrelation zwischen Wärmerückgewinnung und Rekombination. Bei hoher Wärmerückgewinnung senkt Rekombination den Gesamtwirkungsgrad stärker als dieser durch die Wärmerückgewinnung erhöht wird. Bei niedriger Wärmerückgewinnung ist die Rekombination umgekehrt, sodass das reduzierte Material weiter reduziert wird. Dieser Effekt wird durch den Sauerstoffpartialdruck im Wärmetauscher verursacht. Experimentelle Ergebnisse zeigen, dass die Zugabe eines Inertgases die Reoxidation der Ceroxidprobe tatsächlich verlangsamt. Wird dieses Erkenntnis in Simulationen berücksichtigt, erscheint es realistisch, dass Wärmerückgewinnung die Effizienz des Prozesses trotz Rekombination erhöhen kann. Für das indirekte Wärmetauscherkonzept, das eine technisch leichter umsetzbare Alternative zu Gegenstromwärmetauschern sein kann, wurde eine vielversprechende Wärmerückgewinnung berechnet.

Contents

1. Introduction	1
2. Theory and Background	5
2.1. Fundamentals of Concentrating Solar Radiation	5
2.2. Two-Step Solar Thermochemical Redox Cycles	8
2.2.1. Oxygen Partial Pressure Control for Reduction Step	9
2.2.2. Solid-solid Heat Exchanger Concepts	11
2.2.3. Porous Redox Material Structures	15
2.3. Kinetics and Thermodynamics	17
2.3.1. Oxygen Non-Stoichiometry	17
2.3.2. Reaction Kinetics	20
2.3.3. Reaction Equilibria	22
2.4. Experimental Determination of Redox Behaviour	25
2.5. High Temperature Heat Transport	26
2.5.1. Convective Heat Transport	26
2.5.2. Radiation	28
2.5.3. Heat Transport in Porous Media	29
3. Materials and Methods	31
3.1. Modelling the Recombination Effect	31
3.1.1. Reactions and Mass Transport	32
3.1.2. Energy Efficiency	35
3.1.3. Second Law Analysis	39
3.1.4. Modelling Oxidation Kinetics	41
3.2. Experimental Investigation of Recombination Kinetics	42
3.2.1. Test Rig Development	43
3.2.2. Volumes of Test Rig Components	47
3.2.3. Measuring the Temperature Profile in the Furnace	49
3.2.4. Ceria Samples	50
3.2.5. Experimental Procedure	51
3.2.6. Gas Phase Characterisation	56
3.2.7. Determining Oxygen Non-Stoichiometry and Oxidation Rates	63
3.2.8. Numeric Model of Test Rig	68
3.3. Modelling Indirect Heat Recovery	72
3.3.1. Heat Transport Model	73
3.3.2. Model Discretisation	77
4. Results	79
4.1. Simulaton of Redox System with Oxygen Crossover	79
4.1.1. Energy Efficiency	80
4.1.2. Second Law Analysis	90
4.2. Experiments	93
4.2.1. Gas Phase Characteristics	93

4.2.2. Oxidation Experiments	99
4.3. Kinetic Effect in Process Simulation	114
4.4. Indirect Heat Recovery System	118
4.4.1. Reactor and Heat Exchanger Concept	119
4.4.2. Simulation of Indirect Heat Recovery	120
5. Discussion of Recombination and Heat Recuperation Concepts	126
6. Conclusion and Outlook	131
Appendix	134
A. Experimental Raw Data	134
B. Removal of Organic Components in Test Rig	141
C. Test Rig Volume	142
D. Derivation of Initial Values for Test Rig Model	142
E. Ceria Samples	143
F. Scanning Electron Microscope Images of Particles	144
G. Energy-Dispersive X-Ray Spectroscopy of Particles	149
Bibliography	159

List of Figures

1.1. Schematic of a two-step solar thermochemical redox cycle for splitting of H ₂ O or CO ₂	2
2.1. Schematic of different line and point focussing collector concepts.	6
2.2. Non-stoichiometry of ceria at equilibrium as a function of (a) the temperature and (b) the O ₂ partial pressure.	19
3.1. Schematic of the modelled redox cycle.	32
3.2. Depiction of control volumes for balance equations.	34
3.3. Depiction of the stable point of operation for setup 1.	35
3.4. Depiction of the path used to calculate entropies.	40
3.5. Schematic of the test rig.	44
3.6. Photograph of the test rig.	44
3.7. Thermocouples with elements of a high temperature insulation material.	46
3.8. Photograph of the test rig including the reference volume.	48
3.9. Setup for measuring the temperature profile inside the reaction tube.	49
3.10. Ceria samples prior to experiments.	51
3.11. Flow chart of the experimental procedure.	53
3.12. Flow charts of re-oxidation procedure and sub-procedures in Fig. 3.11.	54
3.13. Qualitative depiction of temperature and pressure curves, when (a) N ₂ or (b) O ₂ is fed to the furnace, including definitions of Δp_{BV-F} , Δp_{O_2} and Δp_{N_2}	55
3.14. Schematic of the partial volumes and respective temperatures for the definition of \bar{T}_{max}	63
3.15. Qualitative depiction of temperatures in the test rig.	63
3.16. Depiction of Δt and distinctive pressures, for an exemplary oxidation step.	65
3.17. Schematic of the indirect heat exchanger.	74
3.18. Depiction of the one-dimensional discretisation of the modelled media.	78
4.1. System efficiency of setup 1 as function of the heat recovery ratio.	81
4.2. Thermodynamic states of ceria streams entering or leaving the heat exchanger for setup 1.	81
4.3. System efficiency of setup 1 as function of the heat recovery ratio for H ₂ O and CO ₂ splitting.	83
4.4. Gibbs energy and equilibrium constant for thermolysis reactions.	84
4.5. System efficiency of setup 1 as function of the heat recovery ratio for different values of X_{ox}	85
4.6. Power demand for the production of 1 mol s ⁻¹ of H ₂ with setup 1 at $\epsilon = 0.45$	86
4.7. System efficiency of setup 1 as function of the heat recovery ratio for different values of f_{loss}	88
4.8. System efficiency of setup 2 as function of the heat recovery ratio.	88
4.9. System efficiency of setup 2 as function of the heat recovery ratio for $T_{ox} = 873$ K.	89
4.10. Thermodynamic states of ceria streams entering or leaving the heat exchanger for setup 2.	89

4.11. Entropy expressions per mol of ceria as a function of the heat recovery ratio for H ₂ O splitting with setup 1.	91
4.12. Entropy expressions per mol of ceria as a function of the heat recovery ratio for H ₂ O splitting with setup 2.	92
4.13. Molar volume of O ₂ calculated by ideal gas law and van der Waals equation in comparison.	93
4.14. Temperature profile measured under atmospheric pressure at a set temperature of 1773 K.	94
4.15. Knudsen number for an ideal gas at given temperature and pressure for tube diameters d that are present in the test rig.	95
4.16. Ratio between radiative and convective heat transfer and ratio between the temperature difference and the reference temperature, for $p = 100$ Pa and $f = 0.5$	96
4.17. Ratio between radiative and convective heat transfer and ratio between the temperature difference and the reference temperature, for $p = 100$ Pa and $f = 0.8$	97
4.18. Leakage determined from reference measurements and linear fit as function of temperature T_{K1}	97
4.19. Iterative approach to derive \bar{T} as a function of T_{K1}	98
4.20. Measured pressure curve and pressure curve after subtraction of calculated leakage for a reference measurement.	99
4.21. Measured pressures and temperatures during an experiment with a particle bed without addition of N ₂	100
4.22. Measured pressures for second and third oxidation step of an experiment with a particle bed without addition of N ₂	101
4.23. Pressure curves p_F for three different Δp_{O_2}	102
4.24. Pressure curves p_F for experiments with different samples.	103
4.25. SEM images of ceria samples before experiments.	104
4.26. SEM images of particles, (a) before and (b) after eight experiments.	104
4.27. Diffractograms of particles before and after experiments.	105
4.28. Pressure curves p_F for three different amounts of N ₂	106
4.29. Δt for different Δp_{N_2} as a function of T_{set}	107
4.30. Impact of amount of inert gas on the oxidation kinetics.	108
4.31. Ratio of computed and measured pressure increase as O ₂ enters the furnace, plotted against the corresponding time in the experiment.	109
4.32. $\Delta \delta$ during oxidation steps against time.	110
4.33. \bar{T} for experiments with $\Delta p_{O_2} = 164$ Pa and different Δp_{N_2}	110
4.34. \bar{T} for experiments with $\Delta p_{N_2} = 0$ and different Δp_{O_2}	111
4.35. Depiction of the oxidation kinetics for different Δp_{N_2}	113
4.36. Results of kinetic simulations for H ₂ O splitting with setup 1.	115
4.37. Schematic of Reactor and heat exchanger concepts using movable redox units.	119
4.38. Heat recovery ratio ϵ as a function of charging and discharging time for $d_{HS} = 6 d_{RU}$, $\alpha_{HS} = 10 \text{ W m}^{-2} \text{ K}^{-1}$ and $\epsilon_{HS} = \epsilon_{RU} = 0.5$	121
4.39. Temperature profiles for different points in time as a function of the x -position for $d_{HS} = 6 d_{RU}$, $\alpha_{HS} = 10 \text{ W m}^{-2} \text{ K}^{-1}$ and $\epsilon_{HS} = \epsilon_{RU} = 0.5$	121
4.40. Temperature profile of a charging step for concrete and $d_{HS} = 3 d_{RU}$, $\alpha_{HS} = 10 \text{ W m}^{-2} \text{ K}^{-1}$ and $\epsilon_{HS} = \epsilon_{RU} = 0.5$	122
4.41. Heat recovery ratio ϵ as a function of charging and discharging time for $d_{HS} = 6 d_{RU}$ and $\alpha_{HS} = 10 \text{ W m}^{-2} \text{ K}^{-1}$	123
4.42. Maximal heat recovery ratio ϵ_{max} (a) and respective charging and discharging times (b) as a function of the heat storage thickness.	124

4.43. Heat recovery ratio ϵ for different α_{HS} as a function of charging and discharging time.	125
5.1. Qualitative depiction of different heat transfer approaches.	129
A.1. Pressure and temperature curves for experiment with particle bed 1, $\Delta p_{O_2} \approx 46$ Pa and $\Delta p_{N_2} = 0$ (see table 3.2 for details).	134
A.2. Pressure and temperature curves for experiment with particle bed 1, $\Delta p_{O_2} \approx 162$ Pa and $\Delta p_{N_2} = 0$ (see table 3.2 for details).	135
A.3. Pressure and temperature curves for experiment with particle bed 1, $\Delta p_{O_2} \approx 245$ Pa and $\Delta p_{N_2} = 0$ (see table 3.2 for details).	135
A.4. Pressure and temperature curves for experiment with particle bed 1, $\Delta p_{O_2} \approx 162$ Pa and $\Delta p_{N_2} = 0$ (see table 3.2 for details).	136
A.5. Pressure and temperature curves for experiment with particle bed 1, $\Delta p_{O_2} \approx 167$ Pa and $\Delta p_{N_2} \approx 524$ Pa (see table 3.2 for details).	136
A.6. Pressure and temperature curves for experiment with particle bed 1, $\Delta p_{O_2} \approx 162$ Pa and $\Delta p_{N_2} = 0$ (see table 3.2 for details). Data set corresponds to the experiment shown in Figure 4.21.	137
A.7. Pressure and temperature curves for experiment with RPCs, $\Delta p_{O_2} \approx 164$ Pa and $\Delta p_{N_2} = 0$ (see table 3.2 for details).	137
A.8. Pressure and temperature curves for experiment with RPCs, $\Delta p_{O_2} \approx 164$ Pa and $\Delta p_{N_2} = 0$ (see table 3.2 for details).	138
A.9. Pressure and temperature curves for experiment with RPCs, $\Delta p_{O_2} \approx 168$ Pa and $\Delta p_{N_2} \approx 520$ Pa (see table 3.2 for details).	138
A.10. Pressure and temperature curves for experiment with particle bed 2, $\Delta p_{O_2} \approx 160$ Pa and $\Delta p_{N_2} = 0$ (see table 3.2 for details).	139
A.11. Pressure and temperature curves for experiment with particle bed 3, $\Delta p_{O_2} \approx 43$ Pa and $\Delta p_{N_2} = 0$ (see table 3.2 for details).	139
A.12. Pressure and temperature curves for experiment with particle bed 3, $\Delta p_{O_2} \approx 166$ Pa and $\Delta p_{N_2} \approx 270$ Pa (see table 3.2 for details).	140
B.1. Pressure and temperature curves before and after treatment to remove possible organic components and after execution of all experiments.	141
E.1. Particles in crucible after experiments.	143
E.2. Samples in the reaction tube.	144
F.1. Scanning electron microscope image of ceria particle as before experiments. 200-fold magnified. Corresponds to the particle shown in Figure 4.25(c).	144
F.2. Scanning electron microscope image of ceria particle as before experiments. 2000-fold magnified. Corresponds to the particle shown in Figure 4.25(d).	145
F.3. Scanning electron microscope image of ceria particle as before experiments. 10000-fold magnified.	145
F.4. Scanning electron microscope image of ceria particle after one experiment. 200-fold magnified.	146
F.5. Scanning electron microscope image of ceria particle after one experiment. 2000-fold magnified.	146
F.6. Scanning electron microscope image of ceria particle after one experiment. 10000-fold magnified.	147
F.7. Scanning electron microscope image of ceria particle after eight experiments. 200-fold magnified.	147
F.8. Scanning electron microscope image of ceria particle after eight experiments. 2000-fold magnified.	148

F.9. Scanning electron microscope image of ceria particle after eight experiments. 10000-fold magnified.	148
G.1. Particle surface before experiments with locations at which EDX spectra were recorded.	149
G.2. EDX of spectrum 1 in Figure G.1. Sample: Particles as before experiments.	149
G.3. EDX of spectrum 2 in Figure G.1. Sample: Particles as before experiments.	150
G.4. EDX of spectrum 3 in Figure G.1. Sample: Particles as before experiments.	150
G.5. EDX of spectrum 4 in Figure G.1. Sample: Particles as before experiments.	151
G.6. EDX of spectrum 5 in Figure G.1. Sample: Particles as before experiments.	151
G.7. EDX of spectrum 6 in Figure G.1. Sample: Particles as before experiments.	152
G.8. EDX of spectrum 7 in Figure G.1. Sample: Particles as before experiments.	152
G.9. EDX of spectrum 8 in Figure G.1. Sample: Particles as before experiments.	153
G.10. EDX of spectrum 9 in Figure G.1. Sample: Particles as before experiments.	153
G.11. Particle surface after one experiment with locations at which EDX spectra were recorded.	154
G.12. EDX of spectrum 10 in Figure G.11. Sample: Particles after one experiment.	154
G.13. EDX of spectrum 11 in Figure G.11. Sample: Particles after one experiment.	155
G.14. EDX of spectrum 12 in Figure G.11. Sample: Particles after one experiment.	155
G.15. Particle surface after eight experiments with locations at which EDX spectra were recorded.	156
G.16. EDX of spectrum 13 in Figure G.15. Sample: Particles after eight experiments.	156
G.17. EDX of spectrum 14 in Figure G.15. Sample: Particles after eight experiments.	157
G.18. EDX of spectrum 15 in Figure G.15. Sample: Particles after eight experiments.	157
G.19. EDX of spectrum 16 in Figure G.15. Sample: Particles after eight experiments.	158

List of Tables

2.1. Overview of different concepts of oxygen removal for two-step redox cycles and relevant literature.	11
2.2. Heat exchanger concepts categorized by mode of heat transfer.	14
2.3. Parameters for Equations 2.41 and 2.42.	27
3.1. Specifications of temperature and pressure sensors used in the test rig.	47
3.2. Experimental parameters.	55
3.3. Parameters and constants for gas phase calculations.	57
3.4. Parameters for polynomial fit $C_2 \cdot T^2 + C_1 \cdot T + C_0$ to data from Ref. [145] for μ , ρ , λ and c_p	58
3.5. Parameters used in the test rig model.	69
3.6. States used in the test rig model.	69
3.7. Parameters of the indirect heat recovery model.	77
4.1. Default simulation parameters.	80
4.2. Maximum ratio of system efficiency at a given oxidation rate and system efficiency without solid-solid heat exchanger.	116
4.3. Difference between modelled process and experiments.	117
C.1. Measurement of test rig volume.	142
E.1. Sample weights.	143

Nomenclature

Latin Symbols

\bar{T}	average gas temperature in furnace
\tilde{C}	concentration factor
\tilde{c}_p	specific isobaric heat capacity
\tilde{D}	ambipolar diffusion coefficient
\tilde{K}	surface exchange coefficient
A	area
a	activity
α	thermal diffusivity
C	fit parameter
c_p	molar isobaric heat capacity
d	thickness or diameter
D^*	diffusion coefficient of tracer
e_a	activation energy
f	fraction or (arbitrary) factor between 0 and 1
G	absolute Gibbs energy
g	acceleration of gravity
g	molar Gibbs energy
Gr	Grashof number
H	absolute enthalpy
h	molar enthalpy
K	reaction quotient
k	reaction rate constant
K^*	surface exchange coefficient of tracer
k_∞	pre-exponential factor of reaction rate constant
K_{eq}	equilibrium constant

L	characteristic length
M	molar mass
m	reaction order
N	number of particles
n	amount of substance
Nu	Nusselt number
p	pressure
Pr	Prandtl number
Q	heat
R	universal gas constant
r	radius
R^2	coefficient of determination
Ra	Rayleigh number
S	absolute entropy
s	molar entropy
T	temperature
t	time
U	absolute internal energy
u	molar internal energy
V	volume
v	molar volume
X	conversion
x, y, z	space coordinates
Z	placeholder for absolute thermodynamic quantity
z	placeholder for molar thermodynamic quantity

Greek Symbols

α	absorptivity
α	heat transfer coefficient
β	isobaric volume expansion coefficient
δ	oxygen non-stoichiometry

ϵ	heat recovery ratio
η	efficiency
λ	thermal conductivity
μ	chemical potential
μ	dynamic viscosity
ν	kinematic viscosity
ν	stoichiometric factor
Φ	view factor
ϕ	porosity
ρ	density
σ	Stefan-Boltzmann constant
τ	transmittance
$\tilde{\beta}$	extinction coefficient
ε	emissivity

Reoccurring Sub- and Superscripts

1	at thermodynamic state 1 (any other integer analogously)
12	from thermodynamic state 1 to 2 (any other combination of integers analogously)
o	at standard pressure
amb	ambient
BV	buffer volume
conv	convection
eff	effective quantity
F	furnace
HS	heat storage unit
L	leakage
ox	oxidation
rad	radiation
recomb	recombination
red	reduction
ref	reference

RT reaction tube

RU redox unit

TC thermocouple

TR test rig

Abbreviations

BET	Brunauer-Emmett-Teller
CV	control volume
CPC	compound parabolic concentrator
CR5	counter-rotating ring receiver/reactor/recuperator
DNI	direct normal irradiation
EDX	energy-dispersive X-ray spectroscopy
FTS	Fischer-Tropsch synthesis
GHG	greenhouse gas
HE	heat exchanger
HHV	higher heating value
MBR2	moving brick receiver-reactor
ppi	pores per inch
PU	polyurethane
RPC	reticulated porous ceramic
SEM	scanning electron microscopy
TC	thermocouple
TGA	thermogravimetric analysis
XRD	X-ray powder diffraction

1. Introduction

Reduction of anthropogenic greenhouse gas (GHG) emissions is a widely recognised global challenge. The transition to sustainable technologies is however yet to be achieved. For example, a report from 2021 published by the European Commission [1] states that the targets set ten years earlier in a white paper from 2011 [2] to reduce greenhouse gas emissions in the European Union have largely been missed. According to the white paper [2], GHG emissions have to be reduced by 80 % to 95 % with respect to 1990 by 2050 in order to limit the effect of climate change to less than 2 °C. It is envisioned in said white paper that by the same time, GHG emissions in the transport sector will have been reduced by 60 % compared to 1990, by several measures, amongst which is the development and deployment of sustainable fuels. In aviation for instance, low-carbon sustainable fuels are supposed to reach a share of 40 % by 2050. The aforementioned evaluation of this vision in 2021 [1] showed that while some improvements were achieved, only limited progress has been made and the transport sector is still dominated by fossil fuels. In case of aviation, renewable fuels not yet being cost competitive is mentioned as a reason. To tackle this problem, development of energy efficient processes for the production of renewable fuels is crucial.

Promising candidates for such a process are so-called two-step solar thermochemical redox cycles. Two-step redox cycles are processes, in which a chemical reaction that is otherwise typically difficult to achieve is separated into an oxidation and a reduction step. A redox material, commonly a metal oxide, is used, as oxygen donator and acceptor in these two steps. This way, for example the thermal splitting of water steam into oxygen and hydrogen is possible at significantly lower temperatures than in a single-step-approach (thermolysis) [3, 4]. In the two-step splitting of H₂O, a previously reduced redox material takes up oxygen, thereby oxidising and driving the splitting of H₂O. Afterwards, the redox material is again thermally reduced at high temperatures. Besides the splitting of H₂O, also splitting of CO₂ or a combination of both has been frequently investigated [5]. Both are depicted in Figure 1.1. In case of CO₂-splitting, the product is CO. Combined with H₂O-splitting, either in the same reactor or separately, synthesis gas (syngas), a mixture of H₂ and CO, is produced. This versatile intermediate product can be further processed to different carbonaceous base chemicals or fuels, for example via the Fischer-Tropsch synthesis (FTS) [6]. Based on Refs. [7–9], the reduction of the redox material can be described as



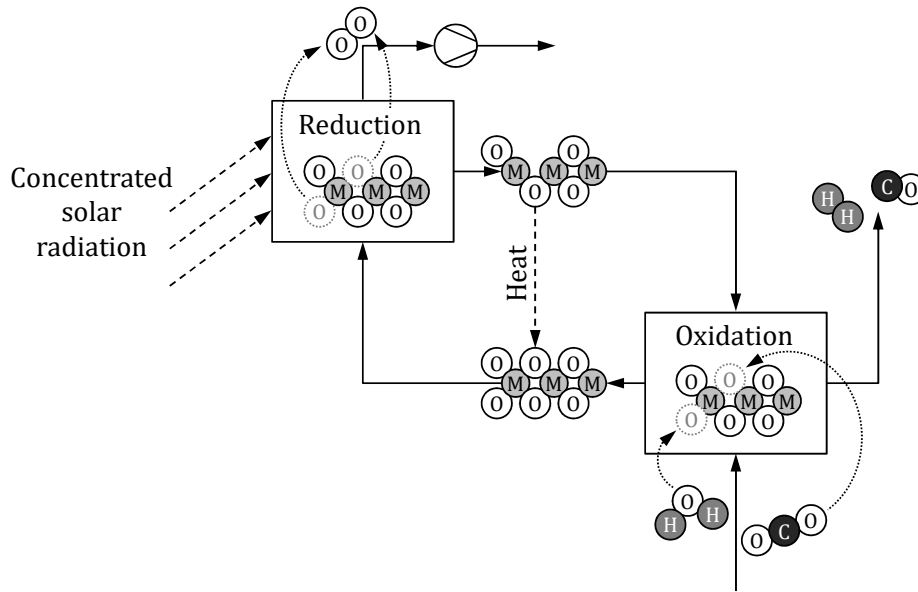
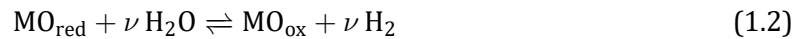
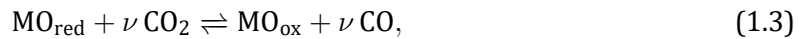


Figure 1.1.: Schematic of a two-step solar thermochemical redox cycle for splitting of H₂O or CO₂. M represents a metal ion in the lattice of the redox material. The process is exemplified for a thermal reduction step supported by vacuum pumping.

the according oxidation with H₂O is given by



and the oxidation with CO₂ reads



where MO_{ox} and MO_{red} represent a redox material, typically a metal oxide, in its oxidised and reduced state, respectively. The stoichiometric factor ν depends on the exact stoichiometry of MO_{ox} and MO_{red}. The reduction is endothermic [7, 8], whereas the oxidation reactions can be either endothermic or exothermic, depending on the redox material [10, 11]. This process can be operated in a sustainable way by providing the heat required for the reduction through concentrated solar radiation, as indicated in Figure 1.1.

Such a redox cycle can be used to produce syngas, which is further processed to a carbon-based solar fuel. During the combustion of the fuel, CO₂ is released to the ambience. However, the theoretically same amount of CO₂ is needed as a feedstock for the redox cycle. If this CO₂-feed is supplied by direct air capture or another renewable carbon source, the resulting negative emissions compensate the emissions of the fuel combustion. This way, the redox process is capable of closing the carbon cycle and thus producing a carbon-neutral fuel. If only H₂O is split, a

product stream consisting only of H_2 and unreacted H_2O can be obtained. Hence, highly pure H_2 can be produced without the need of complex downstream processing.

The reduction typically takes place at a significantly higher temperature than the oxidation. As a consequence, a large share of the process's heat demand is associated with this temperature swing [12, 13]. Thus, heat recuperation between the two reaction steps, as depicted in Figure 1.1, is an important measure towards efficient and competitive two-step solar thermochemical redox cycles [13–16]. In a solid-solid heat exchanger (HE) for this task, the redox material undergoes a temperature change. It is in the material's nature to change its oxygen content as the temperature changes. This property makes these materials suitable for two-step solar thermochemical redox cycles, but at the same time it means that reduction and oxidation may occur not only in the reactors, but also in the HE. Cold oxidised redox material that is heated is expected to release O_2 [17]. If the hot reduced redox material, which is cooled in the HE gets into contact with this O_2 , it might be re-oxidised before the H_2O or CO_2 splitting reaction [17]. This way, the material's potential to produce syngas is reduced, which has a negative impact on the overall efficiency. In the present work, this oxygen crossover between cold and hot redox material is referred to as recombination. Siegrist et al. [17] estimated the extent to which recombination takes place for exemplary operating conditions, implying that the degree of recombination can be relatively low. These estimations are however based on strong and optimistic assumptions, such as an oxygen partial pressure higher than typical for this kind of process [3]. The oxygen partial pressure in the HE, which results from the release and uptake of O_2 by the cold and hot redox material, respectively, was not calculated. Instead, the aforementioned high value was assumed, presumably resulting in an underestimation of the O_2 release and thus the recombination effect. The pioneering work by Siegrist et al. shows that heat recovery might be beneficial despite recombination, which would open up more options in HE development, but at the same time raises the question whether the recombination effect was underestimated in their assessment. This motivates further investigations on the oxygen crossover in solid-solid HEs, which is studied both theoretically and experimentally in the present work.

Since the oxygen crossover is associated with the temperature change in the HE, it is hypothesised in the present work that a correlation between heat recuperation effectiveness and recombination extent can be observed. It is further investigated if the kinetics of the recombination effect can be influenced such that the oxygen crossover can be mitigated. The oxygen transport in the HE can be described by three mechanisms, which occur in five consecutive steps: First, diffusion of oxygen ions in the bulk of the redox material to its surface. Second, oxygen release from the redox material. This step is defined by the surface reaction. Next, the mass transport of O_2 in the gas phase, by convection and/or diffusion. This step is followed by the uptake of oxygen by the redox material, which is again a surface reaction. The last step is again bulk diffusion of oxygen ions. As fast reaction kinetics in the reduction and oxidation reactor are indispensable for an efficient process, it would be unsuitable to modify the redox material such that bulk diffusion and surface reaction are decelerated. Therefore, only manipulation of the transport of O_2 in the HE's gas phase is considered as a measure to mitigate recombination. It is hypothesised

in the present work that an inert gas in the atmosphere can act as a mass transport resistor for the O_2 molecules, which is investigated in experiments using a dedicated test rig. Furthermore, this study aims to answer the question, whether a HE design, in which the recombination effect is not avoided by technical countermeasures, is suitable to improve the process efficiency or not. For this purpose, the recombination effect is modelled and simulated assuming chemical equilibria. In a second step, the model is extended to include constant reaction rates, which are discussed based on the experimental results. In addition, a numeric heat transfer model is used to investigate an indirect heat recovery concept including a heat storage unit, which aims to avoid recombination.

The theory that lays the foundation for this work is explained and an overview over relevant literature and developments made in the field is given in Chapter 2. Thereafter, the methodology of both, theoretical and experimental investigations is presented in Chapter 3. Herein, the model for the calculation of the recombination effect is described, followed by materials and methods for experiments and lastly the numeric model for the indirect HE concept, is given. Results of simulations of the recombination effect under equilibrium assumption, experimental work on the kinetics of recombination, simulations of the recombination for given reaction rates and simulations of the indirect heat exchanger concept are presented in Chapter 4. A discussion of these results and their consequence on different HE designs follows in Chapter 5 before finally conclusions and potential future work are discussed in Chapter 6.

2. Theory and Background

This chapter gives an overview over the theoretical background on which this study is based and the current state of the research in the field. First, the fundamental principles of concentrating and utilising solar radiation are introduced. This section is limited to the basics as the present work is focused on the thermochemistry rather than the concentration of solar radiation. After that, two-step solar thermochemical redox cycles are explained. Here, the investigated redox cycle as well as related developments are presented. Next, the theory on kinetics and thermodynamics, relevant for this study are introduced. This includes the redox behaviour of the redox material ceria, its oxidation and reduction equilibria and the descriptions of kinetic mechanisms.

2.1. Fundamentals of Concentrating Solar Radiation

The goal of solar thermochemistry is to utilize solar heat to directly drive a chemical reaction rather than going the indirect path of converting solar radiation into electricity and performing electrochemical reactions. Thereby, it aims at achieving higher efficiencies by shortening the process chain [18]. Most solar thermochemical processes, especially the two-step solar redox cycle discussed in this work, require high temperatures [13, 19, 20]. These can be achieved by concentrating solar radiation to create a high solar heat flux.

Concentrating systems comprise a collector, commonly a mirror or a set of mirrors and a receiver, onto which the collector focuses the collected solar radiation. There are line focusing systems, which project the radiation from the collector surface onto a linear receiver, e.g. a tube holding a heat transfer medium and point focusing systems, in which the radiation is concentrated on a receiver in a central point [21]. A measure for the degree of concentration is the concentration factor \tilde{C} . It is defined as [22, 23]

$$\tilde{C} = \frac{\dot{Q}_{\text{rec}}}{I A}, \quad (2.1)$$

where \dot{Q}_{rec} is the radiative heat flow that reaches the target, A is the target area and I is the direct normal irradiation (DNI) [23], which is the solar radiation reaching the earth in a straight line from the sun, related to a perpendicular surface area [24]. In many applications, the radiation is absorbed in a cavity. In this case the, target is an opening, referred to as aperture, through which the radiation enters the cavity receiver.

Examples of line focusing systems are linear Fresnel reflector systems with mirrors placed in parallel to the receiver tube and parabolic troughs, which use a curved mirror as collector [21].

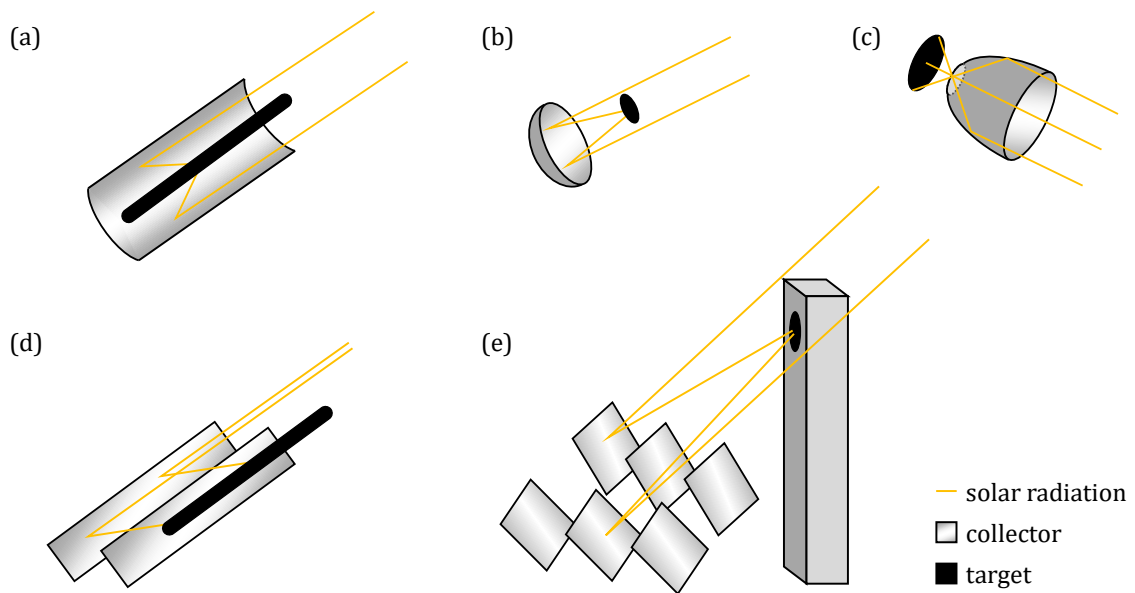


Figure 2.1.: Schematic of different line and point focussing collector concepts. (a): parabolic trough; (b): parabolic dish; (c): compound parabolic concentrator; (d): linear Fresnel reflector; (e): heliostat field with tower.

Such systems typically reach concentration factors of 30 to 100 and operating temperatures of up to 823 K [21, 25]. Both concepts are visualised in Figure 2.1.

Common examples of point focusing systems are solar towers combined with a heliostat field, shown in Figure 2.1(e) and dish systems in which a dish-shaped mirror focusses the solar radiation onto a connected receiver, depicted in Figure 2.1(b) [21]. Heliostats are mirrors, placed in the vicinity of the tower which holds a central receiver. For solar towers, concentration factors are commonly in the range 300 to 1500 and temperatures above 1773 K can be reached [21, 25]. However, for thermochemical applications, higher concentration factors and temperatures were suggested [26, 27] and concentrated solar heat fluxes $\tilde{C} I$ of more than 3 MW m^{-2} were demonstrated at a research plant [28, 29]. Another option to increase the heat flux is by supplementing the system with secondary concentrating optics, such as a compound parabolic concentrator (CPC) [30] that is mounted in front of the receiver [31]. CPCs can also increase the target area, thereby reducing spillage and homogenize the radiation within the receiver [32]. The operating principle of a CPC is illustrated in Figure 2.1(c).

Dish systems reach concentration factors of 1000 to 5000 and temperatures can exceed 2273 K [21, 25]. Due to size limitations, dish systems are typically designed for a thermal power below 100 kW [21].

When solar radiation is concentrated, the following energy loss mechanisms can occur [31]:

- To concentrate solar radiation, the surface of a collector cannot be perfectly perpendicular

to the incoming radiation. Thus, only a projected area, perpendicular to the radiation is hit with the intensity of the DNI. This is described by the so-called cosine loss.

- A fraction of the collector is shadowed, e.g. by other collectors. This effect is called shading.
- The non-ideal reflectivity of a real mirror.
- In heliostat fields, radiation that was reflected by one heliostat might be blocked by another, which is referred to as blocking.
- Atmospheric attenuation, i.e. attenuation of the radiation between collector and target.
- The beam guidance can never be perfect. Therefore, a fraction of the concentrated radiation misses its target. This loss mechanism is called spillage.
- In a system with CPCs, CPC transmission losses can occur, which means that part of the radiation is absorbed or reflected such that it leaves through the CPC aperture.

Due to the necessity of high temperatures, solar thermochemical redox cycles depend on point focussing systems. Especially solar towers are a promising technology for large-scale plants. Receiver and reactor can be two separate elements in an indirectly heated reactor concept, where a heat transfer fluid such as air is heated in the receiver and then transfers heat to the reactor [33, 34]. Richter et al. proposed a concept in which inert heat transfer particles are irradiated and then mixed with reactive particles [35]. Alternatively, a receiver reactor is used, in which the reactive material is directly irradiated [12, 13, 36]. The concentrated solar radiation enters a cavity receiver, which is the reactor, through the aperture. The main cause for losses from such a receiver is typically radiation [13, 37], due to the high operation temperatures. Therefore, the efficiency can often be approximated by the absorption efficiency of a perfectly insulated receiver, which reads [38, 39]

$$\eta_{\text{rec}} = \frac{\alpha \tilde{C} I - \varepsilon \sigma T_{\text{rec}}^4}{\tilde{C} I}, \quad (2.2)$$

where α and ε are the absorptivity and emissivity, respectively, σ is the Stefan–Boltzmann constant and T_{rec} is the temperature of the receiver. Assuming a blackbody receiver, Equation 2.2 is simplified to [22]

$$\eta_{\text{rec}} = 1 - \frac{\sigma T_{\text{rec}}^4}{\tilde{C} I}, \quad (2.3)$$

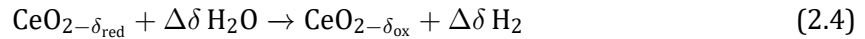
which is commonly used in the literature for simple receiver models, for example in Refs. [11, 18, 23]. Radiation from the ambience can also be considered in the radiation losses, which are then expressed as $\sigma (T_{\text{rec}}^4 - T_{\text{amb}}^4)$ [40, 41]. The effect is however usually negligible, as typically $T_{\text{rec}}^4 \gg T_{\text{amb}}^4$.

In directly irradiated receiver reactors it is necessary to seal the aperture, for example with a quartz glass window [22], to prevent the reactants and products from mixing with ambient air. Reactors with windows on laboratory scale are for example discussed in Refs. [12, 13, 36] and on a larger scale in Ref. [32].

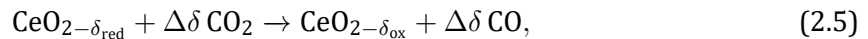
2.2. Two-Step Solar Thermochemical Redox Cycles

Generating hydrogen via a redox cycle is an old concept. One example, in which iron-oxide is used as an oxygen carrier is called steam-iron process, a technology that was developed in the late 19th/early 20th century [42–44]. Thermochemical cycles for hydrogen production, powered by a nuclear heat source, often with more complex reaction schemes containing more than three reaction steps, were investigated especially in the 1960s and 1970s [18, 45–47]. In recent years, the use of concentrated solar radiation has renewed the interest in thermochemical cycles, especially in two-step thermochemical redox cycles.

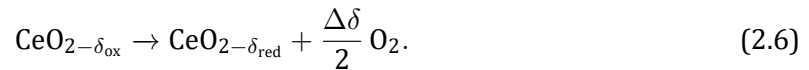
A frequently investigated redox material is non-stoichiometric ceria (cerium(IV) oxide) [13, 46, 48, 49]. Its molecular formula is $\text{CeO}_{2-\delta}$, where δ is the so-called oxygen non-stoichiometry as explained in detail in Section 2.3.1. Ceria has beneficial properties such as good reaction kinetics (also explained in Section 2.3.1), and thermodynamic data on the material is available [50, 51]. It has therefore become a reference material that is commonly used in studies for comparability, as in the present study, or as a benchmark for other materials [8, 49, 52]. However, its thermodynamics which cause the need for high reduction temperatures also pose challenges to the process design and hence material development is still an ongoing task. Amongst other materials that were investigated are doped and undoped iron oxides [53–55], doped ceria [8, 9, 49, 56, 57] or cerium-based mixed-phase ceramics [58], zinc-oxide [55, 59, 60] and perovskites [52, 61, 62]. As mentioned earlier, the redox material is oxidised, when H_2O or CO_2 are split. For ceria this is described by [63]



or



where δ_{ox} and δ_{red} are the oxygen non-stoichiometry after the oxidation and reduction, respectively and $\Delta\delta = \delta_{\text{red}} - \delta_{\text{ox}}$. The oxidation of ceria is exothermic [63] and typically takes place at temperatures of about 873 K to 1373 K [13, 20, 64]. In the reduction, oxygen is released from the redox material's crystal lattice, which requires higher temperatures. For ceria, the temperature of a thermal reduction step is typically in the region of 1773 K [13, 19, 20]. The endothermic reaction is given by [63]



The reduction is favoured at high temperatures and low O_2 partial pressures [50]. An important performance indicator for the solar thermochemical redox cycle is the solar-to-fuel efficiency, which is defined as the heating value of the produced fuel in relation to the solar energy demand of the process [13].

The most advanced reactor concept for two-step solar thermochemical H_2O and CO_2 -splitting are discontinuous reactors, with a stationary monolithic redox material. In such reactors, the

redox material is directly irradiated. Marxer et al. [13] tested a 4 kW reactor holding ceria-elements in the form of a reticulated porous ceramic (RPC) with dual-scale porosity in the mm and μm -range for the conversion of CO_2 to CO at reduction temperatures of up to 1773 K. In the experimental campaign, a solar-to-fuel efficiency of 5.25 % was reached.

After scaling up, the 4 kW reactor to a 50 kW reactor, the whole process-chain from concentration of solar radiation to a liquid fuel was demonstrated on a designated test plant. A heliostat field is used to focus the solar radiation onto the aperture of the reactor, which is placed on a solar tower. Syngas is converted to a liquid fuel via FTS. [28, 29, 65]

Despite the fact that the whole process-chain was successfully demonstrated, improvements in terms of energy efficiency are needed to make the process competitive. Concentration of solar radiation is associated with the loss mechanisms listed above, in Section 2.1. Subsequent to the solar concentration, the main energy demand of a two-step solar thermochemical redox cycle for splitting of H_2O and CO_2 consists of the reaction enthalpy of the endothermic reduction step, heating the redox material from the oxidation to the reduction temperature, evaporating and overheating H_2O and/or heating CO_2 to the oxidation temperature, auxiliary energy demands, such as the vacuum pumps or purification of sweep gas and compensation of heat losses [12, 13]. At the high temperatures relevant for this process, main source for heat losses from the hot receiver to the ambience is radiation [13, 37] which scales with the temperature to the power of 4. The largest share of the overall energy demand, however, is associated with sensible heating of the redox material [12, 13]. This is especially critical for discontinuous reactors, as here not only the redox material, but the whole reactor undergoes a temperatures swing.

In the following, improvements made in the development of two-step solar thermochemical H_2O and/or CO_2 splitting, which are relevant for the present work are described. First, means of reducing the O_2 partial pressure during the reduction step are discussed. Low O_2 partial pressures support the reduction and thus contribute to lower reduction temperatures [50]. Thereafter, solid-solid heat exchanger concepts for the recuperation of sensible heat from the redox material are presented. Lastly, methods for the production of porous ceria structures are described. Suitable porous redox structures are an important factor to achieve more uniform temperature profiles in the material [66], so that a larger portion of the material can be reduced.

2.2.1. Oxygen Partial Pressure Control for Reduction Step

The reduction step can be supported by means of decreasing the O_2 partial pressure, thus increasing the degree of reduction or lowering the necessary reduction temperature [50]. Methods to reach low O_2 partial pressures, which are described in this section are depicted and summarised in Table 2.1. One method is to utilize a vacuum pump [12, 13], as depicted in Figure 1.1. Another option is to sweep the reduction reactor with an inert gas, flushing out the O_2 [64, 67]. Vacuum pumping is however considered to have efficiency benefits over application of a sweep gas [12, 13], especially since Brendelberger et al. [64] showed that the sweep gas demand has been underestimated in the past.

Instead of using a mechanical vacuum pump or a jet pump, a so-called thermochemical oxygen pump [68–73] was suggested. This concept utilizes a second redox cycle, with a secondary redox material, sometimes referred to as pumping material, which can be reduced at lower temperatures. In this context, the primary redox material is sometimes called splitting material, as it is used in the original redox cycle to split H_2O or CO_2 . During the reduction of the splitting material, the pumping material is oxidised with the released O_2 . For this to work, the two materials must share a common atmosphere, while the pumping material is present at significantly lower temperatures than the splitting material. [71–73] In theoretical studies, it was shown exemplarily for the $\text{Co}_3\text{O}_4/\text{CoO}$ redox pair [70], as well as the perovskites $\text{SrFeO}_{3-\delta}$ and $\text{SrMnO}_{3-\delta}$ [72] as pumping materials that thermochemical pumps have significantly lower energy demand than mechanical or jet pumps at low target pressures, but a higher energy demand at higher pressures. Thermochemical oxygen pumping to support the reduction of ceria was experimentally demonstrated with SrFeO_3 by Brendelberger et al. [71] and with more perovskites by Pein et al. [73]. The principle of a thermochemical pumping material can also be used to clean a sweep gas as suggested by Ezbiri et al. [69].

A similar approach was proposed by Ermanoski et al. [74]. Here, the use of a sorbent cycle is suggested, where oxygen can be adsorbed by the sorbent at ambient temperature, thereby creating low oxygen partial pressures for the reduction of the redox material. At higher temperatures up to approximately 623 K the oxygen desorbs and is released to the ambient air. [74] Preliminary experimental tests were conducted on $\text{YBaCo}_4\text{O}_{7+\delta}$ by Xu et al. [75] showing the principle feasibility of the concept. One advantage that this technology might have over thermochemical oxygen pumps is associated with lower operating temperatures, which result in a theoretically lower energy demand [70, 72, 74].

Another option to decrease the O_2 partial pressure is the introduction of a reducing agent [76]. In such a thermochemical reduction step, the reducing agent would act as an oxygen sink, as it undergoes a chemical reaction with O_2 . A suitable reducing agent is CH_4 , which reacts with O_2 forming a syngas [76]. Together with the splitting of H_2O or CO_2 in the oxidation step, the net reaction of this redox cycle equals that of steam methane reforming or dry methane reforming, respectively [10, 11, 77]. It is therefore commonly referred to as redox reforming. In redox reforming, significantly lower O_2 partial pressures can be achieved in the reduction step, compared to a thermal reduction step supported by vacuum pumping or inert gas sweeping [76] and thus lower reduction temperatures and/or a more effective reduction are feasible. However, if the reducing agent does not originate from a renewable source, a fossil fuel, such as natural gas is introduced to the process. In this case, the concept is not carbon neutral and causes net CO_2 emissions. Both theoretical [10, 11, 78–80] and experimental [79–83] investigations of redox reforming were conducted in recent years.

Table 2.1.: Overview of different concepts of oxygen removal for two-step redox cycles and relevant literature.

Vacuum pump	Inert sweep gas	Thermochemical oxygen pump	Sorbent cycle	Reducing agent
Refs. [12, 13]	Refs. [64, 67]	Refs. [68–73]	Refs. [74, 75]	Refs. [10, 11, 76, 78–82]

2.2.2. Solid-solid Heat Exchanger Concepts

The temperature swing between oxidation and reduction step results in a significant heat demand for sensible heating of the redox material [12, 13]. In case of discontinuous reactors, the whole reactor has to be heated after the oxidation step, amplifying this effect. In an experimental study, Marxer et al. [13] find that for their discontinuous reactor design, more than 60 % of the total heat demand of the redox cycle is used for this sensible heating. Several studies pointed out that heat recuperation between hot and cold redox material is necessary to reach high energy efficiencies [13–16]. The heat recovery can be quantified with the ratio of the heat that was recovered in the HE to the heat that is theoretically available from the hot material [7, 84, 85]. Throughout the present study, this quantity is referred to as heat recovery ratio ϵ . Different concepts to achieve heat recuperation for the solid phase were presented in the literature. In the following, an overview over different approaches to realise solid-solid heat recovery within solar thermochemical redox cycles is given. All concepts are summarised and categorised by the mode of heat transfer in Table 2.2.

One approach is the use of rotating elements, which move the redox material through a reduction and an oxidation zone while exchanging heat in-between. An early design of that type was the counter-rotating ring receiver/reactor/recuperator (CR5) [86–90], an assembly of multiple counter-rotating parallel rings. In this concept, the reactive material is placed at the outer diameter of the rings. In an irradiated zone the material is thermally reduced. The rotation then transports the material into a splitting zone where it is oxidised, splitting H_2O or CO_2 . As two adjacent rings rotate in opposite directions, redox material from the hot zone can preheat redox material from the cold zone in a counter-flow manner. [86, 87]

Different simulations of the CR5 concept predict heat recovery ratios of up to 88 % [88, 89]. Despite such a high theoretical effectiveness of the heat recuperation, the solar-to-fuel efficiency was found to be below 1 % in experiments [90]. In addition, the system suffered from technical problems such as cracking of the material, which hindered the rotation of some of the rings and limited mass flow out of the reduction zone [90].

Another example of a concept using counter rotating elements was presented by Lapp et al. [84]. Instead of parallel rings, this concept utilizes concentric cylinders. The outer hollow cylinder is made from the reactive material. It rotates through the oxidation and reduction zone. The inner cylinder is also hollow and consists of an opaque solid. This material is inert and acts as a heat transfer medium. The inner cylinder rotates in the opposite direction of the outer cylinder. In regions in which the outer cylinder is hotter, heat is transferred to the inner ring and in regions in which the inner ring is hotter vice versa. This way the inner ring transports heat from hot parts of the reactive material to colder parts, so that heat is recuperated. A numeric model yields heat recovery ratios of 41 %. Parameter variations can boost ϵ to more than 50 %. However, the optimisation of ϵ alone might not be sufficient to optimise the process, as it can result in a lower reduction temperature and thus a less effective reduction. [84]

Direct counter current heat recovery can be implemented with linearly moving units of redox material instead of rotating elements. Falter et al. modelled the behaviour of such HEs [40, 41, 91]. To that end, they developed a generic model in which heat is transferred between RPCs of ceria separated by a wall. The RPCs pass through a number of HE chambers in which they remain for a given residence time. Heat recovery ratios close to 70 % at a total residence time in the HE of approximately 3000 s are predicted, if the HE is divided into 15 or more chambers. [41]

Another approach to separate RPCs of hot and cold redox material in a counter current HE is to encapsulate each RPC in an individual reactor and move the resulting reactor train rather than the RPCs, as was suggested by Patankar et al. [92–94]. In this concept, heat recovery is realised by radiation through sapphire windows in the reactors and theoretical investigations predict a heat recovery ratio of 80 % for a system that produces 100 kg of H₂ per day with a residence time in the HE of 900 s and a heat recovery ratio of 90 % at a residence time of 2700 s [93]. In another theoretical study, the use of thermochemical oxygen pumping in combination with the reactor train system was investigated, resulting in a higher cycle efficiency as well as a higher H₂ yield compared to vacuum pumping [94].

Ermanoski et al. [12] suggested a continuous particle-based concept, in which reactive particles are transported from an oxidation chamber to a reduction chamber via a screw elevator. In the reduction chamber they are lifted by a second screw elevator to an irradiated zone, where they are thermally reduced. Afterwards, the particles fall into a tube in the center of the second screw elevator. From there, they move back to the oxidation chamber, driven by gravity. This way, counter current heat exchange through the tube wall is implemented. [12] In experiments using sand at temperatures up to 433 K, heat recovery ratios of approximately 25 % to 50 % were observed [95].

Siegrist et al. [17, 96] proposed a concept in which so-called bricks, porous monolithic redox

structures, are cycled between a reduction and an oxidation step. It was called moving brick receiver-reactor (MBR2). The bricks are conveyed through a receiver-reactor where they are directly irradiated and thermally reduced. On their way to the splitting reactor, the hot bricks pass through a heat exchanger where they preheat cold bricks from the oxidation step in a counter flow arrangement. The reactors may be separated from the HE via pressure locks or connected to the HE without separation. [17, 96]

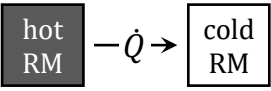
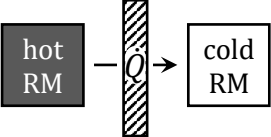
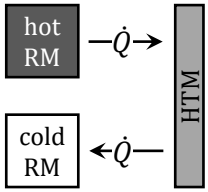
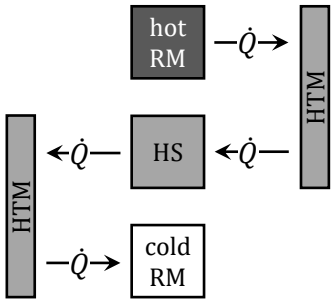
In contrast to the concepts by Falter et al. [40, 41, 91] and Patankar et al. [92–94], Siegrist et al. [17] suggest to avoid physical separation of the two flows of redox material to improve the heat transfer. They estimated the resulting recombination effect roughly as was described in Chapter 1. As measure for the recombination, Siegrist et al. introduce a fraction of recombination f_{recomb} , which is defined as the number of available oxygen vacancies to split H_2O or CO after recombination, divided by the available number of oxygen vacancies, if no recombination had taken place [17].

Indirect heat transfer via a heat transfer medium allows to avoid the recombination effect as hot and cold redox material are separated spatially or in time. It can be used in combination with discontinuous reactor concepts. Brendelberger et al. [15] discussed an approach to recover heat from a stationary monolith receiver reactor. After the reduction step, heat from the hot redox material is used to charge a heat storage with a heat transfer fluid. After the oxidation of the reactive material, the heat transfer fluid is used to discharge the heat storage and preheat the cold redox material for the next reduction step. This way, the phase in which the reactive material is irradiated can be shortened. Simulations show that for a single heat storage unit the solar heat input could be decreased by up to 40 %. [15]

A similar approach was demonstrated in a solar simulator, using a prototype comprising a 4 kW solar reactor and two thermocline heat storage units by Lidor et al. [97]. N_2 is used as an inert heat transfer fluid to charge one of the heat storage units after the reduction reaction. After the oxidation reaction, heat can be recovered from the heat storage unit to preheat the reactor for the upcoming reduction. In experiments, it was found that up to 70 % of sensible heat could be extracted from the RPC in the reactor. However, due to high heat losses through the piping, the temperature in the heat storage unit was insufficient to perform the heat recuperation step. [97]

Indirect concepts can also be applied to continuously operated systems. Felinks et al. [7] suggested a particle based concept. Herein, reactive particles are used as the redox material and are cycled between a reduction and an oxidation reactor. Inert ceramic particles of a different size are used as a heat transfer medium. The inert particles are alternately mixed with hot and cold reactive particles, thereby transferring heat from hot to cold reactive particles. Due to the different size of inert and reactive particles, mechanical separation of the two particle types is possible. Multiple mixing and separating stages approximate a counter current HE. For this approach, Felinks et al. calculated heat recovery ratios in excess of 70 % with a numeric model. This result was found for six stages using ceria as redox material and alumina as heat transfer medium. [7]

Table 2.2.: Heat exchanger concepts categorized by mode of heat transfer. RM: redox material; HTM: heat transfer medium; HS: heat storage unit.

Heat transfer	Concepts	Specifications
Direct		
	CR5 [86–90]	Redox material on counter rotating discs.
	MBR2 [17, 96]	Brick-like redox units in counter flow arrangement.
Through wall		
	Falter et al. [40, 41, 91]	Linear counter flow of redox material.
	Patankar et al. [92–94]	Redox material in reactors moving as reactor train.
	Ermanoski et al. [12]	Redox particles moved by screw elevators.
Via heat transfer medium		
	Lapp et al. [84]	Rotating cylinders, solid heat transfer medium.
	Felinks et al. [7]	Inert ceramic particles as heat transfer medium.
	Yuan et al. [85]	Liquid metal as heat transfer medium.
Via heat transfer medium and storage unit		
	Brendelberger et al. [15]	Gaseous heat transfer fluid, porous heat storage medium.
	Lidor et al. [97]	Gaseous heat transfer fluid, two heat storage units.

The concept of heat transfer particles was also studied for the use in indirectly heated reduction reactors by Richter et al. [35]. Here the heat transfer particles are irradiated instead of the reactive material, which is heated by mixing with the hot heat transfer particles.

Yuan et al. [85] suggested an indirect HE concept based on a liquid metal as a heat transfer fluid. The concept includes an array of discontinuous reactors, arranged in a cycle. These reactors can be operated in a cyclic manner, in which each reactor undergoes a reduction step followed by several heat recuperation steps with the other reactors and an oxidation step, which is again followed by heat recuperation steps. This way, semi continuous operation of the overall reactor array is possible. The liquid metal is used to supply heat for the reduction step and to enable heat recuperation between the reaction chambers. For heat recuperation, the reaction chambers are connected by pipes to allow heat exchange via the liquid metal heat transfer medium. Liquid metal is also heated in a solar receiver to provide heat for the reduction. This indirect approach, like the aforementioned indirect particle approach [35], allows separate optimisation of reactors and receiver. The redox material is coated on tubes inside the reaction chambers through which the liquid metal is flowed. In simulations, heat recovery via the piping network was calculated to reach 80 % of the heat stored in reactors and redox material. [85]

2.2.3. Porous Redox Material Structures

In the early 1960s, Schwartzwalder et al. invented and patented a method for the production of porous ceramic structures [98]. This method is today commonly known as replica method [99–101] or replication method [102, 103]. In this method, an open celled sponge is used as a template, which is coated with a ceramic slurry [98, 99]. After removal of excess slurry [98], a green body is formed as the slurry dries [99]. This green body is then fired to remove organic components and sinter the ceramics [98, 99]. A frequently used template material in the application of the replication method is polyurethane (PU) [99–102].

Furler et al. [102] fabricated pure ceria RPCs via the replication route for a cavity-receiver-reactor. Said reactor was discontinuously operated and experiments were conducted in a solar simulator. The RPCs inside the reactor were directly irradiated reaching up to 1873 K. In the oxidation step, CO₂ was converted to CO. These experiments resulted in an average solar-to-fuel efficiency of 1.73 % (3.53 % peak efficiency). At the time, this was the highest reported efficiency of a solar driven device for CO₂ splitting, which was four times higher than previously achieved efficiencies. This success was attributed to the structure of the redox material: The macroporosity allows effective absorption of concentrated solar radiation, while the density is relatively high so that a high mass loading of the reactor can be achieved. [102]

Later, Furler et al. [20] developed this approach further, fabricating ceria RPCs with dual-scale porosity. To this end, a carbon pore-forming agent, consisting of spherical particles in the μm -range, was added to the ceramic slurry. The pore-forming agent is burnt along with the organic template. The RPCs with dual-scale porosity were shown to yield ten times higher CO evolution rates than samples with simple porosity by thermogravimetric analysis (TGA) (explained in detail in Section 2.4). Experiments with a cavity-receiver-reactor showed a three times faster oxidation, when redox material with dual-scale porosity was used. [20]

Ceria RPCs with dual-scale porosity were also used in cavity-receiver-reactors by Marxer et

al. [13, 103]. This approach helped to achieve the high solar-to-fuel efficiency of 5.25 % [13], mentioned above. This was done in an improved reactor configuration [13, 104], using vacuum pumping instead of inert gas sweeping [13].

The burn-off of the polymer template in the replication method typically leaves hollow struts of the RPC with cavities that have triangular cross-sections [99–101]. Vogt et al. [100] used a vacuum infiltration process to fill such cavities and thereby improve the mechanical stability of RPCs manufactured with the replication method. They were able to double the compression strength of alumina foams with this approach, while the weight of the foams was increased by approximately 10 %. Marxer et al. [13] used the vacuum infiltration method combined with an ultrasonic bath for the manufacturing of aforementioned ceria RPCs.

Polymer templates can also be used to create so called three-dimensionally ordered macroporous structures [105]. To this end, polymer spheres of typically some hundred nm are synthesized [106]. A precursor solution for the ceramic material infiltrates the void space between the polymer beads, which have sedimented into a face-centered cubic colloidal crystal [105, 107]. Calcination at elevated temperatures then removes the polymer and forms the ceramic structure [105]. Venstrom et al. [107] used this method to produce a powder of three-dimensionally ordered macroporous ceria that was compared to other ceria powders without ordered pore network. Via their experiments with a fixed bed tubular flow reactor, they showed an increase of H₂ and CO production rates of 75 % and 175 %, respectively, compared to non-ordered mesoporous ceria, due to the highly accessible reactive surface area.

Macroporosity is an important property of redox materials for solar thermochemical applications, as it allows the concentrated radiation to penetrate into the structure. As mentioned above, this feature contributes to the success of ceria RPCs [102]. To further tailor the redox material's appearance to radiative heat transport, Hoes et al. [66] used the replication method with an ordered 3D printed polymer structure as template. They created different geometries, such as a honeycomb structure, with decreasing cell sizes in the direction of irradiation. These 3D printed polymer structures with a strut thickness of 0.3 mm were coated with a ceria slurry containing carbon fibres as pore forming agent. Sintering at 1873 K removed the organic components and created ceria structures with 1 mm struts. Numerical simulations show that in the ordered structures, the radiation attenuation follows an almost linear decay. Compared to the exponential decay in RPCs, which is described in Section 2.5.3 (see Equation 2.51), this results in a higher radiative intensity in the depth of the material. This behaviour is reflected in a more suitable temperature profile for thermal reduction of the material as measured by Hoes et al. using a solar simulator. Especially in the middle and rear of the structures, the ordered structures reached higher temperatures than the tested RPC, with the honeycomb structure reaching the highest temperatures and the lowest temperature gradient. Consequently, reduction extents calculated, assuming equilibrium conditions, revealed that the ordered structures released up to 3.4 times more O₂ than the RPCs. [66]

Ordered porous ceria structures were also fabricated via the replication method with 3D printed polymer templates and tested by Haeussler et al. [108]. Structures with and without micropores

and a gradient in macroporosity were tested in a solar reactor. Wood particles were used as pore forming agent for the microporosity. Two-step redox cycles performed in the solar reactor indicate an improved reduction extent for ordered ceria structures compared to non-ordered RPCs. The oxidation step on the other hand was not improved by the ordered structure. The experiments further confirm that adding microporosity to the redox structure enhances the oxidation rate significantly. [108]

Direct 3D printing of porous ceria was conducted by Zhang et al. [109]. They performed so-called direct ink writing, a method in which extrusion of a suspension through a nozzle is used to print three-dimensional structures. The ceria suspension was extruded in form of a foam, which contained hollow silica spheres as pore-former. Air bubbles in the ceria foam create pores with an average diameter of 62.2 μm . In a sintering step at 1773 K the silica spheres soften and merge with their surrounding adding a secondary porosity with pores of 19.6 μm on average. These smaller pores connect the larger pores, turning the otherwise closed porosity into an open porosity. In addition to the two types of micropores, macropores can be constructed in the 3D-printed structure. Zhang et al. were able to produce highly porous ceria structures with porosities from 81 % to 92 % via this approach. [109]

Ben-Arfa et al. [110] also applied a direct 3D printing approach for fabrication of porous ceria structures using the robocasting method. Like direct ink writing, robocasting is based on the extrusion of a suspension such as a ceramic slurry. In their work, Ben-Arfa et al. were able to produce fine scaffold structures with struts of 510 μm diameter and a distance of 500 μm between the struts. The latter ensures macroporosity of the structure. Although no pore forming agent was added to the ceria slurry, microporosity in the nm scale was found, even after sintering at 1723 K. The general applicability of these structures for two-step solar thermochemical redox cycles was demonstrated via TGA. [110]

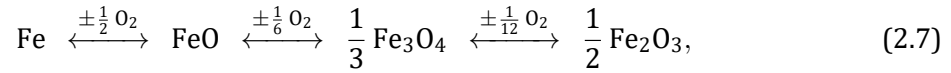
2.3. Kinetics and Thermodynamics

Knowledge of kinetics and thermodynamics of the relevant gas phase reactions as well as oxidation and reduction of the redox material are of utmost importance to describe the investigated process. Therefore, the oxygen non-stoichiometry of ceria and the associated redox behaviour of this material are explained. Subsequently, both the fundamentals and the state of research on thermochemical redox cycles based on ceria are presented with regard to reaction kinetics and equilibria.

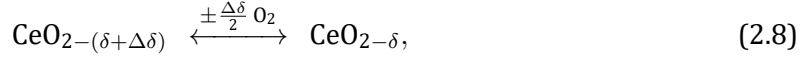
2.3.1. Oxygen Non-Stoichiometry

Ceria is a non-stoichiometric metal oxide. Such materials are characterized by a continuous transition between oxidation states, described by the oxygen non-stoichiometry δ . Therefore, the oxidation and reduction behaviour of ceria differs from materials in which the oxidation state changes in discrete steps according to a fixed stoichiometry. For example the oxidation or re-

duction of iron and iron oxides could take place in several steps such as



while the reduction and oxidation of ceria according to Reaction 2.6 and its reverse reaction can be formulated as



where $\Delta\delta$ can take any value, as long as the total non-stoichiometry stays below a certain upper limit, i.e. $\delta + \Delta\delta < \delta_{\text{UL}}$. Within the range $0 \leq \delta < \delta_{\text{UL}}$, ceria remains in its fluorite phase, which means that there is no change in the crystalline structure [50, 111]. This is again different from the behaviour exemplified in Reaction 2.7. Instead of a rearranged crystalline structure, vacancies are incorporated in the lattice, on positions, where oxygen ions would be placed if the material was fully oxidized [56, 111]. Hence, δ is a measure for the concentration of oxygen vacancies. For example 1 mol of $\text{CeO}_{2-\delta}$ contains δ moles of oxygen vacancies. Figure 2.2 shows the oxygen non-stoichiometry δ of ceria at equilibrium. Here, δ is calculated using a correlation by Bulfin et al. [48] (Equation 2.32), which is explained in Section 2.3.3. The graphs show how δ approaches 0 for low temperatures T and high O_2 partial pressures p_{O_2} as the material is oxidised. At high T and low p_{O_2} , δ approaches the upper limit δ_{UL} as the material is reduced. Due to the non-linear behaviour of the equilibrium- δ with respect to T and p_{O_2} it is particularly interesting to achieve high T and low p_{O_2} to achieve an effective reduction of the material [50]. Due to practical limitations, such as sublimation of ceria [112–114], the possible reduction temperature is however limited. Ceria sublimation was for example observed by Abanades et al. [112, 113] at 2273 K and by Knoblauch et al. [114] above 1600 K. The energy demand for vacuum pumping [70] or processing of sweep gas [64] also limits the range of energetically reasonable p_{O_2} .

Ceria is an oxygen ion conductor [49, 115], which allows fast oxygen transport through the material's lattice [80] from or to reactive sites. Consequently, ceria typically exhibits fast kinetics of reduction and oxidation [46, 49, 80].

The non-stoichiometry changes the way thermodynamic quantities have to be defined or how they can be calculated compared to reactions with a fixed stoichiometry. The reduction or oxidation of ceria can be interpreted as a series of incremental changes $d\delta$ that sum up to a total $\Delta\delta$. This means that thermodynamic quantities such as, for example $\Delta_r h$, $\Delta_r s$ or $\Delta_r g$ become functions of δ . So, while in case of reactions with fixed stoichiometry, absolute quantities scale with the amount of converted substance, in case of non-stoichiometric behaviour, absolute quantities do not only scale with the amount of created vacancies $n_{\text{ceria}} \Delta\delta$, but also depend on the exact value of δ [50, 56, 116]. In other words it makes a difference whether ceria is for example reduced from $\delta = 0.01$ to $\delta = 0.02$ or from $\delta = 0$ to $\delta = 0.01$. One option to incorporate the non-stoichiometry into thermodynamic quantities that characterize a reaction is the following: The operator Δ_r for reaction quantities is defined as the derivative with respect to the extent of

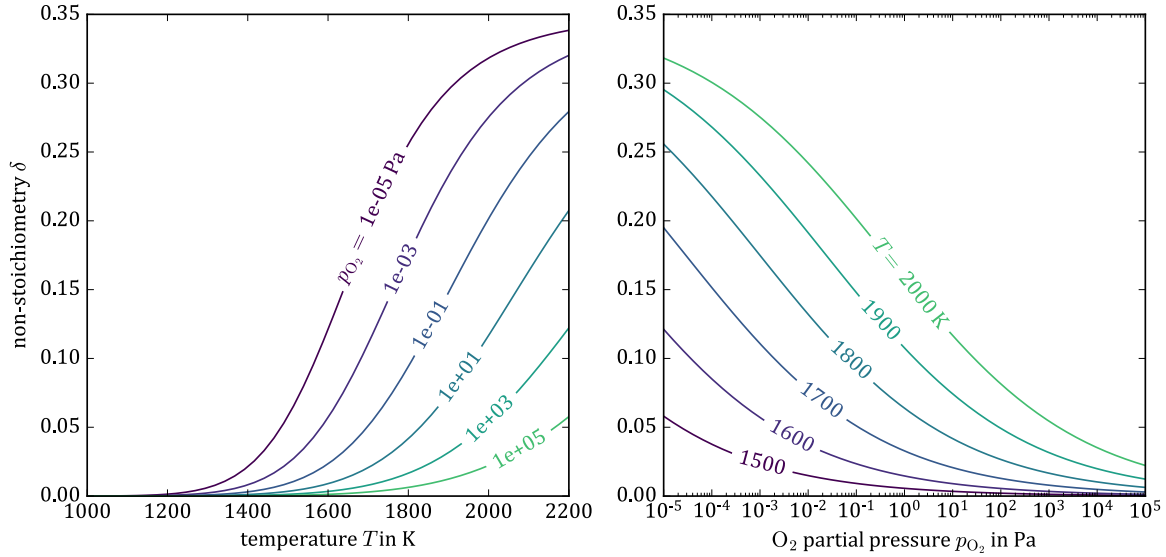


Figure 2.2.: Non-stoichiometry of ceria at equilibrium as a function of (a) the temperature and (b) the O_2 partial pressure.

reaction, given by [117]

$$\Delta_r z = \left(\frac{\partial Z}{\partial \xi} \right)_{T,p}, \quad (2.9)$$

where z and Z are place holders for thermodynamic quantities like Gibbs energy, entropy or enthalpy. In the present work, for thermodynamic quantities, upper case letters denote absolute quantities and lower case letters are used for molar quantities. ξ is the extent of reaction with [117, 118]

$$d\xi = \frac{dn_i}{\nu_i} = \frac{dn_j}{\nu_j}. \quad (2.10)$$

Herein ν_i is the stoichiometric factor of component i in the reaction. Division of dn_i by ν_i makes ξ independent of i . In analogy to Equation 2.9, the reaction progress can also be measured by δ instead of ξ , which allows the introduction of quantities following the pattern [56, 116]

$$\Delta_\delta z = \left(\frac{\partial z}{\partial \delta} \right)_{T,p}. \quad (2.11)$$

Here, $\Delta_\delta z$ (also referred to in literature as Δz or Δ_{z_δ}) describes z per oxygen vacancy. Note that z inside the differential of Equation 2.11 is defined per mol of ceria. Differentiation with respect to δ changes the reference from mol of $CeO_{2-\delta}$ to mol of oxygen vacancies. A similar definition, commonly referred to as $\Delta_{z_{O_2}}$, where z is given per created (or incorporated) oxygen molecule O_2 is used in Refs. [12, 50, 104]. This definition differs from the one given in Equation 2.11 by a factor of 2.

2.3.2. Reaction Kinetics

The overall kinetics of a reaction is the result of mass transport to a relevant area such as a reactive surface and the chemistry, i.e. the reaction rate. This section will first address reaction rates in general and for the relevant reactions studied in the present work, followed by the mass transport mechanisms, relevant for these reactions.

A reaction rate for a participant i can often be expressed in the form [118]

$$\frac{dc_i}{dt} = \nu_i \left(k_1(T) \prod_j c_j^{m_j} - k_2(T) \prod_l c_l^{m_l} \right), \quad (2.12)$$

where $c_i = n_i V^{-1}$ is the molar concentration of species i , ν_i is the stoichiometric factor, $k(T)$ is called the rate constant and m_i is the order of the reaction rate with respect to species i . $k_1(T)$ is the rate constant for the reaction with reactants j and $k_2(T)$ is the rate constant for the reverse reaction with reactants (products of the original reaction) l . For gas-phase reactions, concentrations can be converted to partial pressures and the reaction rate in Equation 2.12 can alternatively be expressed in terms of partial pressures instead of concentrations [48, 118].

The rate constant, contrary to what its name suggests, is a function of the temperature, given by the Arrhenius equation [118]

$$k(T) = k_\infty \exp\left(-\frac{e_a}{RT}\right), \quad (2.13)$$

where the pre-exponential factor k_∞ is the value of $k(T)$ for the temperature T approaching infinity. It is often referred to as frequency factor. e_a is the activation energy.

In simplified versions of Equation 2.12 it can be helpful to take the logarithm of this equation. For example for a reaction that is far enough away from its equilibrium, so that the influence of the reverse reaction on the reaction rate is negligible and where all but one reactants are so abundant that their concentration can be treated as constant, this yields [118]

$$\log\left(\frac{1}{\nu_i} \frac{dc_i}{dt}\right) = \log\left(\tilde{k}_1(T)\right) + m_j \log(c_j). \quad (2.14)$$

Herein, $k_1(T)$ and the constant concentrations are summarized in $\tilde{k}_1(T)$. In a plot of Equation 2.14 against $\log(c_j)$, constants can be identified via the y-intercept and m_j is the slope with respect to $\log(c_j)$ [118]. Together with Equation 2.13, Equation 2.14 yields a straight line if plotted against T^{-1} , which can for example be used to check whether investigated kinetics follow an expected reaction mechanism [49]. This approach can also be directly applied on Equation 2.13, to determine the frequency factor and the activation energy [118].

Bulfin et al. [48] derived a model to describe the reaction rate of the reduction of ceria and its reverse reaction, the oxidation of ceria with oxygen. Fundamentally, the reaction rate is written as [48]

$$\frac{dc_{\text{vac}}}{dt} = k_{\text{red}} c_{\text{O,ceria}} - k_{\text{ox}} c_{\text{vac}} c_{\text{O}_2}^m, \quad (2.15)$$

where c_{vac} is the concentration of oxygen vacancies, $c_{\text{O,ceria}}$ is the concentration of oxygen ions, stored in the ceria lattice that can be removed by reduction without ceria leaving the fluorite phase and c_{O_2} is the concentration of gaseous O_2 . Dividing the concentrations in Equation 2.15 by the constant concentration of cerium c_{ce} yields [48]

$$\frac{c_{\text{O,ceria}}}{c_{\text{ce}}} = \delta_{\text{UL}} - \delta, \quad (2.16)$$

$$\frac{c_{\text{vac}}}{c_{\text{ce}}} = \delta. \quad (2.17)$$

Substituting Equations 2.13, 2.16 and 2.17 into Equation 2.15 and converting the concentration of O_2 into a partial pressure leads to [48]

$$\frac{d\delta}{dt} = (\delta_{\text{UL}} - \delta) k_{\infty, \text{red}} \exp\left(-\frac{e_{\text{a, red}}}{RT}\right) - \delta p_{\text{O}_2}^m k_{\infty, \text{ox}} \exp\left(-\frac{e_{\text{a, ox}}}{RT}\right). \quad (2.18)$$

In addition to the chemical reaction, diffusion of oxygen within the crystal lattice might impact the overall rate. Oxygen is transported through ceria via ambipolar diffusion, which means that oxygen ions and electrons are transported in opposing direction maintaining an overall neutral charge [46, 119]. Ackermann et al. [119] postulate an inverse proportionality of the ambipolar diffusion coefficient on the oxygen non-stoichiometry, $\tilde{D} \propto \delta^{-1}$. Indeed, in a prior study, Chueh and Haile [46] present both calculated and measured ambipolar diffusion coefficients for 15 % samarium-doped ceria, which decrease with increasing δ , although not with an exactly inversely proportional trend. This is supported by measurements of the electrical conductivity [120], from which the ambipolar diffusion coefficient can be calculated with the Nernst-Einstein equation [46, 119]. Opposing these results, Stan et al. [121] find increasing values of \tilde{D} with increasing δ , using TGA experiments coupled to a numerical model. In several studies it is shown that \tilde{D} increases with increasing temperatures [46, 119–122]. A comprehensive summary of ambipolar diffusion coefficients from the aforementioned and more studies is given in Ref. [119]. This comparison also shows considerable deviations between values of different origins.

In oxidation experiments, Bulfin et al. [49] found that with progressing reaction, a rate limiting mechanism occurs. In analogy to Equation 2.14, the logarithm of Equation 2.18, neglecting the reduction expression, was taken and plotted against the inverse of the temperature T^{-1} . A linear regime suggests that here the rate determining mechanism is indeed described by the oxidation expression in Equation 2.18. However, with progressing reaction and increasing temperatures, a deviation from the linear behaviour was observed. It was suggested that in the later stages of the reaction, bulk diffusion might become a limiting factor. In the same study it was also found that the reduction is so fast that despite high heating rates of more than 100 K s^{-1} the reaction rate seemed to be limited by these heating rates. [49]

TGA measurements combined with a numerical model by Ackermann et al. [119] suggest that oxygen removal and uptake in ceria at 1673 K to 1823 K depend on the diffusion. It is shown that during oxidation, the bulk material appears not to be in equilibrium with the gas phase.

Knoblauch et al. [123] present a model, which suggests that there is a diffusion controlled,

a surface exchange controlled and a mixed regime, depending on sample dimensions, diffusion coefficient \tilde{D} and a surface exchange coefficient of oxygen at the interface between gas and solid \tilde{K} . The diffusion coefficient D^* and a surface exchange coefficient K^* of ^{18}O tracer [123, 124] are used to estimate the characteristics of the oxygen transport in ceria. Results imply that for both, powders with a crystal size of 20 μm and a 1 mm thick plane (grain size 20 μm) the kinetics are surface exchange controlled. This is supported by assessment of the oxygen transport with estimated values of \tilde{D} with aforementioned data presented in Ref. [119] and \tilde{K} -values calculated with data from TGA [123]. The same TGA cycles also show that the oxidation kinetics are so fast that the cooling rate of 50 K s^{-1} becomes the limiting factor.

2.3.3. Reaction Equilibria

A chemical reaction causes a change in the composition of the involved components, until an equilibrium is reached. At that point, both reactants and products are present and the reaction and its reverse reaction occur, but there is no net change in composition. [118] An important thermodynamic quantity to describe this behaviour is the reaction Gibbs energy $\Delta_{r,g}$, which is, according to Equation 2.9, the rate at which the Gibbs energy changes with respect to the extent of reaction, given by [117, 118]

$$\Delta_{r,g} = \left(\frac{\partial G}{\partial \xi} \right)_{T,p}. \quad (2.19)$$

The equilibrium of a chemical reaction is reached, when the Gibbs energy of the system is minimal [118]. Consequently, a reaction that decreases the Gibbs energy, moves the system closer to its equilibrium, while a reaction that increases the Gibbs energy, would move the system away from equilibrium. Since reactions have a tendency to approach equilibrium [118], a net change of composition follows a reaction that decreases the Gibbs energy. Given the definition of $\Delta_{r,g}$ in Equation 2.19, this is the case if $\Delta_{r,g} < 0$. Such a reaction is called spontaneous [118]. If at a certain composition, a reaction has a $\Delta_{r,g} > 0$, its reverse reaction meets the condition $\Delta_{r,g} < 0$. Therefore the net change of composition happens in the opposite direction, because the reverse reaction is spontaneous [118]. At equilibrium, there is no change in the Gibbs energy so that $\Delta_{r,g} = 0$ [117, 118].

More generally, the change of the Gibbs energy is described by its total differential, which can be written as [117]

$$dG = V dp - S dT + \sum_i \left(\left(\frac{\partial G}{\partial n_i} \right)_{T,p,n_{j \neq i}} dn_i \right). \quad (2.20)$$

Introducing the chemical potential [117]

$$\mu_i = \left(\frac{\partial G}{\partial n_i} \right)_{T,p,n_{j \neq i}} \quad (2.21)$$

and using the relation between ξ and ν_i given in Equation 2.10 allows to rewrite the total differ-

ential as [117]

$$dG = V dp - S dT + \sum_i \nu_i \mu_i d\xi, \quad (2.22)$$

which corresponds to the Gibbs fundamental equation [117] expressed via $d\xi$, rather than dn_i . This shows that with respect to the total differential in Equation 2.20, dG can be expressed as a function of ξ instead of all n_i , so that

$$dG = V dp - S dT + \left(\frac{\partial G}{\partial \xi} \right)_{T,p} d\xi. \quad (2.23)$$

As explained above, $d\xi$ is the same for all components i . This allows to write the change of Gibbs energy due to a changing composition in a single expression in Equation 2.23 as opposed to the sum used in Equation 2.20. From Equations 2.22, 2.23 and 2.19 follows [118]

$$\Delta_r g = \sum_i \nu_i \mu_i. \quad (2.24)$$

According to this equation, the reaction Gibbs energy can be interpreted as the chemical potential difference between reactants and products [118], weighted by the stoichiometric factors of the reaction. Note that for reactants, $\nu_i < 0$ and for products, $\nu_i > 0$. In that sense, a net conversion of reactants to products takes place, if the $\nu_i \mu_i$ of all reactants have a higher magnitude than the ones of the products, similar to heat, flowing from a body at high temperature to a body at low temperature. The equilibrium is reached when $\nu_i \mu_i$ on reactant and product side have the same magnitude. [118]

The chemical potential consists of two parts: a standard potential μ° at standard pressure and a relative potential expressed via the activity a_i [117]

$$\mu_i = \mu_i^\circ + R T \ln(a_i). \quad (2.25)$$

Equation 2.25 describes the chemical potential of a single component i . A chemical reaction, can be described similarly by [117]

$$\sum_i \nu_i \mu_i = \sum_i \nu_i \mu_i^\circ + R T \ln(K) \quad (2.26)$$

with [117, 118]

$$K = \prod_i a_i^{\nu_i}. \quad (2.27)$$

K is the reaction quotient. It describes the current composition of the system and ranges from 0 to infinity [118]. The reaction quotient that describes the equilibrium composition is called equilibrium constant K_{eq} [117, 118]. For gases, the activities in Equation 2.27 are often approx-

imated via partial pressures according to [118]

$$a_i \approx \frac{p_i}{p^\circ}, \quad (2.28)$$

where $p^\circ = 1 \cdot 10^5$ Pa [117] is the standard pressure. Equation 2.28 is theoretically exact for ideal gases [118]. For pure condensed phases, the activity is 1 [117, 118].

In Equation 2.26, the chemical potential of each component is weighted with the respective ν_i , matching the pattern in Equation 2.24. Using Equation 2.24, Equation 2.26 can therefore be rewritten as [118]

$$\Delta_r g = \Delta_r g^\circ + R T \ln(K), \quad (2.29)$$

where $\Delta_r g^\circ$ corresponds to the sum over $\nu_i \mu_i^\circ$ in Equation 2.26 [117, 118]. Since at equilibrium $\Delta_r g = 0$, the equilibrium composition of the system, described by $K = K_{\text{eq}}$, can be calculated with Equation 2.27, where the equilibrium constant K_{eq} is given by [117, 118]

$$K_{\text{eq}} = \exp\left(-\frac{\Delta_r g^\circ}{R T}\right). \quad (2.30)$$

As described in Section 2.3.1, the non-stoichiometric behaviour of ceria introduces a dependence on δ to thermodynamic quantities such as $\Delta_r g^\circ$, which makes direct application of Equation 2.30 for the reduction and oxidation of ceria difficult. While Equation 2.30 can be used to describe gas-phase reactions in the process, such as the thermolysis reactions of water and carbon dioxide, it is more convenient to choose a different, but related approach to determine the equilibrium of reduction and oxidation of ceria: The equilibrium of a reversible chemical reaction is reached, when the reaction and its reverse reaction are equally fast, i.e. the changes in composition due to reaction and reverse reaction cancel each other out and the reaction is spontaneous in neither direction [118]. The reaction equilibrium is therefore a dynamic equilibrium. As described in Section 2.3.2, Bulfin et al. [48] derived a model to describe the reaction kinetics of the reduction and oxidation of ceria. Based on the idea of the dynamic equilibrium, this model can also be used to describe the reaction equilibrium. After setting the net δ -rate to zero, Equation 2.18 can be rearranged to [48]

$$\left(\frac{\delta}{\delta_{\text{UL}} - \delta}\right) = \frac{k_{\infty, \text{red}}}{k_{\infty, \text{ox}}} p_{\text{O}_2}^{-m} \exp\left(-\frac{e_{\text{a,red}} - e_{\text{a,ox}}}{R T}\right). \quad (2.31)$$

Bulfin et al. [48] determined parameters of this equation for pressures in the range of $1 \cdot 10^{-4}$ Pa to 1000 Pa. For temperatures between 1273 K and 1773 K they fitted the equation to data by Panlener et al. [50] and for higher temperatures, a numerical model by Zinkevich et al. [125] was used, yielding [48]

$$\left(\frac{\delta}{0.35 - \delta}\right) = 8700 \text{ bar}^{0.217} p_{\text{O}_2}^{-0.217} \exp\left(-\frac{195.6 \text{ kJ mol}^{-1}}{R T}\right), \quad (2.32)$$

for p_{O_2} in bar. Alternatively to Equation 2.32, polynomial expressions of the form [12, 104]

$$\log(\delta(P, T)) = \sum_{i=0}^3 C_i P^i + T \sum_{j=0}^2 C_{j+4} P^j + C_7 P T^2 \quad (2.33)$$

or [126]

$$\log(\delta(P, T)) = \sum_{i=0}^2 C_i T^i + P \sum_{j=0}^2 C_{j+3} T^j, \quad (2.34)$$

with $P = \log(p_{O_2}/p^\circ)$ have been fitted to data from Ref. [50].

2.4. Experimental Determination of Redox Behaviour

The release or uptake of oxygen by the redox material causes a mass loss or gain of the solid phase. This way, a change in the oxygen non-stoichiometry can be calculated by measuring the weight of a sample during reduction or oxidation. This can be done via TGA, which requires a precision balance and a furnace that can follow a temperature program [127]. Generally, TGA can be used to analyse various physical and chemical phenomena that include weight change of a sample with changing temperature [127]. In commercial systems, the method is limited to relatively small samples, often of cylindrical shape with a diameter typically < 15 mm and a height < 10 mm [119, 123, 128]. One reason for this is to mitigate the deviation of furnace and sample temperature due to endothermic and exothermic effects [127, 129]. Results are commonly presented as weight or weight difference and temperature curves against time [52, 110, 123, 128]. Several impact factors, such as air buoyancy, cause an apparent weight change even if the mass is constant [127]. Since only small samples are used these effects have a significant impact on the measured weight, which typically has to be corrected by the apparent weight change of the empty crucible [8, 127]. TGA is commonly applied in the field of two-step solar thermochemical redox cycles, for example in Refs. [8, 52, 123]. Here, an oxidant gas for oxidation of the sample and an inert gas for reduction typically flow through the sample chamber [8, 52, 123]. It is an important tool to evaluate the performance of redox materials without the need of a complex customised test rig. It is thus frequently used in the development of new redox materials [8, 52, 128] and redox structures [110]. Despite being a valuable method to compare different redox active materials, the restricted sample size and the given flow conditions limit the comparability of TGA results with real technical systems.

More representative conditions can be achieved in customised test rigs or solar reactor prototypes, where it is not possible to measure the sample weight, however. Instead, the evolution rate or total amount of O_2 during reduction and H_2 or CO during oxidation can be measured. The derivative of δ with respect to time directly follows from these measurements as δ and the amount of O_2 , H_2 or CO are linked via the stoichiometry of Reactions 2.6, 2.4 and 2.5. Determining evolution rates is commonly applied for irradiated test rigs and reactor prototypes [13, 104, 108]. To this end, total mass flow and gas composition need to be obtained. The former is often

defined by mass flow controllers [13, 104, 108] and the latter is measured for example by gas chromatography [13, 104], mass spectrometry [130] and/or different sensors for specific gas species [13, 104, 108, 130].

If a continuous gas flow during experimentation is undesirable, redox experiment and measurement of $\Delta\delta$ can be decoupled. Brendelberger et al. [71] and Pein et al. [73] for example conducted experiments on thermochemical oxygen pumps using tube furnaces. After reduction, the sample was re-oxidised with a gas flow of known O_2 content at the inlet and the O_2 content at the outlet was measured, allowing to calculate the former degree of reduction [71, 73]. This approach however only allows to calculate the final $\Delta\delta$ rather than the kinetics of the reduction.

2.5. High Temperature Heat Transport

Understanding the fundamentals of heat transport is crucial to model heat exchangers and to plan and interpret the experiments undertaken in this work. In the following, firstly convective heat transport based on natural convection is explained. This is important to model heat transfer between hot surfaces and their surroundings as well as to understand the theory behind temperature measurements for experiments. Secondly, radiation is discussed, which plays an important role in the present work, due to the high temperatures in the investigated redox cycle. Lastly, heat transport through porous media such as porous units of redox material, via conduction and radiation, is described.

2.5.1. Convective Heat Transport

An important heat transport mechanism in flowing fluids is convective heat transport. A distinction is made between forced and free convection. While in forced convection, the current results from external forces, in free convection, the current is a consequence of a density gradient in a gravitational field, typically due to a temperature gradient [131]. To model convective heat transport, it is necessary to know the heat transfer coefficient α , which can be obtained from the dimensionless Nusselt number Nu , which is defined as [131, 132]

$$Nu = \frac{\alpha \cdot L}{\lambda}, \quad (2.35)$$

where L is a characteristic length of the surface at which the heat transfer takes place and λ is the thermal conductivity of the surrounding fluid. The Nusselt number can be calculated with empirical correlations using further dimensionless quantities. In case of free convection these are the Prandtl number Pr and the Grashof number Gr or the Rayleigh number Ra [131, 132]. The latter is the product of Pr and Gr , so that Gr and Ra are interchangeable [132]. Prandtl number and Rayleigh number are defined as [131, 132]

$$Pr = \frac{\nu}{a} \quad (2.36)$$

and [132]

$$Ra = \frac{\beta \cdot g \cdot \Delta T \cdot L^3}{\nu \cdot a}, \quad (2.37)$$

where the temperature difference ΔT is defined as $T_{\text{surf}} - T_{\text{fluid}}$, β is the isobaric volume expansion coefficient, g is the acceleration of gravity, ν is the kinematic viscosity and a is the thermal diffusivity. Properties of the fluid have to be evaluated at a reference temperature $T_{\text{ref}} = \frac{1}{2} \cdot (T_{\text{surf}} + T_{\text{fluid}})$ [132]. The isobaric volume expansion coefficient β is defined as [118, 133]

$$\beta = \frac{1}{V} \left(\frac{\partial V}{\partial T} \right)_p \quad (2.38)$$

and can be obtained from the relevant literature, e.g. Ref. [132]. From Equation 2.38 and the ideal gas law follows [118]

$$\beta = \frac{1}{T} \quad (2.39)$$

for ideal gases. Thus, if data for β is not available it might be approximated with Equation 2.39 instead. The thermal diffusivity a is defined as [132]

$$a = \frac{\lambda}{\rho \cdot \tilde{c}_p}, \quad (2.40)$$

where \tilde{c}_p is the specific heat capacity. Using these material properties, Pr and Ra can be calculated and thus Nu can be obtained from an empirical correlation, such as [131, 132, 134, 135]

$$Nu = \left(C_1 + C_2 \cdot (Ra \cdot f(Pr))^{\frac{1}{6}} \right)^2, \quad (2.41)$$

where $f(Pr)$ is defined as [131, 132, 134–136]

$$f(Pr) = \left(1 + \left(\frac{C_3}{Pr} \right)^{\frac{9}{16}} \right)^{-\frac{16}{9}}. \quad (2.42)$$

Depending on the geometry of the surface, the parameters C_1 , C_2 and C_3 have different values [134–136]. They are summarised in Table 2.3 for the two cases, relevant for the present work, namely a vertical flat surface and a horizontal cylinder. Instead of Equations 2.41 and 2.42, sim-

Table 2.3.: Parameters for Equations 2.41 and 2.42.

Case	C_1	C_2	C_3
Vertical flat surface [134, 136]	0.825	0.387	0.492
Horizontal cylinder [135]	0.600	0.387	0.559

ilar equations might be used for other geometries [132].

2.5.2. Radiation

According to the Stefan-Boltzmann law, the radiant emittance of a grey body at temperature T is proportional to T^4 [137]. Consequently, radiation becomes more relevant compared to other heat transport mechanisms at higher temperatures. In case of solar thermochemical redox cycles, radiation is crucial to describe the irradiation of the redox material, the heat transport within a receiver reactor, heat losses from hot components to the ambience, heat transfer within heat exchangers and heat transport into the depth of porous redox materials, with the latter being described in the following section.

The radiation that is emitted from a surface i onto a surface j can be expressed using the view factor Φ_{ij} . It is defined as the portion of radiation emitted from surface i , which reaches surface j [132]. It depends only on geometry [132, 137]. For a grey body i , the radiation emitted to a surface j reads [137]

$$\dot{Q}_{ij}^{\text{emit}} = A_i \varepsilon_i \Phi_{ij} \sigma T_i^4, \quad (2.43)$$

where σ is the Stefan-Boltzmann constant and A_i , ε_i and T_i are the surface area, the emissivity and the temperature of surface i , respectively. In analogy to Equation 2.43, surface j emits radiation \dot{Q}_{ji} onto surface i . On top of that, a part of these radiation terms will be reflected back and forth between the two surfaces, resulting in a net radiation exchange, described by an infinite series [132]. For grey bodies, the following expression can be derived from such a series [131, 132, 137]:

$$\dot{Q}_{ij} = \frac{\sigma \varepsilon_i \varepsilon_j \Phi_{ij}}{1 - \frac{A_i}{A_j} \Phi_{ij}^2 (1 - \varepsilon_i) (1 - \varepsilon_j)} A_i (T_i^4 - T_j^4). \quad (2.44)$$

For certain geometries, Equation 2.44 can be simplified. For two parallel plates, which are large compared to their distance, the expression reads [131, 137, 138]

$$\dot{Q}_{ij} = \frac{\sigma}{\frac{1}{\varepsilon_i} + \frac{1}{\varepsilon_j} - 1} A_i (T_i^4 - T_j^4). \quad (2.45)$$

For a convex surface i that is enclosed by a concave surface j , Equation 2.44 is simplified to [131, 132, 137, 138]

$$\dot{Q}_{ij} = \frac{\sigma}{\frac{1}{\varepsilon_i} + \frac{A_i}{A_j} \left(\frac{1}{\varepsilon_j} - 1 \right)} A_i (T_i^4 - T_j^4) \quad (2.46)$$

and for a hemisphere j above a flat surface i [137]

$$\dot{Q}_{ij} = \frac{\sigma \varepsilon_i \varepsilon_j}{1 - \frac{1}{2} (1 - \varepsilon_i) (1 - \varepsilon_j)} A_i (T_i^4 - T_j^4). \quad (2.47)$$

Depending on the geometry, one of the latter two equations might be used to describe heat losses from a hot component to its surroundings. If the ambience is modelled as a black body, i.e. $\varepsilon_j = 1$,

Equations 2.46 and 2.47 become

$$\dot{Q}_{ij} = \varepsilon_i \sigma A_i (T_i^4 - T_j^4). \quad (2.48)$$

2.5.3. Heat Transport in Porous Media

Heat transport through porous media differs from that in homogeneous media in that the conduction through the solid takes place along tortuous paths and is complemented by radiative heat transfer through the void space and by heat transport through the fluid inside the pores, if present. A simple approach to account for the porosity is the homogenisation approach [139], in which the heterogeneous porous material is treated like a homogeneous material with volume averaged quantities. The superposition of conductive and radiative heat transport can be summarized into an effective thermal conductivity [139]

$$\lambda_{\text{eff}} = \lambda_{\text{cond}} + \lambda_{\text{rad}}. \quad (2.49)$$

Thus, the radiation inside the pores is mathematically treated like heat diffusion according to Fourier's law [140]. Using the Rosseland approximation, λ_{rad} can be expressed as [132, 140]

$$\lambda_{\text{rad}} = \frac{16 \sigma n^2 T^3}{3 \tilde{\beta}}, \quad (2.50)$$

where $\tilde{\beta}$ is the extinction coefficient and n is the real part of the complex refractive index, which is close to unity for media with high porosity [132]. Therefore, in the present work, $n = 1$ is assumed. The extinction coefficient describes how radiation that penetrates the material is weakened on its path through the material due to absorption and scattering [140]. The latter can be further divided into diffraction, reflection and refraction [140]. The resulting transmittance in a direction x is [140]

$$\tau(x) = e^{-\tilde{\beta}(x-x_0)}. \quad (2.51)$$

An important material for the thermochemical redox cycle investigated in this work is reticulated porous ceria with a dual-scale porosity as described in more detail in Section 2.2.3. It has a macroscopic porosity (mm-range) allowing radiation to penetrate deep into the material [141] and a microscopic porosity (μm -range) of the struts, which increases the reactive surface area [126]. The total dual-scale porosity ϕ can be calculated as [126]

$$\phi = \phi_{\text{macro}} + \phi_{\text{strut}} (1 - \phi_{\text{macro}}), \quad (2.52)$$

where ϕ_{macro} is the macroscopic porosity of the material and ϕ_{strut} is the microscopic porosity of the struts. For reticulated porous ceria with a dual-scale porosity, Ackerman et al. [126] found

$$\tilde{\beta} = \frac{-630.674 \phi_{\text{macro}}^2 - 120.060 \phi_{\text{macro}} + 1229.36}{1000 d_{\text{m,pore}}}, \quad (2.53)$$

where $d_{m,pore}$ is the mean pore diameter.

The thermal conductivity λ_{cond} in Equation 2.49 is in itself an effective quantity. It takes into account the thermal conductivities of the solid and fluid phase and the porous nature of the material. Studies on calculating the thermal conductivity of composite materials as a function of the thermal conductivities of their constituents reach back to the late 19th and early 20th century [142]. A comprehensive overview of analytical models for dual-scale reticulated porous structures is given in Ref. [141]. Ackermann et al. [141] obtained digital representations of the three-dimensional geometries of dual-scale ceria RPCs from computer tomography, to which they applied direct pore-level simulations, such as ray-tracing. The results were used to evaluate existing analytical expressions and a so-called modified three-resistor model. The latter reads [141]

$$\frac{\lambda_{cond}}{\lambda_{CeO_2}} = \frac{C_1 \phi \frac{\lambda_f}{\lambda_{CeO_2}}}{C_2 \phi + \frac{\lambda_f}{\lambda_{CeO_2}} (1 - C_2 \phi)} + (1 - C_1 \phi) \left(C_3 \phi \frac{\lambda_f}{\lambda_{CeO_2}} + 1 - C_3 \phi \right). \quad (2.54)$$

For aforementioned ceria RPCs, the fit parameters of Equation 2.54 are [141]

$$C_1 = 0.6223, \quad C_2 = 0.7015, \quad C_3 = 1.0548. \quad (2.55)$$

To calculate λ_{cond} from Equation 2.54, the thermal conductivities of the two phases, namely the solid and the fluid inside the pores are needed. These thermal conductivities are functions of the temperature. For ceria, Ackerman et al. [126] expressed λ_{CeO_2} via the following polynomial based on Ref. [143]:

$$\lambda_{CeO_2} = -1.7234232 \cdot 10^{-9} T^3 + 1.1203174 \cdot 10^{-5} T^2 - 0.024019964 T + 17.800409. \quad (2.56)$$

Data for the thermal conductivity of many fluids is tabulated in the literature and can for example be found in Refs. [132, 144, 145].

3. Materials and Methods

In the following, materials and methods used in the present work are described in detail. First, a model is derived with which the extent of recombination can be calculated for given operating conditions. The model also calculates entropies to assess the feasibility of results based on the second law of thermodynamics. Next, experimental methods for the investigation of recombination kinetics are described. This includes the development of a dedicated test rig, the experimental procedure, characterisation of ceria samples, characterisation of the gas phase in the test rig, methods to assess the experiments and a numeric model of the test rig. Finally, a transient heat transport model for indirect heat recovery via a heat storage unit is described. This indirect concept is investigated as an approach to avoid recombination during heat recuperation.

3.1. Modelling the Recombination Effect

Subsections 3.1.1, 3.1.2 and 3.1.3 of this section are in part based on the following peer-reviewed publications, authored by the author of the present work.

Philipp Holzemer-Zerhusen, Stefan Brendelberger, Martin Roeb, and Christian Sattler. „Oxygen Crossover in Solid-Solid Heat Exchangers for Solar Water and Carbon Dioxide Splitting: A Thermodynamic Analysis“. In: *Journal of Energy Resources Technology* 143.7 (Oct. 2020). 071301. ISSN: 0195-0738. DOI: 10.1115/1.4048772

Philipp Holzemer-Zerhusen, Stefan Brendelberger, Martin Roeb, and Christian Sattler. „Oxygen Crossover in Solid-Solid Heat Exchangers for Solar Water and Carbon Dioxide Splitting: A Thermodynamic Analysis“. In: *Proceedings of the ASME 2020 14th International Conference on Energy Sustainability*. ASME 2020 14th International Conference on Energy Sustainability. V001T13A001. Virtual, Online, June 2020. DOI: 10.1115/ES2020-1608

The redox-cycle is modelled in *Python* 3 [148, 149]. The model covers a receiver reactor for the reduction step, an oxidation reactor, a solid-solid HE and auxiliary energy demands like solar pre heating of feed-streams and electricity generation for vacuum pumps. In the HE, both heat transfer and oxygen crossover between the hot and cold ceria stream (recombination) are considered. All chemical reactions are considered fast and are thus modelled as equilibrium reactions. Given the fast reduction and oxidation kinetics of ceria [46, 49] this approximation seems to be a good starting point for the present study. Investigations of the kinetics follow later on. A schematic of the modelled system is shown in Figure 3.1. It is assumed that the ceria

streams pass pressure locks, which separate the atmospheres of adjacent components, i.e. the oxidation and reduction reactor from the HE. These pressure locks are not further specified and for simplicity it is assumed that they are capable of fully preventing any gas transport between the components. Separation of the atmospheres of the oxidation reactor and the HE are needed to prevent the oxidation product, namely H_2 or CO from entering the HE, where it would act as a reducing agent at elevated temperatures for the just oxidized redox material, again forming H_2O or CO_2 . This reaction could cause a significant decrease of the yield, if it wasn't prevented by separation of the atmospheres. A pressure lock between oxidation reactor and HE, i.e. pressure lock 2 in Figure 3.1, is therefore always considered. Regarding the pressure lock between reduction reactor and HE, two different setups are considered: Setup 1, with this pressure lock and setup 2 without it. Separation of the reduction reactor and the HE seems beneficial to avoid O_2 , which was released in the reaction to oxidise ceria in the HE and thereby amplifying the recombination effect. However, Siegrist et al. [17] suggested to only have one pressure lock, which simplifies the process and performed calculations for this case based on very coarse approximations. This suggestion is therefore investigated in more detail via setup 2 in the present work. The whole system is modelled at steady state operation. Thermodynamic states at the inlets and outlets of HE and reactors are labelled with integers from 1 to 4 as indicated in Figure 3.1.

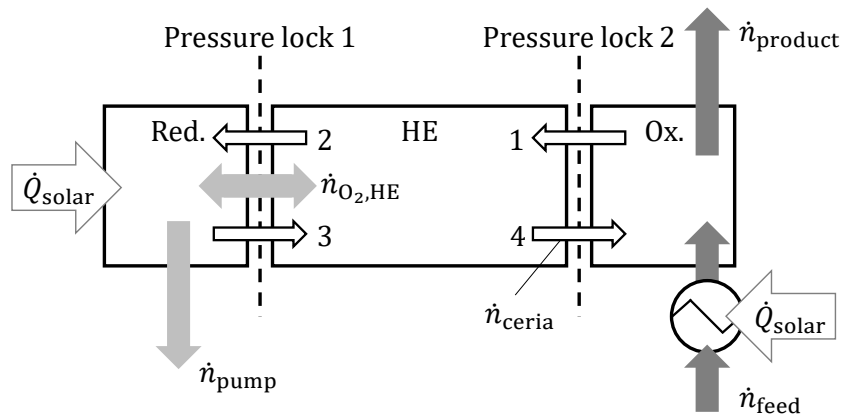


Figure 3.1.: Schematic of the modelled redox cycle. Adapted from Ref. [146] with permission from the American Society of Mechanical Engineers.

3.1.1. Reactions and Mass Transport

It is assumed that the reduction of ceria is supported by vacuum pumping. Application of sweep gas is not investigated. The reaction equilibrium of the oxygen release is calculated with Equation 2.32 [48]. The oxidation of ceria can be described in two steps: First, splitting of H_2O or CO_2 , according to



or



Second, the uptake of oxygen produced herein. This is again described by Equation 2.32 [48]. The equilibrium constant according to Equations 2.28 and 2.27 for Reactions 3.1 and 3.2 reads

$$K_{\text{eq}} = \frac{p_{\text{product}} \cdot \left(\frac{p_{\text{O}_2, \text{ox}}}{p^\circ} \right)^{\frac{1}{2}}}{p_{\text{reactant}}}, \quad (3.3)$$

where the product is H₂ or CO and the reactant is H₂O or CO₂. Partial pressures are

$$p_i = p_{\text{ox}} \cdot \frac{n_i}{n_{\text{ox}}}, \quad (3.4)$$

where p_{ox} and n_{ox} are the total pressure and total amount of gas in the oxidation reactor, respectively. Using Equation 3.4 and the conversion X_{ox} of reactant H₂O or CO₂ given by

$$X_{\text{ox}} = \frac{n_{\text{reactant}, 0} - n_{\text{reactant}}}{n_{\text{reactant}, 0}}, \quad (3.5)$$

Equation 3.3 can be rearranged and solved for the oxygen partial pressure in the reaction reactor, which yields

$$p_{\text{O}_2, \text{ox}} = p^\circ \cdot \left(\frac{K_{\text{eq}} \cdot (1 - X_{\text{ox}})}{X_{\text{ox}}} \right)^2. \quad (3.6)$$

For a given oxidation temperature T_{ox} the equilibrium constant can be calculated with Equation 2.30, as

$$K_{\text{eq}} = \exp \left(- \frac{\Delta_r g^\circ}{R \cdot T_{\text{ox}}} \right), \quad (3.7)$$

where $\Delta_r g^\circ$ is calculated using data from the software *FactSage 7* [150] with the database *FactPS*. The necessary feed stream to achieve a certain amount of product (H₂ or CO) is directly linked to the product stream via the conversion X_{ox} , so that

$$\dot{n}_{\text{feed}} = \frac{\dot{n}_{\text{product}}}{X_{\text{ox}}}. \quad (3.8)$$

Note that here \dot{n}_{product} refers to the amount of desired product and not the total product stream, which also contains unreacted reactants. Reduced ceria acts as an oxygen sink in Reactions 3.1 and 3.2, while it is oxidized. The amount of ceria needed to remove enough oxygen to achieve a given conversion X_{ox} is given by

$$\dot{n}_{\text{ceria}} = - \frac{\dot{n}_{\text{feed}} \cdot X_{\text{ox}} - 2 \cdot \dot{n}_{\text{O}_2, \text{ox}}}{\Delta \delta_{41}}, \quad (3.9)$$

where $\Delta\delta_{41}$ is the difference in non-stoichiometry δ between states 4 and 1 according to Figure 3.1 and $\dot{n}_{O_2,ox}$ is the remainder of oxygen in the product stream, which follows from

$$\dot{n}_{O_2,ox} = \dot{n}_{feed} \cdot \frac{p_{O_2,ox}}{p_{Ox} - p_{O_2,ox}}. \quad (3.10)$$

The pressure in the reduction reactor is controlled by a vacuum pump, which removes oxygen. This includes the oxygen which is released from ceria due to its reduction. In case of setup 2, also oxygen that enters or leaves the reduction reactor from or to the HE has to be considered. The removed amount of oxygen is determined with an atom balance for oxygen around control volume (CV) I of Figure 3.2.

$$\dot{n}_{O_2,pump} = -\frac{1}{2} \Delta\delta_{41} \cdot \dot{n}_{ceria}. \quad (3.11)$$

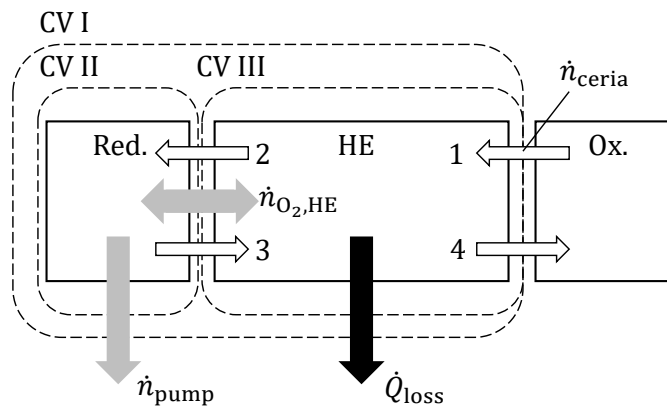


Figure 3.2.: Depiction of control volumes for balance equations. Adapted from Ref. [146] with permission from the American Society of Mechanical Engineers.

The atmosphere in the HE of setup 1 behaves differently from that in setup 2. In setup 1, where the HE-atmosphere is completely isolated from the reactors, a steady state is established in which oxygen release and uptake by the two ceria streams are equal. This means that the change in oxygen non-stoichiometry of the two material streams has the same magnitude, so that $\Delta\delta_{12} = -\Delta\delta_{34}$. This can be explained as follows: If a low O_2 -partial pressure in the HE $p_{O_2,HE}$ was present, the oxygen release would exceed the oxygen uptake so that $p_{O_2,HE}$ would increase. Consequently, the O_2 -release would be reduced and the O_2 -uptake would be increased until the two are equal. The system would therefore move to a stable point of operation, where a $p_{O_2,HE}$ has established at which $\Delta\delta_{12} = -\Delta\delta_{34}$. Similarly, starting at a high $p_{O_2,HE}$, the system would move back to a stable $p_{O_2,HE}$ as less O_2 is released than absorbed, decreasing the O_2 -partial pressure in the HE. This stable point of operation is depicted in Figure 3.3 for an O_2 release from state 1 to 2 and O_2 uptake from state 3 to 4. The resulting steady state is evaluated in the present study. In setup 2, pressure lock 1 does not exist, so that $p_{O_2,HE} = p_{red}$. O_2 can enter or leave the HE from or to the reduction reactor. Thus, the degree of oxidation in the HE can be larger or lower than the degree of reduction. In other words, $\Delta\delta_{12}$ and $-\Delta\delta_{34}$ are not necessarily equal.

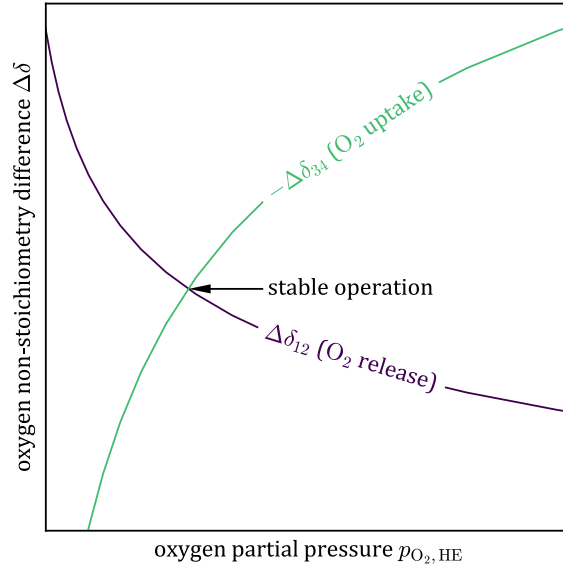


Figure 3.3.: Depiction of the stable point of operation for setup 1.

An oxygen balance around the reduction reactor (CV II) yields the oxygen stream between reduction reactor and HE. It is given by

$$\dot{n}_{O_2, HE} = \frac{1}{2} \Delta\delta_{23} \cdot \dot{n}_{ceria} - \dot{n}_{O_2, pump}, \quad (3.12)$$

where positive values of $\dot{n}_{O_2, HE}$ refer to an oxygen stream from reduction reactor to HE and a negative value vice versa. The oxygen stream $\dot{n}_{O_2, HE}$ can also be expressed as the difference between oxygen release and uptake in the HE, i.e. between states 1 and 2 and states 3 and 4. This is done by substitution of Equation 3.11 into 3.12, which yields

$$\dot{n}_{O_2, HE} = \frac{1}{2} (\delta_1 - \delta_2 + \delta_3 - \delta_4) \cdot \dot{n}_{ceria}. \quad (3.13)$$

For convenience, the quantity $\Delta\delta^* = \delta_1 - \delta_2 + \delta_3 - \delta_4$ is introduced. In case of setup 1, $\Delta\delta^* = 0$, which follows from $\Delta\delta_{12} = -\Delta\delta_{34}$. With the definition of states 1 to 4 according to Figure 3.1, the fraction of recombination [17], introduced in Chapter 2.2.2, reads

$$f_{recomb} = -\frac{\Delta\delta_{34}}{\Delta\delta_{13}}. \quad (3.14)$$

3.1.2. Energy Efficiency

The heat that is exchanged between hot and cold ceria stream in the HE is expressed as the heat recovery ratio ϵ . It is defined as the ratio of heat that is absorbed by the cold stream to the heat

that can maximally be transferred from the hot to the cold stream, given by

$$\epsilon \cdot \int_{T_1}^{T_3} c_{p, \text{ceria}} dT = \int_{T_1}^{T_2} c_{p, \text{ceria}} dT. \quad (3.15)$$

To calculate the heat capacity of ceria $c_{p, \text{ceria}}$, a polynomial is fitted to data from Touloukian and Buyco [51] for CeO_2 , i.e. $c_{p, \text{ceria}}$ is modelled as a function of the temperature, but not of the non-stoichiometry δ . A steady-state energy balance around the HE (CV III) reads

$$0 = \dot{n}_{\text{ceria}} \cdot \left(- \int_{T_1}^{T_2} c_{p, \text{ceria}} dT - \int_{T_3}^{T_4} c_{p, \text{ceria}} dT - \Delta_r h_{12} - \Delta_r h_{34} + \frac{1}{2} \Delta \delta^* \int_{T_{\text{ref}}}^{T_{0_2}} c_{p, \text{O}_2} dT \right) + \dot{Q}_{\text{loss}}. \quad (3.16)$$

Here, $\Delta_r h_{ij}$ is the reaction enthalpy of oxidation or reduction of the redox material in the HE between states i and j . The first two integrals describe the change in enthalpy of entering and leaving ceria streams. The last integral factors in the enthalpy of oxygen entering or leaving the HE from or to the reduction reactor. Here, T_{ref} is the reference temperature at which oxygen evolves or is taken up in the HE. It lies between T_1 and T_3 . Oxygen enters the HE with a temperature $T_{0_2} = T_3$ if more O_2 is taken up than released in the HE, i.e. if $\Delta \delta^* > 0$. If more O_2 is released than taken up in the HE, i.e. $\Delta \delta^* < 0$, oxygen that was released from ceria at T_{ref} , is assumed to leave the HE at $T_{0_2} = \frac{1}{2} (T_2 + T_3)$. For setup 1, $\Delta \delta^* = 0$ as reduction and oxidation always take place to an equal extent as described above. Therefore, the integral over c_{p, O_2} is omitted. For setup 2, it was found that the integral over c_{p, O_2} is small compared to other contributions in Equation 3.16. For $\Delta_r h_{ij}$ an iterative solution is theoretically needed, as it affects the temperatures in the HE, which in turn affects δ_j and thus also $\Delta_r h_{ij}$. The reaction enthalpy $\Delta_r h_{ij}$ mainly depends on the amount of oxygen that is released or taken up by ceria, i.e. on $\delta_j - \delta_i$. Therefore, in setup 1, where reduction and oxidation occur to the same extent, $\Delta_r h_{12}$ and $\Delta_r h_{34}$ largely offset. However, the reaction enthalpy also depends to some extent on the actual values of δ_i and δ_j , so that $\Delta_r h_{12}$ and $\Delta_r h_{34}$ theoretically do not fully offset. Nevertheless, in case of setup 1, $|\Delta_r h_{12} + \Delta_r h_{34}|$ is $\leq 5\%$ of the thermal energy transferred to the cold ceria stream, i.e. the first integral in Equation 3.16 for the majority of investigated heat recovery ratios. The reaction enthalpies are therefore neglected. For setup 2, the influence of the reaction enthalpy might be higher, because $\Delta \delta^* \neq 0$. The correct implementation of the enthalpy of reaction would require, in addition to an iterative approach, the consideration of the second law for the heat transport in the HE. This is necessary to avoid that the heat released at the lower temperature level leads to an increase in the temperature of the hot material flow. An estimation based on a simplified iteration suggests that general trends are the same with and without consideration of the reaction enthalpy for setup 2. For the sake of simplicity it is therefore decided, to neglect $\Delta_r h_{ij}$, so

that for both setups the energy balance given in Equation 3.16 is simplified and together with Equation 3.15 yields

$$\int_{T_3}^{T_4} c_{p, \text{ceria}} dT = -\epsilon \int_{T_1}^{T_3} c_{p, \text{ceria}} dT + \frac{\dot{Q}_{\text{loss}}}{\dot{n}_{\text{ceria}}}, \quad (3.17)$$

which is used to calculate T_4 . The impact of this simplification for setup 2 is discussed together with the simulation results in Chapter 4.1.1. Heat losses to the ambience are determined as a portion of the sensible heat stored in the hot ceria stream. A factor f_{loss} is introduced, which is defined such that

$$\dot{Q}_{\text{loss}} = -f_{\text{loss}} \dot{n}_{\text{ceria}} \int_{T_1}^{T_3} c_{p, \text{ceria}} dT. \quad (3.18)$$

Excessive heat losses or a combination of high heat recovery ratios and significant heat losses might result in very low values of T_4 . Since these points of operation are not very realistic and/or not of technical interest, only cases in which $T_4 \geq T_1$ are studied in this work. From Equations 3.17 and 3.18 follows that $f_{\text{loss}} + \epsilon \leq 1$ must hold in order to guarantee $T_4 \geq T_1$.

For incomplete heat recuperation at $\epsilon < 1$, ceria has to be heated in the receiver reactor. The energy demand for this corresponds to the thermal change in enthalpy

$$\Delta \dot{H}_{\text{ceria}} = \dot{n}_{\text{ceria}} \cdot (1 - \epsilon) \int_{T_1}^{T_3} c_{p, \text{ceria}} dT. \quad (3.19)$$

In addition, the chemical change in enthalpy, i.e. the reduction enthalpy

$$\Delta \dot{H}_{\text{red}} = \dot{n}_{\text{ceria}} \cdot \int_{\delta_2}^{\delta_3} \Delta_{\delta} h d\delta \quad (3.20)$$

has to be compensated by solar heat. Here, $\Delta_{\delta} h$ is the reaction enthalpy of the reduction per δ -increment. Panlener et al. [50] found $\Delta_{\delta} h$ to be in good approximation temperature independent for the relevant δ -range. Bulfin et al. [116] fitted a polynomial to data from Ref. [50], which is used to calculate $\Delta_{\delta} h$ in the present study.

In or prior to the oxidation, the feed stream has to be evaporated and overheated in case of H_2O -splitting or only heated in case of CO_2 -splitting according to

$$\Delta \dot{H}_{\text{feed}} = \dot{n}_{\text{feed}} \cdot (h_{\text{H}_2\text{O}, \text{gas}}(T_1) - h_{\text{H}_2\text{O}, \text{liq}}(T_{\text{amb}})) \quad (3.21)$$

or

$$\Delta \dot{H}_{\text{feed}} = \dot{n}_{\text{feed}} \cdot (h_{\text{CO}_2}(T_1) - h_{\text{CO}_2}(T_{\text{amb}})) \quad (3.22)$$

with the ambient temperature $T_{\text{amb}} = 298$ K. Enthalpy data for H_2O and CO_2 from the database *FactPS* of the software *FactSage 7* [150] is used. Heat recuperation between product and feed stream can improve the overall efficiency of the redox cycle. However, the focus of the present

study is on solid-solid heat recovery, as $\Delta\dot{H}_{\text{ceria}}$ accounts for a high portion of the overall heat demand. In fact, for the standard parameter set discussed in the results, $\Delta\dot{H}_{\text{ceria}}$ is more than 5 times higher than $\Delta\dot{H}_{\text{feed}}$ in case of H₂O splitting and even more than 10 times higher in case of CO₂ splitting. Therefore, heat recovery for the fluid phase is not investigated, here.

For vacuum pumping, an array of vacuum pumps described by Brendelberger et al. [27] is assumed. This three stage pump array consist of two HV40000, one HV8000 and two IDX1300 pumps by Edwards. The volume flow \dot{V}_{array} , which such a pump configuration can remove at a given pressure p_{red} and the necessary power P_{array} are calculated with data from Ref. [27]. The pumping power is then scaled to 1 mol s⁻¹ of product, which yields

$$P_{\text{pump}} = P_{\text{array}} \frac{\dot{V}_{\text{pump}}}{\dot{V}_{\text{array}}}, \quad (3.23)$$

using the volume flow of O₂ \dot{V}_{pump} , which is removed from the reduction reactor per mol s⁻¹ of product. At the low pressures present in the reduction reactor it seems justified to describe the gas-phase as an ideal gas. Consequently, the volume flow is calculated with the ideal gas law, according to

$$\dot{V}_{\text{pump}} = \dot{n}_{\text{O}_2, \text{pump}} \frac{R T_{\text{amb}}}{p_{\text{red}}}, \quad (3.24)$$

where the ambient temperature T_{amb} is used as it is assumed that the gas has to be cooled before it passes the pumps. Radiation losses in the receivers i.e. the receiver reactor for the reduction and the receiver needed to preheat/evaporate the oxidation feed, are considered via an ideal receiver efficiency as discussed in Section 2.1

$$\eta_{\text{rec}} = 1 - \frac{\sigma (T_{\text{rec}}^4 - T_{\text{amb}}^4)}{\tilde{C} I} \quad (3.25)$$

with the receiver temperature $T_{\text{rec}} = T_{\text{red}}$ or $T_{\text{rec}} = T_{\text{ox}}$, the Stefan-Boltzmann constant σ and the concentrated solar flux at the receiver $\tilde{C} I$. This definition also takes into account radiation from the ambience. The efficiency of the the concentrator, for instance the field efficiency of a heliostat field is not included as the main focus of this study is on the redox cycle. Electricity for the pumps is produced with a concentrated solar power plant. The efficiency for conversion of solar radiation to electricity η_{el} is taken from Xu et al. [151]. In accordance with the redox system, here the field efficiency is also excluded, which yields $\eta_{\text{el}} = 0.343$. The total solar energy can be calculated with the mentioned energy contributions and efficiencies as

$$\dot{Q}_{\text{sol}} = \frac{P_{\text{pump}}}{\eta_{\text{el}}} + \frac{\Delta\dot{H}_{\text{ceria}} + \Delta\dot{H}_{\text{red}}}{\eta_{\text{rec, red}}} + \frac{\Delta\dot{H}_{\text{feed}}}{\eta_{\text{rec, ox}}}. \quad (3.26)$$

A system efficiency, defined as a solar-to-fuel efficiency [13], relates the total higher heating value (HHV) of the product to the solar input according to

$$\eta_{\text{sys}} = \frac{\dot{n}_{\text{product}} \cdot \text{HHV}_{\text{product}}}{\dot{Q}_{\text{sol}}}. \quad (3.27)$$

Values of the HHV of H₂O and CO₂ from Ref. [131] are used. Ultimate goal of this investigation is to determine the system efficiency η_{sys} as function of the heat recovery ratio ϵ . To do so, the equations summarized in this section are solved for given values of ϵ .

3.1.3. Second Law Analysis

To verify that the results predicted from this model are in line with the second law of thermodynamics, an entropy balance for the HE is introduced. Generally, the steady-state entropy balance of a control volume is [152]

$$0 = \sum_i \frac{\dot{Q}_i}{T_i} + \sum_i \dot{n}_i s_i + \dot{S}_{\text{irr}}, \quad (3.28)$$

where \dot{Q}_i are heat flows that enter or leave the control volume at the temperature T_i , s_i are the molar entropies of leaving and entering mole flows and \dot{S}_{irr} is the entropy production due to irreversibilities. The second law is violated if the irreversible entropy production is calculated to be negative. The entropy balance used in the present work is established for CV III of Figure 3.2. The only heat flow that crosses the boundaries of this control volume is \dot{Q}_{loss} , accounting for heat losses from the HE to the ambience. The entropy balance for the present case is therefore

$$0 = \frac{\dot{Q}_{\text{loss}}}{T_{\text{loss}}} + \dot{n}_{\text{ceria}} (s_1 - s_2 + s_3 - s_4) + \dot{n}_{\text{O}_2, \text{HE}} s_{\text{O}_2} + \dot{S}_{\text{irr}}. \quad (3.29)$$

T_{loss} is the temperature at which \dot{Q}_{loss} leaves the HE. The HE has a temperature profile, so that heat leaves the system at different temperature levels rather than at a single temperature. This is considered by using a logarithmic mean temperature [132]

$$T_{\text{loss}} = \frac{T_3 - T_4}{\ln \left(\frac{T_3}{T_4} \right)}. \quad (3.30)$$

For $\epsilon = 0$ and $f_{\text{loss}} = 0$, the hot material stream does not change its temperature in the HE, so that $T_4 = T_3$. In this special case, Equation 3.30 yields zero divided by zero. The limit of T_{loss} for $T_4 \rightarrow T_3$ can be determined via the derivatives of numerator and denominator in Equation 3.30 with respect to T_4 , which yields

$$\lim_{T_4 \rightarrow T_3} \frac{T_3 - T_4}{\ln \left(\frac{T_3}{T_4} \right)} = \lim_{T_4 \rightarrow T_3} \frac{-1}{-\frac{1}{T_4}} = \lim_{T_4 \rightarrow T_3} T_4 = T_3. \quad (3.31)$$

Consequently, $T_{\text{loss}} = T_3$, if $T_4 = T_3$. The definition of T_{loss} given in Equations 3.30 and 3.31 is the logarithmic mean temperature of the hot side of the HE. Hence, T_{loss} is overestimated, which is a conservative approximation with respect to the irreversible entropy production. The higher T_{loss} is, the lower is \dot{S}_{irr} , as $\dot{Q}_{\text{loss}} < 0$. Therefore, the model is more likely to predict a violation of the second law if T_{loss} is overestimated.

For convenience, the molar quantities $s_{\text{irr}} = \dot{S}_{\text{irr}} \cdot \dot{n}_{\text{ceria}}^{-1}$ and $q_{\text{loss}} = \dot{Q}_{\text{loss}} \cdot \dot{n}_{\text{ceria}}^{-1}$ are defined.

Using these quantities and the previously introduced $\Delta\delta^*$, the entropy balance can be rearranged to

$$s_{\text{irr}} = -\frac{q_{\text{loss}}}{T_{\text{loss}}} + s_2 - s_1 + s_4 - s_3 - \frac{\Delta\delta^*}{2} s_{\text{O}_2}, \quad (3.32)$$

by dividing Equation 3.29 by \dot{n}_{ceria} . Ceria changes its thermodynamic states within the HE as both temperature and oxygen content change. The molar entropy at a given state, is

$$s_i(T_i, \delta_i) = s_{f,i}(T_{\text{ref}}, \delta_i) + \Delta s_{i,\text{th}}(T_i, T_{\text{ref}}, \delta_i), \quad (3.33)$$

for ceria, or for O_2

$$s_{\text{O}_2}(T) = s_{f,\text{O}_2}(T_{\text{ref}}) + \Delta s_{\text{O}_2,\text{th}}(T_{\text{O}_2}, T_{\text{ref}}), \quad (3.34)$$

where $s_{f,i}$ is the entropy of formation, $\Delta s_{i,\text{th}}$ is the thermal entropy change between a reference temperature T_{ref} and the current temperature T_i . Since the entropy is a state function and therefore independent of how the system has reached a certain state, the change from one thermodynamic state to another can be divided into hypothetical steps that facilitate the calculation of the entropy change. In the present case, the changes that the two ceria streams undergo from a state i to a state j are divided into the following steps, which are displayed in Figure 3.4. The first step is a hypothetical oxidation from δ_i to a reference state $\delta = 0$ at temperature T_i . Next, heating of ceria at the reference state from T_i to T_j follows. The final step is the reduction from $\delta = 0$ to δ_j at T_j . This way, data for CeO_2 , i.e. $\delta = 0$, can be used to describe the thermal entropy change. Substitution of s_i in Equation 3.32 with Equations 3.33 and 3.34 and summarizing the

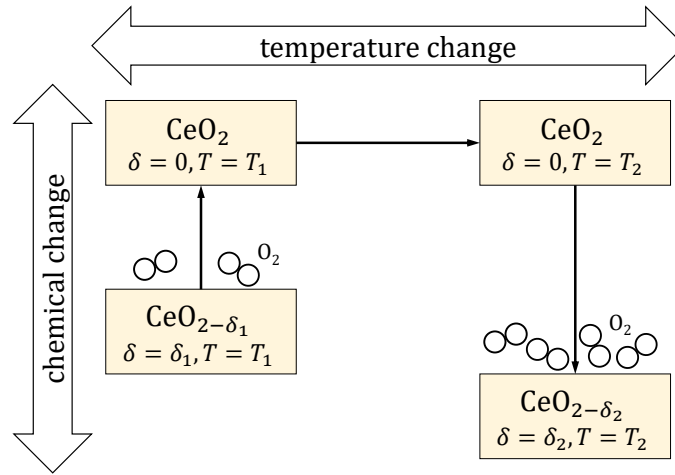


Figure 3.4.: Depiction of the path used to calculate entropies. Adapted from Ref. [146] with permission from the American Society of Mechanical Engineers.

entropies of formation into the reaction entropy of reduction/oxidation of ceria $\Delta_r s_{ij}$ yields

$$s_{\text{irr}} = \underbrace{\Delta_r s_{12} + \Delta_r s_{34}}_{\Delta s_{\text{ch}}} + \underbrace{\Delta s_{12,\text{th}} + \Delta s_{34,\text{th}}}_{\Delta s_{\text{th}}} - \underbrace{\frac{\Delta\delta^*}{2} \Delta s_{\text{O}_2,\text{th}}}_{\Delta s_{\text{O}_2}} - \frac{q_{\text{loss}}}{T_{\text{loss}}}. \quad (3.35)$$

The reaction entropy is calculated in analogy to the reaction enthalpy in Equation 3.20 with a reaction entropy per δ -increment:

$$\Delta_{\text{r}}s_{ij} = \int_{\delta_i}^{\delta_j} \Delta_{\delta}s(\delta, T_{\text{ref}}) d\delta, \quad (3.36)$$

where an equation from Ref. [56] is used to calculate $\Delta_{\delta}s$. The temperature dependence of $\Delta_{\text{r}}s_{ij}$ is relatively weak in the relevant temperature range [56] and $\Delta_{\text{r}}s_{ij}$ is hence assumed to be independent of the temperature. Also, no pressure dependence is considered for the entropy. This is justified for the solid [117], but is a simplification with respect to O_2 . However, for setup 1, the contribution of O_2 to the entropy cancels out as $\Delta\delta^* = 0$. For setup 2, the entropy of O_2 differs by up to 24% in the relevant pressure range [145]. As discussed in the results, Δs_{O_2} is small compared to the other terms in Equation 3.35 and has virtually no impact on s_{irr} . It seems therefore acceptable to neglect the pressure dependence of the entropy of O_2 . The thermal contribution to the entropy change $\Delta s_{ij,\text{th}} = s(T_j) - s(T_i)$ is calculated with data from Refs. [144, 145] for O_2 and Ref. [117] for CeO_2 . Similar to the energy balance discussed above, the contribution of $\dot{n}_{\text{O}_2,\text{HE}}$ to the entropy balance has to be considered, which is done by $\Delta s_{\text{O}_2,\text{th}}$. In case of a net reduction, $\Delta s_{\text{O}_2,\text{th}}$ accounts for the heating of O_2 that has evolved in the HE from T_{ref} to a temperature T_{O_2} . In case of a net oxidation, $\Delta s_{\text{O}_2,\text{th}}$ accounts for the cooling of hot entering O_2 to T_{ref} . Here, T_{O_2} is defined as explained in Section 3.1.2 and the reference temperature T_{ref} is set to an average temperature in the HE, i.e. $T_{\text{ref}} = \frac{1}{4} (T_1 + T_2 + T_3 + T_4)$. This choice has just a minor impact on the result, as $\Delta s_{\text{O}_2,\text{th}}$ is small compared to the other entropy contributions and T_{ref} cancels out in Δs_{th} .

3.1.4. Modelling Oxidation Kinetics

The model described above is based on equilibrium assumptions. This means that both oxidation and reduction of ceria inside the HE are modelled as infinitely fast. As a result, ceria leaves the HE with δ_2 and δ_4 according to the equilibrium at the respective temperatures T_2 and T_4 and the O_2 partial pressure $p_{\text{O}_2,\text{HE}}$. To study the impact of limited reaction rates, the model of setup 1 is modified with a simplistic kinetic approach. Herein, the equilibrium condition for the hot ceria stream, i.e. state 4, is replaced by an average δ -rate. This δ -rate is a constant parameter in the model and its impact is studied by parameter variation. Using this average δ -rate together with a residence time Δt_{res} , the non-stoichiometry values δ_4 and δ_2 can be determined as

$$\delta_4 = \delta_3 + \left(\frac{d\delta}{dt} \right)_{34} \Delta t_{\text{res}} \quad (3.37)$$

and

$$\delta_2 = \delta_1 - \left(\frac{d\delta}{dt} \right)_{34} \Delta t_{\text{res}}. \quad (3.38)$$

A negative δ -rate refers to an oxidation of the hot stream (state 3 to 4). Similar to the equilibrium case, $\Delta\delta_{12} = -\Delta\delta_{34}$ must hold. Therefore, the δ -rate from state 1 to 2 is the negative of the rate from state 3 to 4 as given in Equation 3.38. In this study, it is assumed that the cold ceria stream is always reduced and the hot stream is always oxidised so that $(\frac{d\delta}{dt})_{34} \leq 0$. The residence time is extracted from Figure 8 of Ref. [41] ($n_{\text{he}} = 15$). Between two extracted data points, Δt_{res} is determined via linear interpolation. In Ref. [41], Falter et al. studied a generic model describing counterflow solid heat exchange. The heat exchanger is divided into a number of chambers (n_{he}) along the flow path of the redox material. At high n_{he} the HE is expected to approach the behaviour of a continuous counterflow HE. Results in Ref. [41] were computed for $T_{\text{red}} = 1800 \text{ K}$ and $T_{\text{ox}} = 1000 \text{ K}$.

In reality, the δ -rate is a function of many factors, such as temperature, O_2 partial pressure, oxygen non-stoichiometry external mass transport or the shape of the redox material. Consequently, at given operating conditions a certain $p_{\text{O}_2, \text{HE}}$ would be established in the HE at which oxidation and reduction kinetics are such that $\Delta\delta_{12} = -\Delta\delta_{34}$. Since a universal function for the δ -rate is not known, it is instead given as a parameter and the resulting $p_{\text{O}_2, \text{HE}}$ is calculated to check for feasibility. To compute $p_{\text{O}_2, \text{HE}}$, it is assumed that only the oxidation has kinetic limitations, while the reduction is infinitely fast. Hence, $p_{\text{O}_2, \text{HE}}$ is the equilibrium- p_{O_2} at T_2 and δ_2 . It is calculated using Equation 2.32 [48]. This assumption implies that the reduction is significantly faster than the oxidation. This is a conservative estimation with respect to the feasibility of the assumed oxidation rates for the following reason. The oxidation is faster at higher p_{O_2} , while the reduction is slower at higher p_{O_2} . Note that here the expressions reduction and oxidation refer to a net reduction or oxidation, which is a dynamic process consisting of a reduction and an oxidation reaction, according to Equation 2.18. In this equation, the reduction term is independent of p_{O_2} . However, the net reduction of a redox material is the superposition of the reduction and the oxidation reaction. According to Equation 2.18 it is therefore slow at high p_{O_2} . In a HE in which oxidation and reduction have limited kinetics, $p_{\text{O}_2, \text{HE}}$ settles at a value at which reduction of the one stream and oxidation of the other stream are equally fast. The slower the reduction generally is, the lower $p_{\text{O}_2, \text{HE}}$ has to be to meet this condition. Assuming an infinitely fast reduction therefore yields an upper limit for $p_{\text{O}_2, \text{HE}}$. This implies that in reality $p_{\text{O}_2, \text{HE}}$ might be lower than calculated. In order to mitigate the recombination affect, low oxidation rates and therefore low $p_{\text{O}_2, \text{HE}}$ are beneficial. Thus, the overestimated reduction kinetics and resulting high $p_{\text{O}_2, \text{HE}}$ are a pessimistic estimate.

All quantities except $p_{\text{O}_2, \text{HE}}$, δ_2 and δ_4 are calculated as described in the previous sections.

3.2. Experimental Investigation of Recombination Kinetics

The kinetics of the recombination effect is studied experimentally. To this end, oxidation rates of ceria at high temperatures under vacuum conditions are determined. This investigation aims to firstly determine whether a significant impact of the kinetics on the recombination effect is to be expected, i.e. whether there are kinetic limitations and secondly whether kinetic limitations can

be caused by adding an inert gas to the system. As described in Section 2.4, TGA does not necessarily yield intrinsic kinetics, but rather net kinetics that include different effects of heat and mass transport during the TGA. At the same time, conditions in TGA measurements differ from those of the studied system and seem therefore not to be a suitable method in this context. One reason is the forced convection between reactive gas and sample, which creates a more uniform concentration profile, which is particularly disadvantageous, when studying mass transport in the gas phase and the impact of an inert gas on the net kinetics. Another reason is the small sample size. Small samples of porous materials might not be representative for the bulk behaviour of larger components of the same material, which are likely used in technical applications. Other options discussed in Section 2.4 that rely on the re-oxidation of the redox material do not allow for fast evaluation of different measuring points. However, the experiments are supposed to simulate the behaviour of a redox material that enters a HE in its reduced hot state and cools down on its way through the HE. Hence, different temperature levels are to be studied in a reasonable time frame. Consequently, a novel approach to study the oxidation kinetics of ceria under partial vacuum and high temperatures is developed and described in the following sections.

3.2.1. Test Rig Development

Goal of the test rig development is to be able to study the oxidation of redox materials under O_2 , with the following conditions:

- Determine the degree of oxidation and the oxidation rate.
- Investigate samples sufficiently large to represent the bulk properties of the porous material, e.g. a diameter of approximately 20 mm.
- Avoid flow conditions that are unrepresentative for the investigated process such as in a TGA.
- Study oxidation under vacuum conditions.
- Study the impact of an inert gas on the oxidation rate.

The chosen approach to determine the degree of oxidation is to measure pressures and temperatures to calculate the O_2 uptake. This is done by calculation the amount of substance via mole balances and an equation of state, such as the ideal gas law. Consequently, pressures, gas temperatures and volumes of the test rig components need to be determined. In the following, the final test rig and its development are presented.

The test rig comprises two main parts: a furnace in which the ceria sample is placed and a buffer volume through which O_2 and N_2 can be fed to the furnace. Both are connected to a vacuum pump via valves so that both compartments can be evacuated simultaneously or separately. The test rig is shown in Figures 3.5 and 3.6. The vacuum pump used is a sliding vane rotary vacuum pump type RZ 5 by Vacuubrand. The furnace is an STF 16/180 tube furnace by Carbolite

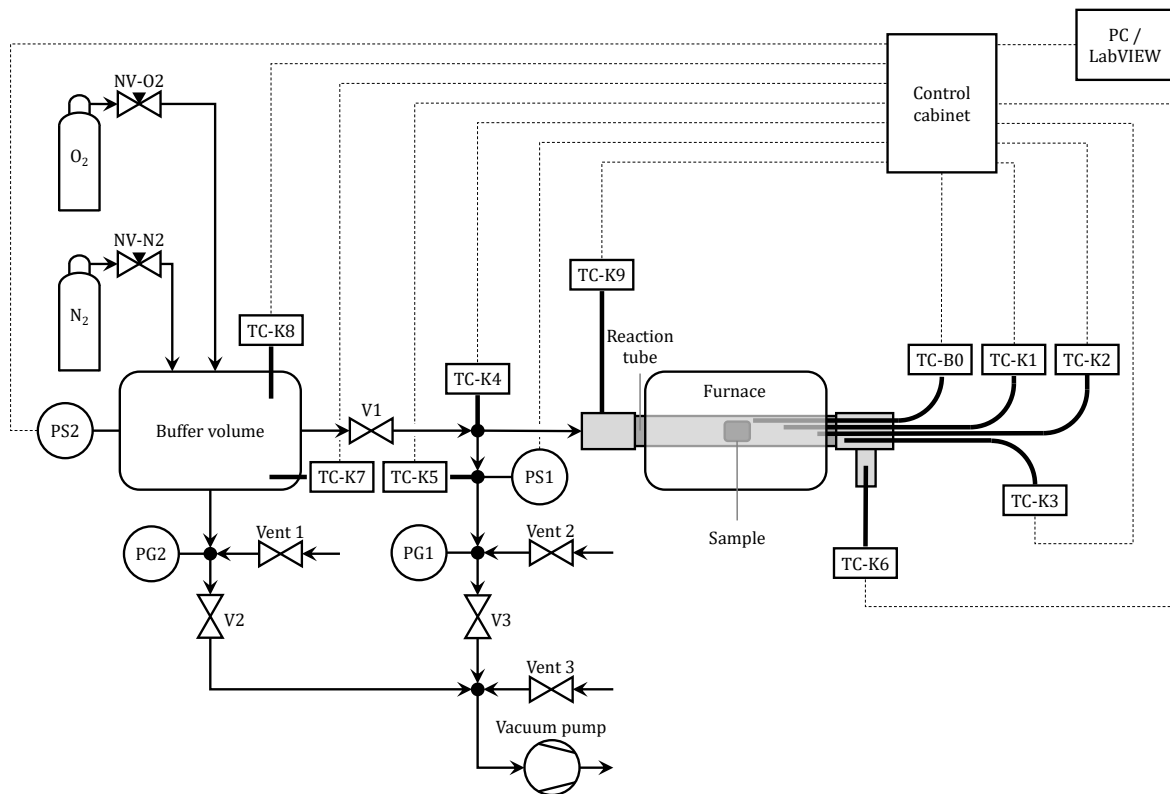


Figure 3.5.: Schematic of the test rig.

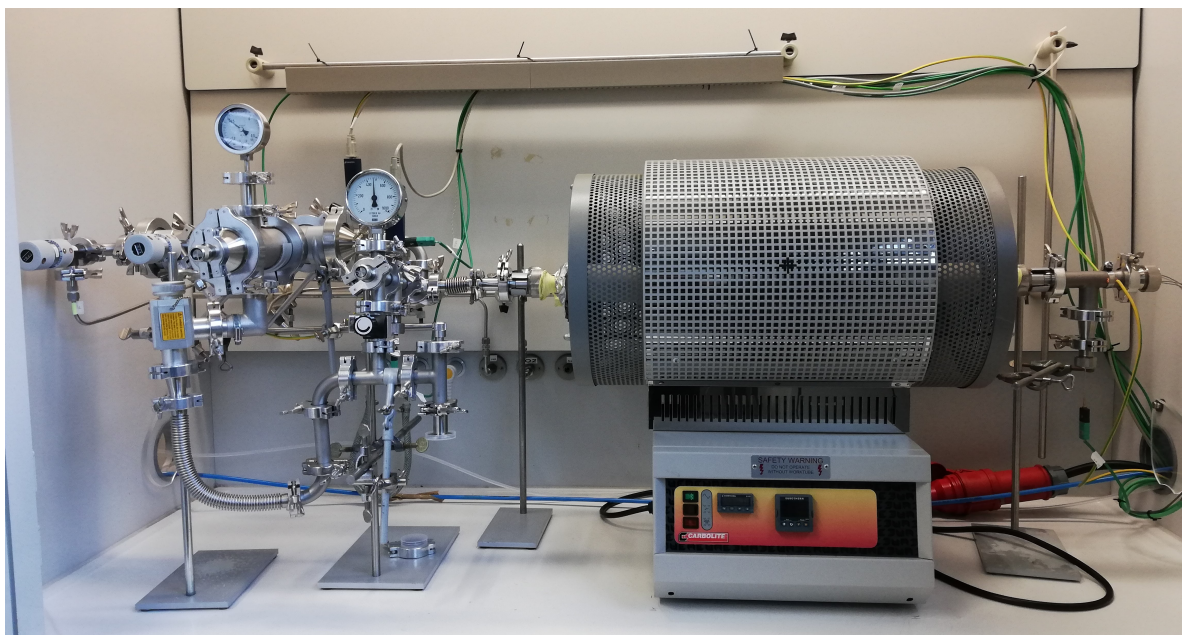


Figure 3.6.: Photograph of the test rig.

(now Carbolite Gero) with a 180 mm wide heated zone in the center. The buffer volume is constructed with tube elements. The sample is placed inside an alumina tube with an inner diameter of 20 mm. This alumina tube is referred to as reaction tube. The reaction tube is placed inside

another alumina tube with an inner diameter of 50 mm. The outer tube protects the furnace in the event of a reaction tube failure. At both ends, the reaction tube has metallic flanges. The length of the reaction tube is 822 mm, including the flanges. Besides the mentioned alumina tubes, all tubes of the test rig are dedicated steel or aluminium vacuum tubes of the standard ISO-KF with inner diameters of 16 mm, 24 mm or 50 mm. As depicted in Figure 3.5, these tubes form three compartments which can be separated from one another by valves: the reaction tube in the furnace plus adjacent tubing, the buffer volume and a pre-chamber to the vacuum pump. Throughout the present work, the reaction tube and its adjacent tubing will be referred to as furnace or furnace volume. It is separated from the buffer volume and the vacuum pump by the valves V1 and V3 shown in Figure 3.5. V1 is a butterfly valve, which allows rapid opening and closing. The vent valve Vent 2 separates the furnace volume from the ambience. The buffer volume is connected to the O₂ and N₂ supply via the needle valves NV-O2 and NV-N2. It is separated from the vacuum pump by V2 and from the ambience by Vent 1. The tubing to the vacuum pump connects V2 and V3 with the pump. Its volume serves as a pre-chamber, which can be connected or disconnected from the ambience with vent valve Vent 3. This is important to control the pressure gradient during start up and shut down of the vacuum pump. After an experiment the vacuum pump is disconnected from the test rig. The test rig is kept at vacuum. For the next operation of the test rig, the vacuum pump is again connected. During the start up, V2, V3 and Vent 3 can be kept closed so that the pre-chamber reaches a lower pressure than the buffer volume and the furnace. Next V2 and/or V3 are opened. This prevents air from entering the test rig in the beginning, to avoid contamination. Before the shut down of the pump, V2 and V3 can be closed and Vent 3 opened. This ensures that gas is not sucked backwards through the pump by a vacuum as this might damage the pump.

Temperatures are measured with thermocouples (TCs) at different points of the test rig as indicated in Figure 3.5. The thermocouple that is placed closest to the ceria sample is a type-B (Pt30Rh-Pt6Rh) TC. All other TCs are of type-K (NiCr-Ni). Throughout this dissertation, TCs are named TC B0 (in case of the type-B TC) or TC K_{*i*} (in case of the type-K TCs), where *i* is an integer from 1 to 9. To prevent TCs from touching the reaction tube, elements of a high temperature insulation material are strung on the TCs, as depicted in Figure 3.7. A suitable material was identified, by preliminary tests, in which different materials were heated in the tube furnace at a rate of 10 K min⁻¹ to 1788 K, i.e. 15 K above the maximum temperature during the experiments and held at that temperature for 1.5 h. Mats made from aluminium silicate fibres are found to be suitable insulation materials that withstand the relevant temperatures and do not interact with the reaction tube. All TCs, except TC K9 measure temperatures inside the test rig, which they enter through dedicated feedthroughs. TC K9 measures the temperature on the surface as a safety measure to prevent the operator from touching hot surfaces. Technical details on TCs are summarized in Table 3.1.

The pressure sensors used to measure the pressure in both buffer volume and furnace are Porter CDG020D capacitance diaphragm gauges by Inficon, labelled PS1 and PS2 in Figure 3.5. These can measure total pressures up to 1024 Pa independent of the gas species. To monitor

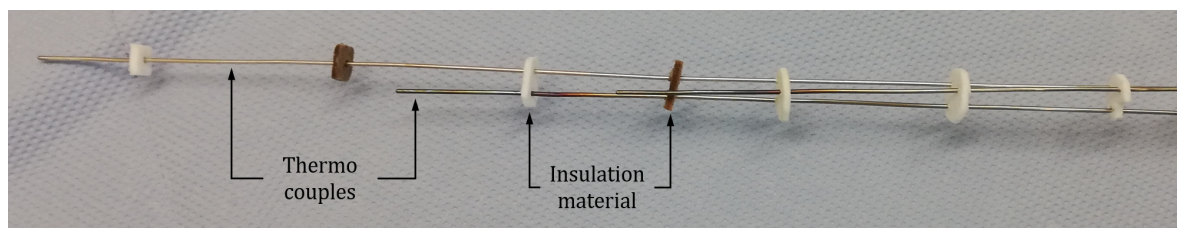


Figure 3.7.: Thermocouples with elements of a high temperature insulation material. Darker elements were subject to elevated temperatures in test runs.

higher pressures, two analogue pressure gauges, PG1 and PG2 are used. Details on all pressure sensors are given in Table 3.1.

Thermocouples and pressure sensors send an analogue voltage signal to the control cabinet where they are processed by Advantech ADAM modules of the 4000 series. ADAM 4018 and ADAM 4018+ modules are used for TC signals, and an ADAM 4017+ module for the pressure sensors' signals. These modules use the standard RS-485 for data transmission, which is converted to RS-232 by an ADAM 4520 module and finally to USB by an RS-232 to USB converter for communication with the computer. Here the measurements are managed by a dedicated *LabVIEW* code. The *LabVIEW* code logs data in steps of 400 ms or multiples of 400 ms. A time step of 400 ms was found to be a sufficient time frame for the processing of data by the ADAM modules. The sheaths of TCs B0 and K1 to K3, i.e. the TCs inside the reaction tube, are earthed via the control cabinet. Without earthing a large noise superposes the signal, in case of high power consumption by the furnace.

During test runs of the setup an unexpected pressure increase during heating was observed. The test rig was first evacuated and then heated. The reaction tube did not hold a reactive sample. In addition to the expected pressure increase due to heating of the gas phase, a steep pressure increase was observed at $T_{B0} \approx 1500$ K during some of the test runs. This might have been due to combustion or decomposition of an organic binder in the aforementioned aluminium silicate fibre mats. To avoid this from happening during the actual experiments, the following procedure was performed to remove possible organic components from the system: the furnace was kept at 1823 K, i.e. 50 K above the maximum temperature during the experiments for 6.5 h at approximately $6 \cdot 10^4$ Pa O_2 . During that time, the atmosphere was six times removed via the vacuum pump and replaced with fresh O_2 . In another run just after this treatment, the unexpected pressure increase was not observed any more. The behaviour of the test rig before and after the treatment, as well as after all experiments is shown in Figure B.1 of Appendix B, where these results are discussed in more detail.

Table 3.1.: Specifications of temperature and pressure sensors used in the test rig.

Name	Specifications	Measuring range	Measuring error	Location
TC B0	Sheath thermocouple type B, \varnothing 1.5 mm class 3 IEC 60584-1: 2014-07	593 K to 1973 K	$\max \{4 \text{ K}, 0.005 \cdot T \}$ (T in °C)	In reaction tube 12 mm from center
TC K1	Sheath thermocouple type K, \varnothing 1.5 mm class 2 DIN EN 60584	73 K to 1473 K	$\max \{2.5 \text{ K}, 0.0075 \cdot T \}$ (T in °C)	In reaction tube 130 mm from center
TC K2	Sheath thermocouple type K, \varnothing 1.5 mm class 2 DIN EN 60584	73 K to 1473 K	$\max \{2.5 \text{ K}, 0.0075 \cdot T \}$ (T in °C)	In reaction tube 200 mm from center
TC K3	Sheath thermocouple type K, \varnothing 1.5 mm class 2 DIN EN 60584	73 K to 1473 K	$\max \{2.5 \text{ K}, 0.0075 \cdot T \}$ (T in °C)	In reaction tube 400 mm from center
TC K4	Sheath thermocouple type K, \varnothing 1.5 mm class 1 DIN EN 60584-1	73 K to 1373 K	$\max \{1.5 \text{ K}, 0.004 \cdot T \}$ (T in °C)	Furnace tubing
TC K5	Sheath thermocouple type K, \varnothing 1.5 mm class 1 DIN EN 60584-1	73 K to 1373 K	$\max \{1.5 \text{ K}, 0.004 \cdot T \}$ (T in °C)	Furnace tubing
TC K6	Sheath thermocouple type K, \varnothing 1.5 mm class 1 DIN EN 60584-1	73 K to 1373 K	$\max \{1.5 \text{ K}, 0.004 \cdot T \}$ (T in °C)	Furnace tubing
TC K7	Sheath thermocouple type K, \varnothing 1.5 mm class 1 DIN EN 60584-1	73 K to 1373 K	$\max \{1.5 \text{ K}, 0.004 \cdot T \}$ (T in °C)	Buffer volume
TC K8	Sheath thermocouple type K, \varnothing 1.5 mm class 1 DIN EN 60584-1	73 K to 1373 K	$\max \{1.5 \text{ K}, 0.004 \cdot T \}$ (T in °C)	Buffer volume
TC K9	Thermocouple type K with copper contact for surfaces, IEC 584	273 K to 473 K	$\pm 1.5 \text{ K}$	On furnace tubing, close to reaction tube
PS1	Inficon Porter CDG020D 3CA3-961-0100	$\leq 1024 \text{ Pa}$	$\pm 1 \%$ of reading	Furnace tubing
PS2	Inficon Porter CDG020D 3CA3-961-0100	$\leq 1024 \text{ Pa}$	$\pm 1 \%$ of reading	Buffer volume
PG1	Analogue manometer by Leybold	0 Pa to $1 \cdot 10^5 \text{ Pa}$	N/A	Furnace tubing
PG2	Analogue manometer by Pfeiffer	0 Pa to $1.6 \cdot 10^5 \text{ Pa}$	$\pm 1.6 \%$ of measuring range	Buffer volume

3.2.2. Volumes of Test Rig Components

During the construction of the test rig, results from modelling the test rig, as described in Section 3.2.8 were used for the coarse dimensioning of the test rig components. The precise buffer and furnace volumes however depend on the design of all components and should be measured as they are crucial quantities for the evaluation of the experiments. To do so, a stainless steel cylin-

der of 292.7 mL is used as a reference volume. The cylinder is attached to the test rig, as shown in Figure 3.8.

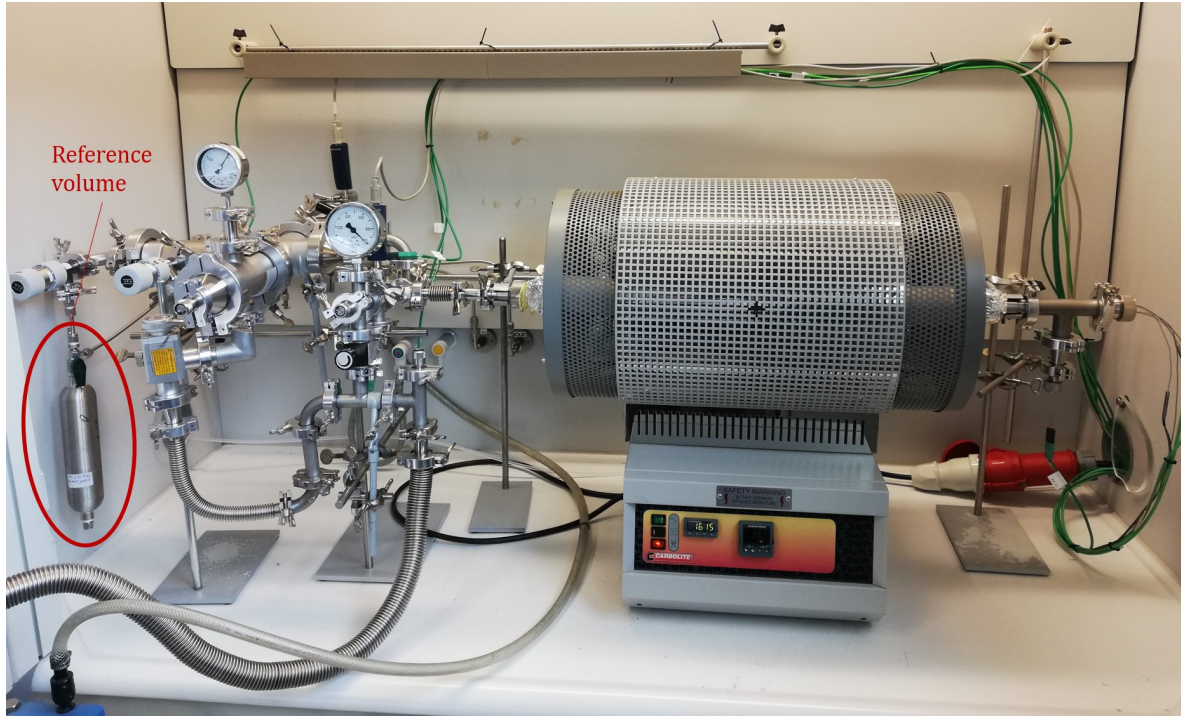


Figure 3.8.: Photograph of the test rig including the reference volume.

Test rig and reference volume are separated by a needle valve. The reference volume is brought to a pressure p_{ref} , while the test rig has a pressure p_0 . This is achieved by first evacuating the whole test rig with the needle valve open, then the test rig is filled with approximately $2 \cdot 10^4$ Pa O_2 (purity: 99.999 %), after which the test rig is again evacuated until p_{ref} is reached. The needle valve is then closed and the test rig (now separated from the reference volume) is evacuated further to p_0 . After the initial pressures have been established, the needle valve is opened and the pressure of the rest rig increases to p_1 . The volume of the test rig can then be calculated with the ideal gas law formulated for states 0 and 1 for the test rig

$$p_0 \cdot V_{\text{TR}} = n_0 \cdot R \cdot T_0, \quad (3.39)$$

$$p_1 \cdot V_{\text{TR}} = n_1 \cdot R \cdot T_1 \quad (3.40)$$

and the reference volume

$$p_{\text{ref}} \cdot V_{\text{ref}} = n_{0,\text{ref}} \cdot R \cdot T_{\text{ref}}, \quad (3.41)$$

$$p_1 \cdot V_{\text{ref}} = n_{1,\text{ref}} \cdot R \cdot T_1 \quad (3.42)$$

together with a mole balance

$$n_{0,\text{ref}} + n_0 = n_{1,\text{ref}} + n_1. \quad (3.43)$$

From equations 3.39 - 3.43 follows the volume of the test rig

$$V_{\text{TR}} = V_{\text{ref}} \cdot \left(\frac{p_{\text{ref}}}{T_{\text{ref}}} - \frac{p_1}{T_1} \right) \cdot \left(\frac{p_1}{T_1} - \frac{p_0}{T_0} \right)^{-1}. \quad (3.44)$$

The valve V1 can either be open, in which case V_{TR} is the sum of buffer and furnace volume or closed, which means that V_{TR} is only the buffer volume. The measurement was repeated with values of p_0 ranging from 38 Pa to 294 Pa and p_{ref} ranging from 770 Pa to 930 Pa. Results are summarized in Table C.1 of Appendix C.

3.2.3. Measuring the Temperature Profile in the Furnace

To get an impression of the temperature profile along the reaction tube of the furnace, temperatures were measured in the open reaction tube at ambient pressure. That means the reaction tube was inserted into the furnace in the same way as in the actual experiments, but wasn't vacuum sealed. Instead, the reaction tube ended on one side with an open ventilating valve and on the other side with a radiation shield out of aluminium foil as shown in Figure 3.9. These

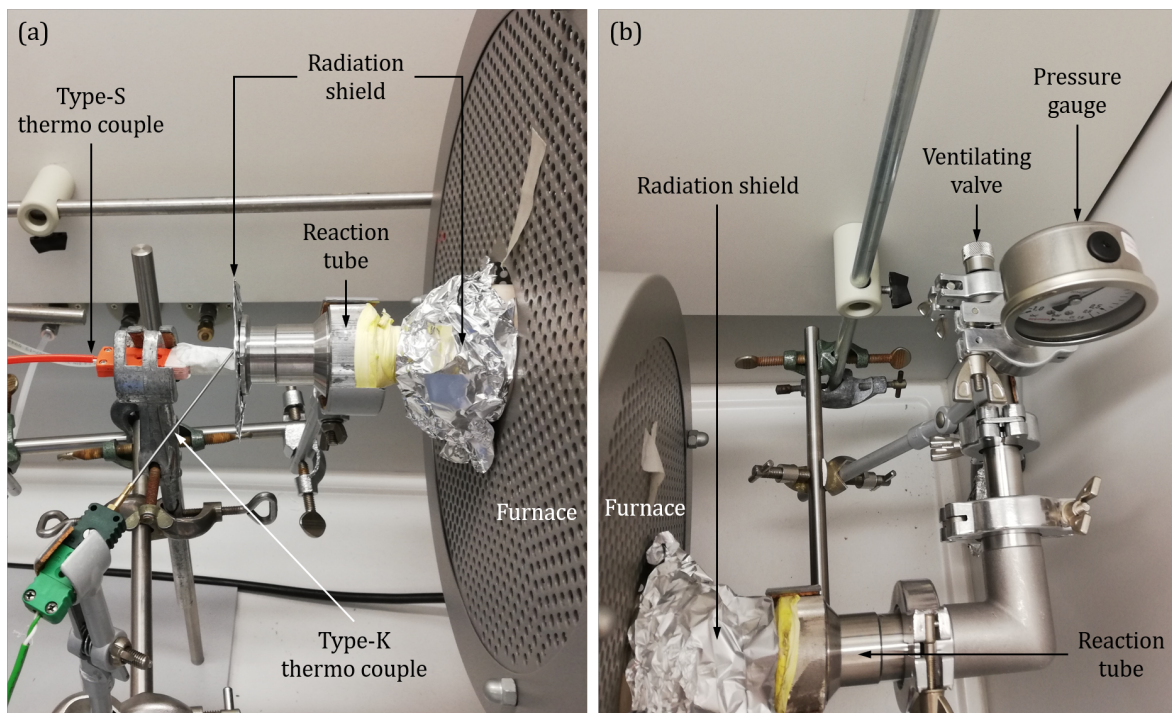


Figure 3.9.: Setup for measuring the temperature profile inside the reaction tube. (a) setup on the left side of the furnace, (b) setup on the right side of the furnace.

elements mitigate radiation losses, but cannot prevent ambient air from entering the system. Hence, the conditions during this measurement differ from the actual experiments and results are rather to be understood as a rough estimation that helps understanding the temperature distribution and designing the experiment. The distinct advantage of the open system is that a thermocouple can be easily moved through the furnace for rapid recording of several measuring

points without constructional changes. Temperature data was measured with a type-S thermocouple, starting in the hot center of the reaction tube, moving in 10 mm to 50 mm steps to one of the colder ends of the tube, i.e. the temperature was measured in one half of the tube. Due to the symmetry of furnace and reaction tube, it is assumed that the measured temperatures can be mirrored at the center. The furnace was set to a target temperature of 1773 K.

3.2.4. Ceria Samples

Two types of ceria samples are used throughout the experiments conducted in this study: a bed of ceria particles and a set of two ceria RPCs. The particles were used before in other projects and are described in Ref. [36]. They have a diameter of 212 μm to 500 μm and a Brunauer-Emmett-Teller (BET) surface area of 109 $\text{m}^2 \text{kg}^{-1}$. The BET surface area was determined within the framework of the present study with a sample of 8.1166 g, using a Surfer gas adsorption porosimeter by Thermo Fischer Scientific. For the experiment, they are placed in an alumina crucible, which is positioned in the reaction tube of the furnace. As described in Section 4.2.1, the temperature is virtually constant within 40 mm in the center of the reaction tube during operation. Therefore, the particles are placed in the crucible such that they occupy a length of approximately 40 mm as shown in Figure 3.10(a). This way, the particles are exposed to the virtually same temperatures as the smaller RPC-sample.

RPCs were originally fabricated within the framework of a bachelor thesis [153] and later prepared for use in the present study. They were produced with the replication method [98]. The procedure is described in detail in Ref. [153] and is summarised in the following: A cylindrical PU foam with a length of approximately 12 mm and a diameter of approximately 20 mm and 30 pores per inch (ppi) is coated with an aqueous slurry of ceria powder (Sigma-Aldrich, < 5 μm , 99.9 % purity). The slurry consists of 77 wt.% ceria, 19 wt.% water, 2.5 wt.% Polyvinylpyrrolidone K30, which acts as a binder, 1 wt.% of the dispersant Dolapix CE 64 (Zschimmer & Schwarz) and 0.1 wt.% anti foaming agent Contraspum KWE (Zschimmer & Schwarz). After coating the PU foam, excess slurry was removed, closed pores were opened with compressed air and the sample was dried for 24 h at room temperature. Next, the PU foam and organic components of the slurry were burnt in a furnace. The furnace was heated with 10 K min^{-1} to 373 K and then further with 1 K min^{-1} until 1623 K were reached. At that point, the temperature was kept constant for 3 h in order to sinter the ceria RPC. [153]

Before their use in the experiments presented here, the ceria RPCs were sintered again in the test rig's tube furnace at 1823 K, i.e. 50 K above the highest temperature during the experiments, for 2 h. During that step, the RPCs typically shrink by approximately 5 % in both height and diameter. In preparation of the experiments, two ceria RPCs were placed in the hot zone of the reaction tube consecutively with contact to each other. To prevent the sample from sintering or otherwise reacting with the alumina reaction tube, the RPCs were wrapped in platinum foil. Images of the ceria samples inside the reaction tube taken with an endoscope are given in Appendix E. The BET surface after the initial sintering at 1623 K is 863 $\text{m}^2 \text{kg}^{-1}$. The BET surface

area was measured with the same instrument as the particles. Due to the structure of the RPCs, only a small sample of 0.716 g could be measured. The small sample translates to a small total surface area, which leads to less accurate measurements compared to larger samples. The resulting value is therefore only to be seen as an estimate.

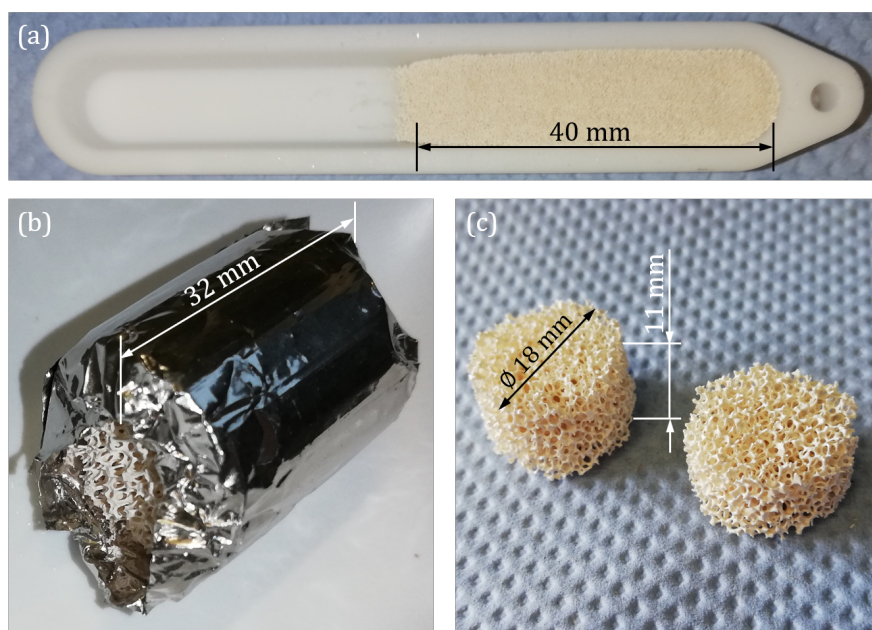


Figure 3.10.: Ceria samples prior to experiments. (a) Particles in crucible, (b) two RPCs in Pt-foil, (c) RPCs without Pt-foil.

To identify whether samples undergo significant microscopic changes or changes in the crystal structure, particle samples are analysed with scanning electron microscopy (SEM), energy-dispersive X-ray spectroscopy (EDX) and X-ray powder diffraction (XRD). In addition, SEM images of RPC-samples as synthesized are taken to compare the two sample types. SEM is used to study the topography of the samples' surface, while EDX gives an impression on the atomic composition. Both are performed with a Zeiss Ultra 55 scanning electron microscope. For EDX, an Ultim Max detector by Oxford Instruments is used. Potential changes in the crystal structure can be identified via XRD, which is performed with a D8 Advance A25 diffractometer by Bruker using a Lynxeye XE-T compound silicon strip detector and a Cu-anode. The investigated 2θ -range was 10° to 80° at a step size of 0.02° . Diffractograms are compared to reference data for CeO_2 from the *Powder Diffraction File* (PDF 75-0076). Particle samples before, after one and after eight experiments were tested.

3.2.5. Experimental Procedure

Experiments on the recombination kinetics are performed with a dedicated test rig, described in Section 3.2.1. The general concept is to first reduce a ceria sample at a high temperature under vacuum conditions. The sample is then brought into contact with a defined amount of oxygen. This is repeated at gradually decreasing temperatures. This way, a flow of reduced ceria from the

hot to the cold end of a solid-solid heat exchanger, while subjected to recombination is emulated. During an oxidation step the furnace is set to a constant temperature T_{set} .

The overall procedure is depicted in Figure 3.11. Prior to an experiment, the sample is oxidised as shown in Figure 3.12(a) to ensure the same starting conditions. To this end, the furnace is heated to 1273 K to avoid kinetic limitation of the oxidation. Then approximately $5 \cdot 10^4$ Pa are introduced and the temperature is held for 1 h, after which the test rig cools down to room temperature. The sample is kept in this oxidising atmosphere for > 14 h. Without this step, the material might remain partially reduced from the previous experiment. After that, again to ensure the same starting conditions, the test rig is flushed to remove air and humidity that might have entered the test rig through leakage as shown in Figure 3.12(b). This is done stepwise by consecutively evacuating and filling the test rig with O_2 to an absolute pressure of $5 \cdot 10^4$ Pa. The O_2 used for this step is the same as during the experiment and has a purity of 99.999%. In total three consecutive steps of evacuating and filling the test rig with O_2 are performed.

After these preparation steps, the sample is reduced. To this end, the test rig is first evacuated, then the furnace is heated to $T_{\text{set}} = 1773$ K at 15 K min^{-1} . 1773 K is within the range of commonly investigated reduction temperatures for ceria [13, 19, 20], as discussed in Section 2.2. During the heating phase, O_2 evolves from the sample and thus the pressure in the furnace rises. The O_2 is removed with the vacuum pump. This is done stepwise via the buffer volume. To do so, the buffer volume is evacuated with the pump, while the furnace is isolated from both buffer volume and pump, by closing the respective valves. Afterwards, the valve between pump and buffer volume is closed, as well. Now, the valve V1, which connects furnace and buffer volume is opened and O_2 is sucked into the buffer volume until the pressures of both compartments equalise. After closing V1, the buffer volume is again evacuated and the process is repeated. Four O_2 -removal steps are performed as shown in Figure 3.12(c). Stepwise removal of gas from the furnace via the buffer volume, allows to calculate the amount of removed O_2 . This is done with the measured pressure and temperature values in the buffer using the ideal gas law. If the furnace was instead constantly connected to the vacuum pump during the reduction phase, it would not be possible to determine the amount of O_2 , since mass flows cannot be measured. Also, calculating the amount of substance with values measured in the furnace is not an option, because the gas temperature there is difficult to obtain, as discussed in Section 3.2.6. Therefore the buffer volume is a crucial element for the experimental procedure and its evaluation.

To study the impact of an inert gas on the oxidation kinetics, experiments in which N_2 with a purity of 99.999% is added to the furnace and experiments without addition of N_2 are performed. For simplicity, experiments in which N_2 is used are referred to as inert gas experiments. In inert gas experiments, N_2 is added once to the furnace, after the reduction of the sample. Pressure curves and relevant pressure differences for this procedure are depicted in Figure 3.13(a). Similar to the aforementioned gas removal step, gas is fed to the furnace through the buffer volume. This is done by first evacuating the buffer volume and then filling it with N_2 until $p_{\text{BV}} \approx p_{\text{F}} + \Delta p_{\text{BV-F}}$ with $\Delta p_{\text{BV-F}} = 310$ Pa or $\Delta p_{\text{BV-F}} = 620$ Pa. After that, V1 is opened so that the pressures in both compartments again equalise. The amount of N_2 that has entered

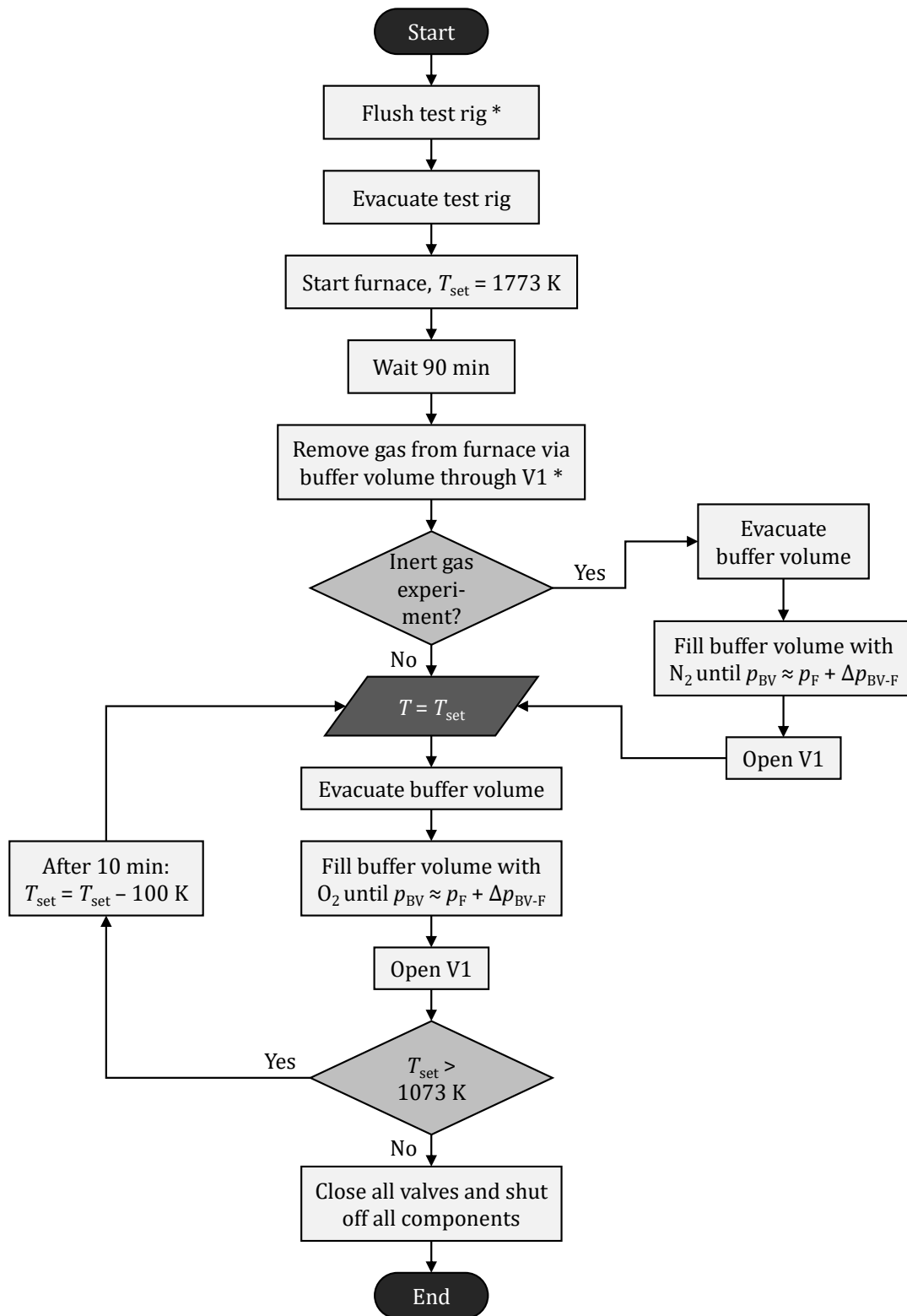


Figure 3.11.: Flow chart of the experimental procedure. The two actions labelled with an asterisk (*) are simplified in this flow chart. They are specified in Fig. 3.12.

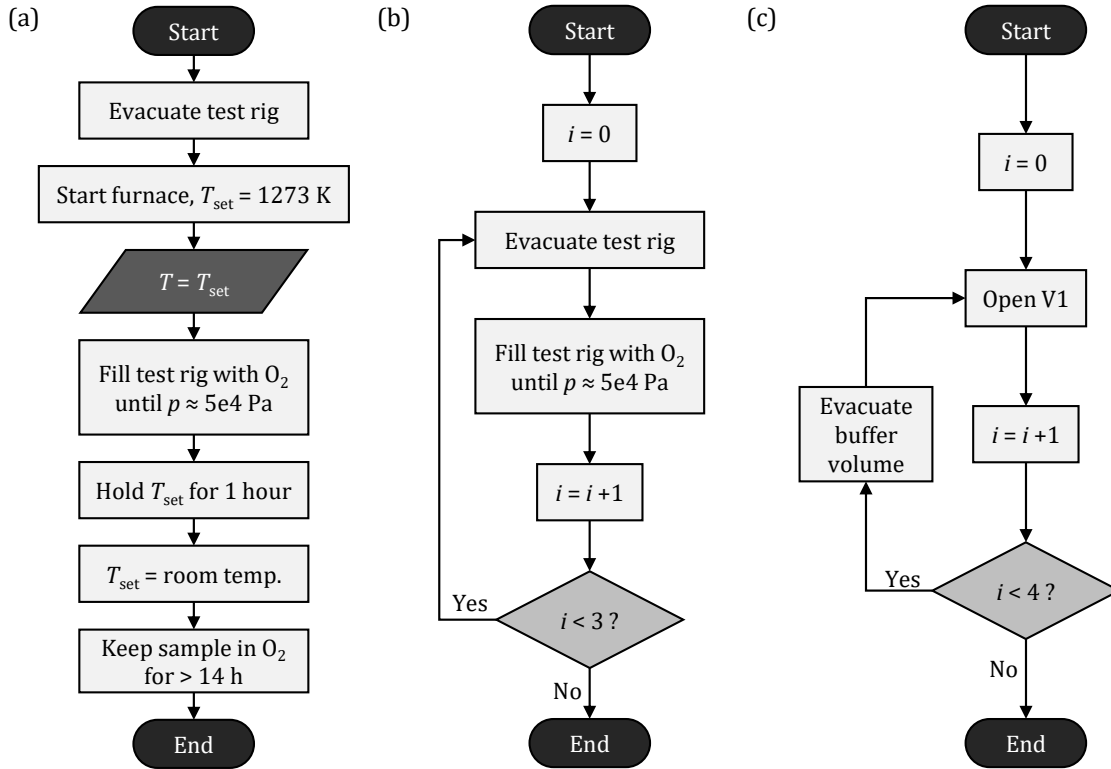


Figure 3.12.: Flow charts of re-oxidation procedure and sub-procedures in Fig. 3.11. (a): Re-oxidation of sample between two experiments (b): Flushing the test rig. (c): Removing gas from the furnace via the buffer volume through V1.

the furnace corresponds to a pressure increase $\Delta p_{N_2} \approx 270$ Pa or $\Delta p_{N_2} \approx 520$ Pa. In an ideal case, in which only the intentionally added N_2 enters the furnace, Δp_{N_2} would be equal to the N_2 partial pressure in the furnace p_{N_2} . However, in reality a small amount of nitrogen from air also enters the furnace due to leakage, so that $p_{N_2} = \Delta p_{N_2} + \Delta p_{N_2, \text{leak}}$. The leakage is addressed in Section 3.2.6. In experiments without inert gas, i.e. $\Delta p_{N_2} = 0$ the addition of N_2 is skipped. Both experiments continue as follows.

Once the furnace has reached its target temperature, O_2 is fed to the furnace in the same way as described for N_2 . In Figure 3.13(b), pressure curves and relevant pressure differences for this step are given. After evacuating the buffer volume, it is filled with O_2 until $p_{BV} \approx p_F + \Delta p_{BV-F}$ and V1 is opened. This time, Δp_{BV-F} is 50 Pa, 200 Pa or 300 Pa. The resulting pressure increase Δp_{O_2} in the furnace is approximately 44.5 Pa, 164 Pa and 245 Pa, respectively. More precise values of Δp_{O_2} are listed in Table 3.2. The oxygen partial pressure in the furnace is given by

$$p_{O_2} = p_F - \Delta p_{N_2} - \Delta p_{N_2, \text{leak}}, \quad (3.45)$$

where p_F is the total pressure in the furnace. Within the limits of accuracy, p_{O_2} is equal for ex-

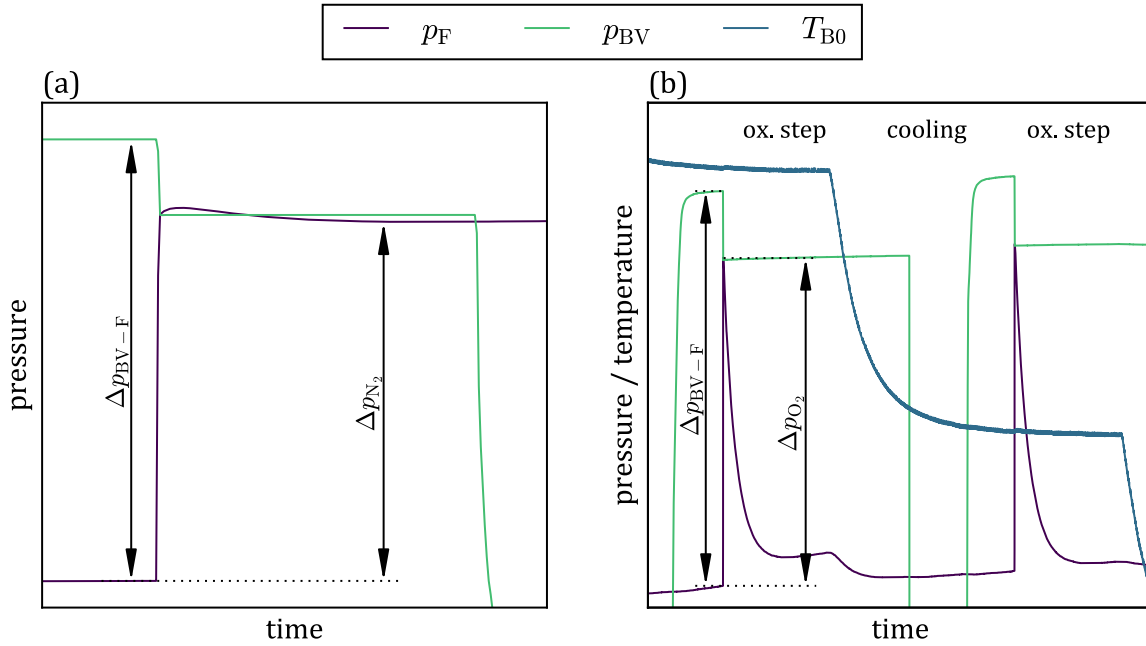


Figure 3.13.: Qualitative depiction of temperature and pressure curves, when (a) N_2 or (b) O_2 is fed to the furnace, including definitions of Δp_{BV-F} , Δp_{O_2} and Δp_{N_2} .

Table 3.2.: Experimental parameters. If more than one experiment was conducted with the same sample and same set of parameters, these experiments were summarized into one table entry (see no. of runs). The value of Δp_{O_2} is the average for all oxidation steps and the error accounts for the highest and lowest value in an experiment/a set of experiments.

Sample	Sample mass	Δp_{O_2}	Δp_{N_2}	No. of runs
Particle bed 1	5.0238 g	46.4 Pa $^{+13\%}_{-15\%}$	-	1
Particle bed 1	5.0238 g	162 Pa $\pm 6\%$	-	3
Particle bed 1	5.0238 g	245 Pa $\pm 2\%$	-	1
Particle bed 1	5.0238 g	167 Pa $^{+1\%}_{-2\%}$	524 Pa	1
Particle bed 2	5.0225 g	160 Pa $^{+5\%}_{-8\%}$	-	1
Particle bed 3	5.0222 g	42.6 Pa $^{+7\%}_{-4\%}$	-	1
Particle bed 3	5.0222 g	166 Pa $\pm 1\%$	270 Pa	1
RPCs	5.0221 g	164 Pa $^{+5\%}_{-10\%}$	-	2
RPCs	5.0221 g	168 Pa $\pm 2\%$	520 Pa	1

periments with and without inert gas. This is important in terms of comparability of different experiments, since p_{O_2} is the relevant measure of concentration with respect to the reaction kinetics as discussed in Section 2.3.2.

The manually operated valve V1 is closed immediately after opening. Afterwards, the system

is kept at constant T_{set} for 10 min, while the sample is oxidised, leading to a pressure decrease. The temperature is reduced by 100 K thereafter and a new oxidation step follows. The next introduction of O_2 into the furnace happens approximately 15 min after the new target temperature has been reached. In total, eight oxidation steps are performed. Two oxidation steps are shown exemplarily in 3.13(b) including the temperature T_{B0} .

3.2.6. Gas Phase Characterisation

For the evaluation of experimental results the gas phase behaviour, especially the temperature of the gas is crucial. To determine how much oxygen is taken up by the ceria sample, the amount of substance has to be calculated from the pressure curves logged during the experiments. To do so, the gas phase has to be described with an equation of state which links pressure, volume, temperature and amount of substance. Pressures are measured as described in Section 3.2.1 and the volume can be determined with the method described in Section 3.2.2. This section covers methods to characterise the gas phase with a focus on its temperature. The ideal gas law seems to be a plausible choice to describe the gas phase, due to the low pressures and high temperatures in the system. First, a method to investigate the validity of the ideal gas law for the present application is described. Second, heat transport in the gas phase and between gas phase and thermocouples is important to understand whether the gas temperature can be measured. The theory for this task is explained based on dimensionless quantities. Third, a method to determine an averaged gas temperature via pressure curves from reference measurements is introduced. Results obtained with these methods are discussed in Chapter 4.2.1.

In the assessment of experiments, the gas phase inside the experimental setup is treated as an ideal gas. This seems to be a fair assumption given that the gas phase consists of O_2 and N_2 at low pressures and temperatures above room temperature. However, to verify this, the ideal gas law is compared to the van der Waals equation. The ideal gas law is [154]

$$p V = n R T, \quad (3.46)$$

where p is the pressure, V the volume, n the amount of substance, R the universal gas constant and T the temperature of the gas phase. The van der Waals equation reads [118]

$$p = \frac{R T}{v - b} - \frac{a}{v^2} \quad (3.47)$$

with the molar volume $v = V \cdot n^{-1}$. This can be rearranged to the cubic equation

$$0 = v^3 - \left(b + \frac{R T}{p} \right) \cdot v^2 + \frac{a}{p} \cdot v - \frac{a b}{p}, \quad (3.48)$$

which is solved numerically for v in *Python 3* [148, 149] using *SciPy's* [155] solver *fsolve*. As an initial value for the solver, v is calculated with the ideal gas law. The molar Volume is then calculated with both the van der Waals equation and the ideal gas law for the relevant temperature

and pressure range of 295 to 1773 K and 10 to 1000 Pa. The relative difference $|v_{vdW} - v_{IG}| \cdot v_{vdW}^{-1}$ is used to verify the assumption that the gas phase can be described as ideal. Values for the universal gas constant and coefficients for the van der Waals equation are listed in table 3.3.

Table 3.3.: Parameters and constants for gas phase calculations.

Quantity	Meaning	Value	Unit	Ref.
R	Universal gas constant	8.314 462 618 153 24	$\text{J mol}^{-1} \text{K}^{-1}$	[154]
k_B	Boltzmann constant	$1.380 649 \cdot 10^{-23}$	J K^{-1}	[154]
$a (\text{O}_2)$	Van der Waals coefficient	0.138 207 3	$\text{Pa m}^6 \text{mol}^{-2}$	[118]
$a (\text{N}_2)$	Van der Waals coefficient	0.136 991 4	$\text{Pa m}^6 \text{mol}^{-2}$	[118]
$b (\text{O}_2)$	Van der Waals coefficient	$3.19 \cdot 10^{-5}$	$\text{m}^3 \text{mol}^{-1}$	[118]
$b (\text{N}_2)$	Van der Waals coefficient	$3.87 \cdot 10^{-5}$	$\text{m}^3 \text{mol}^{-1}$	[118]
$r_{\text{gas}} (\text{O}_2 \ \& \ \text{N}_2)$	Radius of gas molecules	ca. $1.5 \cdot 10^{-10}$	m	[154]
M_{O_2}	Molar mass of O_2	$31.9988 \cdot 10^{-3}$	kg mol^{-1}	[144, 145]

To describe the gas phase with an equation of state, it is crucial to know the gas temperature. The methods described in the following are used to determine whether the gas temperature can be measured reliably in the presented setup. To this end, the heat transport in the gas phase and between gas and thermocouples is characterised. Since the test rig is operated at a partial vacuum, the gas phase has a low density, which might result in a low thermal conductivity of the gas and low convective heat transfer between gas and hot elements, such as the reaction tube and the thermocouples. An important quantity with respect to the thermal conductivity is the Knudsen number Kn , which relates the mean free path of gas molecules to a characteristic length [132], which in case of the present study is the inner tube diameter. The mean free path is given by [154]

$$l_{\text{mfp}} = \frac{1}{4 \pi \sqrt{2} r_{\text{gas}}^2 \left(\frac{N}{V} \right)}, \quad (3.49)$$

where $N \cdot V^{-1}$ is the number density with the total number of molecules N distributed in the volume V and r_{gas} is the radius of gas molecules, given in table 3.3. To calculate the number density, the ideal gas law (Equation 3.46) is used with N instead of n and the Boltzmann constant k_B instead of R . The Knudsen number is defined as [132]

$$Kn = \frac{l_{\text{mfp}}}{d}, \quad (3.50)$$

where d is the inner tube diameter.

To see if the temperature measured by thermocouples is representative for the temperature of the gas phase, radiative and convective heat input into the thermocouples are estimated. For the calculation of the convective heat transfer between gas and thermocouple, a thermocouple is treated as a horizontal cylinder that is subject to free convection. Herein, the dimensionless

Rayleigh number Ra , Prandtl number Pr and Nusselt number Nu are used as described in Chapter 2.5.1. The characteristic length is the diameter of the thermocouple d_{TC} . The relevant temperature difference and the reference temperature at which the properties of the fluid are evaluated are $\Delta T = T_{TC} - T_{gas}$ and $T_{ref} = \frac{1}{2} \cdot (T_{TC} + T_{gas})$, respectively. The isobaric volume expansion coefficient β is calculated with the approximation for ideal gases, given in Equation 2.39 and the thermal diffusivity a is obtained from its definition, given in Equation 2.40. The remaining fluid properties ν , ρ , λ and c_p are calculated with data from Ref. [145]. To this end, data at 100 Pa and temperatures ranging from 273 K to 1773 K was extracted from Ref. [145] and then fitted with second order polynomials of the form $C_2 \cdot T^2 + C_1 \cdot T + C_0$. The parameters C_i are given in table 3.4. The kinematic viscosity ν is calculated via the dynamic viscosity μ with $\nu = \mu \cdot \rho^{-1}$. With those polynomials, the Nusselt number can be calculated with the empiric correlation from

Table 3.4.: Parameters for polynomial fit $C_2 \cdot T^2 + C_1 \cdot T + C_0$ to data from Ref. [145] for μ , ρ , λ and c_p .

Quantity	C_2	C_1	C_0
ρ in kg m^{-3}	$6.814\ 101\ 89 \cdot 10^{-10}$	$-1.972\ 083\ 22 \cdot 10^{-6}$	$1.657\ 943\ 20 \cdot 10^{-3}$
μ in Pa s	$-7.995\ 072\ 71 \cdot 10^{-12}$	$5.001\ 009\ 88 \cdot 10^{-8}$	$7.140\ 333\ 96 \cdot 10^{-6}$
c_p in $\text{J mol}^{-1} \text{K}^{-1}$	$-3.417\ 309\ 73 \cdot 10^{-6}$	$1.229\ 607\ 31 \cdot 10^{-2}$	$2.592\ 394\ 50 \cdot 10^1$
λ in $\text{W m}^{-1} \text{K}^{-1}$	$-8.147\ 051\ 76 \cdot 10^{-9}$	$7.396\ 761\ 50 \cdot 10^{-5}$	$5.757\ 608\ 72 \cdot 10^{-3}$

Chapter 2.5.1. Finally, the heat transfer coefficient α can be calculated with the definition of the Nusselt number given in Equation 2.35. The convective heat flow per unit length then directly follows as

$$\dot{Q}_{conv} = \alpha \pi d_{TC} \Delta T, \quad (3.51)$$

while the net radiative heat flow per unit length between thermocouple and reaction tube (RT) is

$$\dot{Q}_{rad} = \pi d_{TC} \sigma (T_{RT}^4 - T_{TC}^4). \quad (3.52)$$

Both thermocouple and reaction tube are assumed to be black bodies. In the assessment of this model, all temperatures are varied. The reaction tube temperature T_{RT} takes values from 573 to 1773 K, the latter being the maximum set temperature in the experiments. The gas temperature T_{gas} is varied from room temperature to the respective value of T_{RT} . The temperature of the thermocouple T_{TC} is assumed to be between T_{RT} and T_{gas} and is estimated as

$$T_{TC} = f T_{RT} + (1 - f) T_{gas}, \quad (3.53)$$

where f is a factor between 0 and 1. Note that empirical correlations like Equations 2.41 and 2.42 are most reliable for $\Delta T \ll T_{ref}$ [132].

Using the methods described up to this point, it was found that the gas temperature cannot be measured reliably, as will be discussed in Section 4.2.1. Instead, an approach to derive a correlation between an average gas temperature and temperature measurements is made. Herein, gas

temperature and leakage from the ambience into the test rig are linked and therefore both are described in the following. First, an average gas temperature \bar{T} is defined, for which

$$n = \frac{pV}{R\bar{T}} \quad (3.54)$$

holds. Formally, \bar{T} can be derived as follows: The incremental amount of substance in a volume-increment is

$$dn = \frac{p}{R} \cdot \frac{1}{T(x, y, z)} dx dy dz, \quad (3.55)$$

where $T(x, y, z)$ is the gas temperature at any given point (x, y, z) in the Volume V . Integration of Equation 3.55, using Equation 3.54 then yields

$$\bar{T} = \frac{V}{\int_V \frac{1}{T(x, y, z)} dx dy dz}, \quad (3.56)$$

which proves that an average gas temperature \bar{T} that fulfils Equation 3.54 exists. Since only temperatures and pressures are measured in the setup and the gas temperature $T(x, y, z)$ cannot be measured directly, an approach to calculate \bar{T} via the pressure is needed. According to the ideal gas law, for a constant volume, the pressure is a function of temperature and amount of substance. Therefore, the total differential of the pressure can be written as

$$dp = \left(\frac{\partial p}{\partial \bar{T}} \right)_n d\bar{T} + \left(\frac{\partial p}{\partial n} \right)_{\bar{T}} dn. \quad (3.57)$$

With that, the derivative of the pressure with respect to time follows as

$$\frac{dp}{dt} = \left(\frac{\partial p}{\partial \bar{T}} \right)_n \frac{d\bar{T}}{dt} + \underbrace{\left(\frac{\partial p}{\partial n} \right)_{\bar{T}} \frac{dn}{dt}}_{\dot{p}_L}. \quad (3.58)$$

From this equation, it becomes clear that to determine the pressure change due to a temperature change and the pressure change due to a change in the amount of substance separately from each other, the respective other quantity has to be constant ($\frac{dT}{dt} = 0$ or $\frac{dn}{dt} = 0$). In the following, \bar{T} , refers to the average gas temperature of the furnace volume and Equation 3.58 is applied for the same volume.

Reference measurements are conducted, in which the furnace is heated to a certain set temperature T_{set} without a ceria sample. This temperature is then held for 9 hours. Afterwards, the test rig cools down to room temperature. Without a sample, the only change of the amount of substance in the gas phase is due to leakage into the test rig. Leakage is likely to be caused mainly by imperfectly gas tight parts of the test rig through which gas from the environment can enter. Leakage from the buffer volume to the furnace is also possible, even though the relevant pressure difference here is significantly lower than the pressure difference to the environment.

Gas can also enter the test volume from micro-cavities in the materials used. Another leakage mechanism could be diffusion of oxygen through the alumina reaction tube. For convenience the pressure rate due to leakage is named \dot{p}_L as shown in Equation 3.58. After a certain dwelling time at T_{set} , gas phase and furnace reach steady temperatures. At this point, \bar{T} is constant and the pressure change rate equals \dot{p}_L . The main driving force behind the leakage is the pressure difference between test rig and ambience $p_{\text{amb}} - p_{\text{TR}}$. Since at all times $p_{\text{amb}} \gg p_{\text{TR}}$, this pressure difference is virtually constant. Consequently, at steady temperatures the pressure is expected to increase linearly with respect to time, due to leakage. In other words, \dot{p}_L is constant and can be calculated by linear regression. This is done in *Python* 3 [148, 149] with the function *polyfit* from *NumPy* [156]. The linear regression is performed with data measured in the last 3 hours of the temperature dwelling phase, as here the pressure change rate is in good approximation constant in all reference measurements. This way, the leakage can be determined for a certain temperature level. As measure for this temperature level, the temperature measured with thermocouple TC K1 is used, i.e. $\dot{p}_L = f(T_{\text{K1}})$. A total of 11 reference measurements are conducted with T_{set} ranging from room temperature to 1773 K. Hence, 11 data points for \dot{p}_L for different temperatures T_{K1} , plus 9 more data points at room temperature (these are extracted from the cooling phase of most reference measurements) are available. These data points are used for a linear fit of \dot{p}_L to T_{K1} , which is again done using *polyfit* from *NumPy* [156]. The results are shown and discussed in Section 4.2.1. For ideal gases, the expression $\left(\frac{\partial p}{\partial n}\right)_{\bar{T}}$ in Equation 3.58 scales linearly with the gas temperature (see also Equation 3.62). Therefore, using a linear correlation between \dot{p}_L and gas temperature is correct, if the molar leakage flow $\left(\frac{dn}{dt}\right)$ in Equation 3.58 is constant. In reality, the molar flow might also depend to some degree on the temperature of the system. This would for instance be the case if diffusion is a relevant transport mechanism for the leakage or if different coefficients of thermal expansion of the materials used affect the gas tightness of the test rig.

After calculating $\dot{p}_L(T_{\text{K1}})$, the gas phase temperature \bar{T} can be determined. To find \bar{T} as function of T_{K1} , the pressure increase due to temperature change is calculated. Knowing \dot{p}_L , this can be done with the pressure curves from the reference measurements, according to Equation 3.58. During the reference measurements, heating of the furnace starts at the time t_0 . At any time $t_1 > t_0$, the pressure is given by

$$p_{\text{F},1} = n_{\text{F},1} \cdot \frac{R \bar{T}_1}{V_{\text{F}}} \quad (3.59)$$

with the amount of substance in the gas phase

$$n_{\text{F},1} = n_{\text{F},0} + \Delta n_{01}. \quad (3.60)$$

At t_0 , the amount of substance is

$$n_{\text{F},0} = \frac{p_{\text{F},0} V_{\text{F}}}{R \bar{T}_0}, \quad (3.61)$$

where \bar{T}_0 equals the room temperature. The derivative of pressure with respect to the amount of

substance at a constant gas temperature in Equation 3.58 is given by the ideal gas law, according to

$$\left(\frac{\partial p_F}{\partial n}\right)_{\bar{T}} = \frac{R\bar{T}}{V_F}. \quad (3.62)$$

with the definition of \dot{p}_L given in Equation 3.58, Δn_{01} can be derived by integration over time:

$$\Delta n_{01} = \frac{V_F}{R} \cdot \int_{t_0}^{t_1} \frac{\dot{p}_L}{\bar{T}(t)} dt. \quad (3.63)$$

Substitution of Equations 3.63 and 3.61 into Equation 3.60 and substitution of the resulting equation into Equation 3.59 yields

$$p_{F,1} = p_{F,0} \cdot \frac{\bar{T}_1}{\bar{T}_0} + \int_{t_0}^{t_1} \frac{\bar{T}_1}{\bar{T}(t)} \dot{p}_L dt. \quad (3.64)$$

Generally, at a given time t_1 , the gas temperature \bar{T}_1 can be calculated from the measured pressure $p_{F,1}$. Equation 3.64 however shows that to do so, a function $\bar{T}(t)$ or $\bar{T}(T_{K1})$ (as $T_{K1}(t)$ is known these two can be converted into each other) is needed. In other words, the gas temperature \bar{T} is a function of itself. Therefore, an iterative approach is used to solve Equation 3.64 and hence to get \bar{T} as a function of T_{K1} . To this end, the gas temperature is approximated by

$$\bar{T} = C (T_{K1} - T_{amb}) + T_{amb}, \quad (3.65)$$

which is a linear function that fulfils the condition that \bar{T} and T_{K1} are equal at ambient temperature. As a starting point for the iteration, $C = 1$, i.e. $\bar{T} = T_{K1}$ is chosen. Next, the integral in Equation 3.64 is solved numerically with the composite trapezoidal rule using *NumPy's* [156] *trapz* function for this value of \bar{T} . Afterwards, a new value for \bar{T} is calculated with Equation 3.64. These two steps are performed for each of the 11 reference measurements. The point t_1 at which the equation is evaluated is the end of the temperature dwelling, i.e. after 9 h at T_{set} . With these new values of \bar{T} , Equation 3.65 is fitted using the *curve_fit* function in *SciPy* [155] to obtain a new Value for C . With this again the integral in Equation 3.64 is solved and the process described above is repeated until $(C_k - C_{k-1}) \cdot C_{k-1}^{-1} < 10^{-5}$, where k is the number of iterations. The coefficient of determination for the fit of Equation 3.65 is given by [157]

$$R^2 = 1 - \frac{\sum_{i=1}^{11} (\bar{T}_i - \hat{\bar{T}}_i)^2}{\sum_{i=1}^{11} (\bar{T}_i - \bar{\bar{T}})^2}, \quad (3.66)$$

where \bar{T}_i is the gas temperature calculated with data from measurement i , according to equation 3.64, $\bar{\bar{T}}$ is the mean value of all \bar{T}_i and $\hat{\bar{T}}_i$ is the gas temperature as estimated by the linear Equation 3.65.

The final \bar{T} and the leakage \dot{p}_L are calculated for points at which steady temperatures in the setup are established. As explained above, this is necessary to separate the pressure change due to temperature change from the pressure change due to leakage, which in turn is necessary to enable the method described above. During transient phases, i.e. heating and cooling phases, the calculated \bar{T} is therefore only sufficiently accurate, if the gas phase has a small thermal inertia. This can be tested by applying the calculated \bar{T} to Equation 3.64 for a different time t_1 , during a heating or cooling phase. This is done by subtracting the integral expression in Equation 3.64 from the equation and thereby calculating a theoretical pressure curve without leakage which is then checked for plausibility as discussed in Chapter 4.2.1.

As an additional plausibility check, a maximum gas temperature in the furnace can be derived by discretisation of Equation 3.56:

$$\bar{T}_{\max} = \frac{V_F}{\frac{\Delta V_{RT,0}}{T_{B0}} + \sum_{i=1}^3 \frac{\Delta V_{RT,i}}{T_{Ki}} + \frac{\Delta V_{\text{tubing}}}{T_{\text{tubing}}}}, \quad (3.67)$$

where $\Delta V_{RT,i}$ are sections of the reaction tube volume. Due to the limited amount of available temperature measuring points, the system is only discretised in axial direction, i.e. constant temperatures in radial and circumferential direction are assumed. In case of $i = 0$, the section is defined from the center of the tube to the location of the thermocouple TC K1 and a mirrored section in the other half of the reaction tube, as depicted in Figure 3.14. For $i = 1$ and $i = 2$ it is defined as the section ranging from the position of TC K_i to TC $K(i + 1)$ and a mirrored section in the other half of the reaction tube or adjacent tubing. For $i = 3$ the volume is defined from the position of TC K3 to TC K6 and a respective mirrored section. In these partial volumes, the temperature is approximated with the temperature measured by TC B0 and TC K1 to TC K3. The remaining furnace volume, i.e. the rest of the adjacent tubing is

$$\Delta V_{\text{tubing}} = V_F - \sum_{i=0}^3 \Delta V_{RT,i}. \quad (3.68)$$

Here, the temperature is approximated with T_{tubing} , the average temperature measured by TC K4 - TC K6, which is typically close to room temperature. A qualitative depiction of \bar{T}_{\max} and a temperature profile are given in Figure 3.15. The statement $\bar{T} \leq \bar{T}_{\max}$ can be made, if two conditions are met: first, the discrete temperature profile has to overestimate the actual temperature profile one would get if continuous measurement of the temperature with respect to space was possible. Due to the mentioned definitions of temperatures and partial volumes, this condition is always fulfilled as indicated by the discrete profile and the dashed line in Figure 3.15. The second condition is that the gas temperature is below the measured temperatures, since gas and thermocouples do not necessarily have the same temperature. This might not be the case when the system is cooled after being at or close to a steady temperature profile. In that case, due to the thermal inertia of the gas phase, the gas temperature might be temporarily higher than

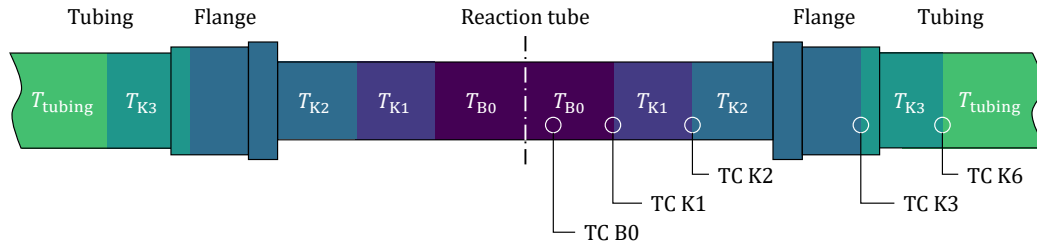


Figure 3.14.: Schematic of the partial volumes and respective temperatures for the definition of \bar{T}_{max} . Each color refers to one partial volume and the corresponding temperature in Equation 3.67.

the measured temperature and theoretically even higher than \bar{T}_{max} , as indicated in Figure 3.15. However, after reaching a steady temperature profile, the temperature of the thermocouples is most likely higher than that of the gas phase due to radiation, which is especially strong close to the center of the reaction tube, because of the high temperatures in this region. Thus, at a steady temperature profile or during any kind of heating phase, e.g. after cold gas is fed to the hot furnace, the gas temperature \bar{T} can most probably not exceed \bar{T}_{max} . This is the case during each oxidation step, so that \bar{T}_{max} can be used for plausibility checks.

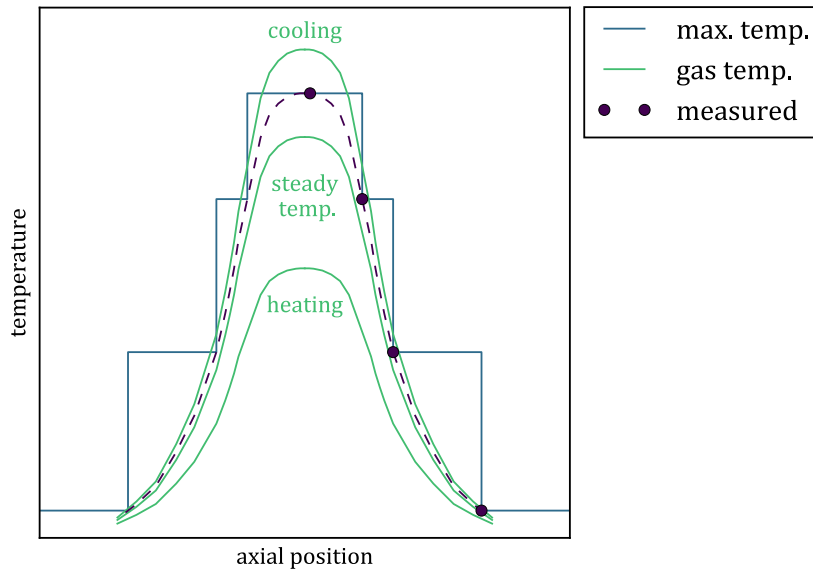


Figure 3.15.: Qualitative depiction of the maximum temperature, temperatures measured by thermocouples and gas temperature during cooling, heating and at a steady temperature profile. The dashed line, represents the unknown temperature profile in-between the measurement points.

3.2.7. Determining Oxygen Non-Stoichiometry and Oxidation Rates

The experimental procedure explained in Section 3.2.5 yields pressure and temperature data. The kinetic of an oxidation step is characterised by the falling pressures after introduction of

O₂. Thus, pressure curves for the furnace $p_F(t)$ give valuable insight into the oxidation kinetics. Comparison of these curves for different Δp_{O_2} and Δp_{N_2} and different ceria samples allows qualitative evaluation of the impact that these three quantities have on the kinetics. As shown in Table 3.2, 12 experiments are conducted and each experiment has eight oxidation steps. Hence, the pressure curves of 96 oxidation steps in total have to be compared among each other. To this end, it is convenient to introduce a measure that can characterise the pressure drop of an oxidation step in a single quantity. This is done as follows: Figure 3.16 shows $p_F(t)$ for a single oxidation step. The pressure jumps from its original value $p_{F,0}$, to a peak value $p_{F,1}$ as O₂ is introduced. After that, $p_F(t)$ falls. The amount of O₂ that at a given point in time t is not or not yet absorbed by the material is described by the pressure difference

$$\Delta p_F = p_F(t) - p_{F,0}. \quad (3.69)$$

This value correlates to a time difference $\Delta t = t - t_0$ as shown in Figure 3.16. This time difference is determined for fixed values of Δp_F of 25 Pa, 50 Pa and 100 Pa and denoted as Δt_{25} , Δt_{50} and Δt_{100} , accordingly. Hence, Δt_i describes the time that is needed for the material to take up a certain amount of O₂ that correlates to a predefined Δp_F . As explained earlier, the measured pressure curve consists of discrete values measured every 400 ms. The exact $p_F(t)$ that matches this values of Δp_F might thus not exist among the measured values. Therefore, Δt is determined by linear interpolation, between the last pressure value that is greater than $p_F(t)$ and the first pressure value that is less than $p_F(t)$. An advantage of this approach is that ambiguity in the definition of Δt is avoided. Due to noise in the pressure signal, there might be more than one point at which Δp_F is reached. In these cases the pressure fluctuates over a short period of time around the value of interest. The interpolation then yields a Δt within this period of time. Another source of ambiguity can be caused by leakage, which might increase p_F after the oxidation is virtually completed. Points after the minimum of p_F , which indicates completion of the oxidation step are therefore not taken into account.

To calculate the change of oxygen non-stoichiometry $\Delta\delta$ and a δ -rate $\frac{d\delta}{dt}$, the amount of O₂ that was taken up by the sample has to be determined. If pressure and gas temperature data is available, this can be done with an equation of state. The comparison of van der Waals equation and ideal gas law discussed in Section 4.2.1 implies that the gas phase can be well described by the ideal gas law. This way δ can theoretically be calculated with a mole balance in combination to the ideal gas law, which yields

$$\delta(t) = \delta_{\text{ref}} + \frac{2}{n_{\text{ceria}}} \cdot \left(\frac{V_F}{R} \left(\frac{p_F(t)}{\bar{T}(t)} - \frac{p_{F,\text{ref}}}{\bar{T}_{\text{ref}}} \right) + \frac{V_{\text{BV}}}{R} \left(\frac{p_{\text{BV}}(t)}{\bar{T}_{\text{BV}}(t)} - \frac{p_{\text{BV},0}}{\bar{T}_{\text{BV},0}} \right) - \int_{t_{\text{ref}}}^t \dot{n}_L dt \right). \quad (3.70)$$

Herein, the reference state can be any point in time during the experiment, as long as δ_{ref} is

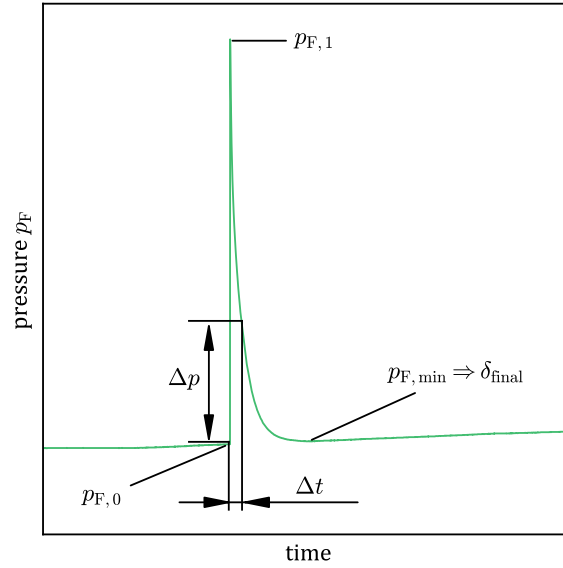


Figure 3.16.: Depiction of Δt and distinctive pressures, for an exemplary oxidation step.

known. With that, $\delta(t)$ and $\Delta\delta = \delta(t) - \delta_0$ directly follow, while a δ -rate can be obtained by des-critisation as $\Delta\delta \cdot \Delta t^{-1}$. As shown later in Section 4.2.1 however, the mean gas temperature $\bar{T}(t)$ and the leakage rate \dot{n}_L cannot be determined reliably with the presented setup. The evaluation of the experiments is adapted to this circumstance as described in the following. As the main portion of O_2 uptake during an oxidation step takes place in a relatively short amount of time, it is decided to neglect the leakage during an oxidation step. When analysing the pressure drop after introduction of O_2 , i.e. when V1 is closed, pressure and temperature of the buffer volume remain constant and Equation 3.70 can be simplified to

$$\Delta\delta(t) = \frac{2 V_F}{n_{\text{ceria}} R} \cdot \left(\frac{p_F(t)}{\bar{T}(t)} - \frac{p_{F,1}}{\bar{T}_1} \right), \quad (3.71)$$

where state 1 was chosen as reference point. As exact determination of \bar{T} is not possible, an exact value of $\Delta\delta(t)$ cannot be calculated either. Instead, a range of possible values of $\Delta\delta(t)$ is calculated within the limits of \bar{T} . An upper limit for \bar{T} is given by \bar{T}_{max} as defined in Equation 3.67. As a lower limit, the temperature of the buffer volume $T_{\text{BV},0}$ is used as cold gas is fed to the furnace at that temperature. With these limits and Equation 3.71, a range of possible $\Delta\delta$ values can be calculated. During oxidation, δ decreases, therefore the difference $\Delta\delta = \delta(t) - \delta_1$ is negative. An upper limit or a maximum value of $\Delta\delta$ as discussed in the following therefore correlates to the minimum of the absolute value $|\Delta\delta|$ and hence the minimum of O_2 uptake. To define an upper limit of $\Delta\delta$, $\bar{T}(t)$ in Equation 3.71 has to be small, while \bar{T}_1 has to be high. The gas temperature has to increase after the introduction of cold gas into the hot furnace at t_1 , i.e. $\bar{T}(t) \geq \bar{T}_1$ must hold. The highest value of $\Delta\delta$, according to Equation 3.71 that fulfils this condition, at least within the limits of minor fluctuations, is reached for $\bar{T}_1 = \bar{T}_{\text{max}}(t_1)$ and $\bar{T}(t) = \bar{T}_{\text{max}}(t)$. For a lower limit, $\bar{T}(t)$ has to be high and \bar{T}_1 has to be low. The lowest value of $\Delta\delta$, according to Equation 3.71

follows if $\bar{T}(t)$ is the highest and \bar{T}_1 is the lowest. This is the case, if at t_1 the gas temperature is given by $\bar{T}_1 = T_{BV,0}$ and then with the next time step jumps to the highest possible temperature, i.e. $\bar{T}(t) = \bar{T}_{\max}(t)$.

In addition to the temperature limits, there is another limitation given by the fact, that the sample cannot take up more oxygen than the amount of O_2 that entered the furnace. This amount is described by

$$\Delta n_{O_2, \text{in}} = \frac{V_{BV}}{R} \cdot \left(\frac{p_{BV,0}}{T_{BV,0}} - \frac{p_{BV,1}}{T_{BV,1}} \right). \quad (3.72)$$

An equivalent quantity $\Delta\delta_{\text{in}}$ is defined for the hypothetical case that all O_2 was taken up by the sample, according to

$$\Delta\delta_{\text{in}} = -\frac{2 \Delta n_{O_2, \text{in}}}{n_{\text{ceria}}}. \quad (3.73)$$

Due to the establishment of a new equilibrium after introduction of O_2 , this value can actually not be reached, but it can be used for the definition of limits. The final upper and lower limits for $\Delta\delta$ are both given by $\max \{ \Delta\delta_{\text{in}}, \Delta\delta(\bar{T}) \}$, where $\Delta\delta(\bar{T})$ is calculated with Equation 3.71, using the limits of \bar{T} as explained above. In addition to this $\Delta\delta$ -range, an estimate value for $\Delta\delta$ can be given if an estimation for \bar{T} is found. A large portion of the furnace volume is outside the heated zone and has a temperature close to room temperature and hence close to the temperature in the buffer volume. Introduction of cold gas from the buffer volume into the furnace and the following heating of the gas phase, might result in strong fluctuations of the local gas temperature in the center of the reaction tube. Given the much lower gas temperature at other points in the furnace volume, the fluctuations might be significantly mitigated with respect to the mean gas temperature \bar{T} . Therefore, the assumption of a constant \bar{T} is used to estimate $\Delta\delta$. In this case, Equation 3.71 is further simplified to

$$\Delta\delta(t) = \frac{2 V_F}{n_{\text{ceria}} R \bar{T}} \cdot (p_F(t) - p_{F,1}). \quad (3.74)$$

The amount of oxygen entering the furnace $\Delta n_{O_2, \text{in}}$ increases the pressure in the furnace between states 0 and 1, according to

$$\Delta n_{O_2, \text{in}} = \frac{V_F}{R \bar{T}} \cdot (p_{F,1} - p_{F,0}). \quad (3.75)$$

Dividing Equation 3.74 by Equation 3.75 yields

$$\Delta\delta(t) = \frac{2 \Delta n_{O_2, \text{in}}}{n_{\text{ceria}}} \cdot \frac{p_F(t) - p_{F,1}}{p_{F,1} - p_{F,0}} \quad (3.76)$$

or with Equation 3.73

$$\Delta\delta(t) = \Delta\delta_{\text{in}} \cdot \frac{p_F(t) - p_{F,1}}{p_{F,0} - p_{F,1}}. \quad (3.77)$$

The according gas temperature \bar{T} can be calculated as

$$\bar{T} = \frac{V_F (p_{F,1} - p_{F,0})}{R \Delta n_{O_2, \text{in}}}, \quad (3.78)$$

following from Equation 3.75. This value for \bar{T} is again based on the assumption that it is constant over the course of an oxidation step. It can be used to discuss the plausibility of $\Delta\delta$ -values calculated under the same assumption.

The aforementioned estimation of $\Delta\delta$ can also be used to determine $\delta(t)$ and the δ -rate. The δ -rate is calculated by discretisation according to

$$\frac{d\delta}{dt} \approx \frac{\delta_{k+1} - \delta_k}{t_{k+1} - t_k} = \frac{\Delta\delta_{k+1} - \Delta\delta_k}{t_{k+1} - t_k}, \quad (3.79)$$

where k and $k + 1$ refer to two successive measuring points. The δ -rate is determined for each oxidation step, starting at state 1 and ending just before the furnace is set to the next temperature level. To calculate the absolute δ -value, first the initial reduction extent δ_{red} has to be computed. It is given by the material balance

$$n(t) = n_{\text{start}} + \int_{t_{\text{start}}}^t \dot{n}_L dt - \Delta n_{\text{pump}} + \Delta\delta_{\text{red}} \frac{n_{\text{ceria}}}{2}, \quad (3.80)$$

where n_{start} is the amount of gas in the furnace, before the furnace is heated and Δn_{pump} is the amount of gas that is removed by the vacuum pump. As the sample undergoes a re-oxidising procedure prior to an experiment and the thermodynamics of ceria dictate, that at room temperature and the relevant pressures, the material is virtually fully oxidised ($\delta \approx 0$) it is assumed that $\Delta\delta_{\text{red}} \approx \delta_{\text{red}}$. Therefore, δ_{red} follows directly from Equation 3.80. Gas is removed by the vacuum pump in four steps via the buffer volume, as described in Section 3.2.5. For each O_2 -removal step, the gas is first moved to the buffer volume, where pressure and temperature are measured, before the material is eventually removed with the pump. The related amount of gas for each step can be calculated in analogy to Equation 3.72. n_{start} and $n(t)$ are calculated with the ideal gas law. While for n_{start} , the gas is at room temperature, for $n(t)$ the same assumption of a constant \bar{T} as before is made and \bar{T} is calculated analogous to Equation 3.78. For the leakage it is shown later in Section 4.2.1 that \dot{n}_L cannot be described reliably as a function of temperature. Instead, the leakage is estimated with the value obtained for room temperature, so that

$$\int_{t_{\text{start}}}^t \dot{n}_L dt \approx \dot{n}_L (\bar{T} = 295 \text{ K}) (t - t_{\text{start}}). \quad (3.81)$$

With the non-stoichiometry after the initial reduction δ_{red} , $\delta(t)$ follows as

$$\delta(t) = \delta_{\text{red}} + \Delta\delta(t). \quad (3.82)$$

As described above, $\Delta\delta(t)$ is calculated for each oxidation step. Since the ceria sample might also be oxidised during the cooling phases between two oxidation steps, $\Delta\delta(t)$ has to be computed for these phases as well in order to calculate $\delta(t)$. Even though T_{set} is reduced by 100 K, as explained above, the fluctuation of \bar{T} is probably significantly lower due to a large portion of the furnace volume being outside of the heated zone. Therefore, the same assumption of a constant \bar{T} is used to estimate $\Delta\delta(t)$ during the cool down. This way, $\Delta\delta$ is calculated for each oxidation step and each cooling phase. In each of these steps, δ starts with the final δ -value of the previous step. As mentioned earlier, the pressure drop due to O_2 uptake by the sample might be followed by a slight pressure increase due to leakage. This yields the incorrect result of an increasing δ . Therefore as final δ -value of the previous step, the minimum value of δ in that previous step is used rather than the δ -value calculated for the final point in time as shown in Figure 3.16.

Under the assumption that the oxidation dominates the reaction kinetics, rather than its back reaction, the reduction, the kinetics can be described by

$$\ln\left(-\frac{d\delta}{dt}\right) - \ln(\delta p_{\text{O}_2}^{0.218}) = -\frac{e_{\text{a,ox}}}{R T_{\text{B0}}} + \ln(k_{\infty, \text{ox}}), \quad (3.83)$$

as suggested in Ref. [49]. Here, the logarithm of Equation 2.18 was taken, neglecting the expression for the reduction. The temperature of the ceria sample is assumed to be T_{B0} , which seems justified as TC B0 is placed in the hot zone together with the sample. The exponent 0.218 is taken from Ref. [48]. For each oxidation step but the first, the oxygen partial pressure is estimated by $p_{\text{O}_2} = p_{\text{F}}(t) - p_{\text{F},0}$, with $p_{\text{F},0}$ as defined in Figure 3.16. Here it is assumed that prior to an oxidation step, all O_2 was removed from the gas phase during the previous oxidation step and cooling phase. For the first oxidation step, there is excess O_2 in the furnace from the initial reduction step. Therefore, instead of $p_{\text{F},0}$, the pressure after the first oxidation and cooling step is used. This is equivalent to using $p_{\text{F},0}$ of the second oxidation step. The measured kinetics follows Equation 3.83, if the left-hand side of the equation, plotted against T_{B0}^{-1} yields a straight line.

3.2.8. Numeric Model of Test Rig

The test rig was modelled in *Python 3* [148, 149] to gain better understanding of the gas-phase-behaviour, when oxygen is fed from the buffer volume to the furnace. The model is used to identify suitable dimensions of the test rig and operating conditions for the experiment and to verify measured peak pressures for the evaluation of the experiments. The peak pressures are difficult to measure, due to the rapid pressure increase when oxygen is fed to the furnace. To find suitable conditions to operate the test rig, the gas-phase temperature \bar{T}_0 and pressure $p_{\text{F},0}$ in the furnace and the pressure in the buffer volume $p_{\text{BV},0}$ can be varied. Here, the subscript 0 indicates the state prior to oxygen entering the furnace from the buffer volume. The model was first used to approximate the dimensions of the test rig during the planning phase. To this end, the volumes of furnace V_{F} and buffer volume V_{BV} were varied. Later, when the model was used to verify peak

pressure measurements, the actual volumes of the final test rig design were set as parameters. These and other parameters of the model are given in Table 3.5. For the model, it is assumed that the buffer volume has a constant temperature of 295 K. It was later observed that the buffer volume indeed approximately remains at this temperature throughout the experiments.

Table 3.5.: Parameters used in the test rig model.

Parameter	Meaning	Value	Source
n_{CeO_2}	amount of substance of ceria sample	0.029 19 mol	measured/calculated (see Table 3.2)
V_{F}	Volume of furnace	$5.38 \cdot 10^{-4} \text{ m}^3$	measured/calculated (see Section 3.2.2)
V_{BV}	Buffer volume	$1.78 \cdot 10^{-3} \text{ m}^3$	measured/calculated (see Section 3.2.2)
M_{O_2}	Molar mass of O_2	$31.9988 \cdot 10^{-3} \text{ kg mol}^{-1}$	Refs. [144, 145]

The model describes the gas phase via balance equations and the ideal gas law. Herein, it is assumed that the transport of oxygen takes place in two consecutive steps: Firstly, the valve between furnace and buffer volume is opened and oxygen flows into the furnace until the pressure in the two chambers is equal. Secondly, the valve is closed and oxidation of the ceria sample results in a new equilibrium with a new pressure. The cool-down phase to the next temperature level after these two steps is modelled as well. The according states, used in the following model description are summarized in Table 3.6. In the first step, a new gas temperature in the furnace

Table 3.6.: States used in the test rig model.

State	Meaning
0	Before O_2 is fed to the furnace.
1	After O_2 was fed to the furnace.
2	After oxidation step.
3	End of cool-down phase.

is established, due to mixing of hot and cold gas. This is described by the energy balance of the furnace

$$0 = u_{\text{F},1} n_{\text{F},1} - n_{\text{F},0} u_{\text{F},0} - (n_{\text{F},1} - n_{\text{F},0}) h(T_{\text{BV}}), \quad (3.84)$$

where n and u are the amount of substance and molar internal energy of O_2 in the furnace, respectively. The indices 0 and 1 refer to the state before and after oxygen from the buffer volume has entered the furnace. Prior to the mixing of hot and cold gas, the furnace's controller establishes a constant temperature, so that heat input and losses offset each other. It is assumed that this is also the case during the mixing step, as it is fast and the total heat capacity of the gas is small compared to that of the solid components of the test rig, so that the temperature of surfaces that are in contact with the ambience is likely not affected significantly. Therefore no heat flow

is considered in Equation 3.84. The amount of substance at state 0 follows from the ideal gas law, as

$$n_{F,0} = \frac{p_{F,0} V_F}{R \bar{T}_0}, \quad (3.85)$$

$$n_{BV,0} = \frac{p_{BV,0} V_{BV}}{R \bar{T}_{BV}}. \quad (3.86)$$

The molar enthalpy h of O_2 is calculated using the Shomate Equation according to Refs. [144, 145]. The pressure dependence of h is neglected as it is small compared to the temperature dependence. For example at 295 K, the enthalpy varies by less than 0.1 % for pressures from 0 Pa to $1 \cdot 10^5$ Pa and at higher temperatures even significantly less [145]. The internal energy is calculated using the definition of the enthalpy, $h = u + p v$, so that

$$0 = u_{F,0} + \frac{p_{F,0} V_F}{n_{F,0}} - h(\bar{T}_0), \quad (3.87)$$

$$0 = u_{F,1} + R \bar{T}_1 - h(\bar{T}_1), \quad (3.88)$$

where $p v$ in Equation 3.88 has been replaced by $R \bar{T}$ using the ideal gas law, and it is assumed that the internal energy and enthalpy of the gas-phase can be calculated with the averaged gas temperature in the furnace \bar{T} from Equation 3.56. Again, h is calculated with the Shomate Equation according to Refs. [144, 145]. Finally, a mole balance for the gas-phase in the furnace combined with the ideal gas law yields

$$0 = n_{\text{total}} - n_{F,1} \left(1 + \frac{\bar{T}_1 V_{BV}}{T_{BV} V_F} \right), \quad (3.89)$$

where $n_{\text{total}} = n_{F,0} + n_{BV,0} = n_{F,1} + n_{BV,1}$ is the amount of O_2 in furnace and buffer volume combined, which is constant during the first step and hence equal for states 0 and 1. The system of equations consisting of the Shomate Equation and Equations 3.84, 3.88 and 3.89 was then solved numerically with the *fsolve* function from *SciPy* [155]. As initial value for the solver, \bar{T}_1 is approximated with an energy balance under the assumption of a constant heat capacity, which yields

$$\bar{T}_1^{\text{init}} = \frac{n_{F,0} \bar{T}_0 + \Delta n_{01}^{\text{init}} T_{BV}}{n_{F,0} + \Delta n_{01}^{\text{init}}}. \quad (3.90)$$

Here, $\Delta n_{01}^{\text{init}}$ is an approximation for the amount of O_2 that enters the furnace $n_{F,1} - n_{F,0}$ with

$$\Delta n_{01}^{\text{init}} = \left(n_{BV,0} \frac{V_F T_{BV}}{V_{BV} \bar{T}_0} - n_{F,0} \right) \cdot \left(1 + \frac{V_F T_{BV}}{V_{BV} \bar{T}_0} \right)^{-1}. \quad (3.91)$$

Equation 3.91 follows from the ideal gas law formulated for the furnace and the buffer volume at state 1 with the approximation $\bar{T}_1 \approx \bar{T}_0$, the fact that $p_{BV,1} = p_{F,1} = p_1$ and the mole balance $\Delta n_{01} = n_{F,1} - n_{F,0} = n_{BV,0} - n_{BV,1}$. A detailed derivation of Equation 3.91 is given in Appendix D. As initial values for h , the Shomate Equation for \bar{T}_1^{init} was used and initial values of $u_{F,1}$ and

$n_{F,1}$ can be calculated with Equations 3.88 and 3.89, but with \bar{T}_1 substituted by \bar{T}_1^{init} .

After aforementioned system of equations was solved numerically, remaining quantities can be derived analytically, according to

$$p_1 = \frac{n_{F,1} R \bar{T}_1}{V_F}, \quad (3.92)$$

$$n_{BV,1} = n_{F,0} + n_{BV,0} - n_{F,1}, \quad (3.93)$$

$$\Delta n_{O1} = n_{F,1} - n_{F,0}, \quad (3.94)$$

$$T_{BV,1} = \frac{p_1 V_{BV}}{n_{BV,1} R}. \quad (3.95)$$

Since the buffer volume is isothermal, $T_{BV,1} = T_{BV}$. Equation 3.95 is only used as plausibility check.

The second step of the model is the oxidation of the ceria sample. It is assumed that during the previous step, O_2 enters the furnace so fast that no oxidation has yet taken place. The valve between buffer volume and furnace can now either be closed, so that the respective atmospheres are separated and in the following different pressures are established in furnace and buffer volume or the valve remains open so that the pressure in both chambers is again equal. In both cases it is assumed that the gas temperature \bar{T}_2 in the furnace has again reached the original value \bar{T}_0 , since the gas phase is constantly heated by the furnace. For the new equilibrium between ceria and gas-phase, the non-stoichiometry of ceria δ is calculated with the correlation proposed by Bulfin et al. [48], given in Equation 2.32. The oxygen partial pressure relevant to determine δ is the total pressure $p_{F,2}$ in the furnace after the new equilibrium is reached, since the atmosphere is assumed to be pure O_2 . This pressure is calculated by the ideal gas law as

$$0 = p_{F,2} - \frac{n_{F,2} R \bar{T}_0}{V_F}, \quad (3.96)$$

where the amount of substance $n_{F,2}$ is determined by the mole balance

$$0 = n_{F,2} - n_{F,1} - \Delta n_{12}, \quad (3.97)$$

if the valve is closed or

$$0 = n_{F,2} - n_{F,1} + n_{BV,2} - n_{BV,1} - \Delta n_{12}, \quad (3.98)$$

in case of an open valve. In both cases Δn_{12} is determined by

$$0 = \Delta n_{12} + \frac{n_{\text{ceria}}}{2} (\delta_0 - \delta_2). \quad (3.99)$$

If the valve remains open, an additional variable is introduced with $n_{BV,2}$ in Equation 3.98. Therefore, to get a fully determined system, an additional equation is needed. This is achieved with

the ideal gas law for the buffer volume at state 2, which reads

$$0 = p_2 - \frac{n_{BV,2} R T_{BV}}{V_{BV}}, \quad (3.100)$$

where $p_{BV,2} = p_{F,2} = p_2$, due to the open valve. The system of equations is again solved numerically with the *SciPy* [155] function *fsolve*. First, the system of equations for the case of an open valve is solved. Here, the initial values for the solver are $\Delta n_{12}^{\text{init}} = 0$, $\delta_2^{\text{init}} = \delta_0$, $n_{F,2}^{\text{init}} = n_{F,1}$, $n_{BV,2}^{\text{init}} = n_{BV,1}$ and

$$p_{F,2}^{\text{init}} = \frac{n_{F,2}^{\text{init}} R \bar{T}_0}{V_F}. \quad (3.101)$$

Next, the system of equations for the case of a closed valve is solved. The initial values $\Delta n_{12}^{\text{init}}$, δ_2^{init} , $n_{F,2}^{\text{init}}$ and $p_{F,2}^{\text{init}}$ for that are the solutions of the case with an open valve.

Afterwards, in a last step, the cooling to the next temperature level $\bar{T}_3 = \bar{T}_0 - 100 \text{ K}$ with a closed valve is simulated. This step can be described by the same equations as the prior step, the oxidation of ceria for the case with a closed valve. The only difference is the use of \bar{T}_3 instead of \bar{T}_0 . As initial values for the solver, values of the prior step with a closed valve are used, i.e. $\Delta n_{23}^{\text{init}} = \Delta n_{12}$, $\delta_3^{\text{init}} = \delta_2$, $n_{F,3}^{\text{init}} = n_{F,2}$ and $p_{F,3}^{\text{init}} = p_{F,2}$.

Comparison of the results with an open and closed valve, respectively and the results of the cool-down were used during the planning phase of the test rig. Based on this initial analysis it was decided to close the valve during the experiments. Hence, results for a closed valve are used to verify the measurement of peak pressure values.

3.3. Modelling Indirect Heat Recovery

This section is in part based on the following patents and peer-reviewed publications, authored or co-authored by the author of the present work.

Stefan Brendelberger, Philipp Holzemer-Zerhusen, Estefania Vega Puga, Martin Roeb, and Christian Sattler. „Study of a new receiver-reactor cavity system with multiple mobile redox units for solar thermochemical water splitting“. In: *Solar Energy* 235 (2022), pp. 118–128. ISSN: 0038-092X. DOI: <https://doi.org/10.1016/j.solener.2022.02.013>

Stefan Brendelberger and Philipp Holzemer-Zerhusen. „Solarstrahlungsreceiver sowie Reaktorsystem mit Solarstrahlungsreceiver“. (German). German pat. DE102020118651B4. 2022

Stefan Brendelberger and Philipp Holzemer-Zerhusen. „Solarabsorbervorrichtung sowie Transportsystem für eine Solarabsorbervorrichtung“. (German). German pat. DE102020118683B4. 2022

An alternative approach to the investigated direct heat recovery system is an indirect concept in which heat is transferred from the hot redox material to a heat storage medium and in a sub-

sequent step from the heat storage medium to a cold unit of redox material. A direct approach offers potentially higher heat recovery ratios, for example up to full heat recovery in an ideal countercurrent HE. In an indirect approach on the other hand, the recombination effect can be eliminated, because of the separation of hot and cold redox material. Oxygen that might be released when heating the cold redox material, can be removed from the HE, before hot reduced redox material enters. In the present work, an indirect concept is studied, in which thin rectangular porous ceria monoliths are used, in the following referred to as redox units. These redox units are mobile and can be inserted into reduction and oxidation reactors and cycled between them. In-between reduction and oxidation, the redox units can be placed between two walls which serve as heat storage media. Hot and cold redox units are alternately placed in this HE setup so that heat is indirectly transferred from the hot to the cold redox unit in a transient manner. The system is modelled in *Python 3* [148, 149]. It is resolved in time and in one spatial dimension. In this model, which is described in the following, the temperature profiles of the heat storage and the redox units are calculated. Based on these temperature profiles, a heat recovery ratio is obtained. The model is used to alternately simulate charging and discharging steps, where charging refers to heating of the heat storage with a hot redox unit and discharging vice versa. A study is performed, in which different combinations of charging and discharging times are investigated to find the best heat recovery ratio.

3.3.1. Heat Transport Model

The heat transport is modelled in x -direction according to Figure 3.17. Gaps between heat storage and redox unit are considered so small as to be insignificant. Heat exchange at the small sides, i.e. perpendicular to x is neglected. The model is meant to estimate the potential of a simple HE design with a heat storage, consisting of two walls surrounding the redox unit. To this end, the heat storage medium is modelled as a generic material whose properties can be varied, rather than choosing a specific heat storage medium. To ensure that realistic values for λ , ρ and \tilde{c}_p of the heat storage medium are chosen, data for two different representative materials is used: A high density concrete [132] and a high temperature insulation material Rath KVS 184/400 [161]. Emissivity ε and heat transfer coefficient α are varied within physically reasonable limits as described below. In addition, different values for the heat storage thickness are investigated.

The heat conduction inside the materials is described by

$$\rho_{\text{eff}} \tilde{c}_p \frac{\partial T}{\partial t} = \frac{\partial}{\partial x} \left(\lambda_{\text{eff}} \frac{\partial T}{\partial x} \right), \quad (3.102)$$

where ρ_{eff} and λ_{eff} are the effective density and the effective thermal conductivity of the material, respectively. In case of the solid heat storage medium, these effective quantities are equal to that of the material. For the porous redox unit, the effective density is given by

$$\rho_{\text{eff}} = \rho_{\text{ceria}} (1 - \phi), \quad (3.103)$$

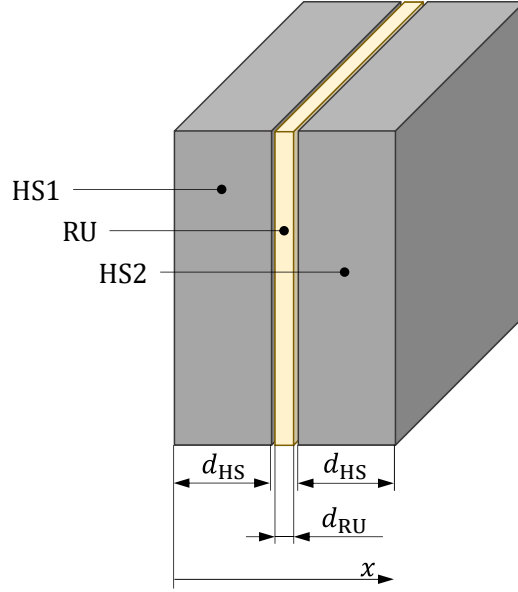


Figure 3.17.: Schematic of the indirect heat exchanger.

where ϕ is the total dual-scale porosity according to Equation 2.52. The effective thermal conductivity of the porous redox unit comprises a conduction term for the solid, using the properties of dual-scale reticulated ceria RPCs, given in Table 3.7 and a radiation term based on the Rosseland approximation, as described in detail in Chapter 2.5.3. For the fluid phase inside the pores, data for O_2 at 1 bar from Ref. [132] is used.

The following boundary conditions are used to solve Equation 3.102:

$$\lambda_{\text{eff}} \frac{\partial T_{\text{HS1}}}{\partial x} \Big|_{x=0} = \varepsilon_{\text{HS}} \sigma (T_{\text{HS1}}^4 - T_{\text{amb}}^4) + \alpha_{\text{HS}} (T_{\text{HS1}} - T_{\text{amb}}), \quad (3.104)$$

$$\lambda_{\text{eff}} \frac{\partial T_{\text{HS1}}}{\partial x} \Big|_{x=d_{\text{HS}}} = \frac{\sigma}{\frac{1}{\varepsilon_{\text{RU}}} + \frac{1}{\varepsilon_{\text{HS}}} - 1} (T_{\text{RU}}^4 - T_{\text{HS1}}^4), \quad (3.105)$$

$$\lambda_{\text{eff}} \frac{\partial T_{\text{RU}}}{\partial x} \Big|_{x=d_{\text{HS}}} = \frac{\sigma}{\frac{1}{\varepsilon_{\text{RU}}} + \frac{1}{\varepsilon_{\text{HS}}} - 1} (T_{\text{RU}}^4 - T_{\text{HS1}}^4), \quad (3.106)$$

$$\lambda_{\text{eff}} \frac{\partial T_{\text{RU}}}{\partial x} \Big|_{x=d_{\text{HS}}+d_{\text{RU}}} = \frac{\sigma}{\frac{1}{\varepsilon_{\text{RU}}} + \frac{1}{\varepsilon_{\text{HS}}} - 1} (T_{\text{HS2}}^4 - T_{\text{RU}}^4), \quad (3.107)$$

$$\lambda_{\text{eff}} \frac{\partial T_{\text{HS2}}}{\partial x} \Big|_{x=d_{\text{HS}}+d_{\text{RU}}} = \frac{\sigma}{\frac{1}{\varepsilon_{\text{RU}}} + \frac{1}{\varepsilon_{\text{HS}}} - 1} (T_{\text{HS2}}^4 - T_{\text{RU}}^4), \quad (3.108)$$

$$\lambda_{\text{eff}} \frac{\partial T_{\text{HS2}}}{\partial x} \Big|_{x=2d_{\text{HS}}+d_{\text{RU}}} = \varepsilon_{\text{HS}} \sigma (T_{\text{amb}}^4 - T_{\text{HS2}}^4) + \alpha_{\text{HS}} (T_{\text{amb}} - T_{\text{HS2}}). \quad (3.109)$$

Here, radiative heat transfer is expressed with the formulae described in Chapter 2.5.2. Between redox unit and heat storage Equation 2.45 for parallel plates is used. For radiation between heat

storage and ambience the expression can be simplified according to Equation 2.48, as explained in Chapter 2.5.2, because $\varepsilon_{\text{amb}} = 1$ is assumed. The heat transfer coefficient α_{HS} is estimated with a constant value. Based on Equation 2.41, α_{HS} typically lies in the range $5.0 \text{ W m}^{-2} \text{ K}^{-1}$ to $7.6 \text{ W m}^{-2} \text{ K}^{-1}$ for wall temperatures between 348 K and 1048 K. These values for α_{HS} were obtained assuming a square outer surface with an edge length of 0.375 m to 2 m, which matches dimensions of redox units studied in a reactor simulation described in Ref. [158]. Due to the one-dimensional resolution of the present HE model, these dimensions are otherwise not relevant for the model. The default value for α_{HS} is $10 \text{ W m}^{-2} \text{ K}^{-1}$, which, based on the aforementioned α_{HS} -range, is a conservative approximation. A value of $5 \text{ W m}^{-2} \text{ K}^{-1}$ is also studied to show the impact of the convective heat transfer.

The concept is based on transient heat transfer, so that the temperature profile is a function of the time. After a sufficient number of charging and discharging steps, the temperature profiles should however stabilize in the sense that at a given point in time, e.g. in the beginning of each charging/discharging step the same temperature profiles are present. Results are obtained for such a point of operation. To this end, Equation 3.102 is solved in space and time for the redox unit and both sides of the heat storage repeatedly until the temperature profiles have stabilized. Since the temperature profiles depend on the model parameters, especially the charging and discharging time, this process has to be repeated for each parameter combination. As a measure for stabilizing temperature profiles, the enthalpy change that the redox unit undergoes as it is heated is used. It is defined as

$$\Delta H_{\text{RU}} = \rho_{\text{ceria}} (1 - \phi) \int_{d_{\text{HS}}}^{d_{\text{HS}}+d_{\text{RU}}} \int_{T_{\text{RU}}^{\text{ox}}(x)}^{T_{\text{RU}}^{\text{end}}(x)} \tilde{c}_{\text{p,ceria}} dT dx, \quad (3.110)$$

where $T_{\text{RU}}^{\text{ox}}$ and $T_{\text{RU}}^{\text{end}}$ are the temperatures of the redox unit after the oxidation and at the end of the heat recuperation, respectively. The stopping criterion is

$$\left| \frac{\Delta H_{\text{RU},i} - \Delta H_{\text{RU},i-1}}{\Delta H_{\text{RU},i}} \right| \leq 0.001, \quad (3.111)$$

where i is the number of the simulation run. It is expected that the final temperature profiles in the two sides of the heat storage are close to steady-state temperature profiles with a constant temperature on the inside, equal to the mean temperature of the adjacent redox unit surface at the end of reduction and oxidation. This case is therefore used as an initial value for the simulations. Hence, it is assumed that on the inside the temperatures are

$$T_{\text{HS1}}^{\text{init}}(x = d_{\text{HS}}) = \frac{1}{2} \cdot \left(T_{\text{RU}}^{\text{red}}(x = d_{\text{HS}}) + T_{\text{RU}}^{\text{ox}}(x = d_{\text{HS}}) \right) \quad (3.112)$$

and

$$T_{\text{HS2}}^{\text{init}}(x = d_{\text{HS}} + d_{\text{RU}}) = \frac{1}{2} \cdot \left(T_{\text{RU}}^{\text{red}}(x = d_{\text{HS}} + d_{\text{RU}}) + T_{\text{RU}}^{\text{ox}}(x = d_{\text{HS}} + d_{\text{RU}}) \right), \quad (3.113)$$

respectively. While on the outside the temperature is determined by convective and radiative steady-state heat transfer to the ambience, which yields

$$-\frac{\lambda_{\text{HS}}}{d_{\text{HS}}} (T_{\text{out}} - T_{\text{in}}) = \alpha_{\text{HS}} (T_{\text{out}} - T_{\text{amb}}) + \varepsilon_{\text{HS-amb}} \sigma (T_{\text{out}}^4 - T_{\text{amb}}^4), \quad (3.114)$$

where the temperature on the inside T_{in} is either $T_{\text{HS1}}^{\text{init}}(x = d_{\text{HS}})$ or $T_{\text{HS2}}^{\text{init}}(x = d_{\text{HS}} + d_{\text{RU}})$ and T_{out} is the initial temperature of one side of the heat storage on its outside, i.e. either $T_{\text{HS1}}^{\text{init}}(x = 0)$ or $T_{\text{HS2}}^{\text{init}}(x = 2 d_{\text{HS}} + d_{\text{RU}})$. The initial steady-state temperature profile of the heat storage is given by a linear progression between T_{in} and T_{out} for each side. The first simulation for a given set of charging and discharging time, which is always a charging step is solved with this initial temperature profile. The final temperature profile of one charging or discharging step is the initial profile for the following discharging or charging step until the aforementioned stopping criterion is fulfilled. i.e. the temperature profiles have stabilised. Based on these profiles, heat recovery ratios are determined, as described below. Next, the simulation starts for a new combination of charging and discharging time with the initial linear temperature profile. The initial temperature profiles for the redox unit are always the same: In case of a charging step, the temperature profile is that at which the redox unit leaves the reduction reactor. In this study a temperature curve with 2000 K in the front and 1781 K in the back is used. It is the result of a receiver reactor simulation, described in detail in Ref. [158]. It is assumed that after the oxidation, the redox unit has a uniform temperature of 1200 K, which is the initial temperature profile of the redox unit for a discharging step.

The heat recovery ratio is defined as

$$\epsilon = \frac{\Delta H_{\text{RU}}}{\Delta H_{\text{RU}}^{\text{red}}}, \quad (3.115)$$

with

$$\Delta H_{\text{RU}}^{\text{red}} = \rho_{\text{ceria}} (1 - \phi) \int_{d_{\text{HS}}}^{d_{\text{HS}} + d_{\text{RU}}} \int_{T_{\text{RU}}^{\text{ox}}(x)}^{T_{\text{RU}}^{\text{red}}(x)} \tilde{c}_{\text{p,ceria}} dT dx, \quad (3.116)$$

where $T_{\text{RU}}^{\text{red}}$ is the temperature of the redox unit after the reduction. Hence, ϵ is the recuperated portion of heat necessary for the redox unit to reach the temperature profile of the reduction step. Material data and parameters for the simulation are summarized in table 3.7.

Table 3.7.: Parameters of the indirect heat recovery model.

Quantity	Meaning	Value	Unit	Ref.
d_{RU}	Thickness of redox unit	0.035	m	
$d_{\text{m, pore}}$	Mean pore diameter of redox unit	$2.5 \cdot 10^{-3}$	m	[20]
ϕ_{macro}	Macroscopic porosity of redox unit	0.71		[20]
ϕ_{strut}	Microscopic porosity of struts in redox unit	0.18		[20]
λ_{conc}	Thermal conductivity of concrete	2	$\text{W m}^{-1} \text{K}^{-1}$	[132]
λ_{ins}	Thermal conductivity of insulation material	0.25	$\text{W m}^{-1} \text{K}^{-1}$	[161]
λ_{gas}	Thermal conductivity of gas in redox unit	0.07	$\text{W m}^{-1} \text{K}^{-1}$	[132]
ε_{amb}	Emissivity of ambience	1		
ρ_{conc}	Density of concrete	2400	kg m^{-3}	[132]
ρ_{ins}	Density of insulation material	400	kg m^{-3}	[161]
ρ_{ceria}	Density of ceria	7220	kg m^{-3}	[111]
$\tilde{c}_{\text{p,conc}}$	specific heat capacity of concrete	1000	$\text{J kg}^{-1} \text{K}^{-1}$	[132]
$\tilde{c}_{\text{p,ins}}$	specific heat capacity of insulation material	1228	$\text{J kg}^{-1} \text{K}^{-1}$	[51, 162, 163]
$\tilde{c}_{\text{p,ceria}}$	specific heat capacity of ceria	470	$\text{J kg}^{-1} \text{K}^{-1}$	[164]
T_{amb}	Ambient temperature	298	K	

3.3.2. Model Discretisation

Equation 3.102 is discretised in time and x -direction. The time is divided into n_t steps and the x -dimension of each component, i.e. the two sides of the heat storage and the redox unit is divided into n_x steps. The step size Δx is the same for all three components, which means that heat storage and redox unit can have different values for n_x . In the present study, systems in which d_{HS} is a multiple of d_{RU} are studied, so that n_x is larger for the two sides of the heat storage than for the redox unit. The integer indices $i_t \in [1, n_t]$ and $i_x \in [1, n_x]$ are used to refer to the current point in time and the x -position, respectively. The temperature at a point in time i_t is calculated with data from the last time step $i_t - 1$, so that the discretised form of Equation 3.102 reads

$$\rho_{\text{eff}} \tilde{c}_{\text{p}} \frac{T_{i_x, i_t} - T_{i_x, i_t - 1}}{\Delta t} = \lambda_{\text{eff}} \left(T_{i_x, i_t - 1}^{\text{edge}} \right) \cdot \frac{T_{i_x + 1, i_t - 1} - T_{i_x, i_t - 1}}{\Delta x^2} - \lambda_{\text{eff}} \left(T_{i_x - 1, i_t - 1}^{\text{edge}} \right) \cdot \frac{T_{i_x, i_t - 1} - T_{i_x - 1, i_t - 1}}{\Delta x^2}. \quad (3.117)$$

Here, the temperature T is either T_{RU} or T_{HS} and is defined as the temperature in the center of a volume element. Also, a second temperature, T^{edge} is introduced, as depicted in Figure 3.18. It is the temperature on the edge between volume elements i_x and $i_x + 1$ and is calculated as

$$T_{i_x, i_t}^{\text{edge}} = \frac{1}{2} (T_{i_x, i_t} + T_{i_x + 1, i_t}). \quad (3.118)$$

It is used to calculate λ_{eff} for the heat transport between two adjacent volume elements. The first and last volume elements are only half the size of the other elements as indicated in Figure 3.18. Thus, T_{1, i_t} and T_{n_x, i_t} are not the temperature in the middle of the respective volume element, but

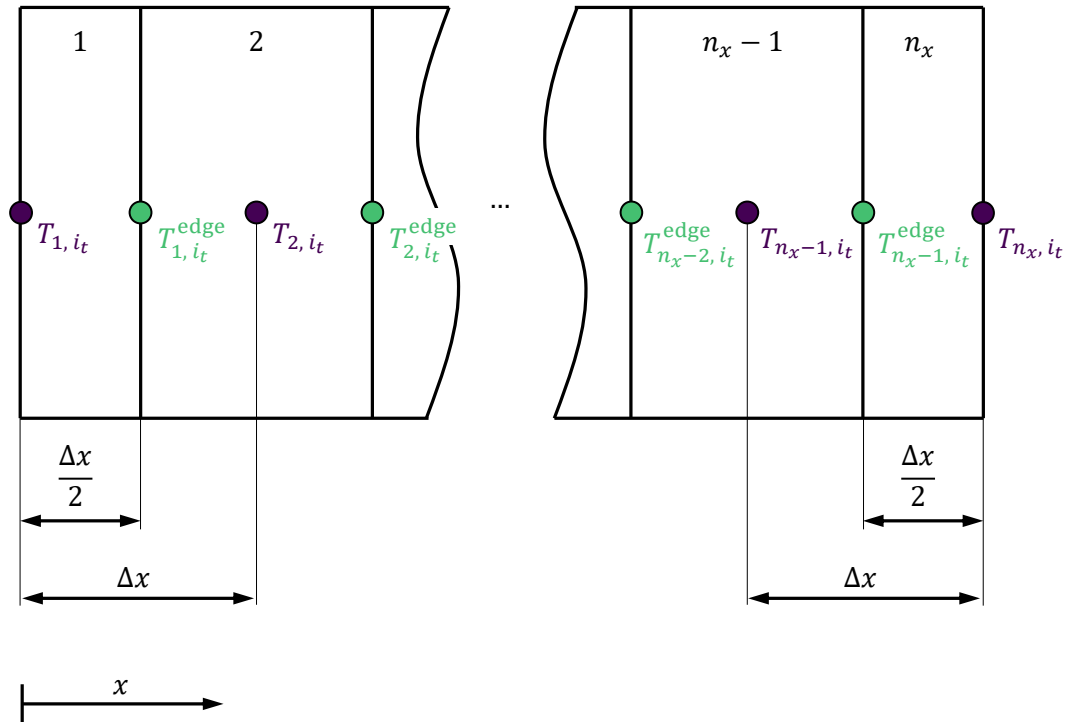


Figure 3.18.: Depiction of the one-dimensional discretisation of the modelled media.

on the outer surface and can be used in the aforementioned boundary conditions. To account for the halved thickness of these two elements, at $i_x = 1$ and $i_x = n_x$, a factor of 2 has to be considered for the right-hand side of Equation 3.117.

4. Results

In this chapter, simulation results and experimental results are presented. The correlation between heat recovery and recombination is shown based on simulations. These results also reveal the impact that recombination has on the overall efficiency of the redox cycle. Experiments on the re-oxidation, which leads to recombination in a HE are performed. The impact that addition of N_2 has on the reaction rates is studied to validate the hypothesis that an inert gas can act as a mass transport resistor. Prior to the investigation of oxidation rates, results of the characterisation of the gas phase in the test rig are presented. These are crucial for the calculation of oxidation rates. Following the experimental results, simulations of the recombination for given reaction rates are shown and discussed in the context of experimental results. Finally, simulations of a simple indirect heat recovery concept are presented. Temperature curves of the components resulting from the transient heat transfer and achievable heat recovery ratios at different combinations of residence times are obtained from the simulations.

4.1. Simulaton of Redox System with Oxygen Crossover

This section is in part based on the following peer-reviewed publications, authored by the author of the present work.

Philipp Holzemer-Zerhusen, Stefan Brendelberger, Martin Roeb, and Christian Sattler. „Oxygen Crossover in Solid-Solid Heat Exchangers for Solar Water and Carbon Dioxide Splitting: A Thermodynamic Analysis“. In: *Journal of Energy Resources Technology* 143.7 (Oct. 2020). 071301. ISSN: 0195-0738. DOI: 10.1115/1.4048772

Philipp Holzemer-Zerhusen, Stefan Brendelberger, Martin Roeb, and Christian Sattler. „Oxygen Crossover in Solid-Solid Heat Exchangers for Solar Water and Carbon Dioxide Splitting: A Thermodynamic Analysis“. In: *Proceedings of the ASME 2020 14th International Conference on Energy Sustainability*. ASME 2020 14th International Conference on Energy Sustainability. V001T13A001. Virtual, Online, June 2020. DOI: 10.1115/ES2020-1608

In this work, the extent to which recombination takes place in a continuously operated redox cycle utilising a solid-solid heat exchanger and the impact that the recombination has on the energy efficiency is investigated. To this end, simulations based on chemical equilibrium assumptions are conducted, using the model described in Chapter 3.1. As a starting point for simulations, default values for parameters are defined. They are summarised in Table 4.1 and used unless

otherwise stated. This parameter set does not represent an optimised system, but seems to be a plausible point of operation for both reactors with respect to the relevant literature, which is also listed in Table 4.1. In this work, the impact of the heat recovery ratio ϵ on the system efficiency η_{sys} is studied. There are two reasons for incomplete heat recovery. First, losses from the HE to the ambience and second the finite dimensions of a HE. In a technically feasible HE, a minimum temperature difference between hot and cold stream is needed to drive the heat transport. So there is always a trade-off between investment costs and heat recovery ratio. In addition, it is hypothesised that the recombination effect introduces another trade-off: that between heat recovery and recombination. In order to understand this trade-off, first a HE without losses to the ambience is simulated. Heat losses are then analysed in a second step.

Table 4.1.: Default simulation parameters.

Parameter	Meaning	Value	Ref.
X_{ox}	Conversion of H ₂ O or CO ₂ in oxidation chamber	0.2	
p_{red}	Pressure in reduction reactor	100 Pa	[70]
p_{ox}	Pressure in oxidation reactor	$1.013\,25 \cdot 10^5$ Pa	[13]
T_{ox}	Temperature in reduction reactor	1073 K	[13, 64, 80]
T_{red}	Temperature in oxidation reactor	1773 K	[13, 19, 113]
T_{amb}	Ambient temperature	298 K	
I_{rec}	Concentrated solar heat flux at the aperture	2.5 MW m^{-2}	[13, 27]
η_{el}	Efficiency of solar power plant	0.343	[151]
f_{loss}	Heat loss factor	0	

4.1.1. Energy Efficiency

Figure 4.1 shows η_{sys} as a function of ϵ , for setup 1 using the standard values from Table 4.1. For reference, the figure also includes results for a theoretical HE, in which no recombination occurs as well as a case without any HE. In the system with recombination, η_{sys} increases with increasing ϵ , for $\epsilon < 0.34$. After reaching a peak value at $\epsilon = 0.34$, η_{sys} decreases with increasing ϵ . The initial positive effect of ϵ on η_{sys} can be explained by a reduced heat demand for sensible heating of ceria due to heat recovery. Here, the system behaves similar to the reference case without recombination. Especially for low ϵ , η_{sys} has a similar slope in both cases. The following decrease of η_{sys} emerges as the recombination becomes more pronounced. This is shown by the progression of f_{recomb} , which is also included in the figure. For low ϵ , f_{recomb} is also low and almost constant, which explains, why the benefits of heat recovery are dominant in this region. Then, around $\epsilon = 0.34$, f_{recomb} increases steeply with respect to ϵ . Hence, at higher ϵ , the recombination has the dominant impact on η_{sys} .

An unexpected result is that for $\epsilon < 0.40$, the HE with recombination yields a higher η_{sys} than

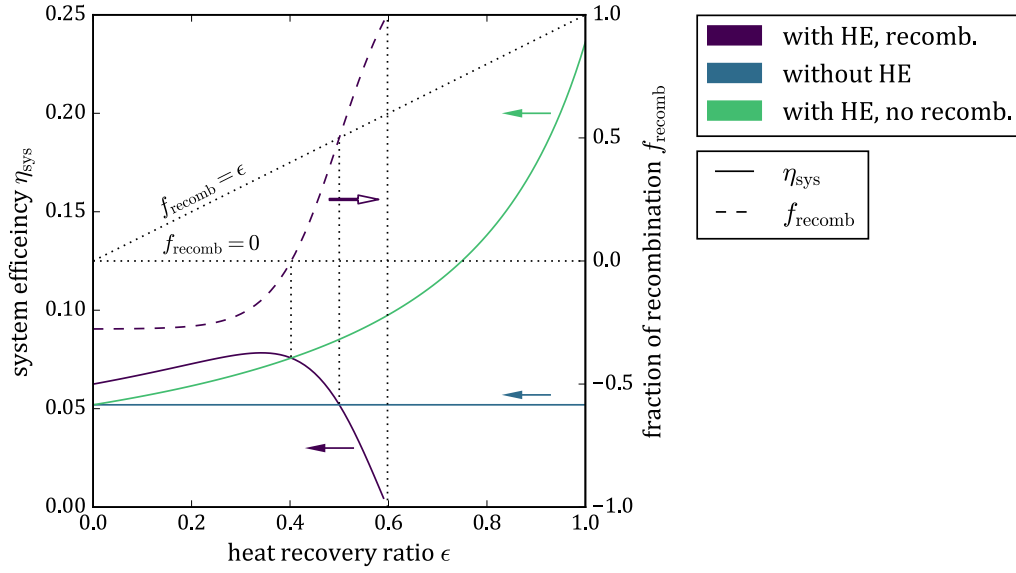


Figure 4.1.: System efficiency of setup 1 as function of the heat recovery ratio. Vertical lines indicate, where f_{recomb} reaches the value 0, ϵ and 1, respectively.

the HE without recombination. In this range, $f_{\text{recomb}} < 0$, which implies that the ceria stream, entering the HE from the reduction reactor, is further reduced in the HE, rather than oxidised as expected. To gain deeper understanding of this effect, the thermodynamic states reached in the HE are investigated. Figure 4.2 shows δ_i and T_i for the states $i \in \{1, 2, 3, 4\}$, defined in Figure 3.1 as a function of p_{O_2} . Lines represent isotherms for the respective temperatures. A case in which

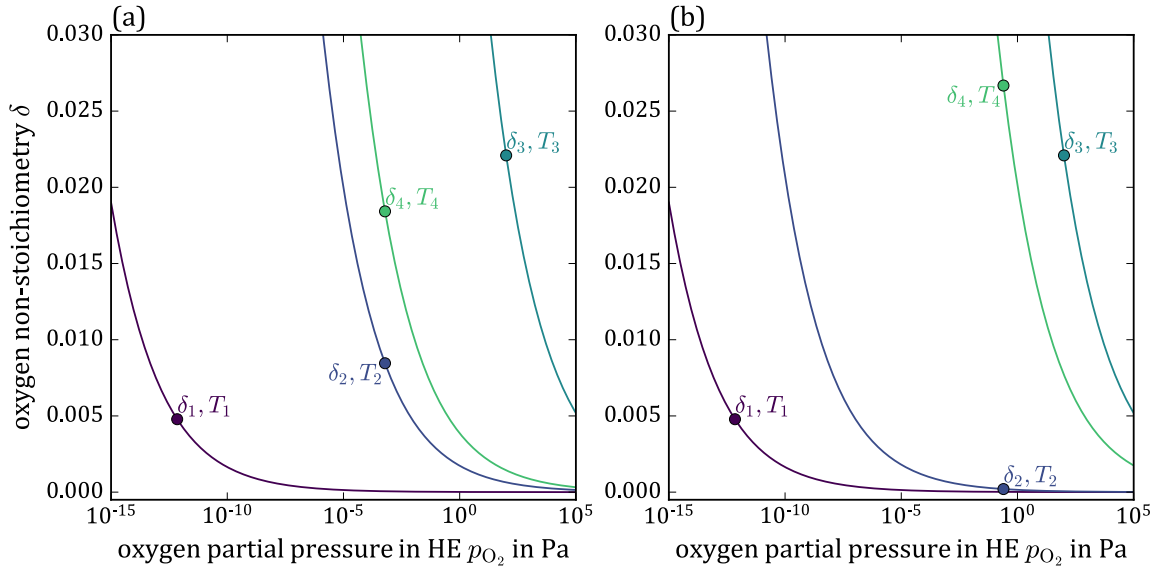


Figure 4.2.: Thermodynamic states of ceria streams entering or leaving the HE for setup 1 at (a) $\epsilon = 0.45$ and (b) $\epsilon = 0.20$. Calculated with Equation 2.32 from Ref. [48].

$f_{\text{recomb}} > 0$ is shown in Figure 4.2(a). Here $\epsilon = 0.45$. States 2 and 4 are reached at the HE outlets. Therefore, in both cases the partial pressure of O_2 is $p_{\text{O}_2, \text{HE}}$. As shown in the figure, $\delta_2 > \delta_1$ and

$\delta_4 < \delta_3$. This means that the ceria stream coming from the reduction reactor is oxidised, while the material coming from the oxidation reactor is reduced. This is the recombination effect as originally expected. Figure 4.2(b) shows a case for $\epsilon = 0.2$, where $f_{\text{recomb}} < 0$. Here, $\delta_2 < \delta_1$ and $\delta_4 > \delta_3$. So, indeed the material entering the HE from the reduction reactor is further reduced, while the material entering from the oxidation reactor is further oxidised. In that sense, the recombination effect is reversed. Reason for the reversed recombination is the O_2 partial pressure in the HE. It is lower than in the reduction reactor and higher than in the oxidation reactor. The impact that $p_{\text{O}_2, \text{HE}}$ has on δ_2 and δ_4 , counteracts that of the temperature change, which the material undergoes in the HE. At low ϵ , the temperature change is small and therefore the impact of p_{O_2} outweighs that of the temperature change. Due to the reversed recombination, the material has an even higher capacity to split H_2O or CO_2 than without recombination. This results in a lower demand of redox material and thus a lower heat demand. At $\epsilon = 0.40$, $f_{\text{recomb}} = 0$ and therefore setup 1 and the theoretical HE without recombination yield the same system efficiency. For the parameters used until now, the positive effect of reversed recombination is limited and it seems more beneficial if the recombination could be suppressed and higher ϵ achieved. All results, including the reversed recombination are checked for plausibility with respect to the second law, later on.

At $\epsilon = 0.5$, Figure 4.1 shows that η_{sys} is equal for setup 1 and the reference case without HE. Here, $\epsilon = f_{\text{recomb}} = 0.5$. Hence, the two effects offset. In other words, according to Equation 3.14, the redox material loses 50 % of its capacity to split H_2O or CO_2 , so that twice the amount of ceria is needed, compared to a system without HE. At the same time, $\epsilon = 0.5$, means that the heat demand to heat a certain amount of ceria from T_{ox} to T_{red} is halved, due to heat recovery. For setup 1, the point, where $\epsilon = f_{\text{recomb}}$ is always reached at 0.5, if no heat losses are considered. As 50 % of the heat is recovered, $T_2 = T_4$ and thus $\delta_2 = \delta_4$. This means hot and cold ceria streams leave the HE at the same temperature and consequently at the same oxygen non-stoichiometry. As explained above, setup 1 has a stable point of operation at which $\Delta\delta_{12} = -\Delta\delta_{34}$, as all the O_2 released by one ceria stream is taken up by the other stream. From this and $\delta_2 = \delta_4$ follows $\Delta\delta_{34} = -0.5 \Delta\delta_{13}$. According to Equation 3.14 this is the case if $f_{\text{recomb}} = 0.5$.

For $\epsilon > 0.34$, η_{sys} decreases to the point where it is even lower than in the case without any HE and finally reaches zero at $\epsilon = 0.60$. This marks the point where the reduction extent is fully lost to recombination. Accordingly, f_{recomb} becomes 1 and the redox material has no capacity left to split H_2O or CO_2 . This point is reached at $\epsilon < 1$, because the recombination is not only a function of the temperature, but also of the O_2 partial pressure. Since $p_{\text{O}_2, \text{HE}} > p_{\text{O}_2, \text{ox}}$, the material is oxidised in the HE to the same degree as in the oxidation reactor already at higher temperatures. Values of ϵ higher than 0.6 therefore do not represent relevant points of operation as splitting of H_2O or CO_2 are not possible. However, they are discussed later in the context of a second law analysis in Section 4.1.2.

Figure 4.3 shows η_{sys} for setup 1 for both, H_2O and CO_2 splitting. Using the standard parameters given in Table 4.1, yields very similar results for both process variants as shown in Figure 4.3(a). Results with a higher oxidation temperature of 1273 K are depicted in Figure 4.3(b). Here,

CO₂ splitting is significantly more efficient than H₂O splitting for the reference cases without recombination. The difference between H₂O and CO₂ splitting, is due to the related thermodynamic properties, which has an impact on the HHV, the heat needed to heat CO₂ or evaporate and overheat H₂O and the equilibrium of the respective thermolysis reaction. The HHV of CO and H₂ is very similar and differs by only 1 % [131]. For both cases, the heat needed to evaporate and/or heat the feed stream are small compared to the overall heat demand. The main difference between H₂O and CO₂ splitting is associated with the equilibrium thermodynamics. Figure 4.4 shows the Gibbs energy $\Delta_r g^\circ$ of the two reactions as well as the resulting equilibrium constants K_{eq} . The O₂ partial pressure $p_{\text{O}_2, \text{ox}}$ in the oxidation scales with K_{eq} , according to Equation 3.3. Figure 4.4 reveals that K_{eq} is similar for both reactions at low T_{ox} , but differs more at high T_{ox} . Consequently, $p_{\text{O}_2, \text{ox}}$ and δ_1 barely differ at low T_{ox} , while at higher T_{ox} , higher $p_{\text{O}_2, \text{ox}}$ and therefore lower δ_1 exist for CO₂ splitting compared to H₂O splitting. The lower δ_1 means that less ceria is needed to produce the same amount of product. Therefore, the heat demand to heat ceria from T_{ox} to T_{red} is reduced and the efficiency is increased. Figure 4.3(b) also shows that over a wide

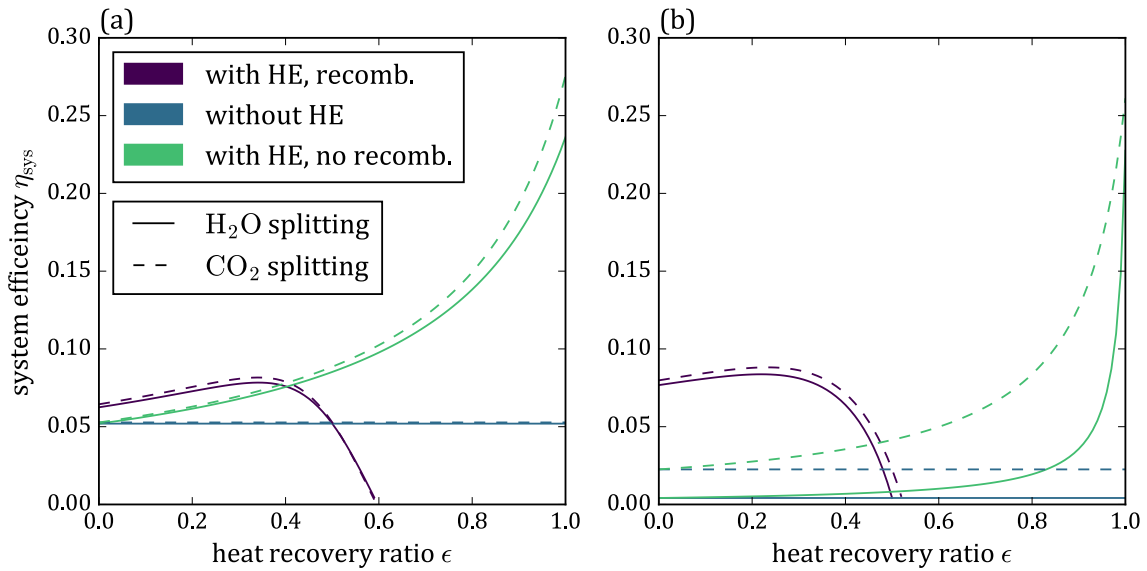


Figure 4.3.: System efficiency of setup 1 as function of the heat recovery ratio for H₂O and CO₂ splitting at (a) $T_{\text{ox}} = 1073$ K and (b) $T_{\text{ox}} = 1273$ K. Figure (b) is adapted from Ref. [146] with permission from the American Society of Mechanical Engineers.

range of ϵ , the recombination is reversed. On top of that, the effect of reversed recombination on η_{sys} seems to be amplified, compared to Figure 4.3(a). While increasing T_{ox} reduces η_{sys} for the reference cases without recombination, η_{sys} is of similar magnitude for both values of T_{ox} , shown in Figures 4.3(a) and 4.3(b), if recombination takes place. The reversed recombination also drastically mitigates the disadvantages of H₂O splitting compared to CO₂ splitting at high T_{ox} , previously discussed. Amplified reversed recombination is due to the oxidation state at the oxidation reactor outlet, represented by δ_1 , as explained in the following. A similar behaviour is observed when X_{ox} , the conversion of H₂O or CO₂, is varied. This is shown in Figure 4.5. At a low conversion of $X_{\text{ox}} = 0.02$, depicted in Figure 4.5(a) there is almost no reversed recombina-

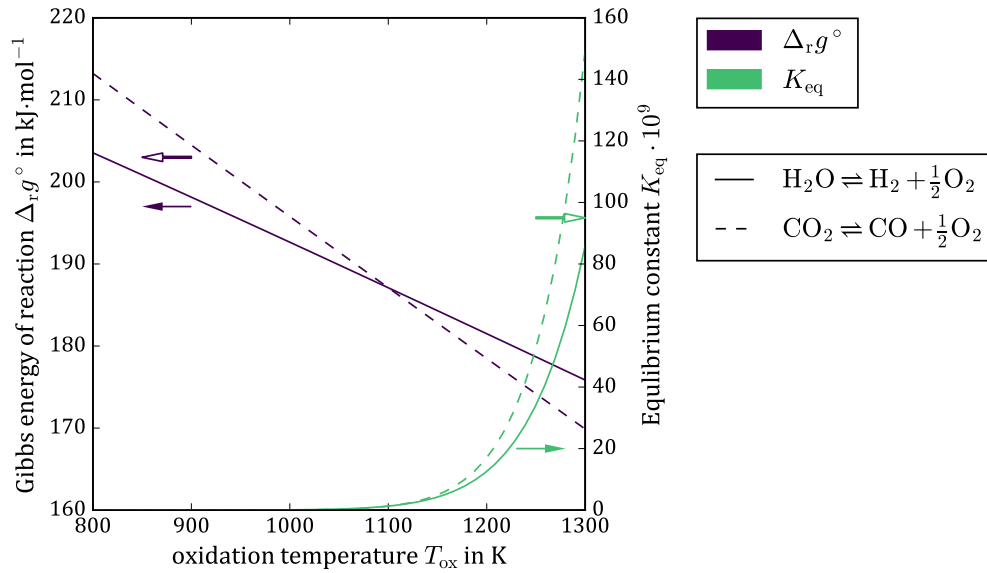


Figure 4.4.: Gibbs energy $\Delta_r g^\circ$ and equilibrium constant K_{eq} for thermolysis reactions.

tion effect. At a higher conversion of $X_{\text{ox}} = 0.5$, shown in Figure 4.5(b), the effect of reversed recombination is again amplified compared to the standard case with $X_{\text{ox}} = 0.2$. A higher conversion results in lower values of $p_{\text{O}_2, \text{ox}}$ and consequently higher δ_1 . In the discussed two-step solar thermochemical redox cycle, the amount of H_2O or CO_2 that can be split, depends on the difference in oxygen non-stoichiometry $\Delta\delta$ between the oxidation reactor's in and outlet. In a system without recombination, the relevant $\Delta\delta$ is $\Delta\delta_{13}$. In a system with recombination it is $\Delta\delta_{14}$. In case of reversed recombination, $\Delta\delta_{14} > \Delta\delta_{13}$ as the redox material gets reduced in the HE from state 3 to 4. This is depicted in Figure 4.2(b). Since in the HE in setup 1, $\Delta\delta_{12} = -\Delta\delta_{34}$ holds, this additional reduction from state 3 to 4 is equal to the degree of oxidation from state 1 to 2. Consequently, the additional degree of reduction due to reversed recombination is limited by the possible degree of oxidation in the HE. The oxidation is bound to the condition $\delta_2 > 0$, which yields $\Delta\delta_{12} < \delta_1$. In other words, the maximally possible extent of reversed recombination is determined by δ_1 . The higher δ_1 , i.e. the less oxidised the redox material is when it leaves the oxidation reactor, the more O_2 can be exchanged between the two ceria streams in the HE. This explains why high T_{ox} and high X_{ox} , shown in Figures 4.3(b) and 4.5(b) result in an amplified reversed recombination effect as they yield higher values of δ_1 . Figure 4.2(b) exemplifies the limits of reversed recombination. Here, the reversed recombination increases the degree of oxidation from $\delta_1 \approx 0.005$ to $\delta_2 \approx 0$. The relevant $\Delta\delta$ that can be used to split H_2O or CO_2 is as large as in a system without recombination, in which the material was almost fully oxidised in the oxidation reactor. Consequently, it is not possible to achieve a $\Delta\delta$ via reversed recombination that can not be achieved in a system without recombination. However, it seems possible to achieve such high $\Delta\delta$, even at relatively large δ_1 . In terms of process optimisation this makes the process more flexible and it seems possible to achieve high $\Delta\delta$ even if the process is operated under conditions that are not ideal with respect to the oxidation reactor, for example at high T_{ox}

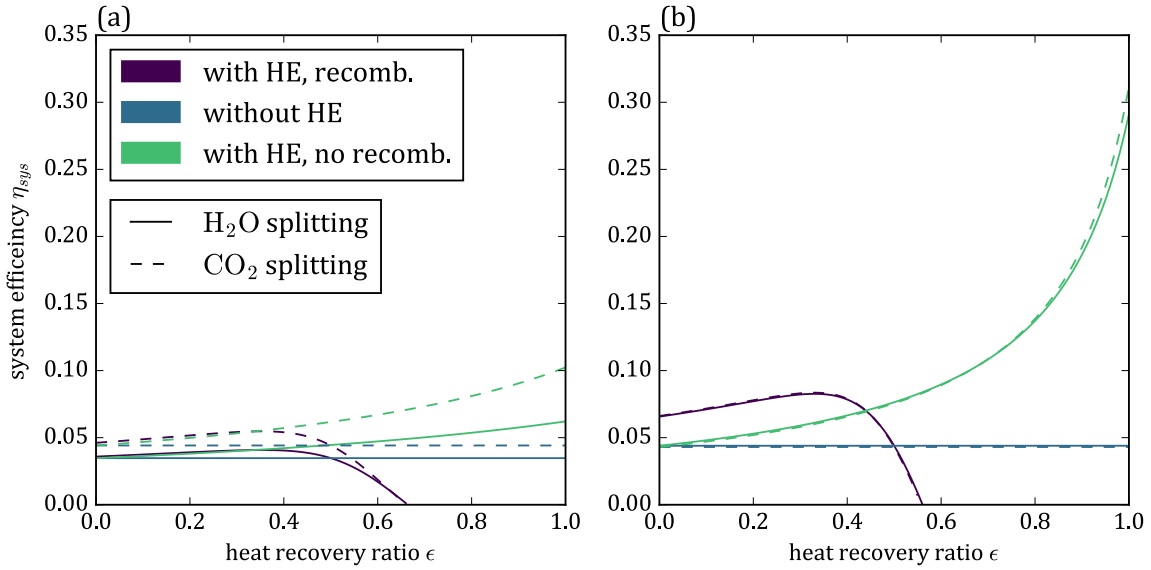


Figure 4.5.: System efficiency of setup 1 as function of the heat recovery ratio for different values of X_{ox} . (a): $X_{ox} = 0.02$; (b): $X_{ox} = 0.5$.

as discussed for Figure 4.3(b). This might in turn allow higher overall system efficiencies.

In Figure 4.6, the power demand of the redox cycle of setup 1 is exemplified for H₂O splitting at $\epsilon = 0.45$, including different parameter variations. Except the varied parameter, the parameter set from Table 4.1 is used. First, the impact of T_{ox} is studied. Results are depicted in Figure 4.6(a). $\Delta\dot{H}_{ceria}$ is the largest fraction of the overall energy demand and therefore has a crucial impact on η_{sys} . It depends on the amount of redox material \dot{n}_{ceria} and the temperature gap between T_{ox} and T_{red} . At constant T_{red} , increasing T_{ox} , decreases this temperature gap. However, it also decreases the extent of oxidation and hence more ceria is needed to produce the same amount of H₂. The trade-off between these two effects results in a minimum of $\Delta\dot{H}_{ceria}$ with respect to T_{ox} . The position of this minimum depends on ϵ , as it impacts the extent of recombination, which in turn has an impact on the amount of ceria needed. Higher T_{ox} lead to a negligible decrease of $\Delta\dot{H}_{red}$. Furthermore, increasing T_{ox} also increases $\Delta\dot{H}_{feed}$ so that more heat is needed to evaporate and overheat the feed stream. This effect is amplified by the fact that a higher T_{ox} leads to a lower receiver efficiency $\eta_{rec, ox}$. Nonetheless, $\Delta\dot{H}_{ceria}$ has the dominant impact on the overall solar heat demand \dot{Q}_{sol} and thus on η_{sys} .

The influence of the conversion X_{ox} is given in Figure 4.6(b). As mentioned above, X_{ox} determines the oxygen partial pressure in the oxidation chamber. Hence, it is directly linked to the achieved degree of oxidation. Higher values of X_{ox} mean higher δ_{ox} , which is why more ceria is needed. In consequence, $\Delta\dot{H}_{ceria}$ rises. On the other hand, a high conversion means less excess reactant, which has to be heated. Therefore, $\Delta\dot{H}_{feed}$ falls with rising X_{ox} . Analogously, very low values of X_{ox} , drastically increase $\Delta\dot{H}_{feed}$. The trade-off between these effects results in an optimum of X_{ox} in terms of minimizing \dot{Q}_{sol} . However, \dot{Q}_{sol} is nearly constant over a wide range of X_{ox} . Only very high and very low values of X_{ox} result in a strongly increasing heat demand.

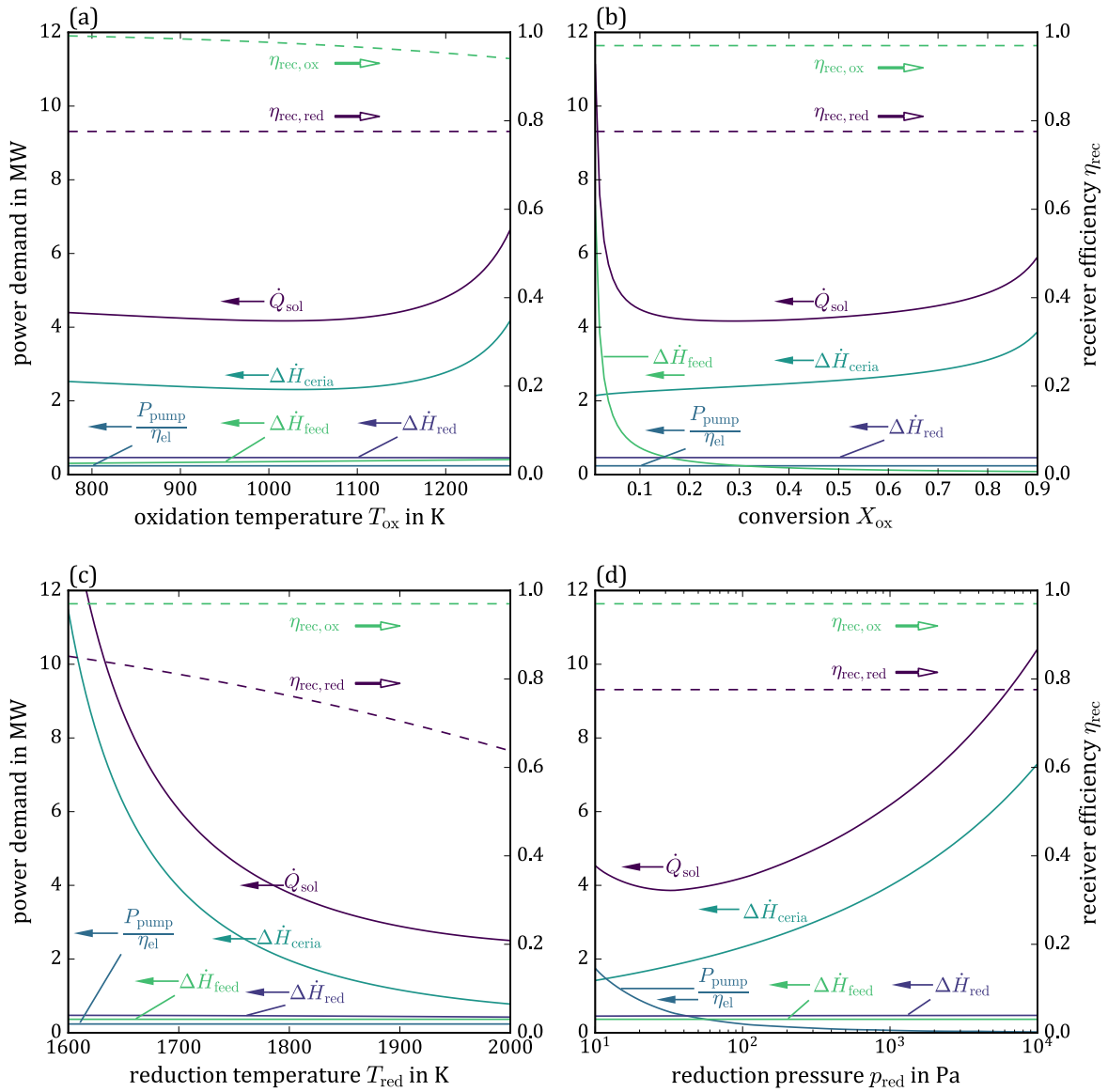


Figure 4.6.: Power demand for the production of 1 mol s^{-1} of H_2 with setup 1 at $\epsilon = 0.45$. The figure shows the total solar power demand \dot{Q}_{sol} and the single contributions according to Equation 3.26. All parameters are set to the value given in Table 4.1, except the variable on the respective abscissa.

It should be noted that the simple process design used in this study does not contain heat integration for the feed stream. Thus, a more sophisticated system with heat recovery for the fluid phase, might offer the option to operate the system at a lower conversion without significantly decreasing the efficiency. As a result, a high degree of oxidation would be possible at elevated T_{ox} , which in turn would reduce the temperature gap. The influence of X_{ox} on $\Delta \dot{H}_{red}$ is negligible with respect to the overall heat demand.

The reduction temperature T_{red} has a similar influence on the heat demand as T_{ox} as shown in Figure 4.6(c). Increasing T_{red} , increases the extent of reduction and therefore decreases the

necessary amount of ceria \dot{n}_{ceria} and thus $\Delta\dot{H}_{\text{ceria}}$. At the same time, a higher T_{red} increases the temperature gap to T_{ox} , which should increase $\Delta\dot{H}_{\text{ceria}}$. For the given parameter set however an optimal T_{red} is not found below 2000 K. An even higher T_{red} might result in practical difficulties such as sublimation of ceria [112, 113], which can, at low vacuum pressures, already occur at lower temperatures [114]. Also, the present study does not consider the temperature profile of the material. In a real system, peak temperatures at the directly irradiated front can drastically exceed the average temperature [66]. Therefore, values above 2000 K are not investigated. High reduction temperatures decrease the receiver efficiency $\eta_{\text{rec, red}}$, which additionally increases \dot{Q}_{sol} . However, also for \dot{Q}_{sol} no minimum is found below 2000 K. Higher reduction temperatures reduce $\Delta\dot{H}_{\text{red}}$, which again only has a minor impact on the system. All in all, it seems reasonable to choose T_{red} as high as technical limitations allow.

Finally, the impact of varying p_{red} is investigated in Figure 4.6(d). In general, decreasing p_{red} decreases $\Delta\dot{H}_{\text{ceria}}$, since it increases the degree of reduction, while the temperature gap between oxidation and reduction stays the same. On the other hand, the power demand for the vacuum pumps P_{pump} is increased at lower pressures. Lower pressures also decrease $\Delta\dot{H}_{\text{red}}$ due to their impact on δ . Once again this effect is however not decisive for the overall heat demand. Ultimately, there is an optimum p_{red} in terms of the overall energy efficiency. For the given parameters it is found at approximately 32 Pa.

The aforementioned parameter variations give insights into the system's behaviour without providing a strict efficiency optimisation. The most important quantity in terms of system efficiency is $\Delta\dot{H}_{\text{ceria}}$. As it depends on ϵ and \dot{n}_{ceria} , the optimal parameter set depends on the performance of the HE.

Next, the impact of heat losses is investigated, by varying f_{loss} . The magnitude of ϵ describes how much heat is transferred from hot to cold ceria stream, whereas f_{loss} is a measure for how much heat is released to the ambience. At $f_{\text{loss}} > 0$, not only the heat being transferred to the cold stream, but also the heat losses to the ambience cool the hot ceria stream. Consequently, higher f_{loss} result in lower T_4 . This in turn affects the recombination effect, without affecting ϵ . The lower T_4 results in a higher degree of oxidation of the reduced ceria stream or in case of reversed recombination a lower degree of reduction. Either way, the potential of ceria to split H_2O or CO_2 is reduced. Therefore, more ceria is needed to produce the same amount of H_2 or CO , which increases the heat demand. The impact of f_{loss} on η_{sys} is illustrated in Figure 4.7. For the whole range of ϵ , a higher f_{loss} leads to a decreased system efficiency. For the reference case with a theoretical HE that is not subject to recombination, heat losses also limit the recoverable heat to $\epsilon \leq 1 - f_{\text{loss}}$ as indicated by vertical lines in Figure 4.7.

With setup 2 the performance of a system with only one pressure lock is investigated. Here, the atmospheres of HE and oxidation reactor are separated, while HE and reduction reactor are connected. This leads to the results of Figure 4.8, where the parameters from Table 4.1 were applied to H_2O splitting. In setup 2, $f_{\text{recomb}} > \epsilon$ for all points of operation. As a result, η_{sys} is always lower than in a system without a HE. The point where $\eta_{\text{sys}} = 0$ is already reached at $\epsilon = 0.28$. As discussed later, the results for setup 2 with the standard parameter set violate the

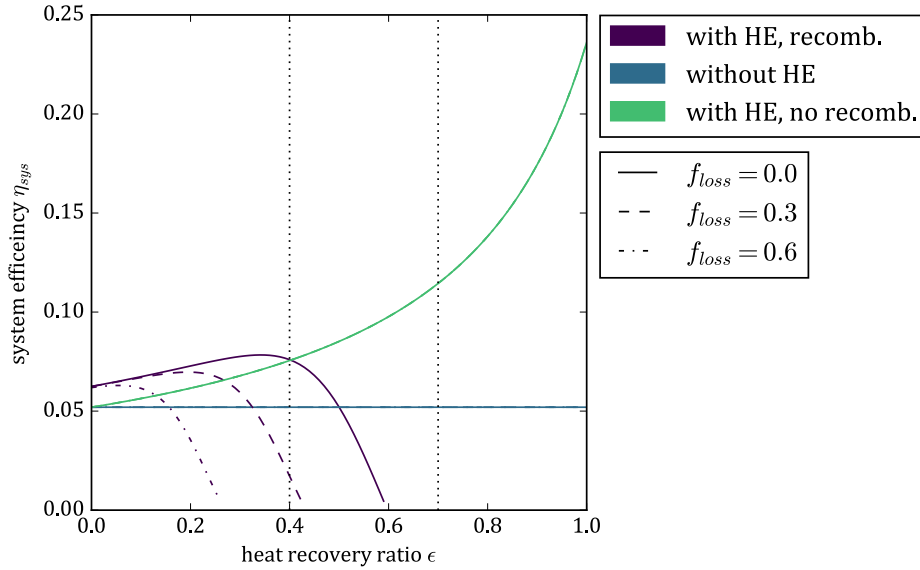


Figure 4.7.: System efficiency of setup 1 as function of the heat recovery ratio for different values of f_{loss} . Vertical dotted lines mark $\epsilon = 0.7$ and $\epsilon = 0.4$, the possible maximum of ϵ for $f_{loss} = 0.3$ and $f_{loss} = 0.6$, respectively.

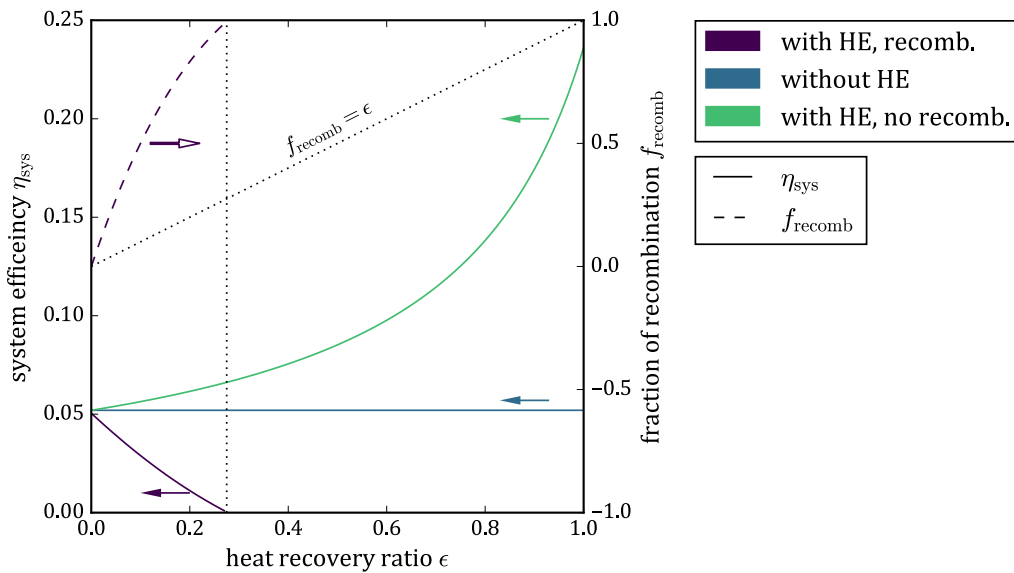


Figure 4.8.: System efficiency of setup 2 as function of the heat recovery ratio. The vertical line indicates, where f_{recomb} reaches 1.

second law for the whole range of ϵ . Reducing T_{ox} to 873 K, yields the results shown in Figure 4.9. Here, for almost all values of ϵ , no violation of the second law is detected. At $T_{ox} = 873$ K, the performance is slightly improved and $\eta_{sys} = 0$ is only reached at $\epsilon = 0.45$. However, the efficiency is still lower than in a system without HE. The reason for the high recombination extent and the resulting low efficiency is additional O_2 coming from the reduction reactor. A large portion of O_2 that was just released from the redox material by thermal reduction is taken up by the same material as it cools down in the HE. As depicted in Figure 4.10, $\delta_2 < \delta_1$ and $\delta_4 < \delta_3$ indicate that

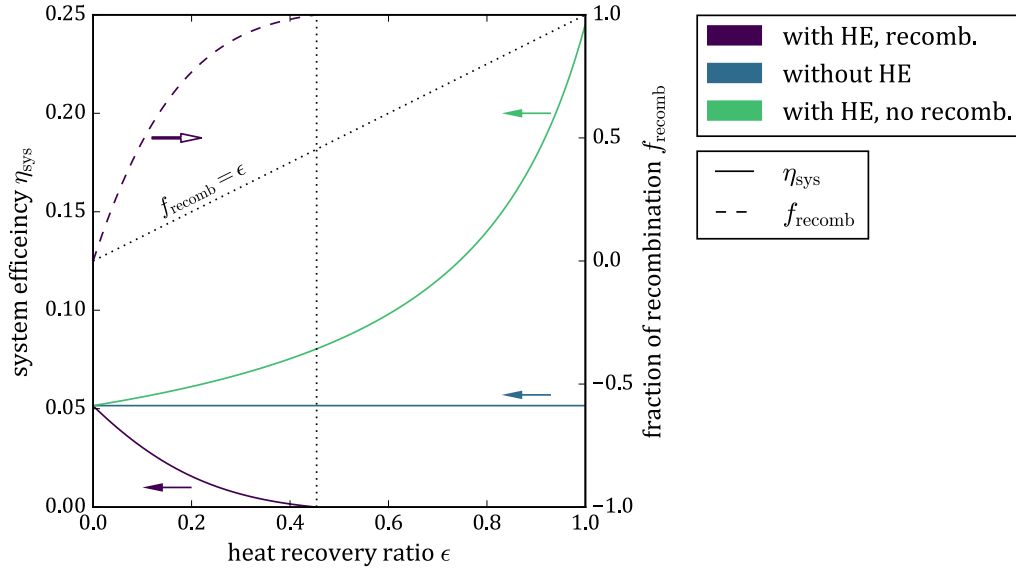


Figure 4.9.: System efficiency of setup 2 as function of the heat recovery ratio for $T_{\text{ox}} = 873 \text{ K}$. The vertical line indicates, where f_{recomb} reaches 1.

both material streams are oxidised in the HE. In contrast to setup 1, the O_2 partial pressure in the HE of setup 2 has the highest possible value, which is the pressure in the reduction reactor, i.e. $p_{\text{O}_2, \text{HE}} = p_{\text{O}_2, \text{red}}$. Hence, $p_{\text{O}_2, 2} = p_{\text{O}_2, 3} = p_{\text{O}_2, 4}$ in Figure 4.10. From a thermodynamic point of view, it is this high $p_{\text{O}_2, \text{HE}}$ that causes the large degree of re-oxidation in the HE. The

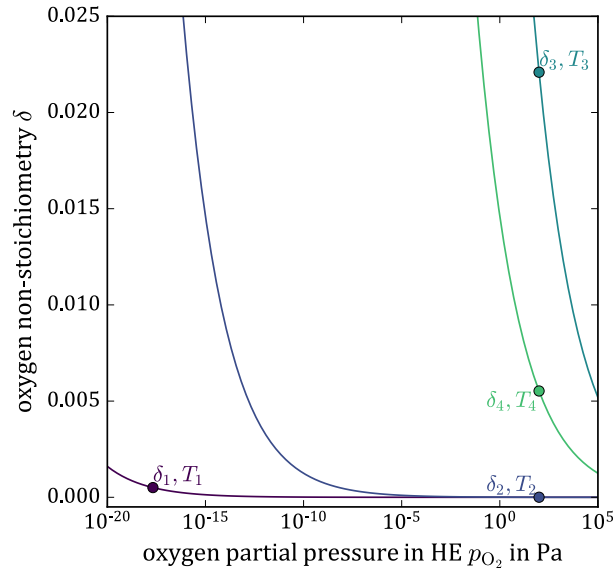


Figure 4.10.: Thermodynamic states of ceria streams entering or leaving the HE for setup 2 at $\epsilon = 0.2$ and $T_{\text{ox}} = 873 \text{ K}$. Calculated with Equation 2.32 from Ref. [48].

combination of the high $p_{\text{O}_2, \text{HE}}$ and the steep slope of the isotherm at T_4 in Figure 4.10, illustrate the thermodynamics that result in low values of δ_4 .

As explained in Chapter 3.1.2, the reaction enthalpy for oxidation of ceria inside the HE was

neglected. In contrast to setup 1, in which one stream is always oxidised and the other reduced, thus attenuating the influence of the reaction enthalpy, in setup 2 both streams are oxidised. Therefore, the impact of neglecting the reaction enthalpy might be more significant for setup 2. Recalculating T_4 and δ_4 , with a simple iterative approach including the reaction enthalpies, implies that the general trends depicted in Figures 4.8 and 4.9 do not change and that with or without consideration of the reaction enthalpies, setup 2 is less efficient than a process without HE. The only exception is for small values of ϵ , where the iteration leads to a heat transfer from cold to hot ceria stream. This unphysical result indicates that the iterative approach to take the reaction enthalpy into account is not suitable for the given zero-dimensional model and requires a more sophisticated model and it is not further considered in the present work.

4.1.2. Second Law Analysis

In the present work, a simplified generic model of a real system is used to understand the phenomena associated with recombination and to estimate their impact on the process. Reactions are simplified, in the sense that they are assumed to be infinitely fast, resulting in equilibrium conditions in both reactors and the HE. The gas in the HE is assumed to be ideally mixed and due to the lack of spatial resolution of the HE model, only inlet and outlet conditions are specified or calculated. To test whether the model yields plausible results, despite these simplifications, a second law analysis is performed. The entropy balance presented in Equation 3.35 is used, to check if results obey the second law. The condition $s_{\text{irr}} \geq 0$ has to be met for the second law to hold.

Figure 4.11(a) shows the entropy terms for setup 1 for the parameters from Table 4.1. For values of ϵ close to 0, the second law is violated as $s_{\text{irr}} < 0$. For most simulated points of operation however, the second law is obeyed. This is the case, regardless of the direction of the oxygen transport between the two ceria streams. Hence, the points of operation at which the recombination effect was found to be reversed seem possible according to this analysis. At these points, which are found at $\epsilon < 0.40$, the sum of the chemical contributions to the entropy Δs_{ch} is below 0. Due to the strongly positive thermal contribution Δs_{th} , the entropy balance nevertheless yields a net positive entropy production. The violation of the second law for low values results from negative values of Δs_{ch} , due to reversed recombination, while Δs_{th} is positive, but small. This implies that the predicted oxygen transfer due to $p_{\text{O}_2, \text{ox}} \leq p_{\text{O}_2, \text{HE}} \leq p_{\text{O}_2, \text{red}}$, while the two ceria streams undergo no or almost no temperature change is impossible. As Δs_{th} increases quickly with increasing ϵ , the second law is only violated in a very small parameter range.

At $\epsilon = 0.4$, Δs_{ch} becomes positive as f_{recomb} becomes positive. For $\epsilon > 0.60$, the chemical entropy term is again below 0. As discussed above, at $\epsilon = 0.60$, the recombination fully oxidises the reduced ceria stream, meaning that $\delta_4 = \delta_1$. Hence, the redox material cannot split any H_2O or CO_2 . At even higher ϵ , the model results in $\delta_4 < \delta_1$. Consequently, Equation 3.9 yields $\dot{n}_{\text{ceria}} < 0$, indicating a process that operates backwards. The model is however not designed for such results, which contradict the compositions of streams at the reactors' inlets and outlets.

Results for $\epsilon > 0.60$, do therefore not represent a physically meaningful system and are not further discussed.

Figure 4.11(b) shows results for setup 1, in which heat losses from the HE to the ambience are considered. Here, $f_{\text{loss}} = 0.3$, while all other parameters are the ones given in Table 4.1. As $\epsilon \leq 1 - f_{\text{loss}}$ must hold, heat recovery ratios up to 0.7 are possible. The heat loss has an impact on T_4 and with that on δ_4 . Consequently, both Δs_{th} and Δs_{ch} are different from the results in Figure 4.11(a). However, Δs_{ch} is still similar and also starts with negative values due to reversed recombination for $\epsilon < 0.27$. It is again negative for $\epsilon > 0.43$, where the model results in $\delta_4 < \delta_1$ and $\dot{n}_{\text{ceria}} < 0$. The heat loss also introduces the term $-q_{\text{loss}} \cdot T_{\text{loss}}^{-1}$ to the entropy balance. Figure 4.11(b) reveals largely negative values of Δs_{th} . Due to positive values of $-q_{\text{loss}} \cdot T_{\text{loss}}^{-1}$ in the same order of magnitude, $s_{\text{irr}} > 0$ is however fulfilled for most points of operation. Again the second law is violated for heat recovery ratios close to 0. Recalling that a pessimistic estimation for T_{loss} was chosen, it is possible that also low values of ϵ are actually feasible.

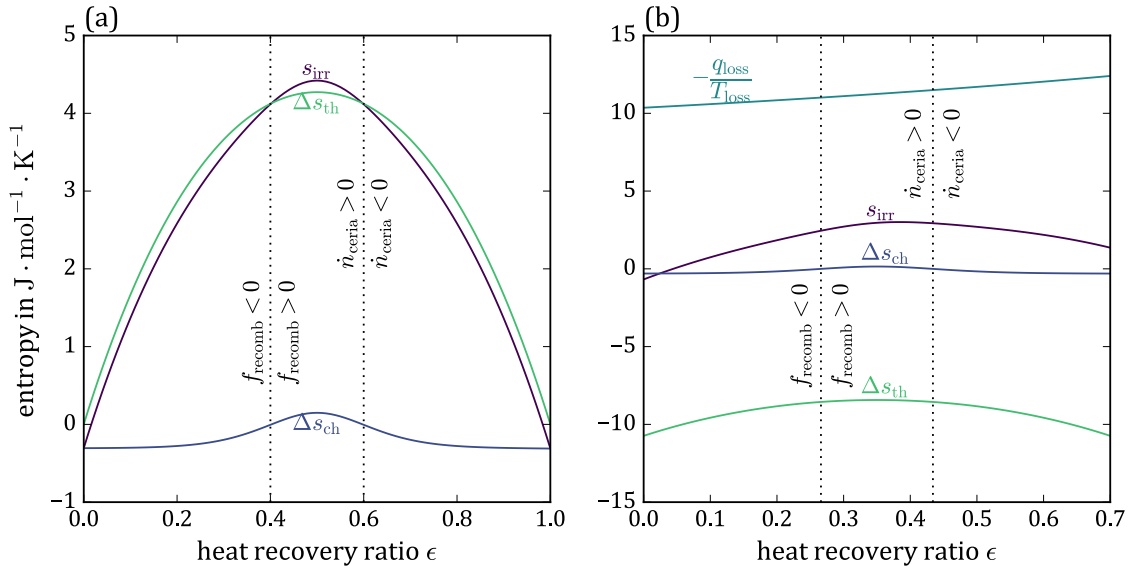


Figure 4.11.: Entropy expressions per mol of ceria as a function of the heat recovery ratio for H_2O splitting with setup 1. (a) all parameters as in Table 4.1, (b) $f_{\text{loss}} = 0.3$, all other parameters as in Table 4.1.

It was mentioned above that the results for setup 2 violate the second law for all points of operation, if the parameter set from Table 4.1 is used. This is depicted in Figure 4.12(a). Here, $s_{\text{irr}} < 0$ for all ϵ . Δs_{th} is identical to the results for setup 1 given in Figure 4.11(a). The biggest difference between the two setups is that in setup 2, O_2 can enter from the reduction reactor. This impacts Δs_{ch} , as more O_2 is taken up by ceria in the HE and also adds the term Δs_{O_2} to the entropy balance. While Δs_{O_2} has barely an impact, as it is close to 0 for all ϵ , negative values of Δs_{ch} for all points of operation result in $s_{\text{irr}} < 0$. Results show that the hot ceria stream, which enters the HE from the reduction reactor, is always oxidised in setup 2. For results that are meaningful in the sense that $\dot{n}_{\text{ceria}} > 0$, also the cold ceria stream coming from the oxidation reactor is oxidised. Only at high ϵ at which the cold stream is heated to a high T_2 , reduction of that

stream is predicted by the model. Since these points are found in the region where $\dot{n}_{\text{ceria}} < 0$ they are not relevant. Due to the additional oxygen uptake in the HE, Δs_{ch} is negative even though f_{recomb} is positive.

Comparison of Figures 4.12(a) and 4.12(b) shows that the reduction of the oxidation temperature yields changes in Δs_{ch} and Δs_{th} . The lower oxidation temperature results in reduced T_1 , T_2 and T_4 , which affects δ_1 , δ_2 and δ_4 . The largest impact of the oxidation temperature on Δs_{ch} is associated with a lower δ_1 . At $T_{\text{ox}} = 873$ K, Δs_{th} is significantly increased compared to $T_{\text{ox}} = 1073$ K. Similar to setup 1 at $T_{\text{ox}} = 1073$ K, setup 2 at $T_{\text{ox}} = 873$ K results in the second law being violated for ϵ close to 0, but at most points of operation, the second law is obeyed.

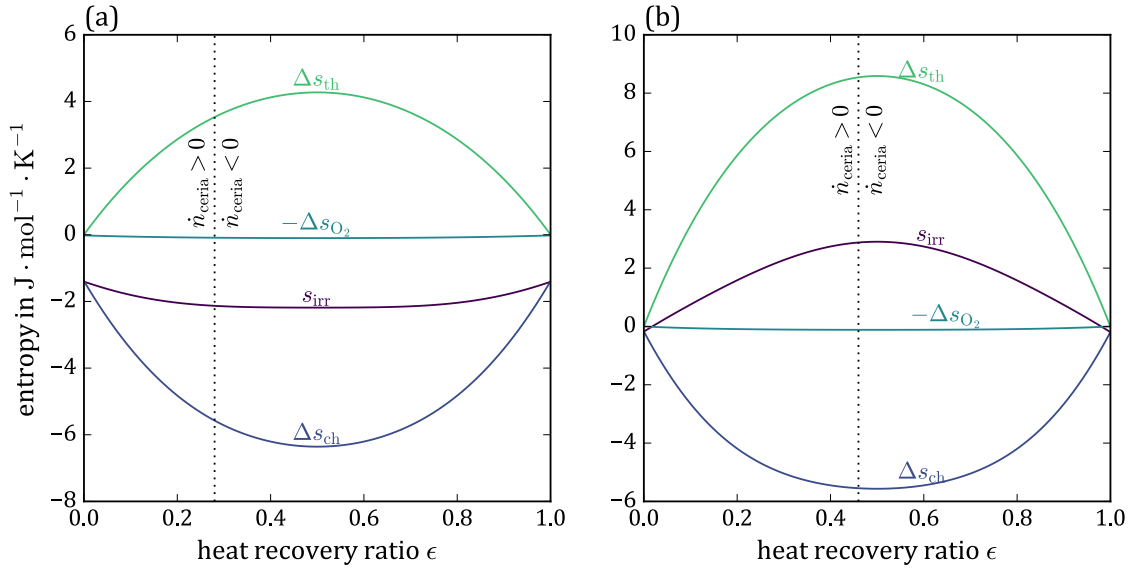


Figure 4.12.: Entropy expressions per mol of ceria as a function of the heat recovery ratio for H_2O splitting with setup 1. (a) all parameters as in Table 4.1, (b) $T_{\text{ox}} = 873$ K, all other parameters as in Table 4.1.

The second law analysis presented in this work is based on an entropy balance around the HE. This approach considers the states at the HE inlets and outlets, namely states 1 to 4. It therefore shows, if the simultaneous net changes of state from 1 to 2 and from 3 to 4 are feasible. It is not possible to test an arbitrary point inside the HE for feasibility due to the lack of spatial resolution of the model. A point of operation that is found to violate the second law with the presented analysis, is infeasible. On the other hand, $s_{\text{irr}} \geq 0$ only suggest that the net change of states is possible. Whether a real HE can achieve the according point of operation depends on the HE layout and has to be analysed with a more detailed model for the specific HE design. To prove that a continuous HE design exists that is capable of reaching the predicted thermodynamic states 1 to 4, it has to be shown that the second law is not violated at any point within the HE. To this end, incremental entropy balances, at least along the flow direction of the redox material, would be needed. A spatially resolved model goes beyond the scope of the present work, but the presented results give a first impression on the feasibility of the process and imply that the presented results are plausible.

4.2. Experiments

Simulation results presented in Chapter 4.1 show that the recombination effect might substantially limit the efficiency potential of the investigated redox cycle. These results were obtained under the assumption of infinitely fast reactions in the HE, which raises the question, whether the finite reaction rates of a real system would mitigate the recombination effect to the extent that the redox cycle reaches a competitive efficiency. Also it is hypothesized that introduction of an inert gas in the HE atmosphere can limit the mass transport in the gas phase, thus weaken the recombination. The oxidation rates of ceria are therefore studied under vacuum conditions with and without addition of nitrogen as an inert gas. In the following, first the behaviour of the gas phase in the test rig is analysed, followed by the evaluation of re-oxidation experiments.

4.2.1. Gas Phase Characteristics

Prior to the actual experiments, the characteristics of the gas phase within the test rig was studied, as it has a crucial impact on the assessment. This is done by theoretical considerations and reference measurements in which the test rig is operated without a reactive sample, as described in Section 3.2.6. Results are discussed in the present section.

To verify that the gas phase within the test rig can be treated as an ideal gas, the molar volume v of the gas is calculated with the ideal gas law and the van der Waals equation of state for the relevant pressure and temperature range. Results for O_2 are compared in Figure 4.13. The

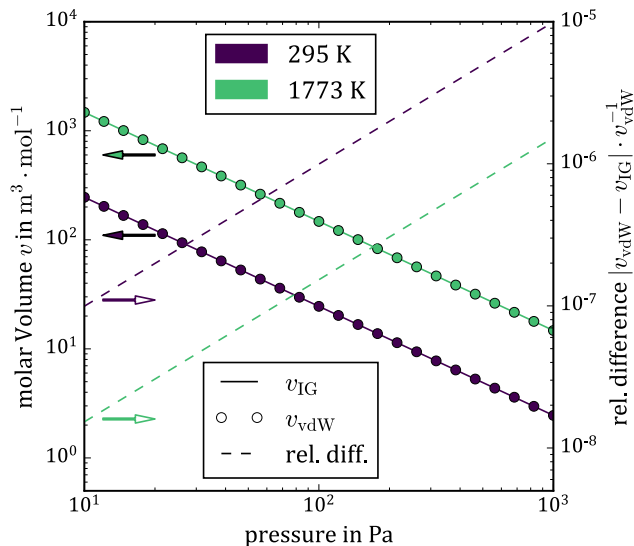


Figure 4.13.: Molar volume of O_2 calculated by ideal gas law and van der Waals equation in comparison. The secondary axis shows the relative difference.

graphs show good agreement between the two methods. In fact the relative difference of v for the two equations is always below 10^{-5} . Calculations for N_2 show very similar results and are excluded from figure 4.13 for the sake of clarity. The maximal relative difference in case of N_2 is

even below that for O₂ shown in the graph. Hence, it seems justified to use the ideal gas law to describe the gas phase throughout the experiments.

The furnace used in the test rig, has an active heating region in its center of 180 mm in axial direction, while the reaction tube has a total length of 822 mm. Therefore, a temperature gradient is expected, which is measured as described in Section 3.2.3. Results are given in Figure 4.14. The graph shows that indeed a distinct temperature profile is present in the reaction tube.

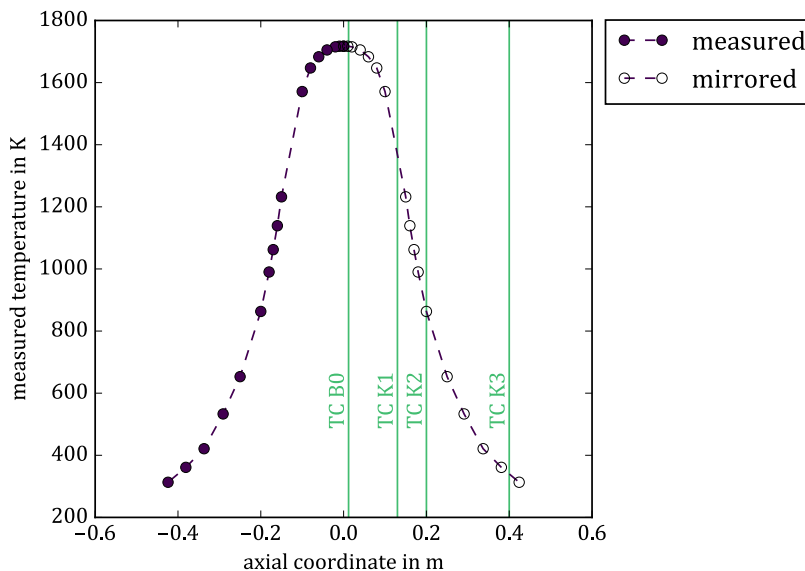


Figure 4.14.: Temperature profile measured by type-S thermocouple under atmospheric pressure at a set temperature of 1773 K. Vertical lines represent the position of thermocouples in the furnace during the experiments.

Within a length of 40 mm in the center of the reaction tube, the temperature is practically constant. Further away from the center, the temperature is significantly lower. Based on this result, the positions of four thermocouples in the reaction tube, which are also shown in the figure, are defined. During the actual experiments, different set temperatures are used and the test rig is operated at a partial vacuum. The temperature profile shown here was measured for a set temperature of 1773 K at atmospheric pressure. Hence, in general the temperature profile during an experiment will be different, but the results in Figure 4.14 show that the temperature has a spacial distribution and that a more thorough investigation of the gas temperature is needed, which is provided in the following.

A low pressure in the gas phase results in a low density and a long mean free path of the molecules. Depending on the actual pressure and density level, this might result in a low heat conductivity of the gas and hence a slow dynamic behaviour of the gas when heated or cooled. During the experiments, pressures are typically in the range of 10 Pa to 1000 Pa, which raises the question whether the gas phase has a reduced heat conduction, which results in a delay between temperature changes in the gas phase and those measured by thermocouples.

The Knudsen number, the ratio of the mean free path and the inner tube diameter, characterises the gas behaviour. At $Kn \ll 1$, the gas can be described as a continuum, in which the

heat conductivity is independent of the density, while strongly rarefied gases at $Kn \gg 1$ are in a free-molecule regime, where the heat flux is proportional to the density [132].

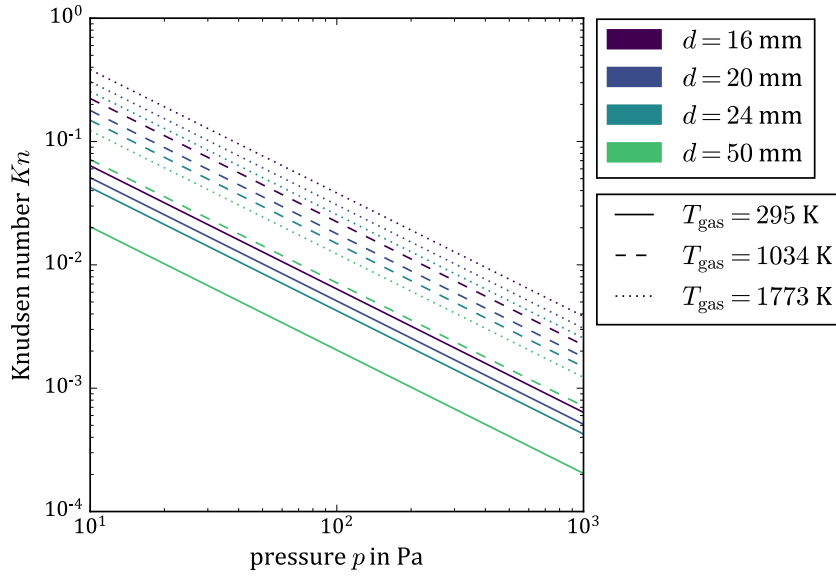


Figure 4.15.: Knudsen number for an ideal gas at given temperature and pressure for tube diameters d that are present in the test rig.

Figure 4.15 shows the Knudsen number Kn in the relevant pressure and temperature range for the tube diameters used in the test rig. The Knudsen number lies in the range $2 \cdot 10^{-4} < Kn < 0.4$. Even though $Kn < 1$ in the experiments, the gas cannot always be clearly categorized as continuum. In fact, Ref. [132] defines that the continuum regime is reached at $Kn < 10^{-2}$. Especially at high temperatures and low tube diameters such as in the reaction tube, the Knudsen number is relatively high, while at lower temperatures and larger tube diameters, such as in the surrounding tubes and the buffer volume the Knudsen number is rather small. These results suggest that during experiments the gas phase will be in a continuum regime in colder parts of the test rig, while the gas in the reaction tube might be in a transitional regime between continuum and free-molecule regime [132]. Therefore, the gas phase might at least locally have a reduced heat conductivity, so that thermal inertia might make measurements of a dynamically changing gas temperature difficult. However, this examination alone does not allow a clear assessment of whether the gas temperature can be measured reliably or not. This motivates further investigation of the gas temperature.

To gain deeper understanding of whether the temperatures measured by thermocouples are representative for the gas temperature, the radiative heat transfer between reaction tube and thermocouple and the convective heat transfer between gas phase and thermocouple are estimated with the methods described in Section 3.2.6. Figure 4.16 shows the ratio of \dot{Q}_{rad} and \dot{Q}_{conv} . Here, the temperature of the thermocouple is the mean value of the temperatures of the gas phase T_{gas} and the reaction tube T_{RT} , i.e. according to Equation 3.53, $f = 0.5$. It can be seen from Figure 4.16 that $\dot{Q}_{\text{rad}} > \dot{Q}_{\text{conv}}$ for all values of T_{gas} and T_{RT} . The ratio of the two heat trans-

fer rates is almost constant for the whole range of T_{gas} . Figure 4.17 shows results for $f = 0.8$,

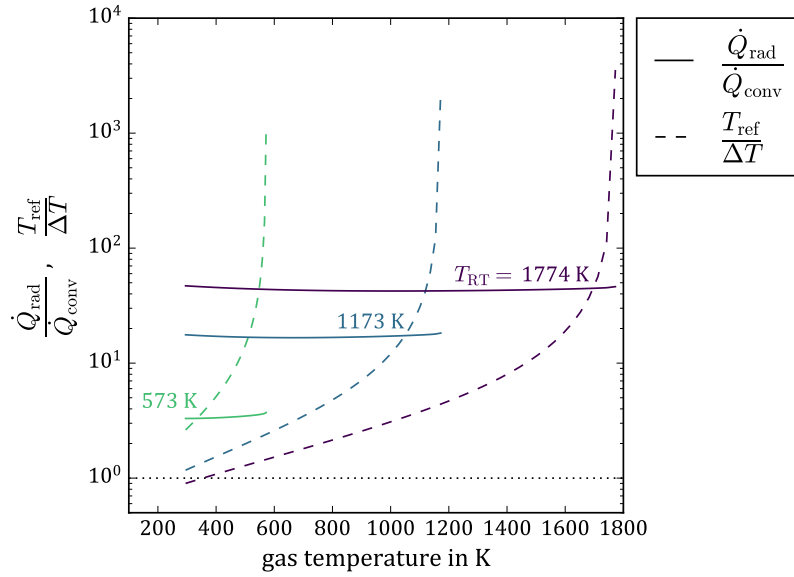


Figure 4.16.: Ratio between radiative and convective heat transfer and ratio between the temperature difference and the reference temperature, for $p = 100$ Pa and $f = 0.5$, i.e. $T_{\text{TC}} = 0.5 T_{\text{RT}} + 0.5 T_{\text{gas}}$.

which means that still $T_{\text{gas}} < T_{\text{TC}} < T_{\text{RT}}$, but this time T_{TC} is closer to T_{RT} . In this case, the ratio of \dot{Q}_{rad} and \dot{Q}_{conv} is smaller than before and for $T_{\text{RT}} = 573$ K the net radiative heat transfer rate is even slightly lower than the convective heat transfer rate. These results imply that for a large range of temperatures $\dot{Q}_{\text{rad}} > \dot{Q}_{\text{conv}}$ holds, but that by no means a generally valid assumption like $\dot{Q}_{\text{rad}} \gg \dot{Q}_{\text{conv}}$ or $\dot{Q}_{\text{rad}} \ll \dot{Q}_{\text{conv}}$ can be made. This means that the gas temperature has an impact on the temperature measured by the thermocouple, but whenever $T_{\text{gas}} \neq T_{\text{RT}}$ the measured temperature is likely closer to T_{RT} than T_{gas} , in particular at high temperature levels. Especially in transient phases, for example when cold gas is fed to the hot system, the thermocouple might react slowly to the rapid change in T_{gas} . Therefore, the temperatures measured by thermocouples are not a reliable measure for the gas temperature and thus a different approach to quantify the gas temperature is developed.

The ratio of T_{ref} and ΔT is also depicted in Figures 4.16 and 4.17. As mentioned earlier, the empirical correlations used to determine \dot{Q}_{conv} are most reliable for $\Delta T \ll T_{\text{ref}}$ [132]. As indicated in the figures, this condition is well met at high gas temperatures, but not so much at lower temperatures. The results discussed in this section are therefore only a first approximation.

As it becomes clear in the assessment above that neither the local gas temperature T_{gas} nor the average gas temperature \bar{T} can be measured reliably, an alternative approach is needed. As explained in Section 3.2.6, reference measurements are performed to derive a correlation between measured temperatures and \bar{T} and to determine the leakage into the test rig as a function of measured temperatures. The pressure change rate due to leakage \dot{p}_{L} is determined with data from said reference measurements. Results are shown in Figure 4.18. As described in Section 3.2.6, the leakage is determined after 6 h of dwelling at T_{set} , so that a steady temperature is estab-

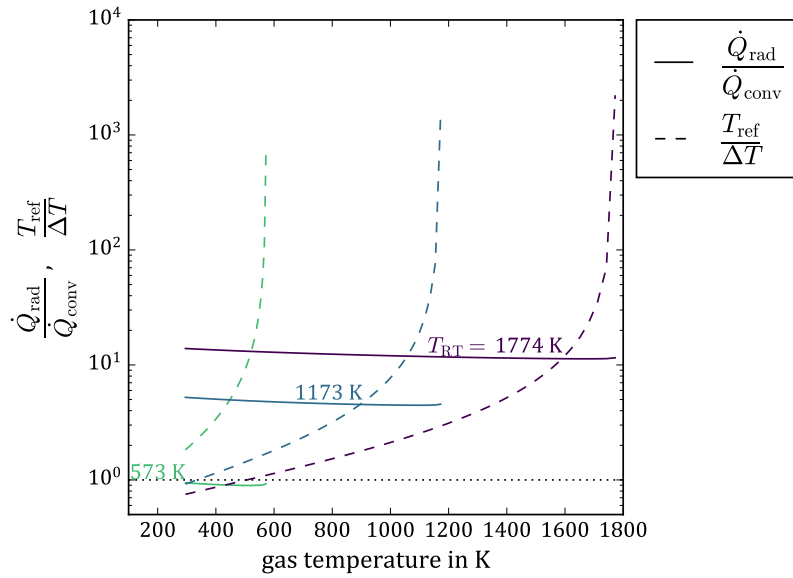


Figure 4.17.: Ratio between radiative and convective heat transfer and ratio between the temperature difference and the reference temperature, for $p = 100$ Pa and $f = 0.8$, i.e. $T_{TC} = 0.8 T_{RT} + 0.2 T_{\text{gas}}$.

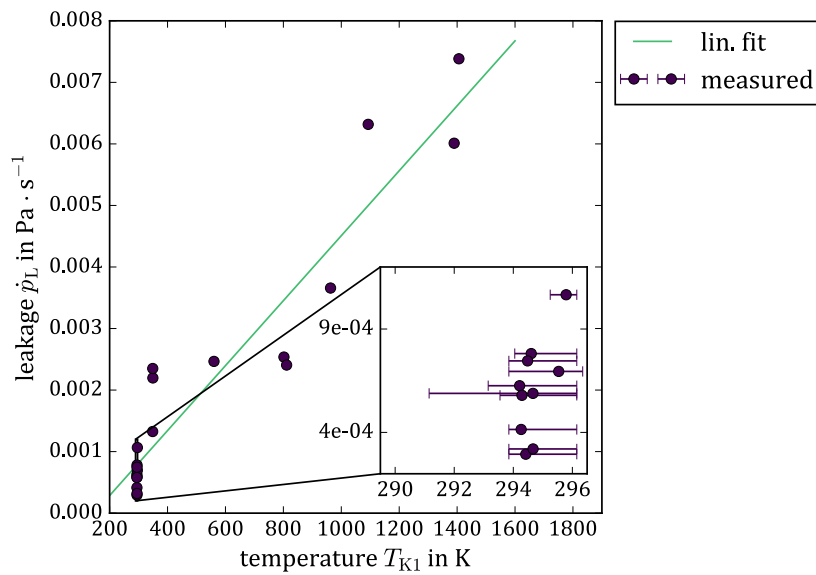


Figure 4.18.: Leakage determined from reference measurements and linear fit as function of temperature T_{K1} . Fluctuations in the temperature are given by error bars, ranging from maximum to minimum temperature.

lished. However, minor fluctuations in the temperature are always present. This is considered in Figure 4.18 by error bars, which range from maximum to minimum temperature. The linear regression shown in Figure 4.18 approximates these results with an R^2 -value of 0.90. With this correlation for \dot{p}_L , the gas temperature \bar{T} is calculated in an iterative approach explained in Section 3.2.6. Figure 4.19(a) depicts \bar{T} after the first and final iteration. Again, linear regression is used to derive a continuous correlation between T_{K1} and \bar{T} . Figure 4.19(b) shows the evolution

of the fit-parameter C and the coefficient of determination R^2 . The iteration converges quickly and the stopping criterion $(C_k - C_{k-1}) \cdot C_{k-1}^{-1} < 10^{-5}$ is met after 5 iterations. After the final iteration, $R^2 = 0.52$, which implies a poor agreement between fit and data. During experiments,

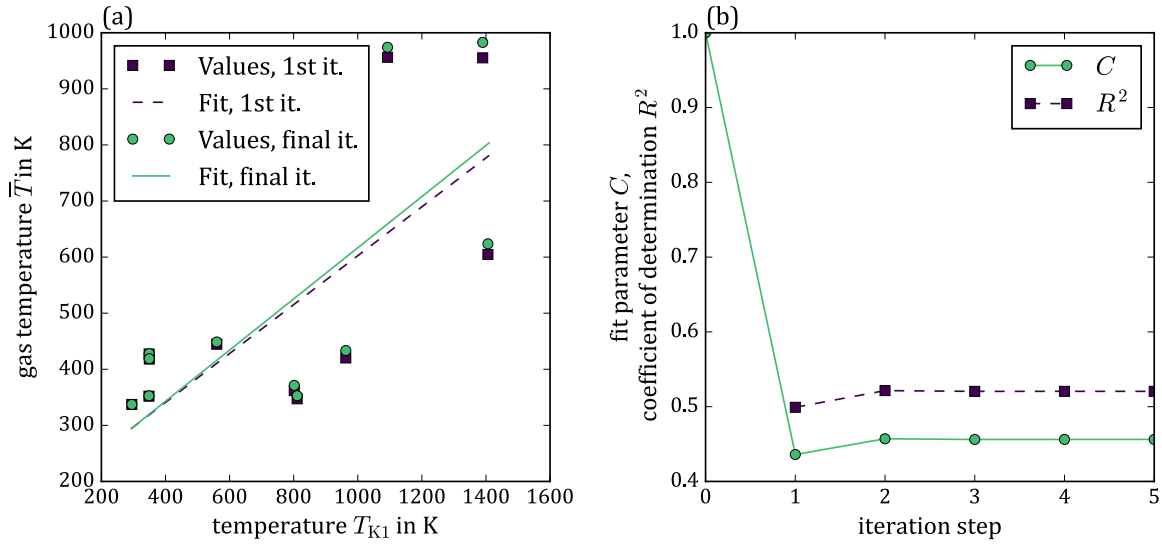


Figure 4.19.: Iterative approach to derive \bar{T} as a function of T_{K1} . (a): Results of first and last iteration step. Data points show results calculated with Equation 3.64. Lines show linear fit to data points according to Equation 3.65. (b): Evolution of fit parameter C and coefficient of determination R^2 over iteration progress.

the maximum gas temperature \bar{T}_{\max} , given by Equation 3.67, is in the range 407 K to 466 K. In Figure 4.19(a), these values are exceeded. A reason for this could be the thermal inertia of the gas phase. As mentioned above, \bar{T} in Figure 4.19(a) is calculated after a dwelling time at T_{set} of 6 h. During experiments, gas enters the hot reaction tube at room temperature and it takes the gas phase some time to reach the final steady temperature. As indicated above, the gas phase might react slowly to temperature changes. Thus the gas temperature in an experiment might be significantly lower than estimated in Figure 4.19(a). Also results depicted in Figure 4.20 support this theory. The graphs show a pressure curve during a reference measurement and a theoretical pressure curve without leakage, calculated with \dot{p}_L and \bar{T} from Figures 4.18 and 4.19(a). During heating and temperature dwelling phase the pressure curve without leakage seems plausible. A sudden pressure increase is indicated, as the furnace starts to cool down, which seems implausible. As the temperature drops, the slope of the pressure should decrease as well. The theoretical pressure curve without leakage results from subtracting the integral in Equation 3.64 from p_1 , given in the same equation. If the gas phase reacts slowly to temperature changes, the gas temperature during the cooling phase (\bar{T}_1 in the integral) is higher than the final steady temperature, which would be reached after a sufficient dwelling time. It would therefore be underestimated by the linear fit discussed above. With that, the whole integral in Equation 3.64 is underestimated and hence the calculated pressure is higher than plausible. This is exactly what can be seen in Figure 4.20, suggesting that the lack of consideration of thermal inertia in the model is

the reason for the poor predictability of the transient behaviour.

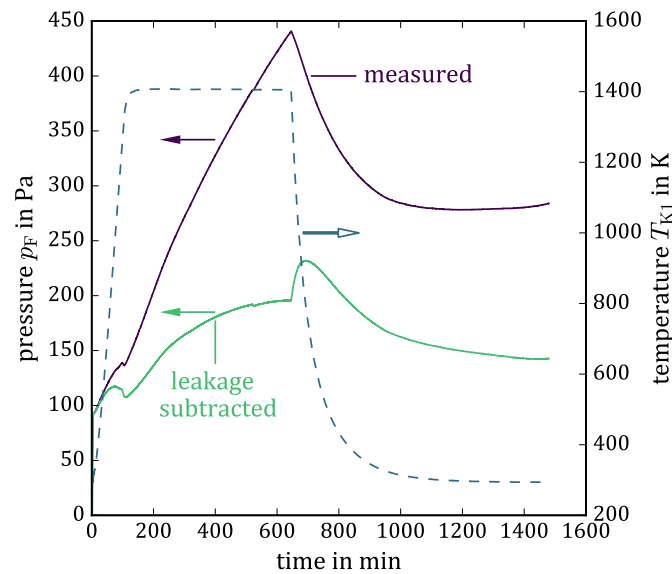


Figure 4.20.: Measured pressure curve and pressure curve after subtraction of calculated leakage for a reference measurement.

In conclusion, the results of this section show that no generally valid correlation between \bar{T} and T_{K1} could be found. The investigated model did not result in satisfactory results. The main reason appears to be the missing consideration of thermal inertia in the simple linear correlation. The thermal inertia might in reality also have an effect on the leakage, which has also been expressed in simplified form via a linear relationship with T_{K1} . The leakage in turn influences the determination of \bar{T} . These simplifications result in a poor prediction of \bar{T} and especially its transient behaviour by the model. Consequently, \bar{T} can only be estimated within the bounds $T_{\text{amb}} < \bar{T} < \bar{T}_{\text{max}}$. As mentioned above, \bar{T} does not exceed 466 K during experiments. This means, that \bar{T} lies in the range 295 K to 466 K. It therefore seems to be an acceptable approximation to perform the assessment of the experiments assuming a constant \bar{T} during an oxidation step, as given in Equation 3.78 and described in detail in Chapter 3.2.7. This assumption is used and its plausibility is discussed in the following section.

4.2.2. Oxidation Experiments

Oxidation rates of ceria under vacuum conditions are studied experimentally, to determine, whether the kinetics have a decisive impact on the recombination effect and whether the presence of an inert gas (N_2) is a suitable measure to counteract this effect. Oxidation experiments are performed in a dedicated test rig, developed in the framework of the present work, as described in Chapter 3.2. The experimental procedure is designed to mimic the processes that a reduced element of redox material undergoes on its way from the hot to the cold end of the HE.

Pressures and temperatures as measured are exemplified in Figure 4.21 for an experiment in which the ceria sample was a particle bed and no N_2 was added. Raw data for all experiments can

be found in Appendix A. Figure 4.21 incorporates the whole experimental procedure as described in Figures 3.11 and 3.12 and the start of the cooling phase after the experiment. Steep pressure

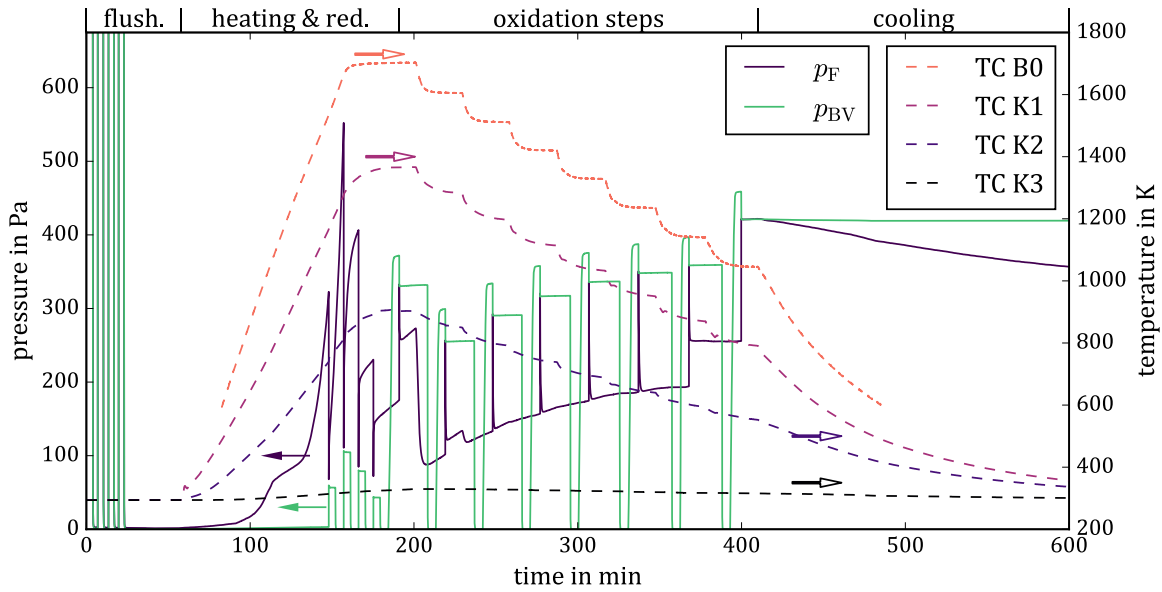


Figure 4.21.: Measured pressures and temperatures during an experiment with a particle bed without addition of N_2 .

fluctuations in the beginning are due to flushing the test rig with O_2 in preparation of the actual experiment as described by Figure 3.12(b). Afterwards, during the heating phase, the pressure in the furnace p_F rises, due to three effects: leakage, heating of the gas phase and reduction of ceria. The latter being dominant once sufficient temperatures are reached. The valve V1 between furnace and buffer volume is closed, which is why the pressure in the buffer volume p_{BV} is almost constant and only increases slightly due to leakage. Evolving O_2 is then removed from the furnace as described by Figure 3.12(c) via the buffer volume. This is the reason for pressure fluctuations in both compartments after approximately 150 minutes.

Subsequently, when the maximum temperature is reached, the actual oxidation experiment starts. The buffer volume is filled with O_2 until $p_{BV} - p_F$ reaches a certain value. In the example depicted in Figure 4.21 this pressure difference is 200 Pa. p_{BV} and p_F then rapidly converge as V1 is opened, leading to a pressure jump in the furnace of $\Delta p_{O_2} \approx 164$ Pa. p_{BV} then stays constant as V1 is closed shortly after being opened, while p_F rapidly falls, because oxygen is taken up by ceria and p_F approaches a new equilibrium. These oxidation steps are the main focus of this investigation and are assessed in detail below. The figure shows that in some oxidation steps, p_F drops to approximately the value it had before O_2 was added ($p_{F,0}$), while in other cases only part of the O_2 seems to be absorbed. The latter being the case for the first two and the last two steps in case of the experiment shown in Figure 4.21. This is highlighted exemplarily in Figure 4.22 for the second and third oxidation step of the same experiment.

After each oxidation at a constant set temperature of the furnace T_{set} , the furnace is cooled down and T_{set} is 100 K lower than in the previous step. While the ceria sample cools down,

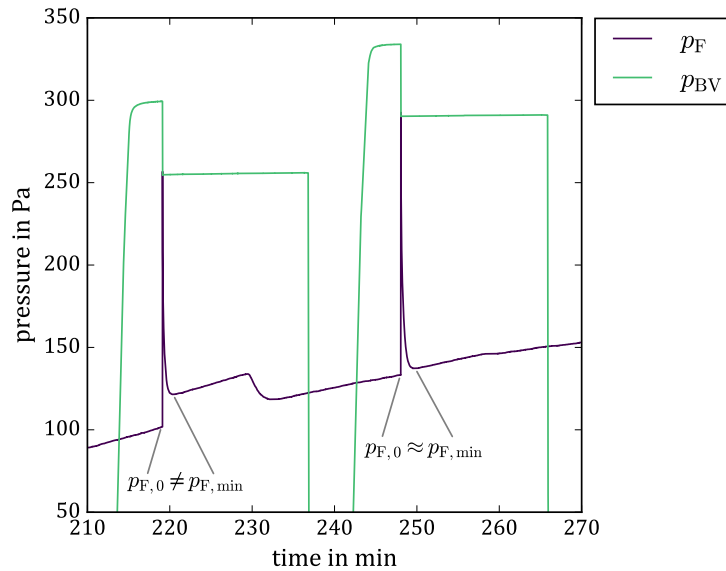


Figure 4.22.: Measured pressures during an experiment with a particle bed without addition of N_2 . The figure shows a magnified representation of the second and third oxidation step of Figure 4.21.

excess O_2 still present in the gas phase is now taken up by the sample. In case of Figure 4.21 this effect is most pronounced after the first two oxidation steps. As mentioned earlier, in these two steps not all of the available O_2 was absorbed, so that more O_2 can be taken up during the cooling phase. In other oxidation steps, virtually all of the available O_2 was removed from the gas phase as the sample was oxidised. Consequently almost no O_2 remains to be taken up during the cooling phase. Only in the cooling phase after the first oxidation step, p_F drops to a value lower than prior to the addition of O_2 . This indicates that also O_2 from the initial reduction of ceria, is absorbed. After the following oxidation steps, p_F seems to settle at a base line, which increases over time. The fact that here during the cooling phase p_F does not drop below the level it had before the oxidation, implies that virtually no O_2 is left in the furnace and the pressure level of the base line is due to N_2 that has entered the system, in form of air leaking into the test rig. As mentioned above, the oxygen uptake during the two last steps is incomplete. In contrast to the two first steps, here the remaining O_2 is not absorbed during the cooling phase, which suggests that the material is almost fully oxidized, i.e. $\delta \approx 0$. This hypothesis is backed by the results presented in Figure 4.23. Here, Different amounts of O_2 are fed to the furnace, by setting different pressure difference between buffer volume and furnace. Hence, the pressure in the furnace is increased by different values Δp_{O_2} . In the experiment with $\Delta p_{O_2} \approx 44.5$ Pa, the sample takes up O_2 even in the last oxidation step. Given the fact that in this experiment significantly less O_2 is fed to the furnace it is likely that the sample is not fully oxidized due to oxygen shortage. In the experiment with $\Delta p_{O_2} \approx 245$ Pa on the other hand, the sample seems to be completely oxidized during the fourth oxidation step, as no significant pressure drop is observed in the following steps. Note that in the last step, a smaller amount of O_2 was fed to the furnace ($\Delta p_{O_2} \approx 142$ Pa instead of 245 Pa) as otherwise the pressure would have exceeded the measuring range of the pressure

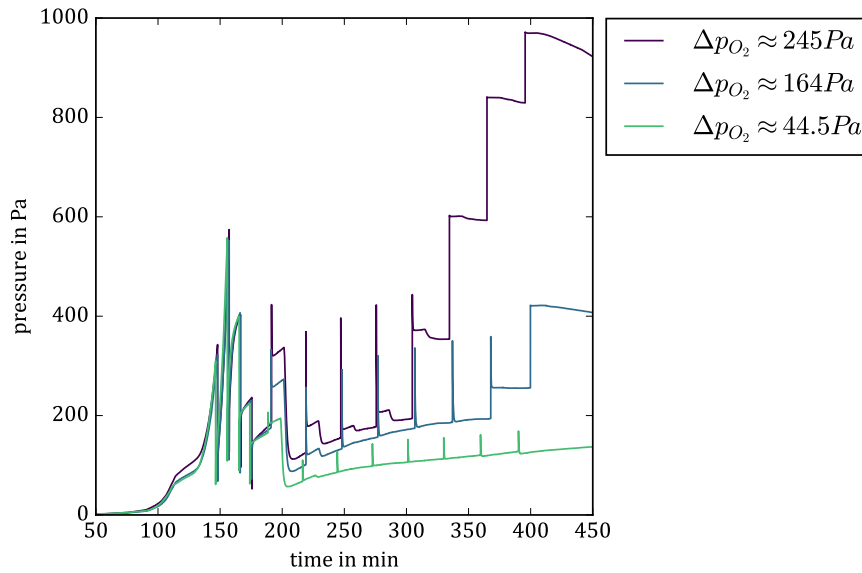


Figure 4.23.: Pressure curves p_F for three different experiments. Different amounts of O_2 are fed to the furnace, resulting in different pressure jumps Δp_{O_2} .

sensor. In this experiment, it is also evident that during all oxidation steps, the oxidation is not complete, as excess O_2 is absorbed by the sample during each cooling step.

In conclusion, the pressure curves in Figure 4.23 imply that $\Delta p_{O_2} \approx 164 \text{ Pa}$ is suited to virtually fully oxidise the material over the course of seven or eight oxidation steps. This value is therefore used for further investigations discussed in the following.

Figure 4.24 shows results for different sample types for experiments with $\Delta p_{O_2} \approx 164 \text{ Pa}$. As described in Section 3.2.4, both particle beds with an approximate specific surface of $109 \text{ m}^2 \text{ kg}^{-1}$ and RPCs with an approximate specific surface of $863 \text{ m}^2 \text{ kg}^{-1}$ were used. The different topography of the two sample sized is illustrated by SEM images given in Figure 4.25. Smaller grain sizes on the RPC surface shown in Figure 4.25(b) compared to the surface of a particle, shown in Figure 4.25(d) might explain the higher BET surface of RPCs. Besides minor fluctuations and a slightly different dynamic in the initial reduction step, the two sample types do not differ significantly. During all oxidation steps, the pressure curves shown in Figure 4.24 are in good agreement. Only one outlier, an experiment with particles (dotted line in Figure 4.24), shows somewhat different pressure values: After the reduction, the pressure level is lower than in the other experiments. Throughout the oxidation steps, the pressure is then a bit higher and the sample takes up more oxygen during the two last oxidation steps. Said experiment was the second overall experiment conducted in this study. It was only recognized after this experiment that a re-oxidation of the sample after an experiment as described in Section 3.2.5 might be necessary. Such a re-oxidation procedure was then introduced for the following experiments. Incomplete oxidation prior to the mentioned experiment would explain the lower pressure after the reduction, as the material was already partially reduced and therefore released less O_2 and it would also explain why more O_2 was absorbed by the material in the end of the experiment. More experiments were conducted

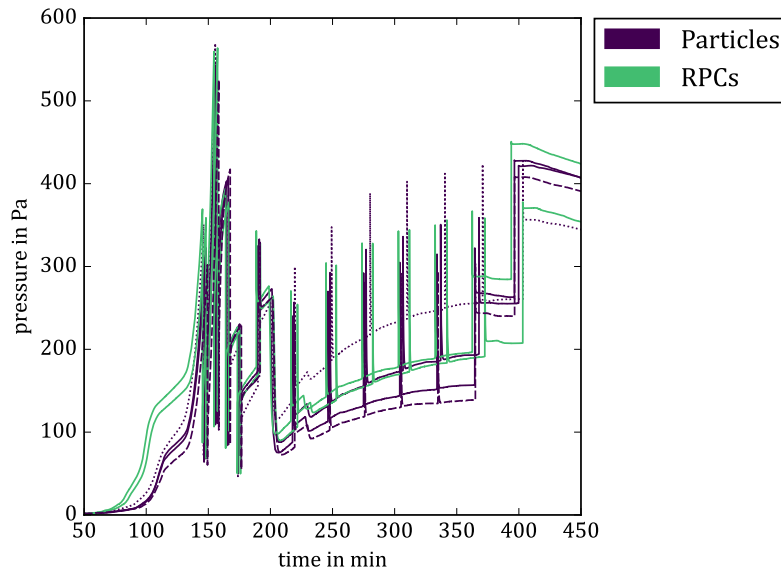


Figure 4.24.: Pressure curves p_F for experiments with different samples. In all cases $\Delta p_{O_2} \approx 164$ Pa. Dashed line: Experiment with second particle sample (particle bed 2 in table 3.2). All other experiments with particles use the same sample (particle bed 1 in table 3.2). Dotted line: Outlier as discussed in text.

with the same particle bed. Therefore, it should be verified that the differing pressure curve is indeed due to the lack of re-oxidation and not due to contaminations of the sample or microscopic changes or changes in the crystal structure that might occur after several experiments. To this end, the experiment was repeated with the same parameter set and a new particle bed, which this time was oxidized prior to the experiment (dashed line in Figure 4.24). This experiment was in good agreement with other experiments that used the first particle bed, as can be seen in Figure 4.24, which implies that the repeated use of the particle bed did not affect the performance of the sample. In addition, SEM images of particles before, after one and after eight experiments were recorded and EDX and XRD measurements with the same samples were performed. SEM images show no significant difference in the microscopic appearance of the particles, as can be seen in Figure 4.26. More SEM images are shown in Appendix F. XRD reveals no phase change due to repeated experiments. The diffractograms depicted in Figure 4.27 show good agreement between all three samples and reference data for CeO_2 . Results of EDX support the XRD results: For several spectra of all samples the atomic composition is virtually entirely made up of Ce and O. Results are depicted in Appendix G. The Spectra also show peaks of Pt and C, which can be explained by the fact that samples were coated in Pt and fixed with a carbon-tape in preparation of the analysis. Minor Al peaks in some of the results (typically less than 1 %) might be due to abrasion from alumina components such as the crucible or might simply be errors in the measurement. As shown in Appendix E, sintering of particles during experiments appears to be negligible, no significant weight change of the samples was observed after the experiments and the position of the sample was stable, as well.

Next, the influence of Δp_{N_2} is discussed. In experiments with different Δp_{N_2} , the same amount

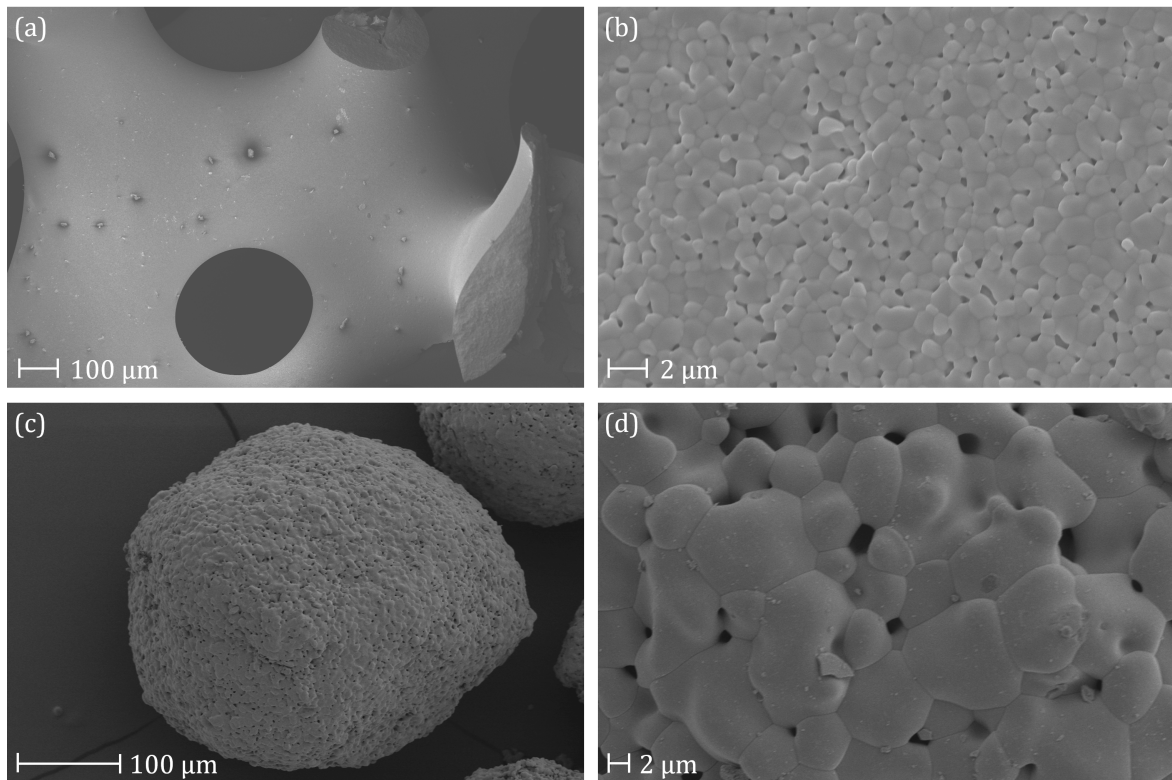


Figure 4.25.: SEM images of ceria samples before experiments. (a) and (b): RPCs; (c) and (d): particles.

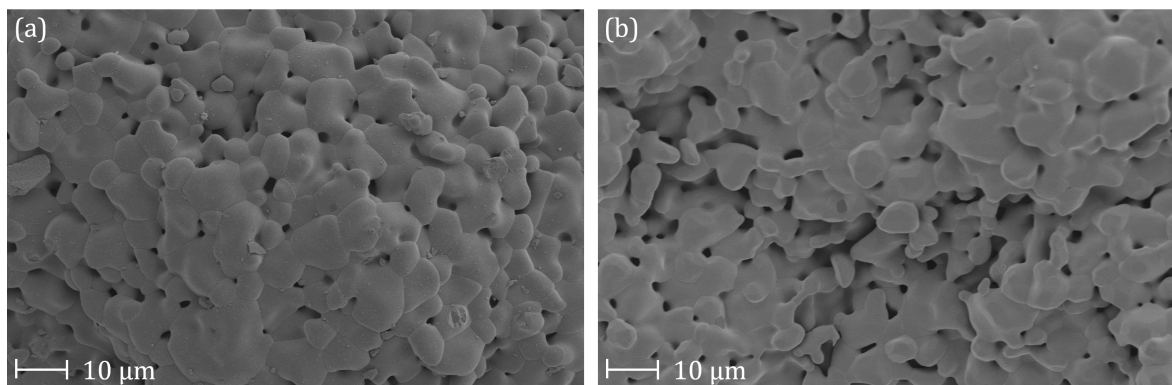


Figure 4.26.: SEM images of particles, (a) before and (b) after eight experiments.

of O_2 is fed to the furnace with $\Delta p_{O_2} \approx 164$ Pa. Consequently, the approximately same O_2 -partial pressure, but different N_2 -partial pressures are present in the different experiments. Results are depicted in Fig. 4.28. The pressure curves are almost identical during the reduction phase, which indicates good reproducibility of this step. The addition of N_2 after the reduction causes different pressure levels during the oxidation. The figure shows that for $\Delta p_{N_2} = 0$ a pressure drift exists as also seen in previously discussed results. For higher Δp_{N_2} there is almost no pressure drift. The general pressure level depends on the amount of substance and the temperature. Due to

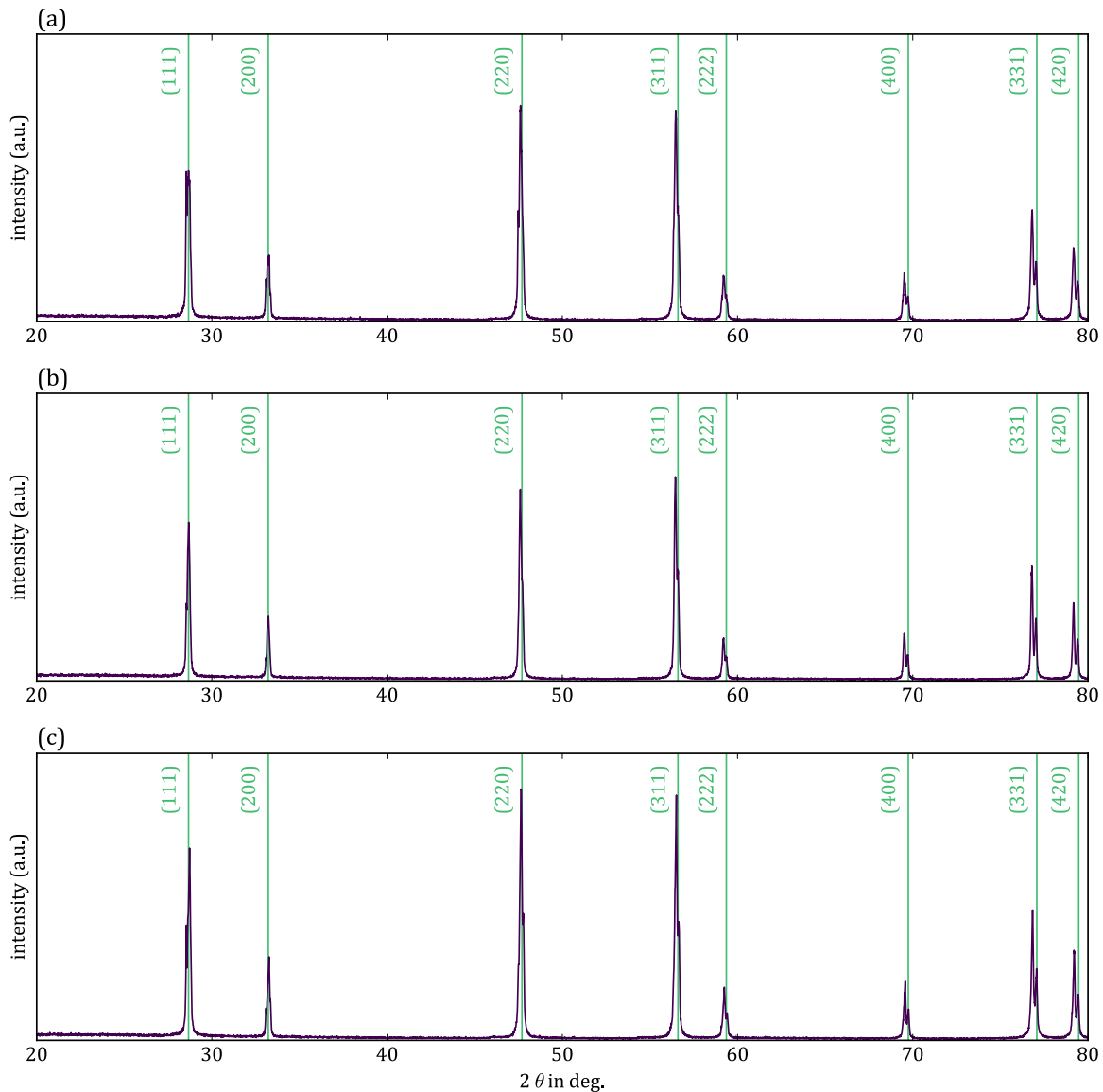


Figure 4.27.: Diffractograms of particles (a) as before experiments, (b) after one experiment and (c) after eight experiments. The 2θ range was 10° to 80° . Reference data for CeO_2 (PDF 75-0076).

leakage into the system, the amount of substance increases, which increases the pressure, while a falling gas temperature would decrease the pressure. According to the ideal gas law, the pressure change, caused by a temperature change scales linearly with the amount of substance. One explanation for the pressure drift not being present for higher Δp_{N_2} could therefore be the higher amount of substance in the gas phase, which leads to a higher pressure reduction due to falling temperatures, which offsets the pressure increase due to leakage. Another reason could be that for $\Delta p_{\text{N}_2} = 0$, the gas temperature does in fact increase over time. As discussed in Section 4.2.1, the gas phase seems to have a considerable thermal inertia. This means that during the initial heating of the test rig from room temperature to 1773 K, the gas temperature follows its steady-state-temperature with a certain delay. Afterwards, during the oxidation steps, the temperature

is decreased gradually. As the gas temperature catches up with its steady-state-temperature, it will decrease as well. Since heat conductivity and convective heat transfer between gas and reaction tube are lower at lower pressure levels, the point at which the gas temperature transitions from increasing to decreasing might be reached later in case of $\Delta p_{N_2} = 0$. Hence, in that case, the temperature might increase over time for significant parts of the experiment.

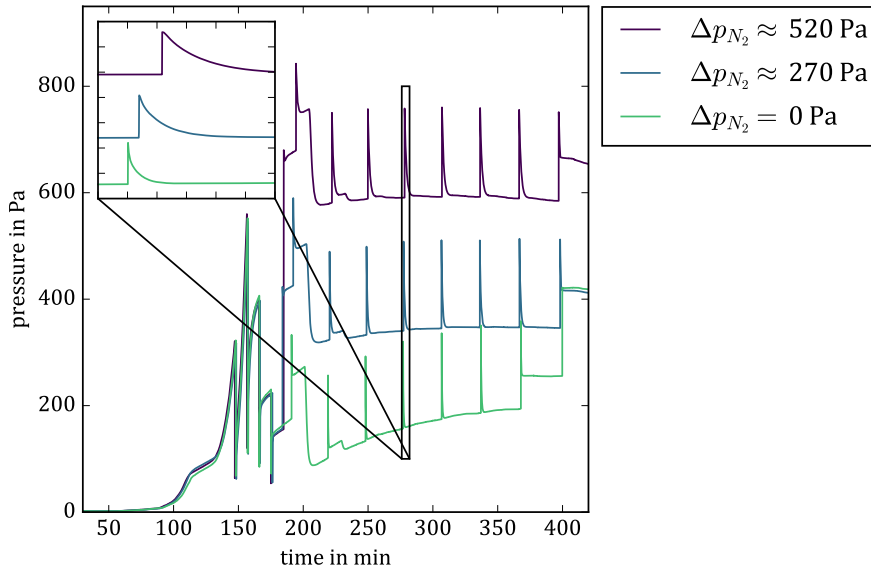


Figure 4.28.: Pressure curves p_F for three different experiments. Different amounts of N_2 are fed to the furnace, initially.

Figure 4.28 also shows that the oxygen uptake is slower, the higher Δp_{N_2} as indicated by a more shallow pressure drop after addition of O_2 . This suggests that the addition of N_2 in fact decelerates the oxygen uptake as hypothesised. This is further investigated using Δt_{25} , Δt_{50} and Δt_{100} as defined in Section 3.2.7. Figure 4.29 shows these three Δt_i as a function of T_{set} for different Δp_{N_2} . Each data point in Figure 4.29 corresponds to one oxidation step. The temperature axis is inverted to match the course of time, as T_{set} starts at 1773 K and then drops in increments of 100 K to the final value of 1073 K. Results for the different ceria samples, namely Particles and RPCs do again not differ significantly. Different values of Δp_{N_2} on the other hand have a substantial impact on Δt and a clear trend is evident: The more N_2 is added, the longer it takes for the sample to take up the O_2 . It can also be seen that at the beginning and the end of the experiment, O_2 is absorbed slower than in-between. This is most apparent for the very first and very last step, i.e at $T_{set} = 1773$ K and $T_{set} = 1073$ K as shown for Δt_{100} in Figure 4.29(c). A value for Δt_{25} and Δt_{50} doesn't even exist for these two oxidation steps. As discussed above, in the first and last oxidation step the sample absorbs less O_2 , and a remaining pressure difference, as defined in Section 3.2.7, of $\Delta p = 25$ Pa or $\Delta p = 50$ Pa is never reached. The trend of Δt with increasing Δp_{N_2} is given in Figure 4.30. The graphs show an almost linear dependence of Δt on Δp_{N_2} in the studied range. The fluctuation of Δt with different experiments and different oxidation steps is considered by error bars, showing the range from lowest to highest value. Note that

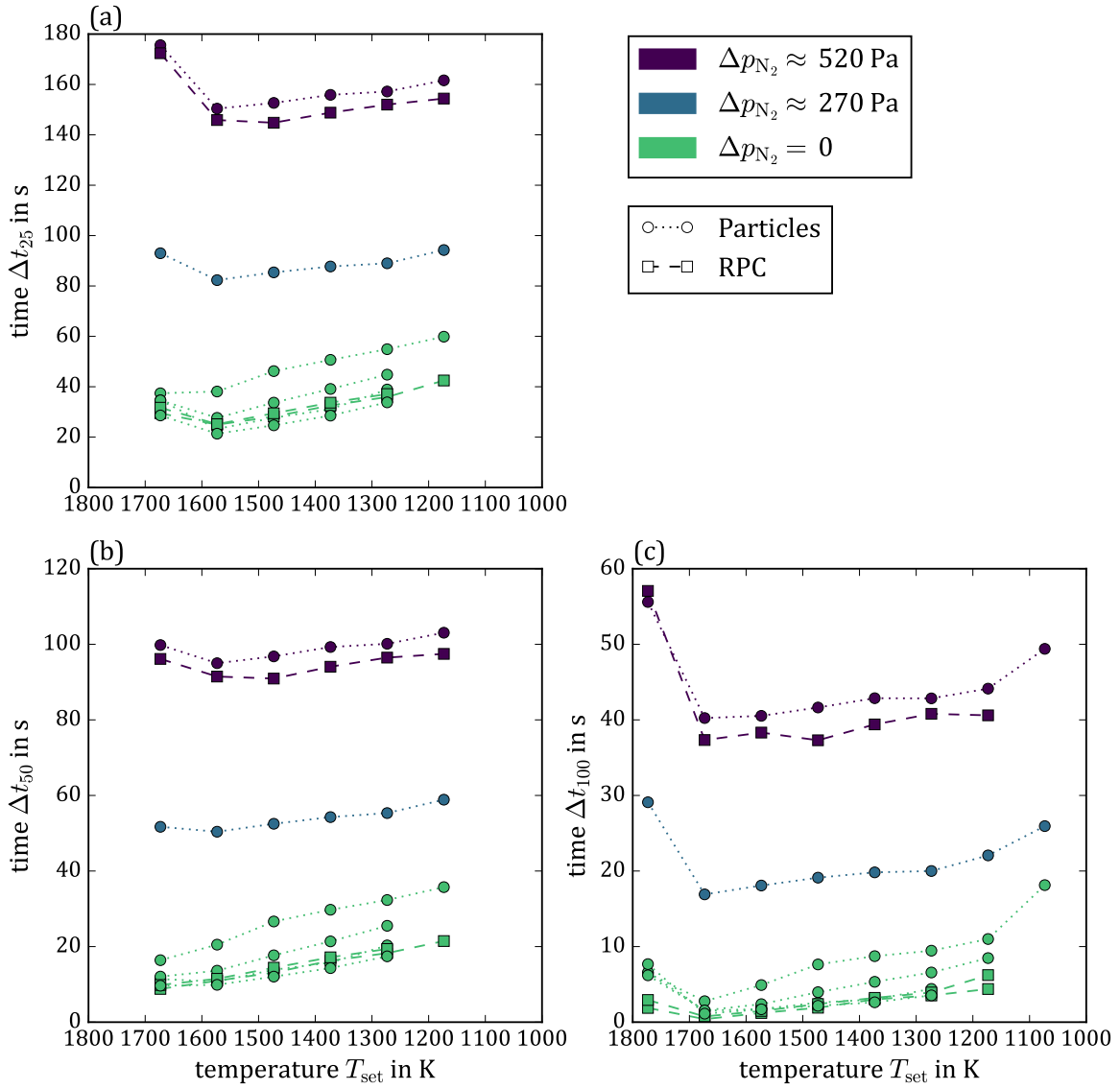


Figure 4.29.: Δt for different Δp_{N_2} as a function of T_{set} . Each data point corresponds to one oxidation step. (a) Δt_{25} , (b) Δt_{50} and (c) Δt_{100}

the actual partial pressure of N_2 is higher than Δp_{N_2} as additional N_2 from air enters the test rig via leakage.

The absorbed O_2 causes a change in oxygen non-stoichiometry $\Delta\delta$, which is proportional to the amount of substance taken up by the sample. This can in theory be calculated with the ideal gas law. As explained in Section 4.2.1, however, values of the average gas temperature \bar{T} cannot be stated reliably and thus an exact value for $\Delta\delta$ cannot be computed this way. Instead, a range within an upper and a lower limit of $\Delta\delta$ can be given using mole balances and a possible temperature range, as explained in detail in Section 3.2.7. In addition to this range, $\Delta\delta$ is calculated assuming a constant \bar{T} , which can then be calculated as well, using Equation 3.78. This assumption is checked for plausibility afterwards.

The calculation of $\Delta\delta$ is based on the pressure change in the furnace. To this end it is cru-

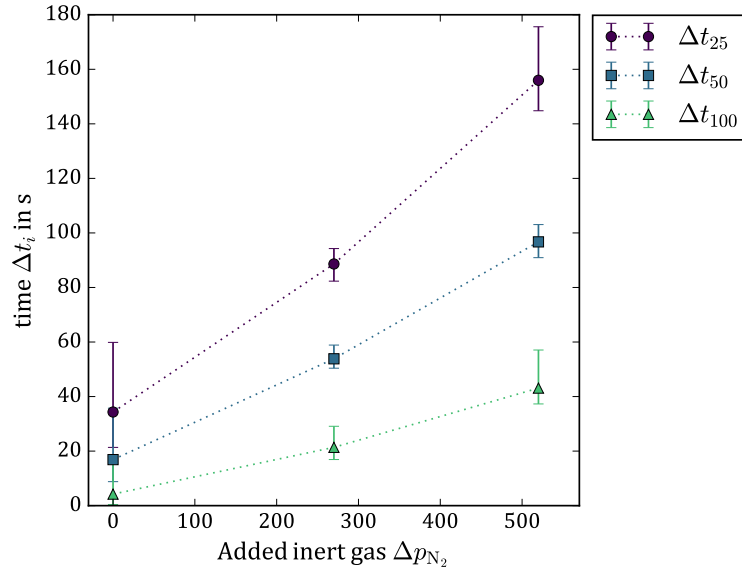


Figure 4.30.: Impact of amount of inert gas on the oxidation kinetics. Markers show mean values of Δt_i , obtained from all oxidation steps of all experiments with $\Delta p_{O_2} \approx 164$ Pa as a function of Δp_{N_2} . Error bars show the range from lowest to highest value of Δt_i .

cial to know the pressure difference $\Delta p_{O_2} = p_{F,1} - p_{F,0}$, where $p_{F,1}$ is the peak pressure after O_2 is fed into the furnace and $p_{F,0}$ is the pressure just before the introduction of O_2 . The pressure jumps from $p_{F,0}$ to $p_{F,1}$ in typically less than 1 s. Technical limitations allow a minimum time step of 400 ms at which signals from the sensors can be logged. This raises the question whether the time resolution is sufficient to reliably determine the peak pressure $p_{F,1}$. A too low time-resolution might lead to an underestimation of $p_{F,1}$. To examine if the measured peak pressures are representative for the actual peak pressures, the measurements are compared to computations with the numeric model described in Section 3.2.8. The model calculates the peak value $\hat{p}_{F,1}$ based on the measured $p_{F,0}$ and \bar{T} as input parameters. An exact value of \bar{T} is not known. Results are instead obtained for \bar{T} within the limits of the highest possible value \bar{T}_{\max} and the lowest possible value, which is room temperature. Figure 4.31 shows the ratio between the computed pressure increase $\hat{p}_{F,1} - p_{F,0}$ and the measured pressure increase $p_{F,1} - p_{F,0}$. Results are obtained for every oxidation step in all 12 experiments. Except for a few outliers, all calculated and measured pressure differences are in good agreement. For more than 91 % of all values the deviation between calculation and measurement is less than ± 4 %. As can be seen in the magnified section, error bars show the range of calculated values, according to $\bar{T} = \bar{T}_{\max}$ and $\bar{T} = 295$ K, while the marker highlights the mean value. The impact of \bar{T} is negligible as for all data points this range is below 0.1 %-pt.. As supported by the good agreement of predicted and measured pressures, $\Delta\delta$ is in the following calculated based on the measured pressure difference Δp_{O_2} .

$\Delta\delta$ -curves are given for two exemplary experiments with $\Delta p_{N_2} = 0$ and $\Delta p_{N_2} \approx 520$ Pa in Figure 4.32. The graphs show $\Delta\delta$ over time. Each curve corresponds to the uptake of oxygen during one oxidation step. By definition, $\Delta\delta < 0$ in an oxidation step, since δ decreases when ceria is

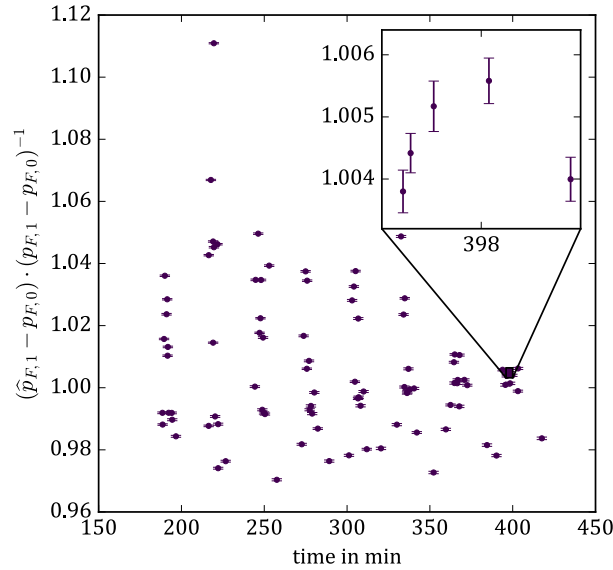


Figure 4.31.: Ratio of computed and measured pressure increase as O_2 enters the furnace, plotted against the corresponding time in the experiment. Error bars show the range from values computed with $\bar{T} = \bar{T}_{\max}$ to values computed with $\bar{T} = 295$ K. Markers highlight mean values.

oxidised. Therefore, lower values of $\Delta\delta$ correspond to larger amounts of O_2 being absorbed by the material. In many cases the steep decrease of $\Delta\delta$ is followed by an increase. This is due to a corresponding increase in the pressure, which is most likely caused by leakage. Therefore, there is no actual increase in $\Delta\delta$, but more likely $\Delta\delta$ establishes a near constant value after the steep decrease. Again, the graphs show that the oxidation is faster if no N_2 is added. For all cases depicted in Figure 4.32, $\Delta\delta$ calculated for a constant \bar{T} stays within the limits. Uncertainty is higher in the first and last oxidation step. As discussed before, in these steps, O_2 is not fully taken up by the sample, which means that residual O_2 remains in the furnace. In Figure 4.32, the lower limit for $\Delta\delta$ is in most cases given by the $\Delta\delta$ -value reached if all the O_2 was taken up by the sample. Therefore, the actual $\Delta\delta$ -value should be significantly higher than the lower limit in the first and last oxidation step. The result calculated for a constant \bar{T} is in line with this.

As mentioned before, \bar{T} can be calculated under the assumption that it is constant during one oxidation step. This can help to further investigate the plausibility of this assumption. Results for $\Delta p_{O_2} = 164$ Pa are given in Figure 4.33. For reference, the figure features \bar{T}_{\max} , where error bars show the range from lowest to highest value during an oxidation step. Only small fluctuations are however evident. Data points represent the calculated \bar{T} . As can be seen, for all oxidation steps in all experiments, $\bar{T} < \bar{T}_{\max}$ holds. In case of $\Delta p_{N_2} = 0$, the data is widely scattered, but for each individual experiment, typically a rising trend for \bar{T} is visible. This behaviour is also found for other values of Δp_{O_2} if $\Delta p_{N_2} = 0$, as shown in Figure 4.34 for $\Delta p_{O_2} \approx 44.5$ Pa and $\Delta p_{O_2} \approx 245$ Pa. Values for higher Δp_{N_2} in Figure 4.33 show a different progression. Here, \bar{T} slightly increases from the first to second oxidation step and then follows \bar{T}_{\max} at a roughly constant displacement. Herein, the curve for $\Delta p_{N_2} \approx 270$ Pa is similar to those for $\Delta p_{N_2} \approx$

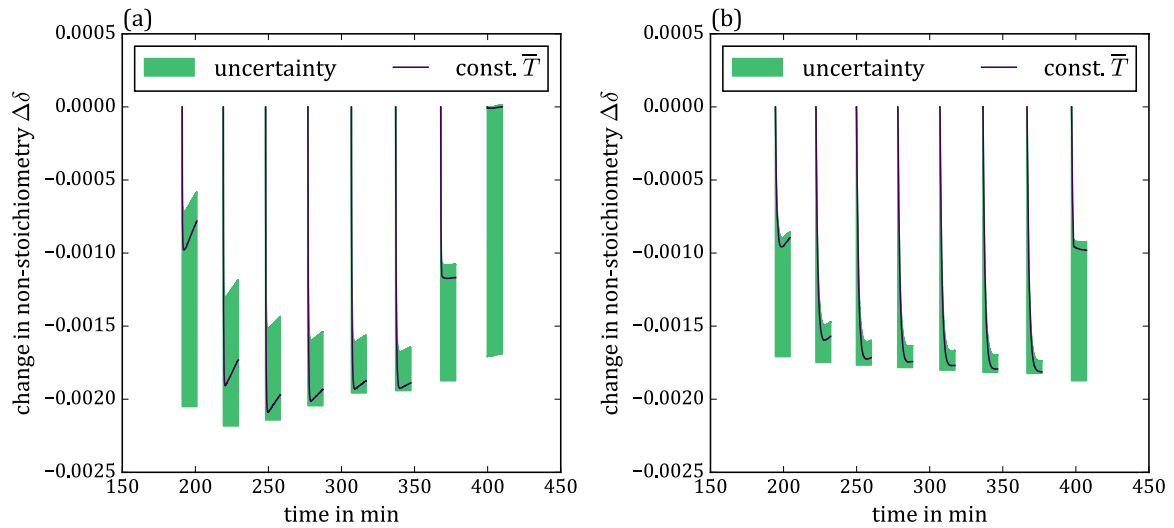


Figure 4.32.: $\Delta\delta$ during oxidation steps against time for $\Delta p_{O_2} \approx 164$ Pa and (a) $\Delta p_{N_2} = 0$ and (b) $\Delta p_{N_2} \approx 520$ Pa. Curves show $\Delta\delta$ calculated under the assumption of a constant gas temperature \bar{T} . The filled area shows the range within theoretically possible limits, based on mole balances and the possible temperature range.

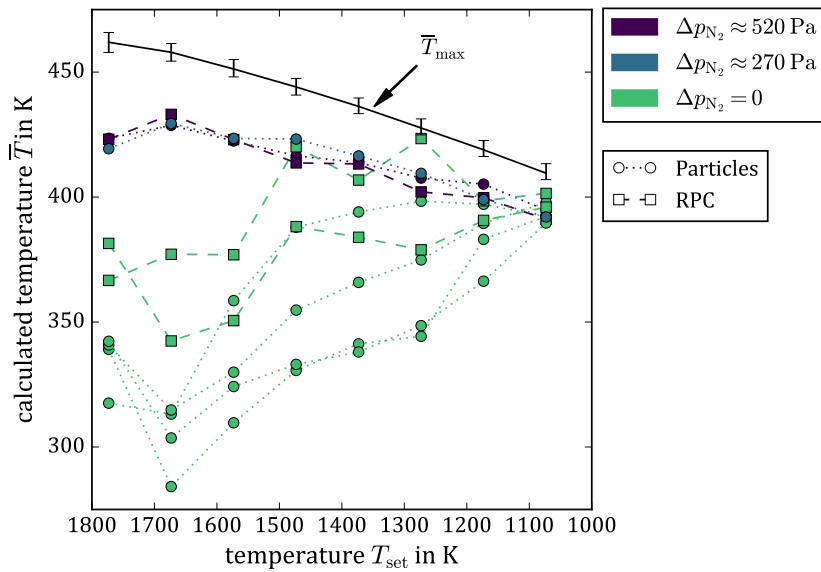


Figure 4.33.: \bar{T} for experiments with $\Delta p_{O_2} = 164$ Pa and different Δp_{N_2} .

520 Pa. These results support the aforementioned theory that in case of low pressure levels and therefore low amounts of substance in the gas phase, \bar{T} reacts slowly to external influences. For $\Delta p_{N_2} = 0$, \bar{T} approaches \bar{T}_{\max} only after four to eight oxidation steps which indicates that until then the gas phase was still heating up, as \bar{T} follows the furnace temperature with a great delay (remember that prior to the temperature levels shown in Figure 4.33, the furnace was heated from room temperature to 1773 K). For higher levels of Δp_{N_2} , the delay between gas and furnace temperature seems to last only until the second oxidation step. All in all, the assumption of a

constant \bar{T} yields plausible results and even though the results cannot be validated it seems justified to use this assumption for rough estimations. It is therefore used in the following to calculate a δ -rate.

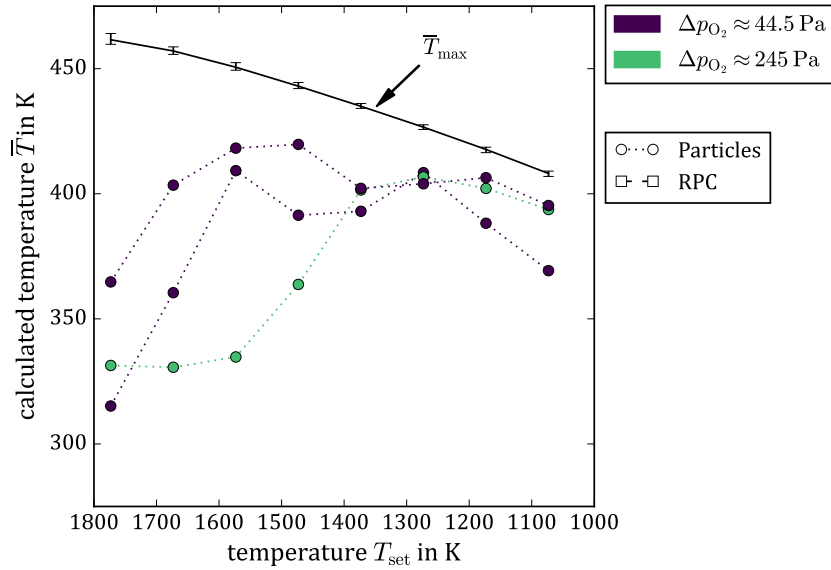


Figure 4.34.: \bar{T} for experiments with $\Delta p_{N_2} = 0$ and different Δp_{O_2} .

From $\Delta\delta(t)$, values for $\delta(t)$ and the δ -rate, i.e. its derivative with respect to time can be calculated, as shown in Figure 4.35. For three representative experiments with particle-samples, $\Delta p_{O_2} = 164$ Pa and different Δp_{N_2} , $\delta(t)$ is shown in Figure 4.35(a). One would expect that in the beginning, δ has the same value in all experiments, as the reduction is always performed in the same way. Similarly, δ is also expected to be the same at the very end of all experiments, due to the results shown above that imply full oxidation of the sample after all experiment with $\Delta p_{O_2} = 164$ Pa. Only the curves in-between should differ due to the different oxidation rates. In fact Figure 4.35(a) shows this expected behaviour. Especially the curves for $\Delta p_{N_2} \approx 520$ Pa and $\Delta p_{N_2} \approx 270$ Pa show good agreement with almost identical δ -values in the beginning and end and only slightly different dynamics during the oxidation steps. The curve for $\Delta p_{N_2} = 0$ Pa shows a stronger deviation with somewhat higher initial and final δ -values. Given the simplifications that were made to obtain δ , this deviation however seems to be within tolerable limits and plausible results are obtained.

The δ -rate for the same three experiments is depicted as function of the time in Figure 4.35(b). The figure shows values for every oxidation step. Building the derivative of δ amplifies the noise. A clear trend is however still visible. As expected from the $\Delta\delta$ -curves in Figure 4.32, the δ -rate starts with a highly negative value in every oxidation step and then converges to zero. The magnified area in Figure 4.35(b) reveals that by addition of N_2 , the initial δ -rate can be decreased by an order of magnitude. Note that the curves are slightly displaced in time with respect to each other. This is due to the manual operation of the test rig.

These results as well as results presented above show that at higher N_2 levels, the oxidation

of ceria with O_2 is significantly slower than it is at lower N_2 levels as was hypothesized in the beginning of the present study. N_2 in the atmosphere does not impact the partial pressure of O_2 , which is in good approximation the same for all experiments with the same Δp_{O_2} , i.e. experiments in which the same amount of O_2 is added for each oxidation step. As discussed in Section 2.3.2, p_{O_2} is the measure of concentration relevant for the intrinsic reaction kinetics. Therefore, addition of N_2 should not impact the surface reaction. The presence of N_2 in the gas phase also has no direct influence on the bulk diffusion of oxygen inside the redox material. This implies that the effect of higher N_2 contents is due to mitigation of mass transport of O_2 in the gas phase. Combined with the observation that the oxidation is slower, the higher the N_2 content is, this suggests that the net oxidation rate is limited by the mass transport in the gas phase. This is supported by the previously presented results, which show that the choice of the ceria sample, namely a particle bed or an RPC has no significant impact on the kinetics. This is the case even though at $863 \text{ m}^2 \text{ kg}^{-1}$ the BET surface area of RPCs is significantly larger than that of the particle bed at $109 \text{ m}^2 \text{ kg}^{-1}$. As mentioned in Section 3.2.4, due to small RPC samples for the BET measurements, these numbers are only an estimate. The fact that the different samples yield such similar results also indicates that bulk diffusion might not be the limiting step with respect to the net oxidation rate. This again supports the theory that the limiting factor is mass transport in the gas phase, which is also backed up by the results shown in Figure 4.35(c). Following an approach from Ref. [49], the expression on the ordinate is based on Equation 2.18, which describes the kinetics of reduction and oxidation of ceria, neglecting the term for the reduction in that equation. The O_2 partial pressure during the experiments is estimated as explained in Chapter 3.2.7. The expression in Figure 4.35(c) should yield a straight line when plotted against T_{B0}^{-1} , if the surface reaction is the rate limiting mechanism. Here, it is assumed that the sample has the same temperature as measured by the TC B0. Figure 4.35(c) shows the results for all oxidation steps in all experiments with $\Delta p_{O_2} = 164 \text{ Pa}$. Values almost form distinct vertical lines because each oxidation step is performed at a fixed set temperature of the furnace so that data is only available for these temperatures. Over the given range of T_{B0}^{-1} , the data shows no clear trend, but instead has a wide distribution of values on the ordinate. Rather than following a trend with T_{B0}^{-1} , values change significantly during each oxidation step and for all oxidation steps values are in a similar range. The fact that the data is not arranged in a straight line means that the measured kinetics does not follow the oxidation rate term in Equation 2.18. This is in agreement with the theory that the rate determining step is the mass transport in the gas phase. However, the deviation from a straight line could also mean that neglecting the reduction term in Equation 2.18 is a too strong simplification. Especially at high temperatures and towards the end of an oxidation step this might be the case. As discussed above, the experimental results indicate that neither bulk diffusion in the solid nor the surface reaction, but rather mass transport in the gas phase limits the net rate of oxygen uptake by the redox material. In the investigated pressure range, application of an inert gas like N_2 was shown to be an effective measure to reduce this net rate.

In Figure 4.35(d), the δ -rate is shown as a function of the actual oxygen partial pressure p_{O_2} minus the oxygen partial pressure just before a reduction step $p_{O_2,0}$. Before an oxidation step, the

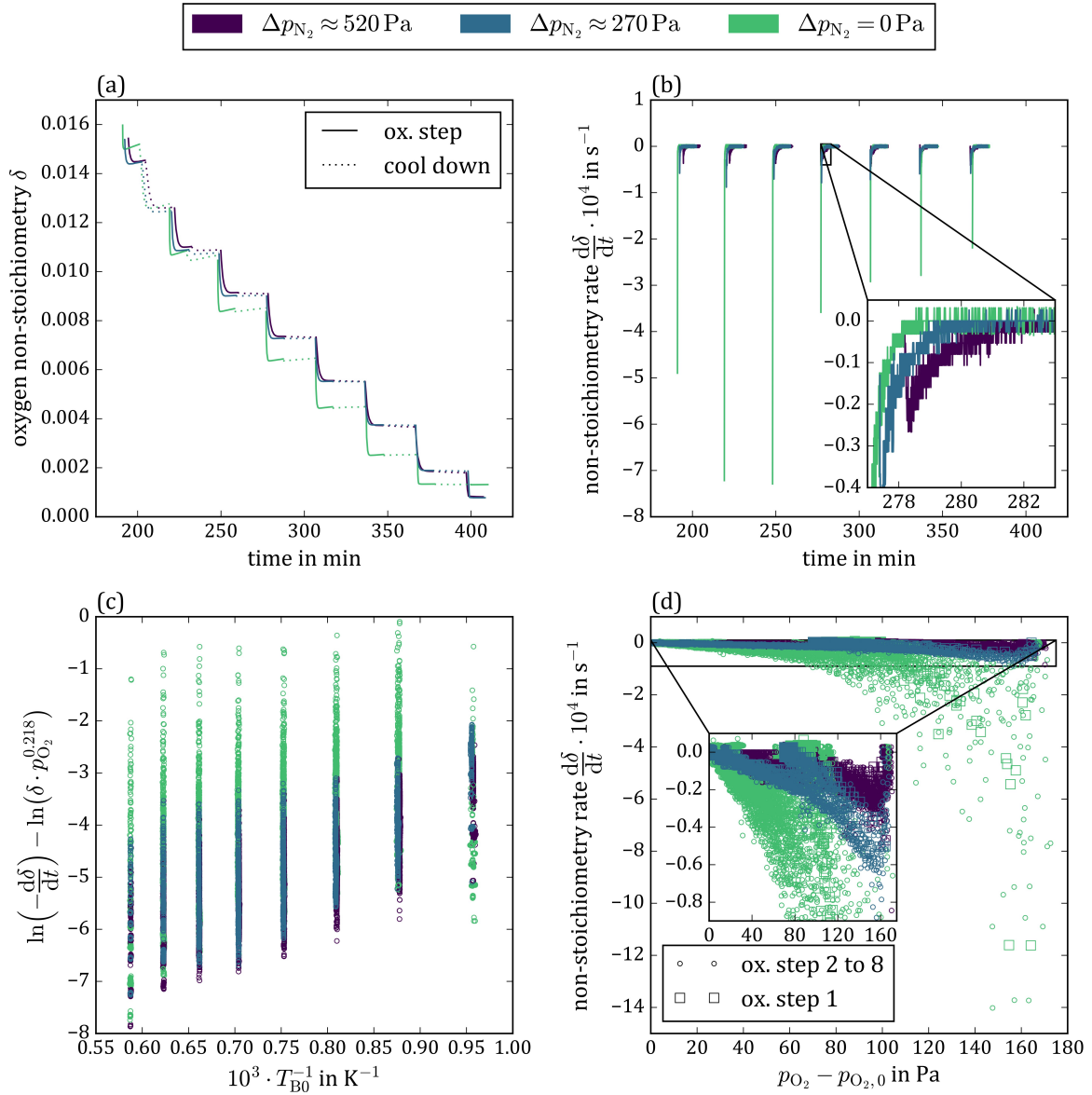


Figure 4.35.: Depiction of the oxidation kinetics for different Δp_{N_2} . (a): $\delta(t)$ over time for three representative experiments with particle-samples at $\Delta p_{O_2} = 164$ Pa; (b): δ -rate for the same experiments as in (a), depicted as function of the time; (c): logarithm of the oxidation kinetics based on Equation 2.18 for all experiments with $\Delta p_{O_2} = 164$ Pa; (d): δ -rate as a function of $p_{O_2} - p_{O_2,0}$ for all experiments with $\Delta p_{O_2} = 164$ Pa.

sample and the surrounding atmosphere are in an equilibrium that has been established after the previous oxidation step or in case of the first oxidation step, after the initial reduction. $p_{O_2,0}$ is therefore the equilibrium partial pressure of O_2 before O_2 is fed to the furnace. As discussed in the context of Figure 4.21, after an oxidation step and the following cooling phase, virtually all O_2 seems to be taken up by the redox material. Hence, $p_{O_2,0} \approx 0$ for all oxidation steps, but the first. In the first oxidation step, p_{O_2} is higher than in the other steps and $p_{O_2,0} > 0$, because of residual

O_2 of the initial reduction. Even though, the graph shows a wide distribution of values, a coarse trend is visible. Results for the first oxidation step are in line with those of all other oxidation steps if plotted against $p_{O_2} - p_{O_2,0}$. The fact that the δ -range depends on $p_{O_2} - p_{O_2,0}$ rather than p_{O_2} supports the assumption that the net oxidation rate is not determined by the surface reaction. In the first oxidation step, the higher p_{O_2} should result in a faster oxidation if limited by the surface reaction. This is not the case. Also δ and T_{B0} are highest during the first step, which should yield higher reaction rates if the surface reaction was the rate determining step. In contrast to Figure 4.35(b), Figure 4.35(d) contains data for all experiments with $\Delta p_{O_2} = 164$ Pa. Again, it becomes clear that addition of N_2 decreases the δ -rate by an order of magnitude, for some extreme values even by two orders of magnitude.

4.3. Kinetic Effect in Process Simulation

To this point, the recombination effect was simulated based on equilibrium assumptions (Section 4.1), whereas the re-oxidation kinetics were studied experimentally (Section 4.2). The next step is to consider oxidation kinetics in simulations of the recombination effect for a deeper understanding of its impact on the system efficiency.

Simulations presented in Section 4.1 yield that at high heat recovery ratios ϵ , re-oxidation of ceria in the HE diminishes the system efficiency η_{sys} to the point where the system is less efficient than a system without solid-solid heat recovery. These simulations are based on the assumption of an infinitely fast oxidation of the redox material, meaning that the material is oxidised to the equilibrium state. This raises the question whether the finite reaction rate of a real system mitigates this efficiency penalty, so that high ϵ and high η_{sys} can be achieved. Experimental results presented in Section 4.2 give insights into the kinetics of oxidation in a transient manner. The present section shows simulation results of a continuously operated system including a simple kinetic approach. These results are then discussed in the context of the experimental results.

The kinetic model is based on the previously presented equilibrium model, given in Chapter 3.1. Only setup 1 is used, because the results of Section 4.1 show a poor performance of setup 2. The equilibrium conditions for the hot ceria stream is replaced by a given mean reaction rate and a correlation between ϵ and residence time as explained in detail in Chapter 3.1.4. For the residence time, data was extracted from Ref. [41]. Due to losses to the ambience, the maximum heat recovery ratio found in Ref. [41] was approximately 0.7. To match this circumstance, the kinetic model of the present work is executed with $f_{loss} = 0.3$ and $\epsilon \leq 0.7$. The results in Ref. [41] were obtained for $T_{red} = 1800$ K and $T_{ox} = 1000$ K, resulting in a temperature gap of 800 K. For the results shown in the following, $T_{red} = 1773$ K and $T_{ox} = 1073$ K are chosen, for better comparability with the experimental results, which are obtained in that temperature range. Due to the lower temperature gap of 700 K, the residence time from Ref. [41] seems to be a pessimistic approximation.

Results of kinetic simulations for H_2O splitting are given in Figure 4.36. Here, the parameters of Table 4.1 are used, except $f_{loss} = 0.3$. Figure 4.36(a) shows η_{sys} as a function of ϵ for differ-

ent reaction rates. Negative reaction rates denote an oxidation of the material. These oxidation rates refer to the hot ceria stream, which enters the HE from the reduction reactor. As constant, negative reaction rates are used, reversed recombination is not included in this simulation. As a reference, the results obtained from the equilibrium model at the same parameter set are shown. These correspond to infinite reaction rates. The limiting case for a reaction rate of zero is represented by the reference case of a HE without recombination. Figure 4.36(a) shows that for low values of ϵ , the finite oxidation rates result in a lower η_{sys} than the equilibrium case. This is due to the fact that reversed recombination is considered in the equilibrium model, but not in the kinetic model. Finite reaction rates would indeed reduce the oxygen crossover in both directions and hence also mitigate reversed recombination. However, a slower reaction will probably not fully suppress the effect of reversed recombination and negative reaction rates might not be a realistic assumption for low ϵ . That being said, results for higher ϵ are still a reasonable estimation. This is supported by the results shown in Figure 4.36(b). Since in the presented model, the oxidation is kinetically limited, while the reduction is still infinitely fast, one would expect higher $p_{\text{O}_2, \text{HE}}$ in the kinetically limited case compared to the equilibrium case. This is in fact the case for large values of ϵ , but not for low values.

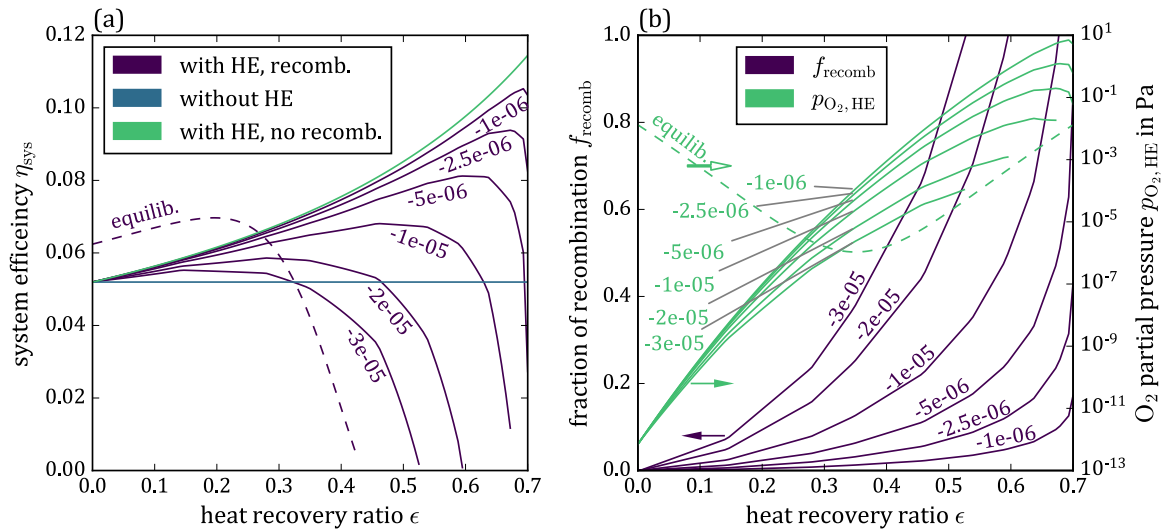


Figure 4.36.: Results of kinetic simulations for H₂O splitting with setup 1. In (a) η_{sys} is shown for different oxidation rates. As a reference, the results of the equilibrium model are included. In (b) f_{recomb} and $p_{\text{O}_2, \text{HE}}$ are shown. For both figures, $f_{\text{loss}} = 0.3$ all other parameters as in Table 4.1. Curves are labelled with the respective value of the average oxidation rate in the HE in s^{-1} .

For low ϵ , the system efficiencies calculated for different oxidation rates are close to that of the reference case without recombination, as can be seen in Figure 4.36(a). The curves of the kinetic model then diverge from that reference case with increasing ϵ and finally drop to low values as they approach the maximum ϵ of 0.7. The slower the oxidation is, the closer is the curve of η_{sys} to the case without recombination. The decreasing efficiency close to $\epsilon = 0.7$ is

caused by the residence time in the HE. The residence time increases progressively with the heat recovery ratio. Achieving a high value of ϵ , therefore requires a drastically higher residence time compared to a low ϵ . At given oxidation rates, a higher residence time results in a larger degree of oxidation in the HE and hence in a higher fraction of recombination, as depicted in Figure 4.36(b). This also causes $p_{\text{O}_2, \text{HE}}$ to decrease close to $\epsilon = 0.7$. The O_2 partial pressure refers to the equilibrium conditions of the cold ceria stream as its reduction is assumed to be infinitely fast. This equilibrium is influenced by $p_{\text{O}_2, \text{HE}}$ and the temperature T_2 at which the cold stream leaves the HE to the reduction reactor. Increasing ϵ increases T_2 and thus δ_2 and f_{recomb} . Therefore, at higher ϵ , higher values of f_{recomb} can be reached even at higher $p_{\text{O}_2, \text{HE}}$. For this reason $p_{\text{O}_2, \text{HE}}$ rises with increasing ϵ over a wide range of the latter. However, as f_{recomb} increases more steeply close to $\epsilon = 0.7$, also lower $p_{\text{O}_2, \text{HE}}$ are needed to achieve the corresponding degree of reduction defined by δ_2 .

The system efficiency reaches zero, when the potential to split H_2O or CO_2 with the redox material is fully lost to recombination, i.e. when $f_{\text{recomb}} = 1$. For all oxidation rates, the second law is obeyed for almost all points of operation. Only $\epsilon \leq 0.02$ results in negative s_{irr} .

These results show that for oxidation rates in the order of $-1 \cdot 10^{-6} \text{ s}^{-1}$ the recombination can be mitigated to the point where the system can compete with a HE in which no recombination occurs. In this range, η_{sys} can roughly be doubled compared to a system without HE. At oxidation rates with a higher magnitude than $-1 \cdot 10^{-5} \text{ s}^{-1}$ only moderate efficiency improvements are possible. The maximum efficiency improvement compared to a redox cycle without HE is summarized for all investigated oxidation rates in Table 4.2.

Table 4.2.: Maximum ratio of system efficiency at a given oxidation rate and system efficiency without solid-solid heat exchanger. An infinite oxidation rate (equilibrium assumption) results in a higher efficiency than some of the finite oxidation rates, because reversed recombination is only considered in the equilibrium case (see Figure 4.36(a)).

$\frac{d\delta}{dt}$	$\max \left(\frac{\eta_{\text{sys}}}{\eta_{\text{sys, no HE}}} \right)$
0 (no recomb.)	2.20
$-1.0 \cdot 10^{-6} \text{ s}^{-1}$	2.03
$-2.5 \cdot 10^{-6} \text{ s}^{-1}$	1.81
$-5.0 \cdot 10^{-6} \text{ s}^{-1}$	1.56
$-1.0 \cdot 10^{-5} \text{ s}^{-1}$	1.31
$-2.0 \cdot 10^{-5} \text{ s}^{-1}$	1.13
$-3.0 \cdot 10^{-5} \text{ s}^{-1}$	1.06
$-\infty$ (equilib.)	1.34

The feasibility of oxidation rates in the range of $-1 \cdot 10^{-6} \text{ s}^{-1}$ to $-3 \cdot 10^{-5} \text{ s}^{-1}$ is discussed based on the experimental results presented in Section 4.2. Experiments and continuous process have distinct differences that do not allow the direct extraction of a value or function that describes the oxidation or reduction rate of ceria from the experiments and use it in the simulations. It is important to be aware of these differences, which are summarized in Table 4.3 to understand

the limitations of this comparison. In the experiments presented above, the oxidation takes place

Table 4.3.: Difference between modelled process and experiments.

Continuous process (model)	Experiments
When an element of redox material enters the HE from the reduction reactor, p_{O_2} is reduced, as $p_{O_2,red} > p_{O_2,HE}$	When O_2 is introduced, p_{O_2} is increased and then falls over time. $p_{O_2}(t) > p_{O_2,0}$
The temperature of the redox material that enters the HE from the reduction reactor is decreased in the HE, i.e. $T_{red} > T_4$	The furnace is set to a constant temperature during an oxidation step, i.e. $T_{set} = const..$
Reduction of one stream of redox material in the HE represents a continuous O_2 supply for the oxidation of the other stream.	Initial supply of a certain amount of O_2 , followed by transient oxidation of redox material.
Steady state between ceria streams and atmosphere is established, in which the average oxidation and reduction rates of the two material streams are equal and an according p_{O_2} is reached.	Initial amount of O_2 and initial p_{O_2} in an oxidation step are independent of the oxidation rate.

in a transient manner and thus the δ -rate depends on the reaction progress. Oxidation rates are higher in the beginning, when the system is further away from the equilibrium. As explained earlier, in the modelled process, a steady state is established, in which $\Delta\delta_{12} = -\Delta\delta_{34}$. If infinitely high reduction and oxidation rates are assumed, this steady state is defined by the equilibrium O_2 partial pressure $p_{O_2,HE}$. At finite reaction rates, the steady state also results in an associated $p_{O_2,HE}$, which however differs from the equilibrium O_2 partial pressure. High values of $p_{O_2,HE}$ mitigate the reduction. It is therefore expected that as the oxidation of the hot ceria stream is kinetically limited, the reduction of the cold stream raises the pressure until reduction and oxidation are balanced. If this stable point of operation is found at a very high $p_{O_2,HE}$, this might result in higher oxidation rates than those measured at low p_{O_2} in the experiments. It is therefore important to discuss $p_{O_2,HE}$ as well as the δ -rates.

Due to the transient oxidation during an experiment, it is not possible to give a single value for the oxidation rate suited for the simulations. However, the experimental results give a range of oxidation rates, which can be used to assess how realistic the average oxidation rates assumed in Figure 4.36 are. Figure 4.35 shows that for $\Delta p_{N_2} \approx 520$ Pa, the vast majority of measured δ -rates is found in the range 0 s^{-1} to $-3 \cdot 10^{-5} \text{ s}^{-1}$. The oxidation is fastest in the beginning, when the O_2 partial pressure is high. Here, $p_{O_2} \approx \Delta p_{O_2}$, except for the first oxidation step in an experiment. In case of the results given in Figure 4.35 that means that p_{O_2} typically starts at roughly 164 Pa and then drops to almost 0 Pa. Figure 4.36(b) shows that in the modelled redox cycle, $p_{O_2,HE}$ is in the range $7 \cdot 10^{-13}$ Pa to 7 Pa. Given this range, oxidation rates with a significantly lower magnitude than $-3 \cdot 10^{-5} \text{ s}^{-1}$ seem realistic. This is especially the case, when taking into account that the reduction of the cold ceria stream is modelled as infinitely fast, so that $p_{O_2,HE}$ should be

even lower when considering limited kinetics for both reactions. Thus, by adding 520 Pa of N₂ to the HE's atmosphere, it might be possible to increase the system efficiency by a factor of 1.5 to 2, according to Table 4.2. There is however no reason to limit the amount of N₂ to such a small value. It is for example possible to operate the HE at atmospheric pressure, where the atmosphere mainly consists of N₂. This is a strong indication that in a real system the recombination effect can be significantly mitigated by addition of an inert gas so that η_{sys} can indeed be increased considerably.

All in all, temperature, O₂ partial pressure and N₂ partial pressure ranges imply that slow oxidation at rates of $-5 \cdot 10^{-6} \text{ s}^{-1}$ or even slower, at which the recombination effect would be significantly reduced, might be possible. Given the differences listed in Table 4.3 this is to be seen as a first estimation. The partial pressures of O₂ in the modelled process and the low partial pressures of N₂ evaluated in experiments indicate that it is a conservative estimation.

4.4. Indirect Heat Recovery System

This section is in part based on the following patents and peer-reviewed publications, authored or co-authored by the author of the present work.

Stefan Brendelberger, Philipp Holzemer-Zerhusen, Estefania Vega Puga, Martin Roeb, and Christian Sattler. „Study of a new receiver-reactor cavity system with multiple mobile redox units for solar thermochemical water splitting“. In: *Solar Energy* 235 (2022), pp. 118–128. ISSN: 0038-092X. DOI: <https://doi.org/10.1016/j.solener.2022.02.013>

Stefan Brendelberger and Philipp Holzemer-Zerhusen. „Solarstrahlungsreceiver sowie Reaktorsystem mit Solarstrahlungsreceiver“. (German). German pat. DE102020118651B4. 2022

Stefan Brendelberger and Philipp Holzemer-Zerhusen. „Solarabsorbervorrichtung sowie Transportsystem für eine Solarabsorbervorrichtung“. (German). German pat. DE102020118683B4. 2022

The results presented so far show how the recombination effect might impact the efficiency of a redox cycle with a direct solid-solid heat exchanger and how this effect can be mitigated by means of kinetic limitations. Alternatively, an indirect HE concept, such as the simple design described in Chapter 3.3 can be used, meaning that a heat storage medium is used to transport the heat in two steps from the hot to the cold redox material. In this concept, the additional heat transfer step might render the heat recovery less effective compared to a direct approach. However, using an indirect concept, the recombination effect can theoretically be avoided as hot and cold redox material are not exposed to each other. In the following, the efficiency potential of such an indirect concept is analysed.

4.4.1. Reactor and Heat Exchanger Concept

A reactor and HE concept is developed that allows quasi-continuous operation of the redox cycle. Similar to the MBR2 concept that motivated this work, movable units of redox material (redox units) are used. These can be introduced into a receiver reactor as depicted in Figure 4.37(a), where they are thermally reduced. Figure 4.37(a) schematically shows the reduction principle for a single redox unit, while in reality it is presumably more practical to use several individually movable redox units. After the reduction, the redox units can be removed from the receiver

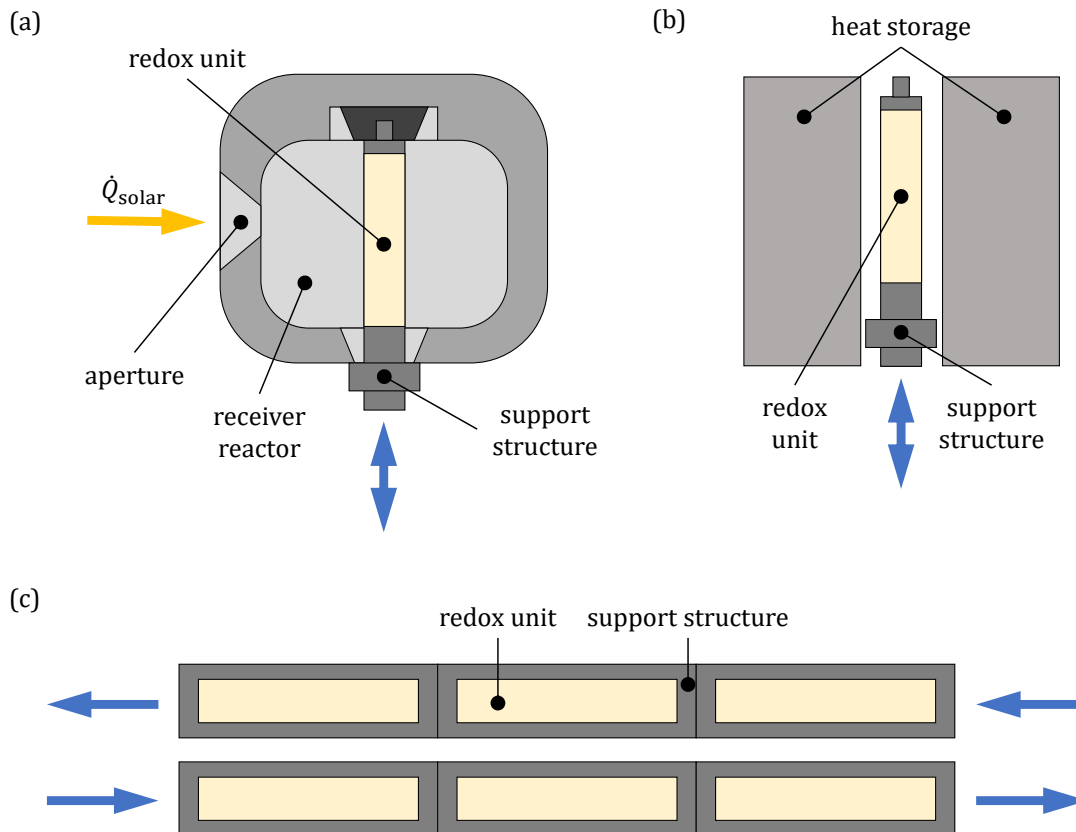


Figure 4.37.: Schematic of Reactor and heat exchanger concepts using movable redox units. (a): Receiver reactor with redox unit (based on Ref. [159]); (b): Indirect HE for redox units; (c): Direct HE for redox units (top view, based on Ref. [160]).

reactor and moved to an oxidation reactor. The reduction of a redox unit is transient as in a discontinuous reactor design. However, as multiple redox units can be introduced to or removed from the reactor individually, a quasi-continuous operation can be established. This reactor design also overcomes a critical disadvantage of current state-of-the-art discontinuous reactor designs, which is the need to alternately cool and heat the reactor between reduction and oxidation. As the receiver reactor is solely used for the reduction it can be permanently operated around the reduction temperature. Only the redox material and potential support structures have to be

heated instead of the whole reactor. This reduces the thermal mass that contributes to the heat demand for sensible heating drastically.

This reactor design can be combined with different HE concepts. A direct HE approach, in which the redox units are moved through the HE in countercurrent is depicted in Figure 4.37(c). In such a HE, the redox units would be subject to recombination. This approach corresponds to the investigations in Sections 4.1, 4.2 and 4.3. An indirect HE design is depicted in Figure 4.37(b). Here, a heat storage consisting of two walls surrounding the redox unit is utilized. In a first step, heat is transferred from a hot reduced redox unit to the heat storage, thus charging the latter. In a second step, the heat storage is discharged as a cold redox unit coming from the oxidation step is heated in preparation for its reduction. Due to the temporal separation of the two steps, the O_2 that might have been released from the redox material during the discharging step can be removed, e.g. via flushing with an inert gas or by vacuum pumps. This way, the hot reduced redox unit is not re-oxidised in the HE, so that recombination is avoided. This indirect approach is modelled as described in Chapter 3.3. Simulation results are presented and discussed in the following.

4.4.2. Simulation of Indirect Heat Recovery

The heat recovery ratio ϵ is calculated for different combinations of charging and discharging time. If not stated differently, $\alpha_{HS} = 10 \text{ W m}^{-2} \text{ K}^{-1}$ and $\epsilon_{RU} = \epsilon_{HS} = 0.5$ are used. Results for $d_{HS} = 6 d_{RU}$ are given in Figure 4.38. Using material properties of concrete for the heat storage medium, the peak heat recovery ratio is $\epsilon_{\max} = 0.210$ and it is found at $t_{\text{dis}} = 150 \text{ s}$ and $t_{\text{char}} = 150 \text{ s}$. Applying data for the insulation material yields $\epsilon_{\max} = 0.178$ at $t_{\text{dis}} = 540 \text{ s}$ and $t_{\text{char}} = 720 \text{ s}$. For both the charging and the discharging step, there is a trade-off with respect to the duration: Long charging and discharging times increase the total heat that can be transferred between redox unit and heat storage. On the other hand longer durations of the two steps also increase losses to the ambience. Due to the lower thermal conductivity of the insulation material, ϵ_{\max} is reached at higher t_{dis} and t_{char} compared to concrete. This effect is especially pronounced for t_{char} . Figure 4.39 shows the temperature profile of the heat storage and the redox unit at the beginning and the end of a discharging step and after one-tenth of t_{dis} for the combination of t_{char} and t_{dis} that yields ϵ_{\max} in Figure 4.38. The significantly longer charging time for material properties of the insulation material results in higher temperatures of the heat storage at the interfaces to the redox unit. At the same time, the temperatures at the interfaces to the ambience is lower. In consequence, as can be expected, the lower thermal conductivity yields a steeper temperature profile, highlighting the better insulating capabilities. However, this property also results in a mitigated heat transfer to the redox unit, which not only results in longer charging and discharging times, but also a lower final temperature level of the redox unit and thus lower heat recovery ratios, as depicted in Figure 4.38.

The aforementioned trade-off between desired heat transfer and heat losses with respect to the charging and discharging times is exemplified in the temperature profiles given in Figure

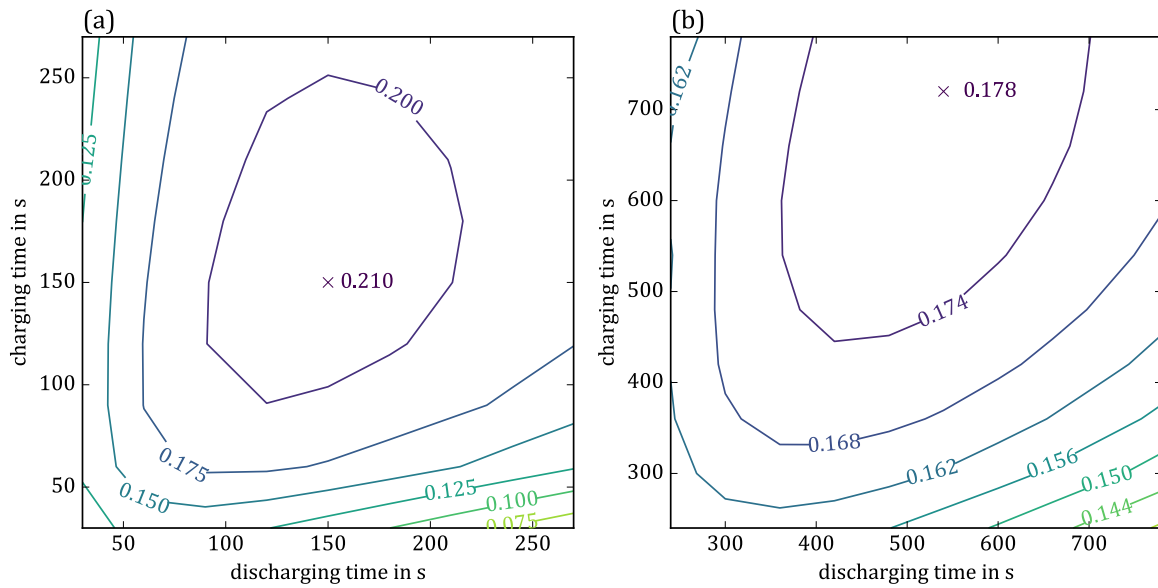


Figure 4.38.: Heat recovery ratio ϵ as a function of charging and discharging time for $d_{\text{HS}} = 6 d_{\text{RU}}$, $\alpha_{\text{HS}} = 10 \text{ W m}^{-2} \text{ K}^{-1}$ and $\epsilon_{\text{HS}} = \epsilon_{\text{RU}} = 0.5$ with data for ρ_{HS} , λ_{HS} and $\tilde{c}_{\text{p,HS}}$ from Table 3.7 for (a) concrete and (b) insulation material.

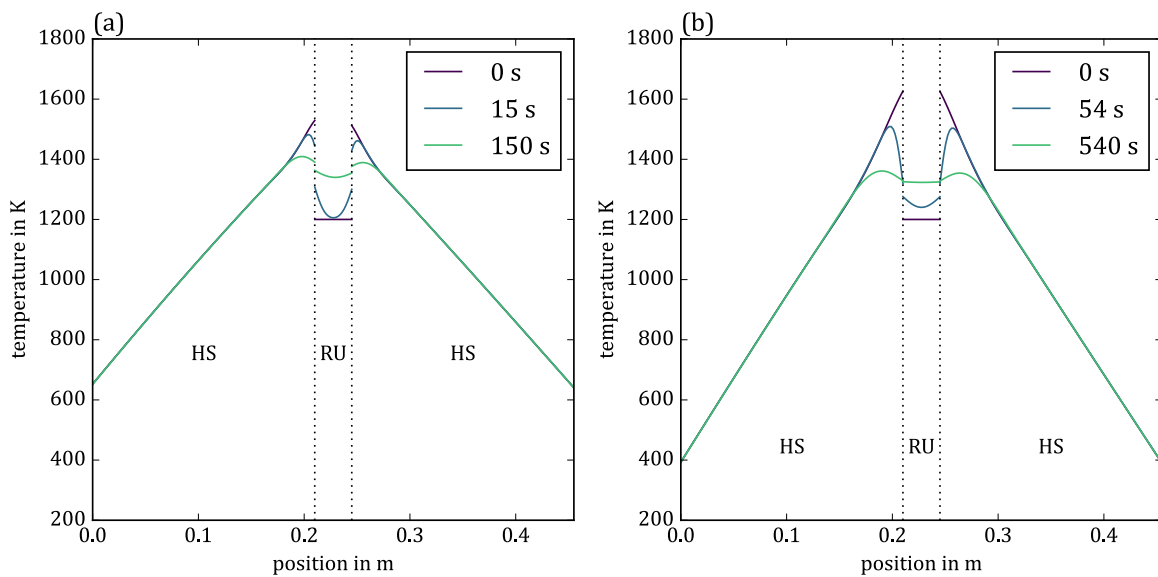


Figure 4.39.: Temperature profiles for different points in time as a function of the x -position for $d_{\text{HS}} = 6 d_{\text{RU}}$, $\alpha_{\text{HS}} = 10 \text{ W m}^{-2} \text{ K}^{-1}$ and $\epsilon_{\text{HS}} = \epsilon_{\text{RU}} = 0.5$ with data for ρ_{HS} , λ_{HS} and $\tilde{c}_{\text{p,HS}}$ from Table 3.7 for (a) concrete and (b) insulation material.

4.40. The case depicted in Figure 4.40(a) shows a disadvantageous combination of $t_{\text{char}} = 30 \text{ s}$ and $t_{\text{dis}} = 270 \text{ s}$. The long discharging time results in increased losses to the ambience and consequently a lower temperature level compared to the case shown in Figure 4.40(b). Due to the

short charging times, the heat storage is only heated in the thin layers close to the redox unit. Thus, during the discharging step, heat can only be recovered from a small fraction of the heat storage. As a result, the heat recovery ratio is low, which reflects in the low temperature level of the redox unit. In fact, the redox unit's temperature is first increased and then reduced to the point where it is lower than prior to the heat recovery process due to the long discharging time. In addition to increasing losses to the ambience, long charging and discharging times might have a negative impact on the overall process performance and/or investment costs. If the time that redox units spend inside the heat exchanger exceeds the time inside the reduction and/or oxidation reactor, the consequence might be downtime of the reactors, decreasing the total efficiency. This could be counteracted by increasing the number of redox units and heat exchangers, which could be operated in a staggered mode. This would however increase the investment costs of the overall plant.

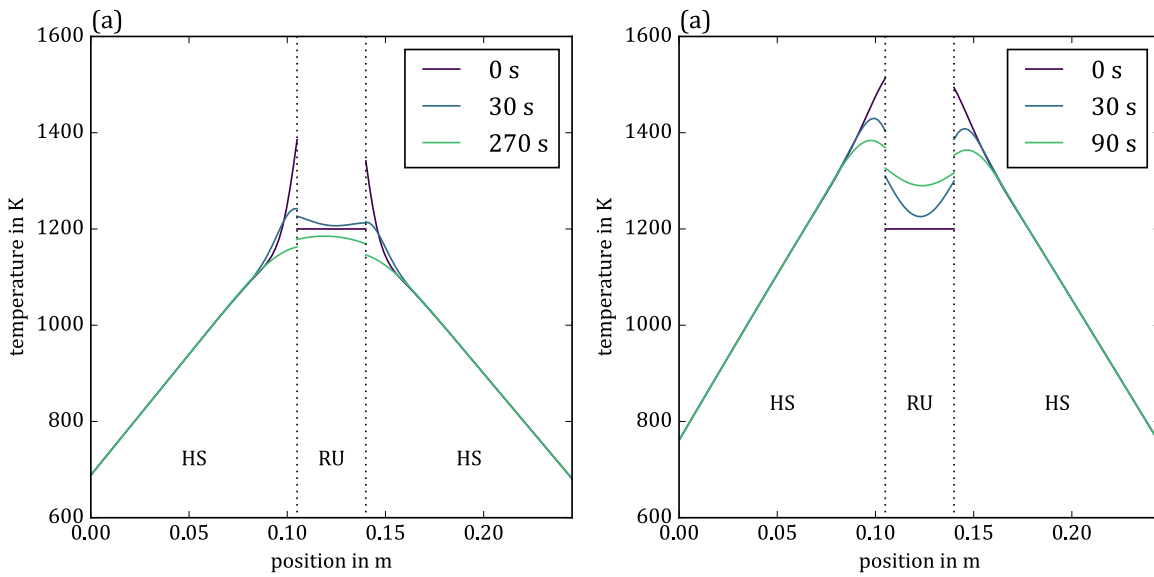


Figure 4.40.: Temperature profile of a charging step for $d_{\text{HS}} = 3 d_{\text{RU}}$, $\alpha_{\text{HS}} = 10 \text{ W m}^{-2} \text{ K}^{-1}$ and $\varepsilon_{\text{HS}} = \varepsilon_{\text{RU}} = 0.5$ with data for ρ_{HS} , λ_{HS} and $\tilde{c}_{\text{p,HS}}$ from Table 3.7 for concrete. (a): disadvantageous case with $t_{\text{char}} = 30 \text{ s}$ and $t_{\text{dis}} = 270 \text{ s}$; (b): best case with $t_{\text{char}} = 120 \text{ s}$ and $t_{\text{dis}} = 90 \text{ s}$.

In terms of process optimisation, an important quantity besides the already discussed material properties ρ_{HS} , λ_{HS} and $\tilde{c}_{\text{p,HS}}$ is the emissivity of the materials ε_{HS} and ε_{RU} . The default value used to this point is $\varepsilon_{\text{HS}} = \varepsilon_{\text{RU}} = 0.5$. Figures 4.41(a) and 4.41(b) show results for $\varepsilon_{\text{HS}} = \varepsilon_{\text{RU}} = 0.2$ and $\varepsilon_{\text{HS}} = \varepsilon_{\text{RU}} = 0.8$, respectively. Comparison to the aforementioned results in Figure 4.38(a) reveals that higher values of ε lead to higher heat recovery ratios and lower charging and discharging times. Consequently, higher emissivities increase the process efficiency due to improved heat recovery. At the same time, the shorter charging and discharging periods reduce investment costs and/or downtime of the reactors as explained above. Both the improved heat recovery and shorter charging and discharging durations can be explained by enhanced heat

transport between redox unit and heat storage. The disadvantage of amplified radiative losses at the outer wall surface is comparably low. The outer wall temperature is significantly lower than the inner temperature and the temperature of the redox unit. Since radiative heat transfer rates are proportional to T^4 , the advantage of improved heat transport between redox unit and heat storage therefore outweighs additional heat losses. In the present work, systems with $\varepsilon_{\text{HS}} = \varepsilon_{\text{RU}}$ were studied. However, generally the emissivities of the different surfaces are independent of each other. Further improvement might be achieved using $\varepsilon_{\text{HS}} \neq \varepsilon_{\text{RU}}$.

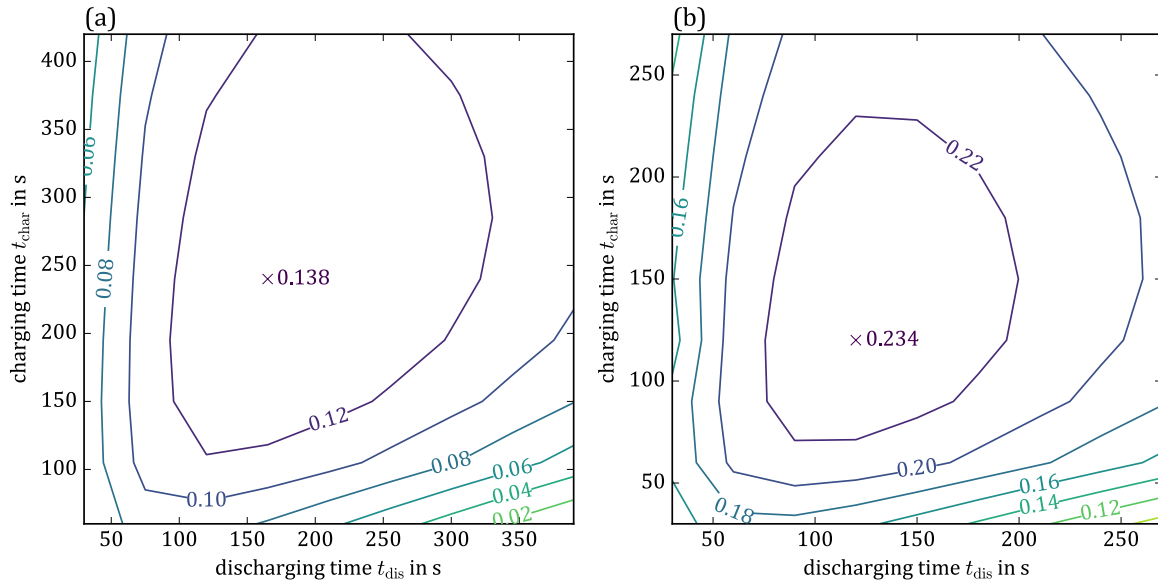


Figure 4.41.: Heat recovery ratio ϵ as a function of charging and discharging time for $d_{\text{HS}} = 6 d_{\text{RU}}$ and $\alpha_{\text{HS}} = 10 \text{ W m}^{-2} \text{ K}^{-1}$ with data for ρ_{HS} , λ_{HS} and $\tilde{c}_{p,\text{HS}}$ from Table 3.7 for concrete. (a): $\varepsilon_{\text{HS}} = \varepsilon_{\text{RU}} = 0.2$; (b): $\varepsilon_{\text{HS}} = \varepsilon_{\text{RU}} = 0.8$.

Also variation of the heat storage thickness has an impact on the possible heat recovery ratio. Thicker walls reduce heat losses to the ambience and have a larger total heat capacity. Figure 4.42(a) shows how the heat recovery ratio ϵ increases with increasing wall thickness. For the material properties of concrete, $0.145 \leq \epsilon \leq 0.274$ is found, while using properties of the insulation material yields $0.132 \leq \epsilon \leq 0.225$, for a heat storage thickness 3 to 12 times higher than that of the redox unit. The advantage with respect to ϵ that concrete has over the insulation material increases with increasing wall thickness. One reason for this could be decreased heat losses: The advantage of a higher thermal conductivity is that heat is transported into the depth of the material more quickly so that a larger portion of the material can contribute to storing the heat. The disadvantage is an increase of losses to the ambience. The larger thickness, which reduces total losses to the ambience can compensate this shortcoming. Thicker heat storages also offer a higher thermal mass. To fully utilize this thermal mass, longer charging and discharging times are needed as indicated in Figure 4.42(b). This is especially the case for materials with low heat conductivity as represented by the insulation material. A thicker heat storage requires

both longer charging and discharging time to achieve ϵ_{\max} . However, when comparing heat storages of different dimensions at the same t_{dis} and t_{char} , the thicker heat storage always reaches a higher heat recovery ratio even if not operated at the ideal t_{dis} and t_{char} . Ultimately, the ideal

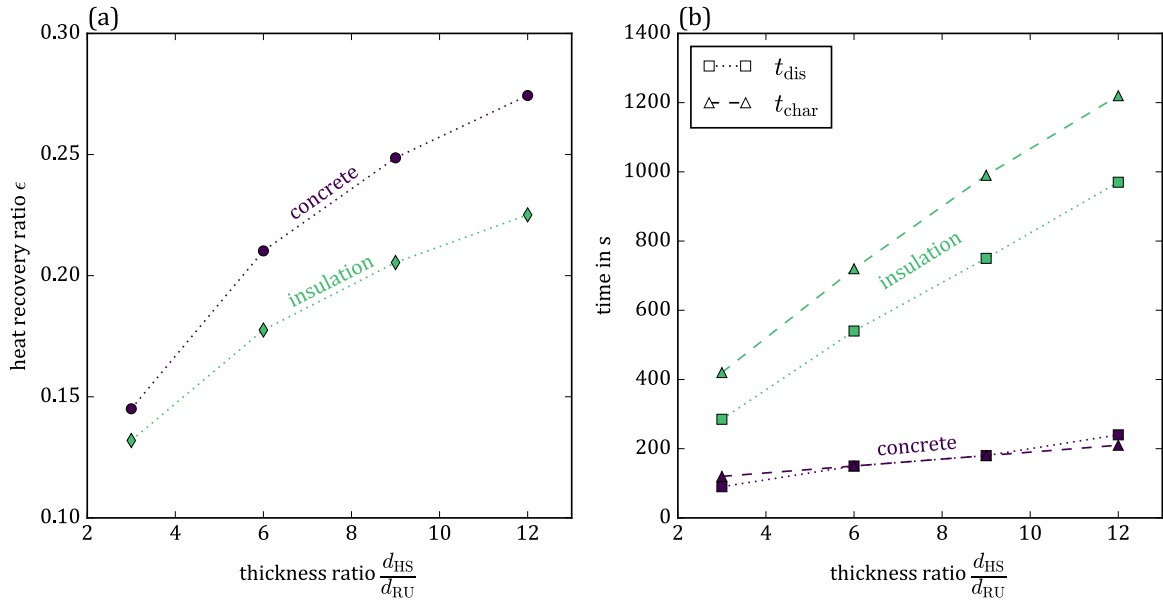


Figure 4.42.: Maximal heat recovery ratio ϵ_{\max} (a) and respective charging and discharging times (b) as a function of the heat storage thickness with data for ρ_{HS} , λ_{HS} and $\tilde{c}_{p, \text{HS}}$ from Table 3.7 for concrete and insulation material and $\alpha_{\text{HS}} = 10 \text{ W m}^{-2} \text{ K}^{-1}$ and $\epsilon_{\text{HS}} = \epsilon_{\text{RU}} = 0.5$.

dimensions depend on the trade-off between effectiveness and investment costs.

As mentioned above, the heat transfer coefficient between heat storage and ambient air was estimated conservatively as $\alpha_{\text{HS}} = 10 \text{ W m}^{-2} \text{ K}^{-1}$. The actual value of α_{HS} depends on the outer wall temperature and typically lies in the range $5.0 \text{ W m}^{-2} \text{ K}^{-1}$ to $7.6 \text{ W m}^{-2} \text{ K}^{-1}$ as explained in Chapter 3.3.1. The impact that α_{HS} has on the simulation results is shown in Figure 4.43, where results for $\alpha_{\text{HS}} = 5 \text{ W m}^{-2} \text{ K}^{-1}$ and $\alpha_{\text{HS}} = 10 \text{ W m}^{-2} \text{ K}^{-1}$ are compared. As expected, a lower heat transfer coefficient yields a higher heat recovery ratio due to reduced losses to the ambience. Reducing α_{HS} from $10 \text{ W m}^{-2} \text{ K}^{-1}$ to $5 \text{ W m}^{-2} \text{ K}^{-1}$, slightly increases ϵ_{\max} from 0.210 to 0.215. The location of ϵ_{\max} in terms of t_{char} and t_{dis} is the same. This shows that while for a lower α_{HS} the heat recovery is slightly elevated, the overall trends are similar and using $\alpha_{\text{HS}} = 10 \text{ W m}^{-2} \text{ K}^{-1}$ appears to yield an adequate estimation for ϵ .

Based on the presented results, heat recovery ratios in excess of 0.27 seem realistic. Especially considering possible improvements in the material choice for the heat storage, this value might be exceeded. As shown above, a higher emissivity for example might yield a better performance of the heat recovery system. To further improve the presented indirect heat recovery concept, a composite heat storage, consisting of a good heat conductor with a suitable heat capacity on the inside and a good insulator on the outside to facilitate sufficient heat storage with low heat

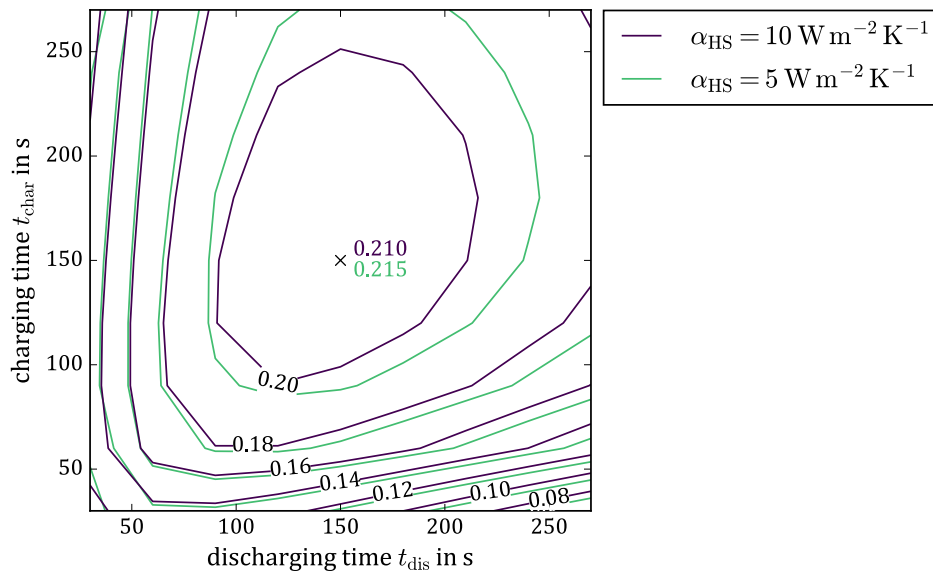


Figure 4.43.: Heat recovery ratio ϵ for different α_{HS} as a function of charging and discharging time for $d_{\text{HS}} = 6 d_{\text{RU}}$ and $\varepsilon_{\text{HS}} = \varepsilon_{\text{RU}} = 0.5$ with data for ρ_{HS} , λ_{HS} and $\tilde{c}_{\text{p,HS}}$ from Table 3.7 for concrete.

losses might be beneficial. As discussed in Section 4.3, based on findings by Falter et al. [41], a counterflow HE might yield a heat recovery ratio of up to 0.7, but might be subject to recombination. Given the results for the indirect HE and the results for a continuous approach shown in Figure 4.36, an indirect HE design could be an adequate alternative to a counterflow HE, which suffers from the recombination effect. An indirect HE might be beneficial, if the recombination in a countercurrent concept cannot be mitigated sufficiently and has the advantage of a simpler process design.

5. Discussion of Recombination and Heat Recuperation Concepts

In the following, the results presented in this work are compared to the previous work by Siegrist et al. [17]. Subsequently, the impact of the heat recovery effect on different HE concepts is discussed as well as the advantages and disadvantages of the different concepts for application in solar thermochemical redox cycles. For a detailed description of the mentioned HE concepts the reader is referred to Chapter 2.2.2.

For their MBR2 concept, Siegrist et al. [17] proposed a HE design without separation of the hot and cold stream. They assess the system for various combinations of f_{recomb} and ϵ , freely varying the two parameters and conclude that such a design can increase the overall efficiency, as long as $f_{\text{recomb}} < \epsilon$ holds. As discussed in Chapter 4.1, f_{recomb} and ϵ are linked via the temperatures in the HE and thus f_{recomb} is a function of ϵ as for example shown in Figure 4.1. Siegrist et al. [17] also suggested to simplify the process by only separating the HE from one of the reactors. They estimated the recombination effect, based on the assumption that if at given O_2 partial pressure and temperatures, the cold stream releases less O_2 than the hot stream takes up thermodynamically, then the excess O_2 uptake simply does not take place. As discussed in Chapter 4.1, in such a case the hot stream would create a local low p_{O_2} either sucking gas from the reactor or if that is prevented by a pressure lock, lowering p_{O_2} in the HE to the point where O_2 release and uptake are equal. Based on aforementioned simplifications, Siegrist et al. [17] found a low f_{recomb} for a case in which oxidation reactor and HE share a common atmosphere. However, it was assumed that $p_{\text{O}_2, \text{ox}} = 1 \cdot 10^4 \text{ Pa}$ and thus $p_{\text{O}_2, \text{ox}} \gg p_{\text{O}_2, \text{red}}$. In reality, $p_{\text{O}_2, \text{ox}}$ is determined by the thermodynamics of the thermolysis reaction and is typically significantly lower than $p_{\text{O}_2, \text{red}}$ [3], which is determined by the vacuum pump. The high p_{O_2} chosen by Siegrist et al. explains the low extent of recombination. On top of that, the lack of a pressure lock between oxidation chamber and HE might result in the splitting product, namely H_2 or CO , entering the HE and re-reacting with ceria, decreasing the yield. However, to check whether it is in fact beneficial to not separate the HE from the reactor with the higher p_{O_2} , setup 2 as defined in Chapter 4.1 was investigated in the present work. In this setup, HE and reduction reactor are not separated. The results showed that vast amounts of O_2 enter the HE from the reduction reactor, where they re-oxidise the reduced redox material, so that this setup is impractical. For a setup with two pressure locks, isolating the HE, it was found in the present study that $f_{\text{recomb}} < \epsilon$ for low values of ϵ so that indeed it is possible to improve the process efficiency with a HE even though recombination takes place. However, if the reaction is fast it was also found that if larger values of ϵ are reached, $f_{\text{recomb}} > \epsilon$,

meaning that such a HE reduces the process efficiency. Based on experimental results and the simulations presented in Chapter 4.3 it was shown that introduction of an inert gas in the HE is a promising approach to mitigate recombination. For the MBR2 and similar HE designs this means that an improvement of the overall efficiency can likely be expected also at higher heat recovery ratios. Addition of an inert gas so that the total pressure in the HE is above that in the reactors can also prevent or at least reduce leakage of O_2 from the reduction reactor or product gas from the oxidation reactor into the HE, which would decrease the overall efficiency as discussed above. Furthermore, the inert gas would likely have an impact on the heat recovery effectiveness. The higher total pressure enhances convective heat transport. On the other hand, thermal energy might be lost due to inert gas leaving the HE, e.g. through pressure locks. In comparison to concepts in which the hot and cold streams are separated, higher heat recovery ratios appear feasible, as separating elements like a wall typically also hinder the heat transfer. All in all, the MBR2 concept seems a legitimate HE option, if two pressure locks are used and inert gas is supplied to the HE. Similar conclusions can be drawn for the CR5 concept [86–90], in which the redox material is transported on counter rotating parallel rings. Basically, this approach uses the same direct counter current HE principle as the MBR2, just with circular instead of linear motion. Diver et al. [87] also suggest the use of an inert gas, but rather to prevent crossover between the reactors than O_2 crossover between hot and cold redox material. A permanent argon flow, injected in-between oxidation and reduction chamber was provided to block cross flow between the reaction chambers [87]. If the HE design allows it, a forced inert gas flow from the hot to the cold redox material could mitigate the recombination effect. On the other hand, for many designs, forced convection might introduce turbulence which can enhance the gas transport between the hot and cold redox material and consequently intensify the recombination. For many concepts, it therefore appears suitable to establish an almost still inert gas atmosphere to mitigate recombination. In case of the CR5 concept, it seems rather difficult to implement an inert gas atmosphere as a mass transport resistor due to the vacuum pumping and the injection of CO_2 or steam in the respective reaction sections, which are not actively separated from the HE section. The same applies for the concept suggested by Lapp et al. [84], in which counter rotating cylinders are used. Even though the heat transfer is indirect, i.e. via a heat transfer medium, hot and cold regions of the redox material are not hermetically sealed from each other. Again, it seems difficult to implement an inert gas atmosphere to mitigate recombination, due to the permanent injection of CO_2 or steam in the oxidation section and an inert purge gas in the reduction section.

The particle concept by Ermanoski et al. [12] features counter current heat recovery through a screw elevator's wall. Similar to the aforementioned rotating systems, there are no pressure locks that separate the reaction zones from the HE. According to Ermanoski et al. [12], the packed bed of particles inside the connection tube provides an effective seal to allow for pressure separation and prevent mixing of products. Whether or not this seal is also sufficient to prevent the recombination effect, presumably depends on the temperature profile achieved with this concept, which determines the distance that O_2 would have to travel in order to cause signifi-

cant recombination. An inert gas atmosphere with a high total pressure seems difficult for this concept as well, due to the lack of separation of the heat recuperation zone from the vacuum pump. However, it is presumably more realistic to modify this concept and add pressure locks to it compared to the rotating systems. Hence, it might be feasible to significantly mitigate the recombination effect.

In indirect heat transfer concepts, the recombination can be avoided as hot and cold redox material are fully separated. However, in concepts in which a heat transfer fluid has contact to the hot and cold redox material, O_2 which was released from the cold redox material should be removed from the heat transfer fluid before it gets into contact with the hot redox material. Otherwise, a recombination effect would likely occur in which the O_2 is transported by the heat transfer fluid. Regarding the indirect concept discussed in Chapter 4.4, it is necessary to remove oxygen from the HE chamber after the discharging step, by either vacuum pumping or inert gas sweeping. As stated before, simple indirect concepts have a lower heat recuperation potential compared to direct concepts. This is depicted in Figure 5.1. Figure 5.1(b) shows a co-current HE with a heat transfer medium or a transient HE with a heat storage such as the one investigated in Chapter 4.4. Due to the two step-heat transfer, hot and cold stream settle at two different temperature levels. Compared to the direct HE depicted in Figure 5.1(a) this leads to a smaller exploitation of the thermal energy stored in the hot stream. For counter-current arrangements, the indirect approach can theoretically lead to 100 % heat recovery if the HE is infinitely large and ideally insulated. In a real system however, a certain minimal temperature difference is needed. Again, due to the two heat transfer steps in the indirect approach, this might reduce the heat recuperation, as shown in Figures 5.1(c) and 5.1(d). For the simple indirect concept studied in the present work, heat recovery ratios of up to 0.274 were found. As discussed in Chapter 4.4, changes to the material choice will likely improve this performance. At the same time however, the analysis indicates that with such a simple single-stage design, it is unlikely to get close to the performance of a counter current HE. Falter et al. [41] found heat recovery ratios of approximately 70 % for a quasi counter current HE using a separating wall between hot and cold redox material. Based on this, it seems realistic that for a real counter current HE without separation of hot and cold stream $\epsilon > 0.7$ can be achieved. Consequently, direct counter current HEs are a promising option to reach high ϵ and improve the efficiency of the redox system, if the recombination effect is sufficiently mitigated according to the discussion above. Simple indirect HE concepts on the other hand offer an alternative that can avoid the recombination effect, while achieving moderate heat recovery. Increasing the complexity of indirect approaches can improve the heat recovery. Lapp et al. [84] predict theoretical heat recovery ratios of 41 % or under optimistic conditions even 50 %. Felinks et al. [7] calculate $\epsilon \geq 0.7$ in a quasi counter current approach. These more complex concepts however come with major technical challenges similar to direct counter current HEs. Simple indirect HE designs, for instance single-stage concepts, are easier to implement. This is a distinct advantage for solar thermochemical redox cycles, as the gas tightness and high temperatures pose serious technical challenges, especially to the design of moving components. This is stressed by the fact that operation without failure while achiev-

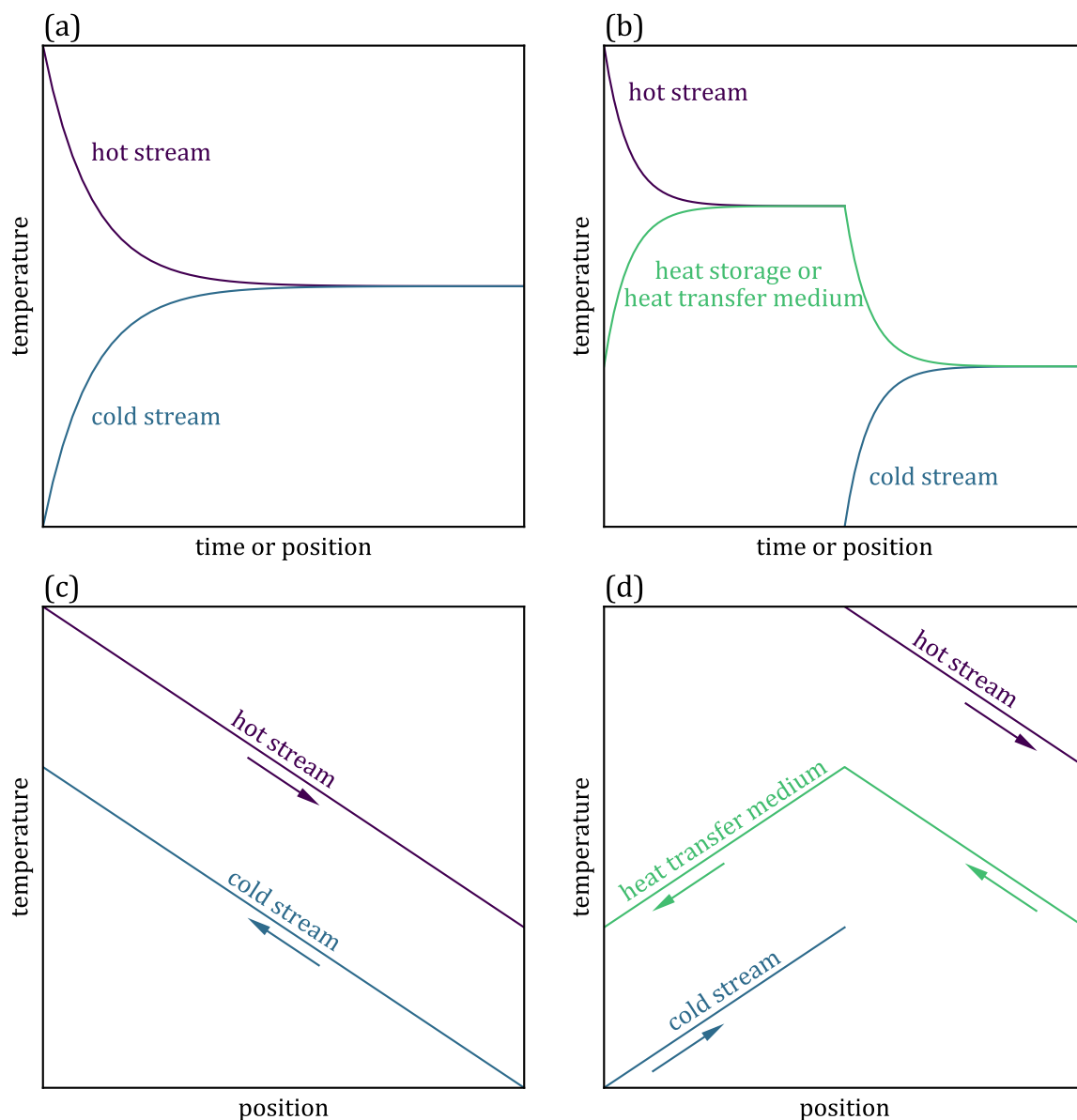


Figure 5.1.: Qualitative depiction of different heat transfer approaches. (a): Direct co-current or transient heat exchanger; (b): Indirect co-current or transient heat exchanger; (c): Direct counter-current heat exchanger; (d): Indirect counter-current heat exchanger.

ing high heat recovery ratios under realistic conditions of the very promising concepts reviewed in Chapter 2.2.2 is yet to be experimentally demonstrated.

Another interesting finding of the present work is a reversed recombination effect at low heat recovery ratios, which means that the reduced redox material gets further reduced in the HE. This effect increases the redox material's potential to split H_2O or CO_2 compared to a system without recombination and the same δ_{ox} and δ_{red} and can thus increase the overall efficiency. It is however important to mention that reversed recombination cannot increase $\Delta\delta$ beyond the point that could be reached without reversed recombination under different operating condi-

tions. The reversed recombination effect is a result of the incomplete oxidation of redox material in the oxidation reactor, as explained in more detail in Chapter 4.1.1. Thus, in a system without recombination, a similar $\Delta\delta$ value could be achieved by a higher degree of oxidation, i.e. δ_{ox} close to 0, which can be accomplished via a low oxidation temperature or a large surplus of oxidant (H_2O or CO_2). However, reversed recombination adds a degree of freedom to the process optimisation as high $\Delta\delta$ can be achieved even if the oxidation is not ideal. This for example allows higher oxidation temperatures, reducing the temperature swing and thus the energy demand associated with sensible heating of the redox material.

6. Conclusion and Outlook

The undesirable crossover of O_2 in solid-solid HEs for two-step thermochemical redox cycles, referred to as recombination was studied both theoretically and experimentally. The potential extent of recombination was investigated using a *Python* 3 [148, 149] model. This model is based on the assumption that the reduction and oxidation of the redox material inside the HE are fast compared to the heat transfer and thus chemical equilibrium between leaving streams and gas phase was assumed. A second law analysis was performed on simulation results. Experiments were conducted in a dedicated test rig to assess the kinetics of oxidation of ceria under conditions representative for a solid-solid HE for solar thermochemical redox cycles. It was also investigated whether addition of an inert gas into the HE can decelerate the re-oxidation of the redox material. The aforementioned *Python* model was then extended by a simple kinetic approach describing the oxygen crossover. To this end, given constant reaction rates were assumed for the oxidation, and literature values [41] were used to estimate the residence time needed to achieve a given heat recovery ratio. Based on the experimental results, realistic reaction rates are discussed and the model yields the according effect on the efficiency. Lastly, one-dimensional transient heat transport was modelled in *Python* 3 [148, 149] to investigate a simple indirect HE design, which utilises heat storage units.

The equilibrium-model reveals the correlation between heat recovery and recombination that was hypothesised in the introduction. At higher heat recovery ratios ϵ , higher fractions of recombination f_{recomb} are found. At moderate degrees of heat recovery, a reversed recombination effect is predicted. The hot redox material coming from the reduction reactor is further reduced in the HE, while the cold oxidised material is further oxidised. This effect is due to the O_2 partial pressure in the HE, which affects the redox state opposite way compared to the temperature change. At low ϵ , the effect of the O_2 partial pressure outweighs that of the temperature change. Reversed recombination adds a degree of freedom with respect to process optimisation as large changes of the oxygen non-stoichiometry $\Delta\delta$ can be reached even if the oxidation takes place at comparatively high temperatures and/or low amounts of excess reactant. It is however not possible to reach higher $\Delta\delta$ -values than in a system without reversed recombination, in which the oxidation is optimised. At large degrees of heat recovery, recombination results in an oxidation of the reduced redox material in the HE. At a certain point, the efficiency improvements due to heat recovery are fully compensated by the efficiency penalty caused by recombination. For a system without losses to the ambience, this point is reached at $\epsilon = f_{\text{recomb}} = 0.5$. If heat losses are considered, this point is already reached at lower ϵ . At even higher heat recovery ratios, the system is less efficient than a reference case without heat recuperation. H_2O -splitting and

CO₂-splitting show similar trends. At elevated oxidation temperatures, CO₂-splitting might have efficiency benefits over H₂O-splitting, due to the thermodynamics of the respective thermolysis reactions. This effect is however largely compensated by (reversed) recombination. If HE and reduction reactor are not separated by a pressure lock, O₂ released from the redox material during the reduction is taken up by the same material as it cools down in the HE, which amplifies the recombination effect. In such an arrangement, recombination always outweighs the benefits of heat recuperation. For most points of operation, the simulation results obey the second law of thermodynamics. For a HE that is isolated from both reactors, the second law is only found to be violated for very low values of ϵ . If HE and reduction reactor share a common atmosphere, the second law analysis states that the process is only feasible at low oxidation temperatures, e.g. 873 K instead of the default value of 1073 K.

Experiments confirm the hypothesis that addition of an inert gas like N₂ to the atmosphere in the HE is a suitable measure to decelerate the recombination. Uptake of O₂ by the ceria sample was found to be significantly slower for experiments conducted in a N₂ atmosphere. After addition of O₂ the time until the pressure has dropped to a certain value, due to oxidation of the sample can be used as a metric for the oxidation rate. It takes approximately 4.5, 5.7 and 10.2 times longer until the amount of added O₂, expressed as Δp_{O_2} , drops from originally 164 Pa to 25 Pa, 50 Pa and 100 Pa, respectively, if 520 Pa of N₂ are added to the atmosphere, compared to an experiment without addition of N₂. This demonstrates the effectiveness of inert gas to counteract re-oxidation in a HE. This is especially true when the low amounts of added N₂ are considered. In a real system much higher p_{N_2} are possible. The system could for example be operated at atmospheric pressure. In this case, the inert gas could also help to prevent O₂ from the reduction reactor and H₂ and H₂O or CO and CO₂ from the oxidation reactor from entering the HE. Furthermore, the experiments show that with respect to the oxidation kinetics, particles and RPCs behave similarly, despite a significantly larger BET surface area of the RPCs compared to the particles. The oxidation rates do not obey an equation that describes the kinetics of the oxidation reaction. Together with the impact that N₂ has on the kinetics and the fact that both sample types behave similarly, this finding indicates that the rate limiting mechanism is the mass transport in the gas phase. This in turn supports the hypothesis that an inert gas acts as a mass transport resistor for O₂. Due to the lack of reliable measurement of the gas temperature, the non-stoichiometry had to be estimated assuming a constant temperature over the course of an oxidation step. The trend of both $\Delta\delta$ and calculated gas temperatures and comparison with their respective theoretical minima and/or maxima indicate that this assumption yields plausible results. SEM, EDX and XRD suggest that the ceria samples do not undergo any phase change or change in composition and structure.

Parameter variation of oxidation rates using the kinetic model yields significant efficiency improvements, if oxidation rates are sufficiently low. Given the results of the experimental campaign, it seems possible to increase the system efficiency by a factor of 1.5 to 2 with a HE. This is especially the case as the model indicates very low O₂ partial pressures, which is an argument for a slow oxidation. In addition, the aforementioned option to increase the N₂ content further

supports the theory that significant efficiency improvements can be made.

Simulations of a simple indirect heat recuperation approach via a heat storage unit were conducted with different material properties for the heat storage medium. Thermal conductivity, density and specific heat capacity of concrete and an insulation material were chosen, while the emissivity was varied between 0.2 and 0.8 to study a representative range of material properties. For an emissivity of 0.5, heat recovery ratios of up to 0.274 for material properties of concrete and 0.225 for material properties of the insulation material are found. Higher heat recovery ratios seem possible if a more suitable material is identified. Especially, increasing the emissivity and combining a suitable heat storage medium with a good insulator appear to be promising approaches to enhance the performance of this concept. Based on the investigations on recombination, the simple indirect HE might be outperformed by direct countercurrent HEs, despite the ability of the indirect concept to avoid recombination. The simple indirect approach is however likely easier to implement, which is important as realisation of complex systems at the relevant high temperatures is challenging.

The presented results are indicative for the objectives of potential future studies. Experiments on the recombination, which use two redox material samples, one representing the hot stream and the other representing the cold stream in a HE could reproduce the behaviour of a real HE more closely. Such a setup could also be used to study reversed recombination. Furthermore, it would be of particular interest to investigate recombination at higher p_{N_2} with such a setup. The existing setup could be improved by a more accurate determination of the gas temperature and consequently the oxygen non-stoichiometry. Here, a more sophisticated model to calculate the average gas temperature from the measured temperatures in the reaction tube seems to be a promising approach. A spatially resolved model of recombination in a countercurrent HE would further deepen the understanding of the phenomenon and its effect on a real system. A second law analysis of such a model would be able to assess the feasibility of results for all points inside the HE and would thus contribute to a realistic estimation of the recombination effect. Finally, a prototype of a direct counter current heat exchanger without separation of the two material streams is desirable to demonstrate the usefulness of this heat recuperation approach.

Appendix

A. Experimental Raw Data

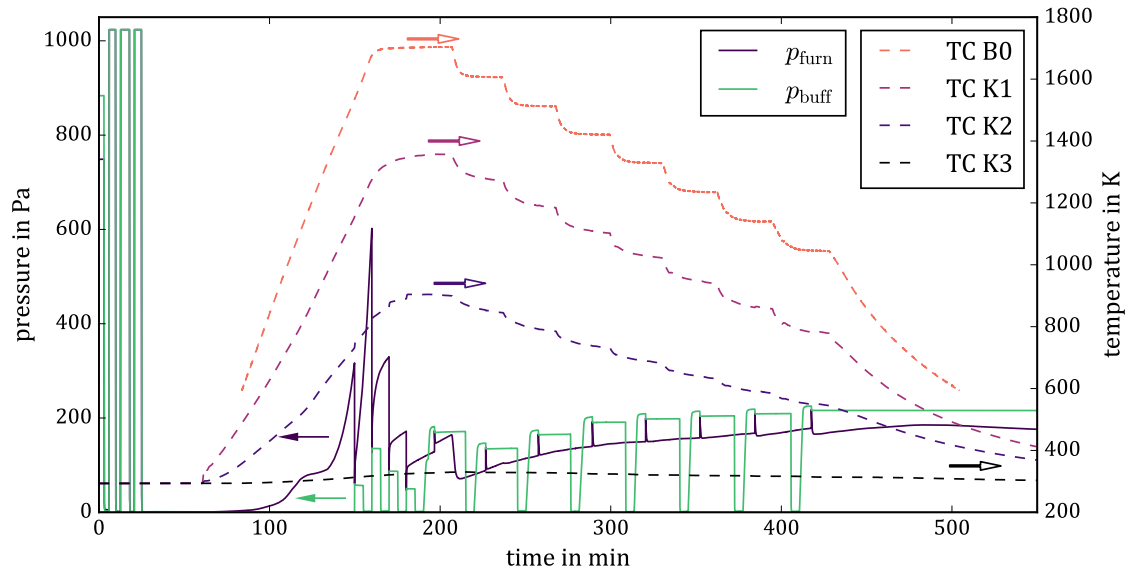


Figure A.1.: Pressure and temperature curves for experiment with particle bed 1, $\Delta p_{\text{O}_2} \approx 46$ Pa and $\Delta p_{\text{N}_2} = 0$ (see table 3.2 for details).

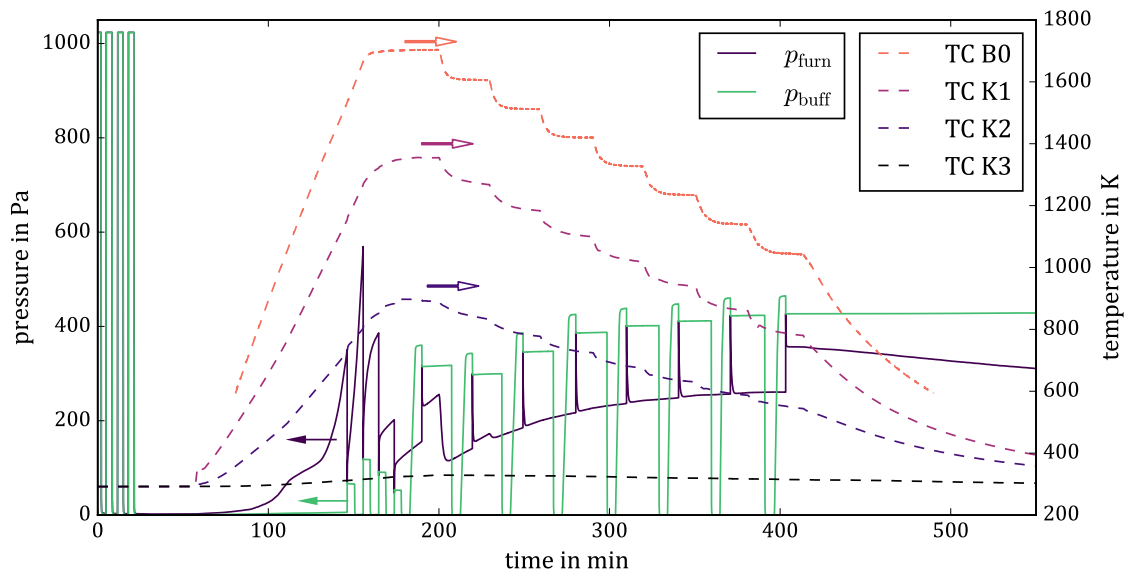


Figure A.2.: Pressure and temperature curves for experiment with particle bed 1, $\Delta p_{O_2} \approx 162$ Pa and $\Delta p_{N_2} = 0$ (see table 3.2 for details).

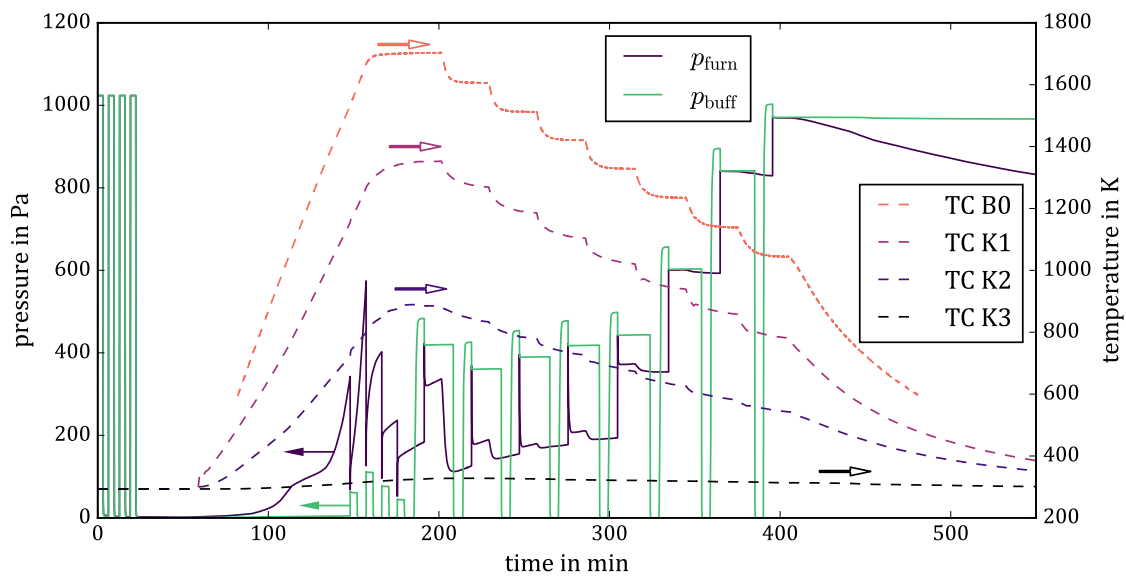


Figure A.3.: Pressure and temperature curves for experiment with particle bed 1, $\Delta p_{O_2} \approx 245$ Pa and $\Delta p_{N_2} = 0$ (see table 3.2 for details).

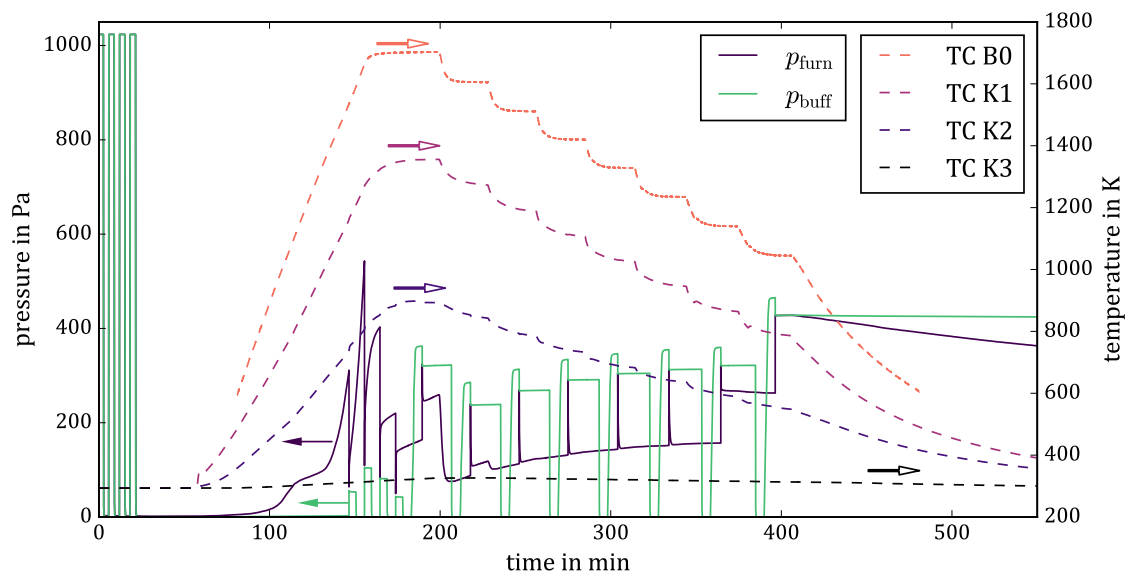


Figure A.4.: Pressure and temperature curves for experiment with particle bed 1, $\Delta p_{O_2} \approx 162$ Pa and $\Delta p_{N_2} = 0$ (see table 3.2 for details).

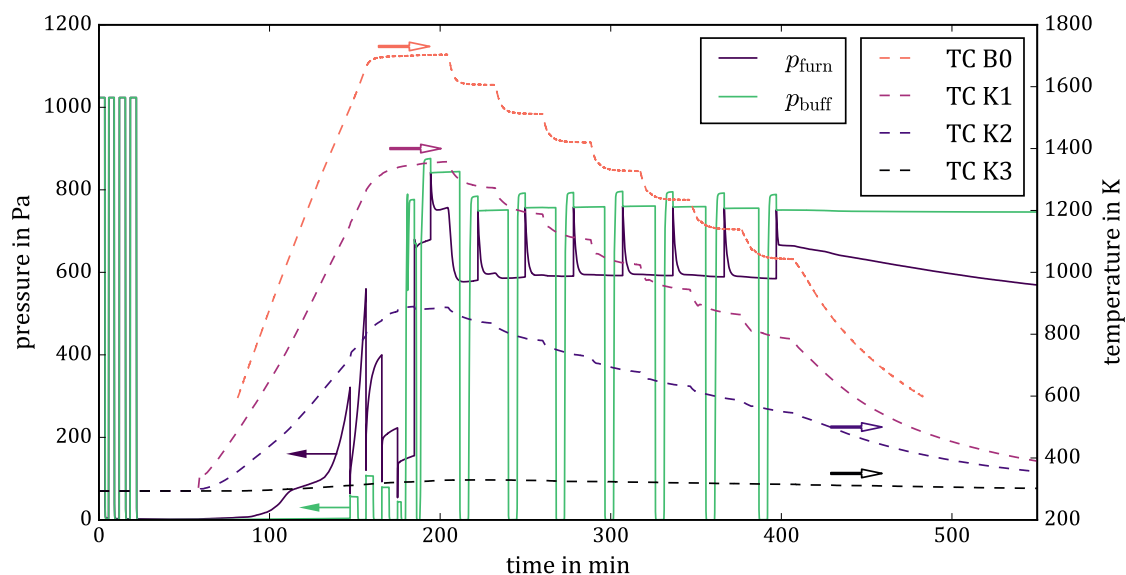


Figure A.5.: Pressure and temperature curves for experiment with particle bed 1, $\Delta p_{O_2} \approx 167$ Pa and $\Delta p_{N_2} \approx 524$ Pa (see table 3.2 for details).

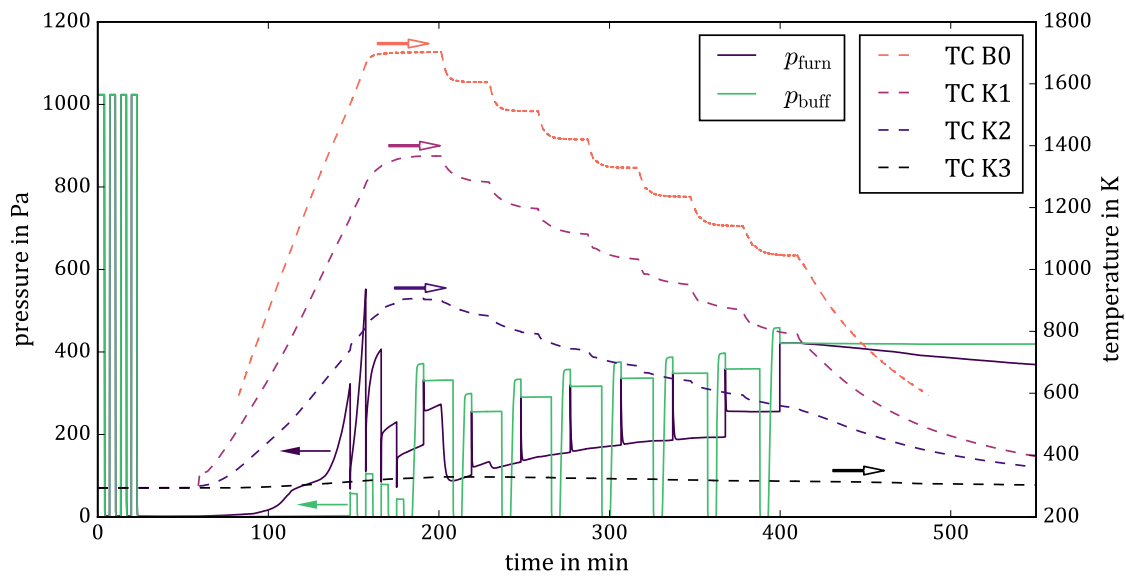


Figure A.6.: Pressure and temperature curves for experiment with particle bed 1, $\Delta p_{\text{O}_2} \approx 162$ Pa and $\Delta p_{\text{N}_2} = 0$ (see table 3.2 for details). Data set corresponds to the experiment shown in Figure 4.21.

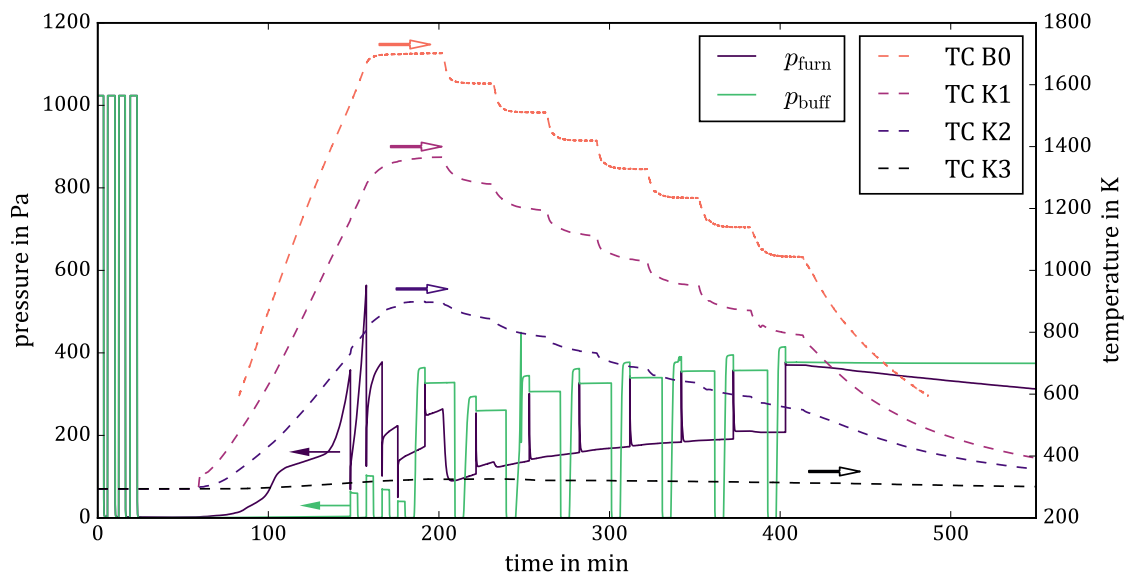


Figure A.7.: Pressure and temperature curves for experiment with RPCs, $\Delta p_{\text{O}_2} \approx 164$ Pa and $\Delta p_{\text{N}_2} = 0$ (see table 3.2 for details).

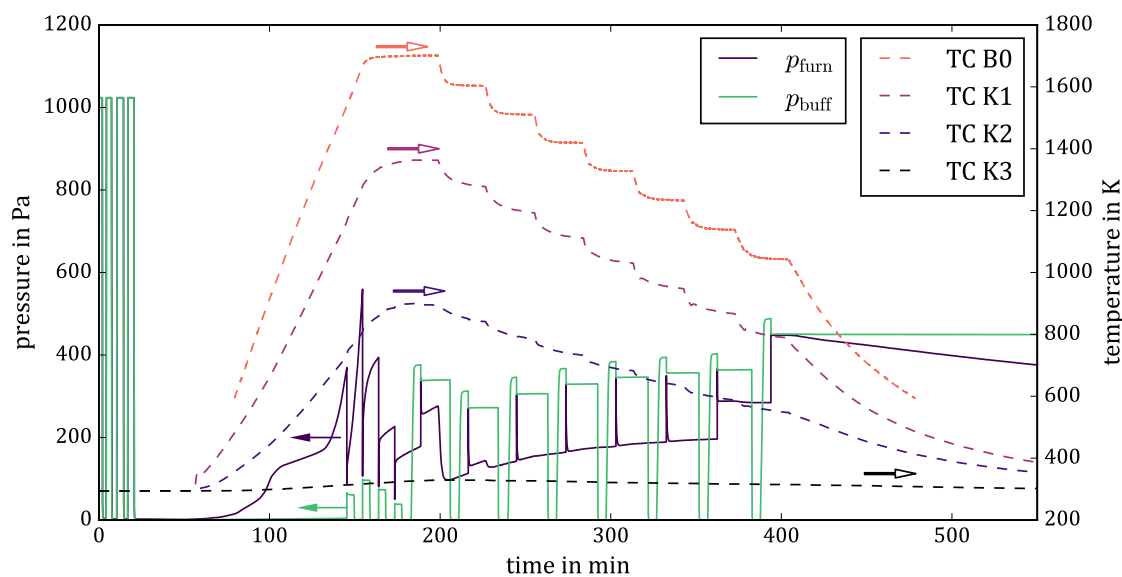


Figure A.8.: Pressure and temperature curves for experiment with RPCs, $\Delta p_{\text{O}_2} \approx 164$ Pa and $\Delta p_{\text{N}_2} = 0$ (see table 3.2 for details).

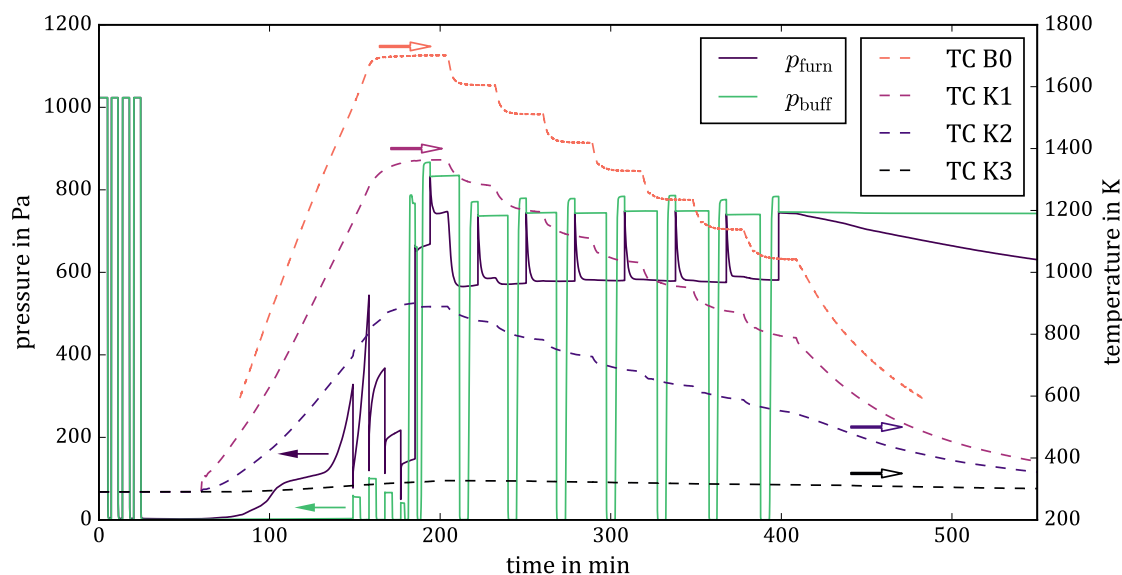


Figure A.9.: Pressure and temperature curves for experiment with RPCs, $\Delta p_{\text{O}_2} \approx 168$ Pa and $\Delta p_{\text{N}_2} \approx 520$ Pa (see table 3.2 for details).

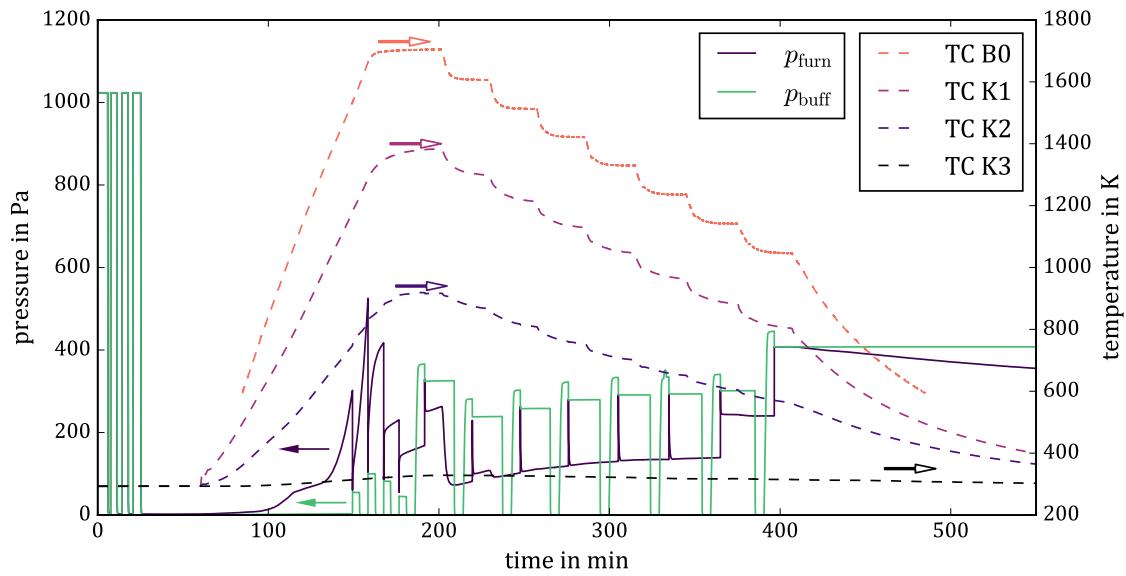


Figure A.10.: Pressure and temperature curves for experiment with particle bed 2, $\Delta p_{\text{O}_2} \approx 160$ Pa and $\Delta p_{\text{N}_2} = 0$ (see table 3.2 for details).

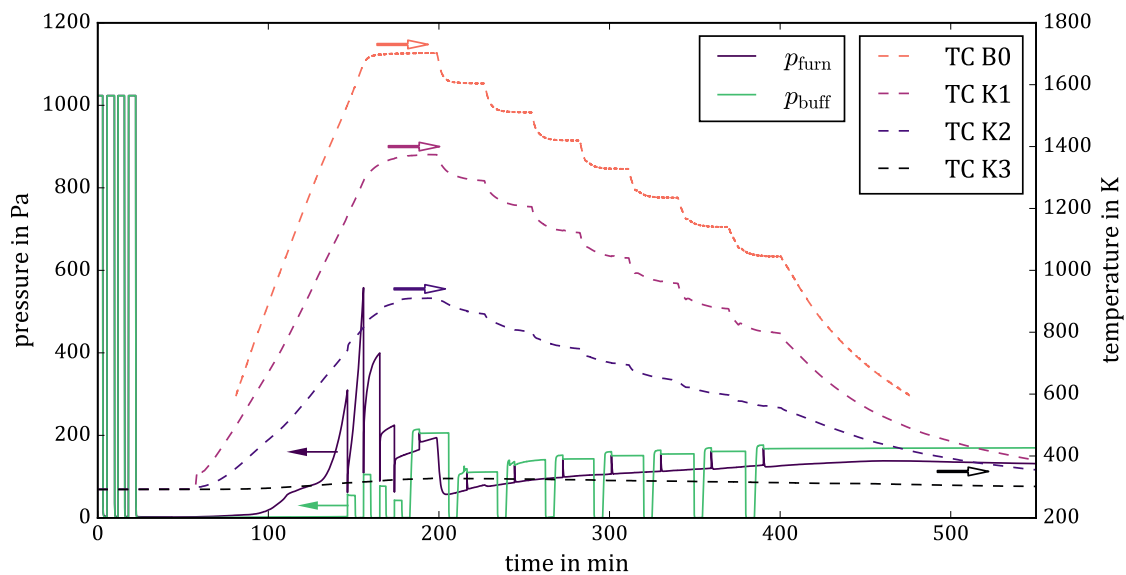


Figure A.11.: Pressure and temperature curves for experiment with particle bed 3, $\Delta p_{\text{O}_2} \approx 43$ Pa and $\Delta p_{\text{N}_2} = 0$ (see table 3.2 for details).

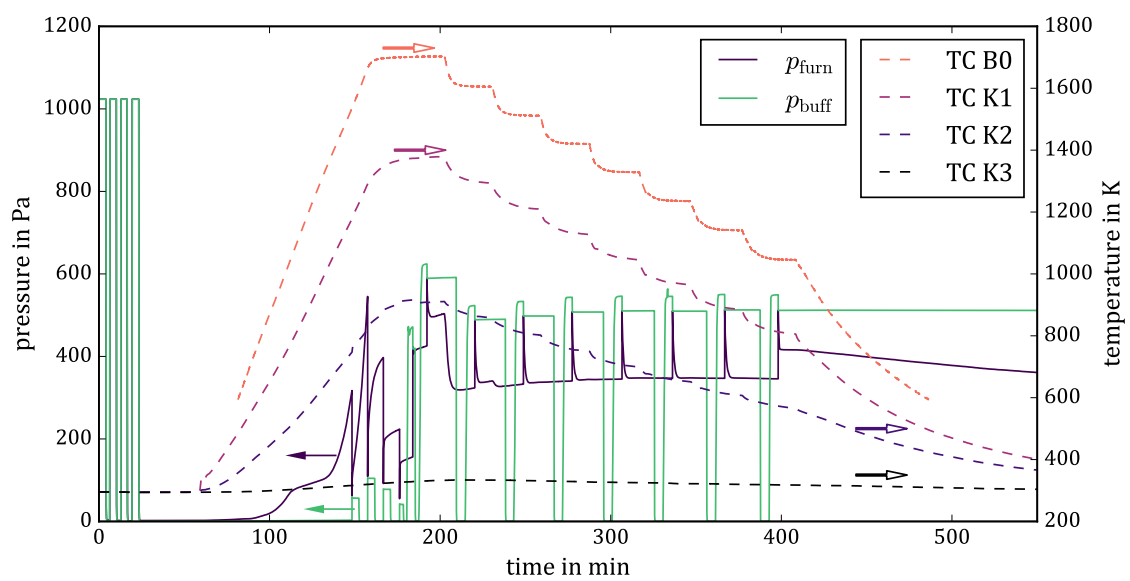


Figure A.12.: Pressure and temperature curves for experiment with particle bed 3, $\Delta p_{\text{O}_2} \approx 166$ Pa and $\Delta p_{\text{N}_2} \approx 270$ Pa (see table 3.2 for details).

B. Removal of Organic Components in Test Rig

As mentioned in Chapter 3.2.1, an unexpected pressure increase during test runs was observed. The evacuated test rig without a reactive sample was heated. The heating of the gas causes an expected pressure increase. At $T_{B0} \approx 1500$ K however the pressure increases more steeply than before. Pressure and temperature are depicted in Figure B.1. This behaviour might have been

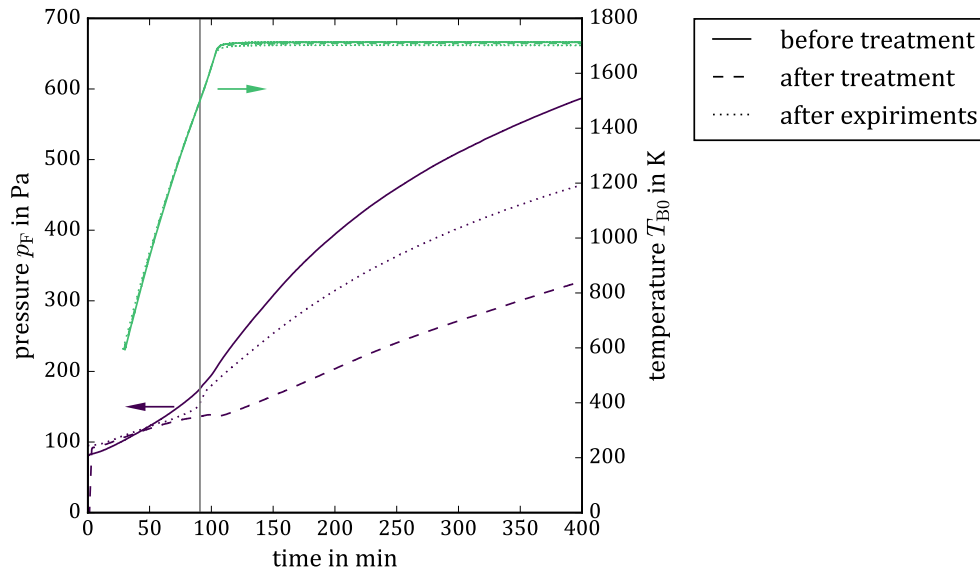


Figure B.1.: Pressure and temperature curves before and after treatment to remove possible organic components and after execution of all experiments. A vertical line highlights the point at which $T_{B0} = 1500$ K. The time scale of each run is shifted so that $T_{B0} = 1500$ K is reached at the same time.

caused by combustion or decomposition of an organic binder in the aluminium silicate fibre mats used to hold the thermocouples in place. Therefore the treatment described in Chapter 3.2.1 to remove organic components from the test rig was performed. After this treatment, the pressure increases less steeply after reaching $T_{B0} \approx 1500$ K. A reference run after performing all experiments shows a similar pressure increase as before the above treatment, but to a lesser extent. This is also depicted in Figure B.1. Prior to this reference run, the test rig was opened to remove the sample, allowing ambient air to enter the test rig. Humidity and/or other contaminants that have entered the test rig in this way could have accumulated in micro-cavities and adsorbed or absorbed onto the materials of the test rig. At higher temperatures these contaminants could enter the gas phase, which would explain the increase in pressure. The original pressure increase during the initial test runs might have been caused by both effects: decomposition or combustion of organic components and contaminants from air, entering the gas phase. The results suggest that the aforementioned treatment removed both organic components and other contaminants.

C. Test Rig Volume

Table C.1.: Measurement of test rig volume.

Measurement	Compartment	Volume	Average
1	buffer + furnace	2.28 L	2.32 L
2	buffer + furnace	2.28 L	
3	buffer + furnace	2.37 L	
4	buffer + furnace	2.33 L	
5	buffer	1.79 L	1.78 L
6	buffer	1.80 L	
7	buffer	1.79 L	
8	buffer	1.73 L	
Difference	furnace	-	0.538 L

D. Derivation of Initial Values for Test Rig Model

The initial value \bar{T}_1^{init} in chapter 3.2.8 is determined using an approximated value for the amount of oxygen that is moved from the buffer volume to the furnace Δn^{init} . This is calculated using the assumption that the temperature in the furnace stays constant despite the fact that a cold gas stream enters, hence

$$n_{F,1}^{\text{init}} = \frac{p_1^{\text{init}} V_F}{R \bar{T}_0}. \quad (\text{D.1})$$

With that

$$\Delta n_{01}^{\text{init}} = \frac{p_1^{\text{init}} V_F}{R \bar{T}_0} - n_{F,0} \quad (\text{D.2})$$

follows. Since, the pressure is equalized between buffer volume and furnace after opening the connecting valve, $p_{BV,1} = p_1$ holds, so that the ideal gas law for the buffer volume at state 1 reads

$$n_{1,BV}^{\text{init}} = \frac{p_1^{\text{init}} V_{BV}}{R T_{BV}}. \quad (\text{D.3})$$

The amount of oxygen leaving the buffer volume equals the amount entering the furnace, so that

$$\Delta n_{01}^{\text{init}} = n_{F,1}^{\text{init}} - n_{F,0} = n_{0,BV} - n_{1,BV}^{\text{init}}. \quad (\text{D.4})$$

Equation D.3 can be rearranged and $n_{1,BV}^{\text{init}}$ can be substituted using Equation D.4, which yields

$$p_1^{\text{init}} = \frac{(n_{0,BV} - \Delta n_{01}^{\text{init}}) R T_{BV}}{V_{BV}} \quad (\text{D.5})$$

This expression can be substituted into Equation D.2, resulting in

$$\Delta n_{01}^{\text{init}} = \frac{V_F T_{\text{BV}}}{V_{\text{BV}} \bar{T}_0} \cdot (n_{0,\text{BV}} - \Delta n_{01}^{\text{init}}) - n_{\text{F},0}, \quad (\text{D.6})$$

which can be ultimately rearranged to

$$\Delta n_{01}^{\text{init}} = \left(n_{\text{BV},0} \frac{V_F T_{\text{BV}}}{V_{\text{BV}} \bar{T}_0} - n_{\text{F},0} \right) \cdot \left(1 + \frac{V_F T_{\text{BV}}}{V_{\text{BV}} \bar{T}_0} \right)^{-1}. \quad (\text{D.7})$$

E. Ceria Samples

As shown in Figure E.1, particles form clusters, presumably due to sintering. However, these formations are very loose and disassemble, when touched or removed from the crucible. Sintering between particles is therefore believed to play a minor role.

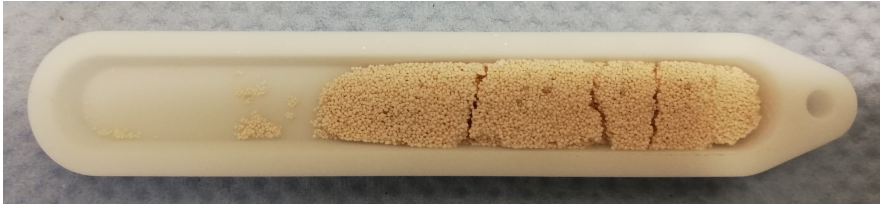


Figure E.1.: Particles in crucible after experiments.

All samples were weighed before and after experiments. Results are given in Table E.1. No significant difference of sample mass before and after experiments was found. This indicates that during assembly, experiments and removal, breakage of RPCs and particles dropping out of the crucible is negligible.

Table E.1.: Sample weights.

Sample	Mass before experiments	Mass after experiments	rel. mass difference
Particle bed 1	5.0238 g	4.9890 g	0.69 %
Particle bed 2	5.0225 g	5.0173 g	0.10 %
Particle bed 3	5.0222 g	5.0179 g	0.086 %
RPCs	5.0221 g	4.9080 g	2.3 %

Determining the position of the samples using an endoscope revealed that the samples did not move during the experiments. Pictures taken with the camera of the endoscope are shown in Figure E.2.

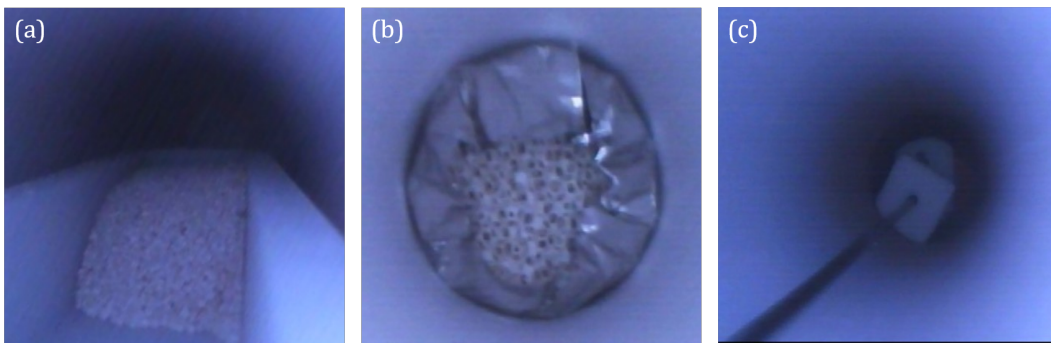


Figure E.2.: Samples in the reaction tube. (a) particle bed in crucible, (b) RPCs wrapped in Pt-foil, (c) thermocouple and insulation material.

F. Scanning Electron Microscope Images of Particles

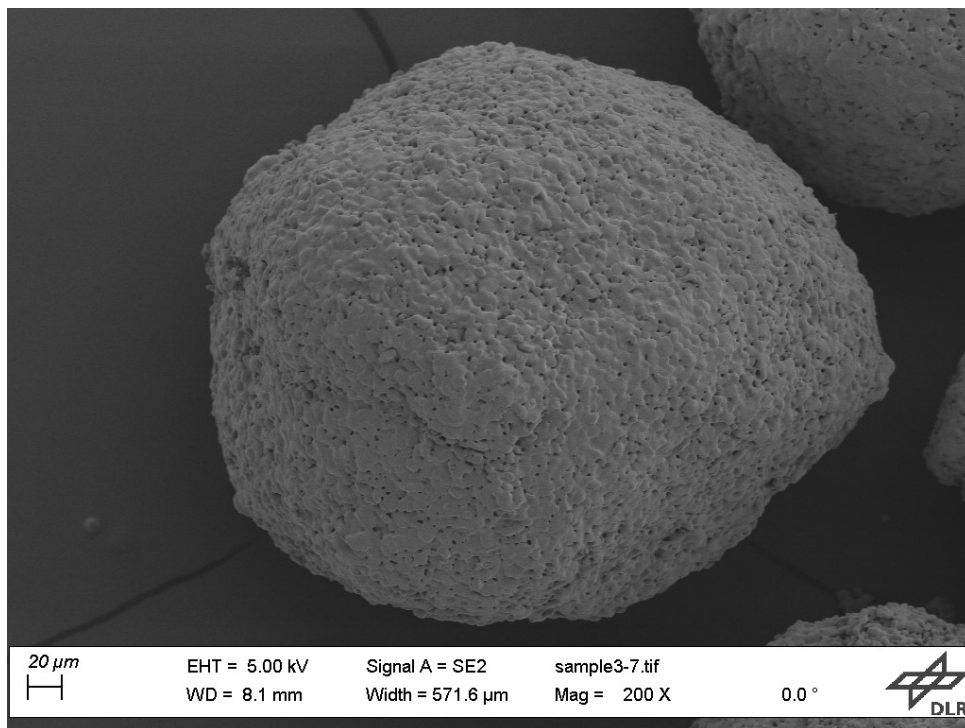


Figure F.1.: Scanning electron microscope image of ceria particle as before experiments. 200-fold magnified. Corresponds to the particle shown in Figure 4.25(c).

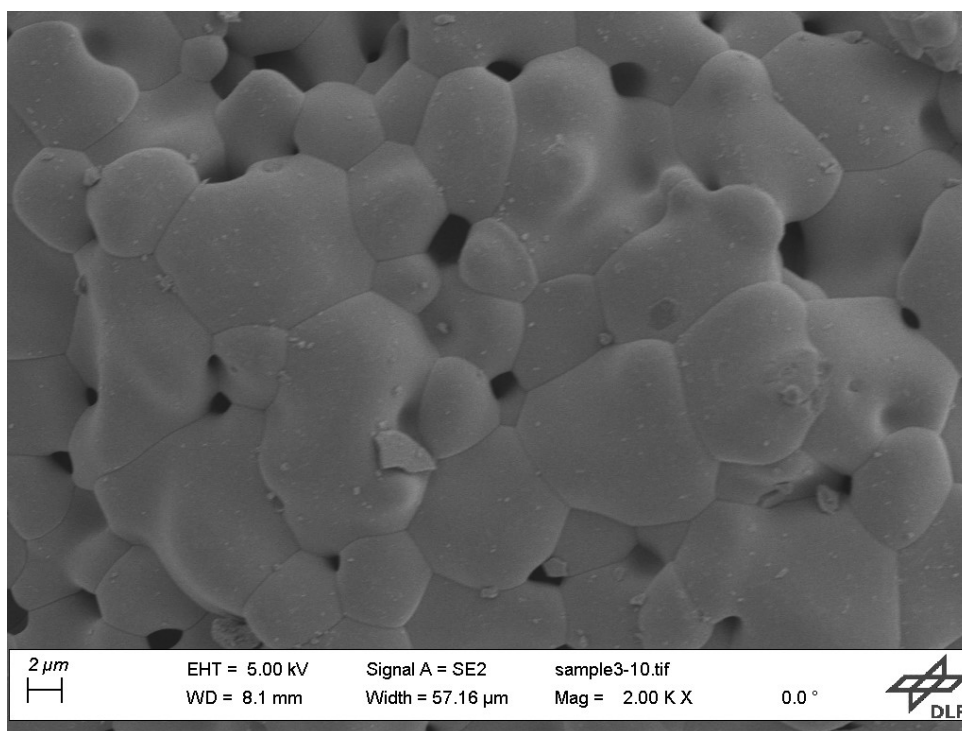


Figure F.2.: Scanning electron microscope image of ceria particle as before experiments. 2000-fold magnified. Corresponds to the particle shown in Figure 4.25(d).

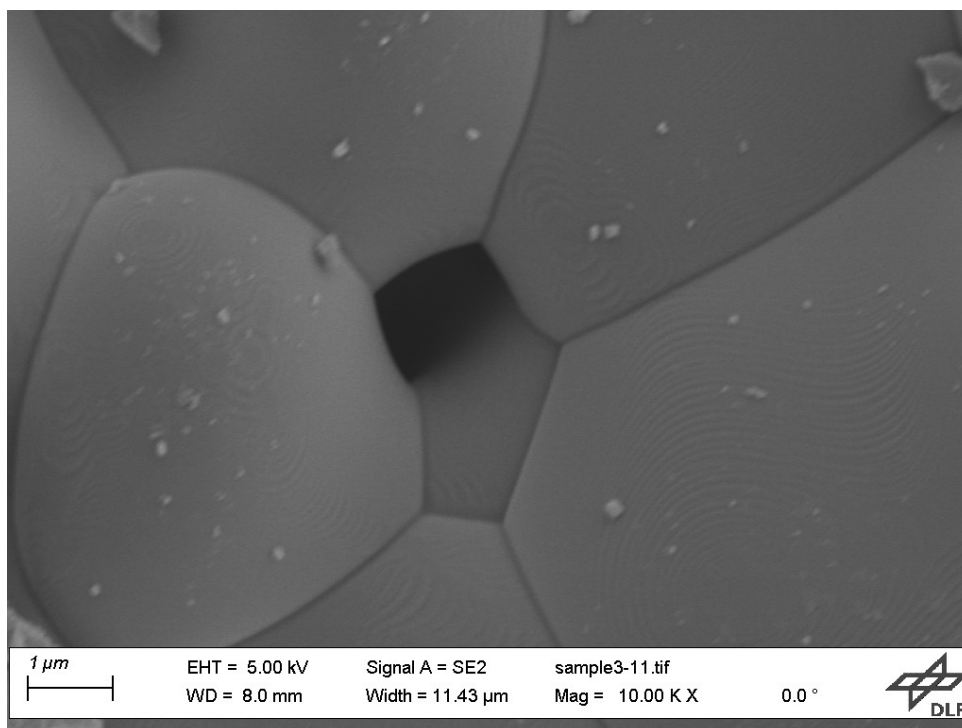


Figure F.3.: Scanning electron microscope image of ceria particle as before experiments. 10000-fold magnified.

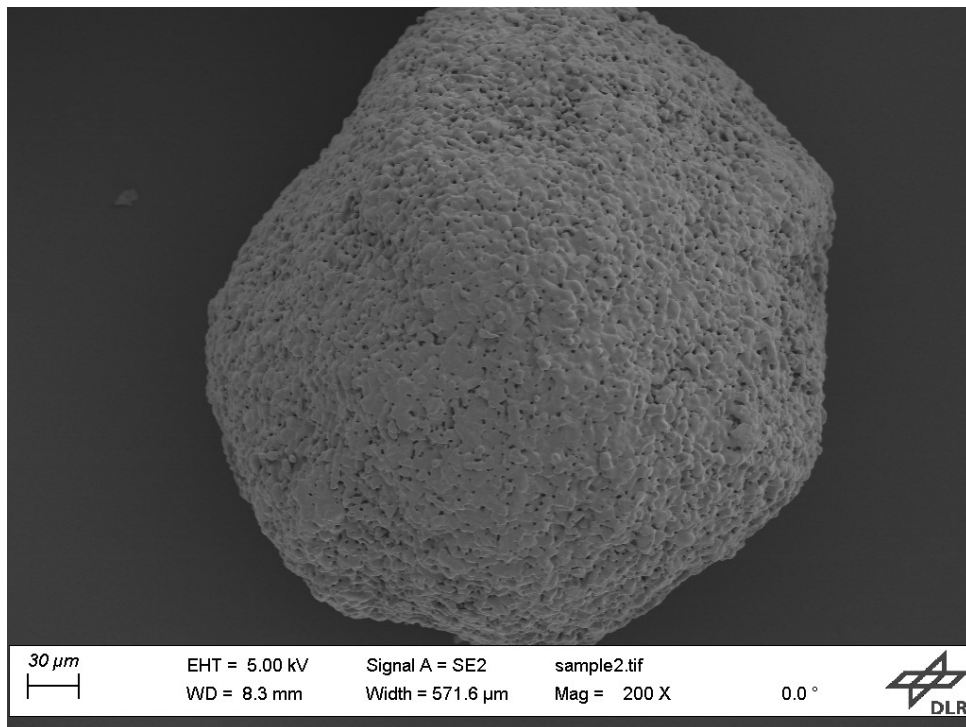


Figure F.4.: Scanning electron microscope image of ceria particle after one experiment. 200-fold magnified.

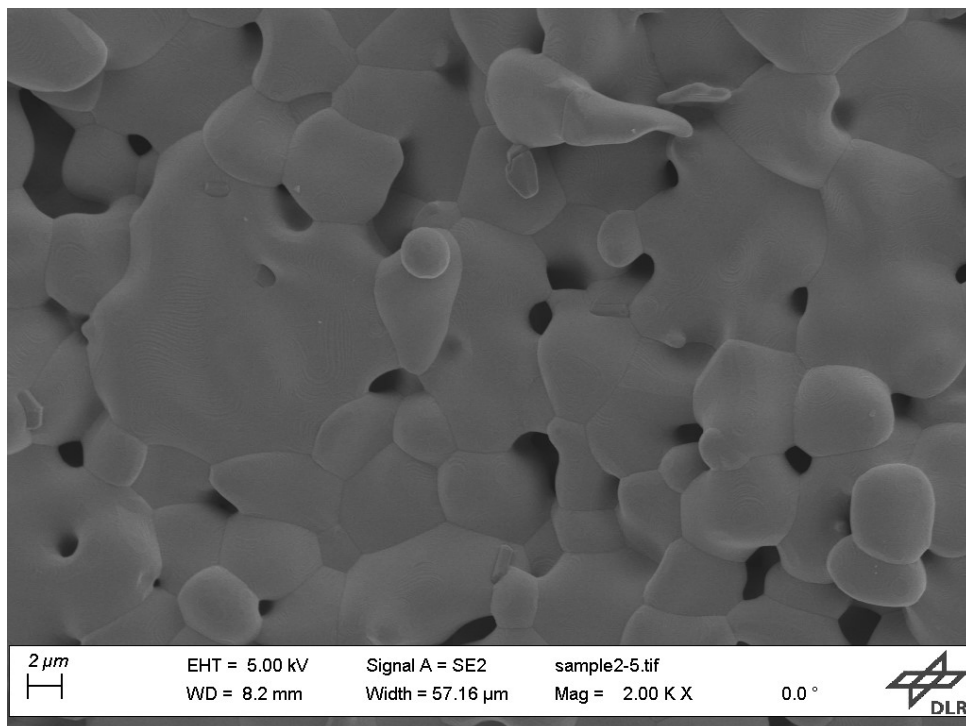


Figure F.5.: Scanning electron microscope image of ceria particle after one experiment. 2000-fold magnified.

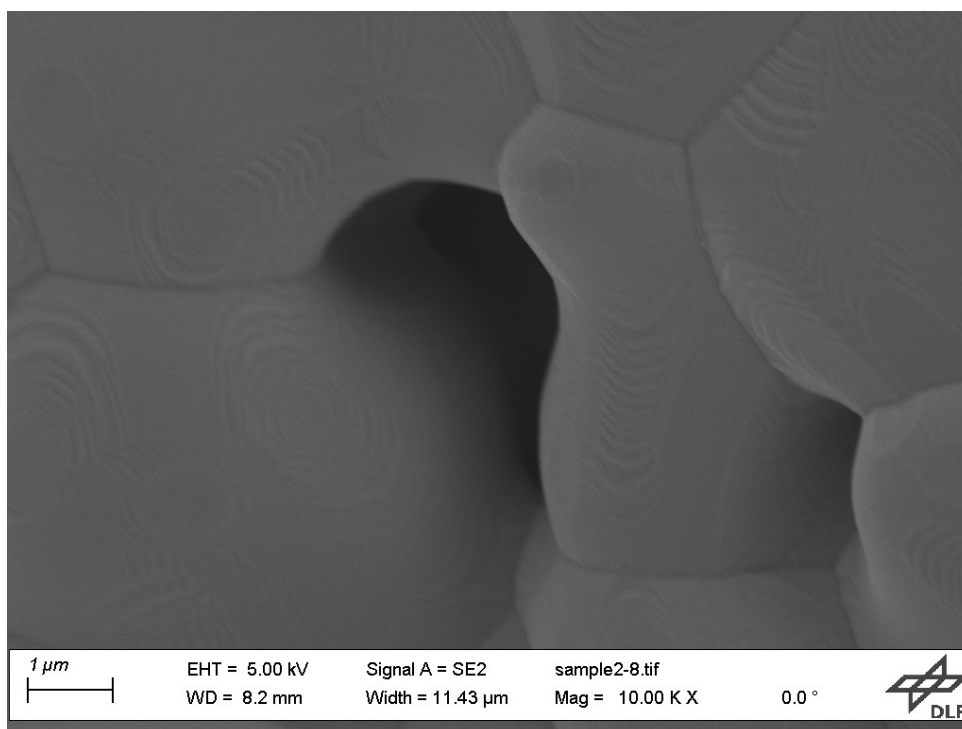


Figure F.6.: Scanning electron microscope image of ceria particle after one experiment. 10000-fold magnified.

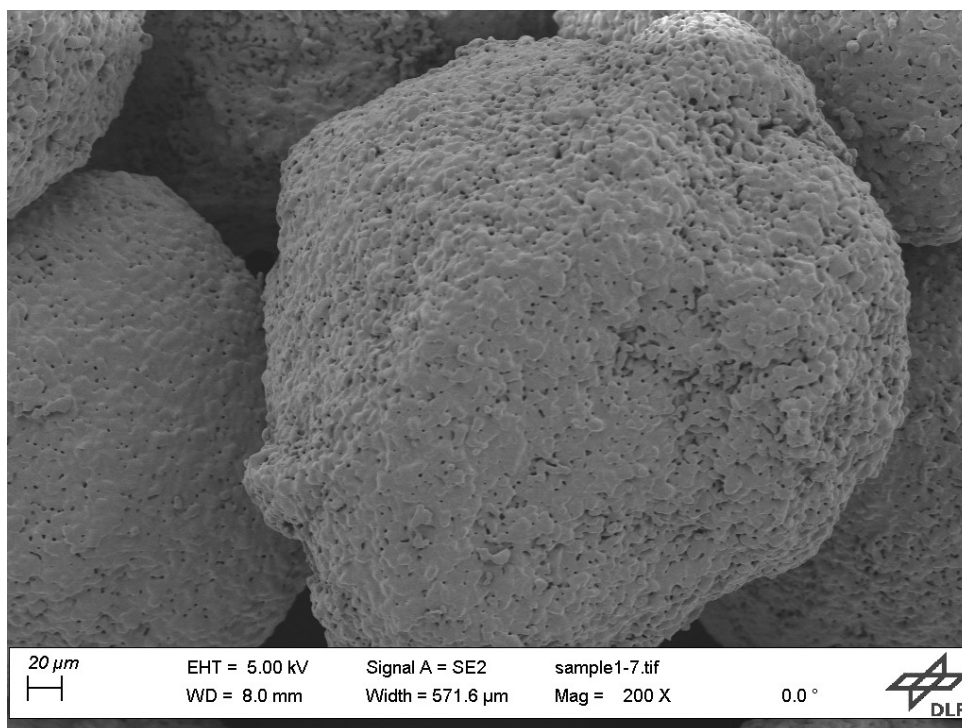


Figure F.7.: Scanning electron microscope image of ceria particle after eight experiments. 200-fold magnified.

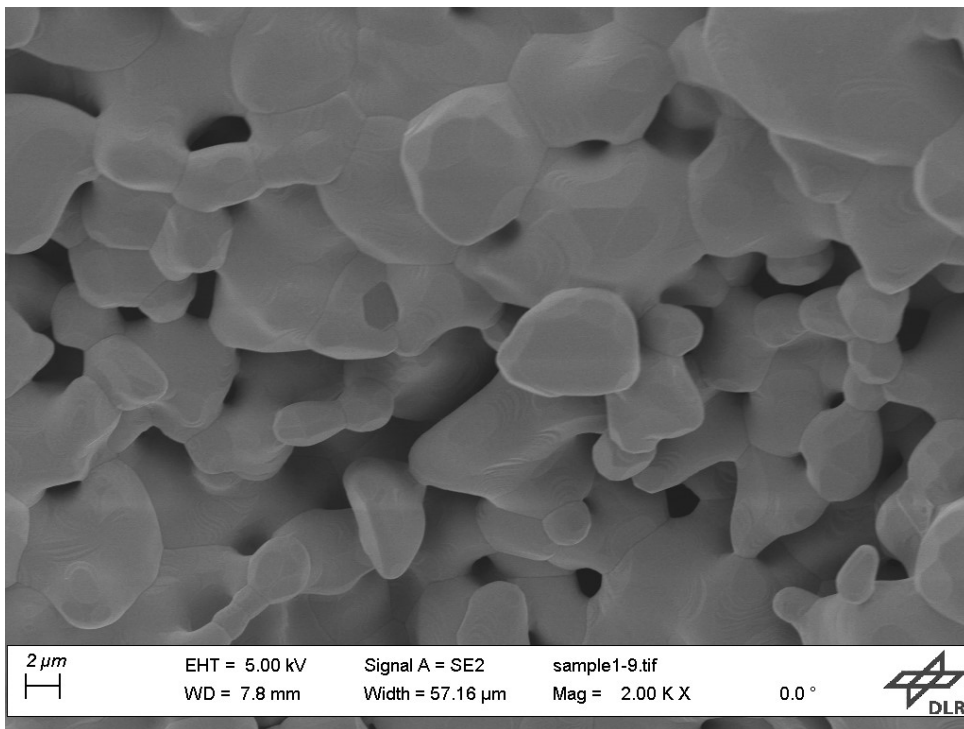


Figure F.8.: Scanning electron microscope image of ceria particle after eight experiments. 2000-fold magnified.

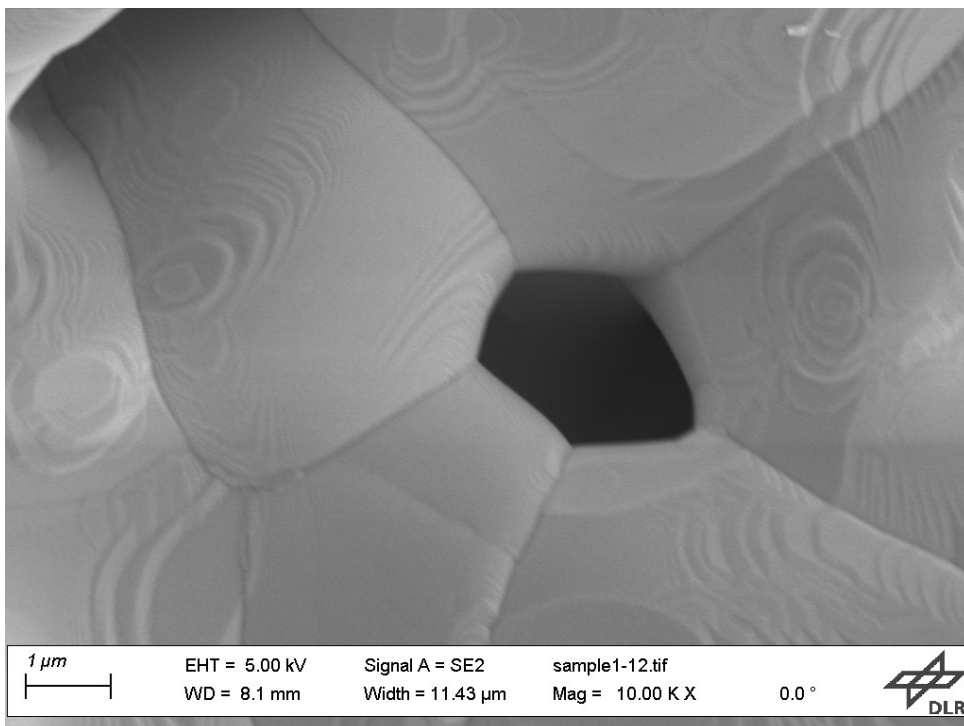


Figure F.9.: Scanning electron microscope image of ceria particle after eight experiments. 10000-fold magnified.

G. Energy-Dispersive X-Ray Spectroscopy of Particles

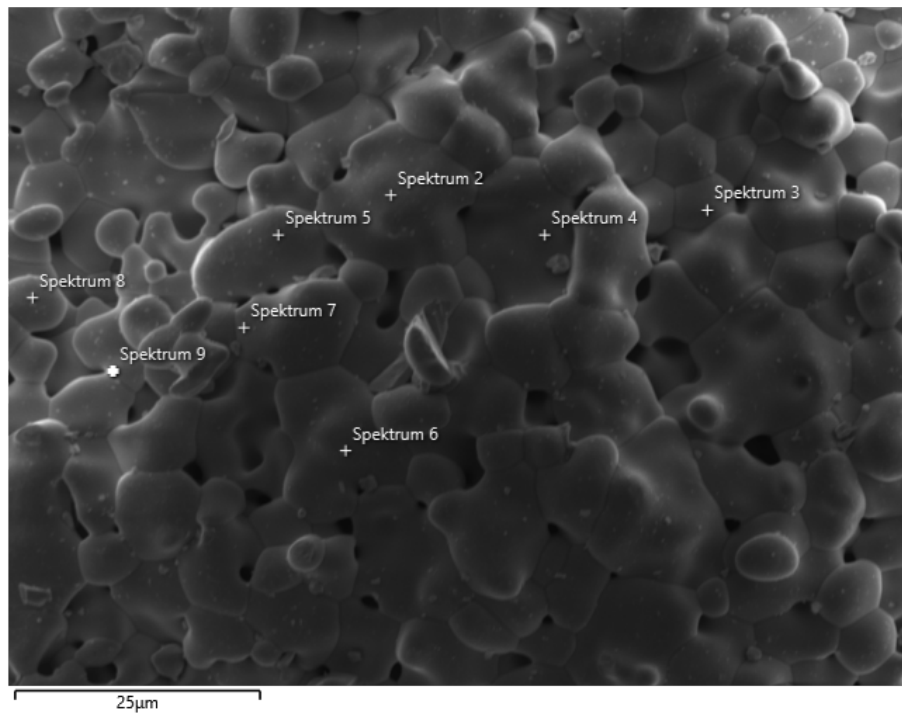


Figure G.1.: Particle surface before experiments with locations at which EDX spectra were recorded.

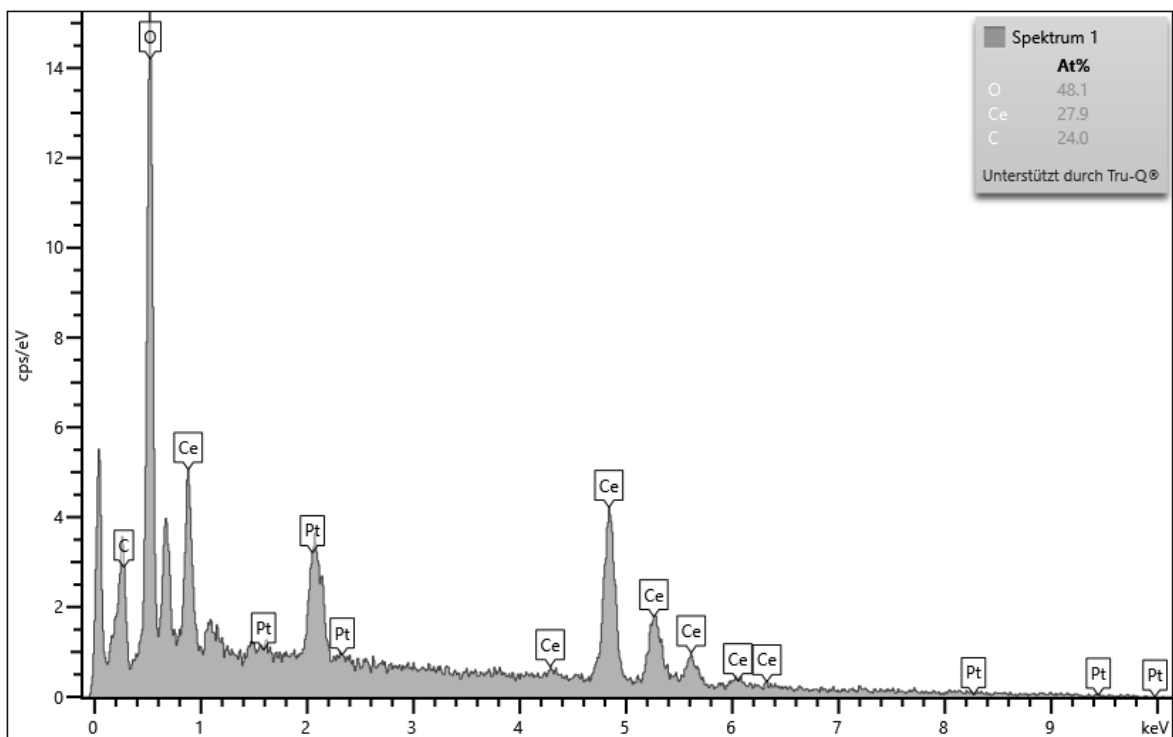


Figure G.2.: EDX of spectrum 1 in Figure G.1. Sample: Particles as before experiments.

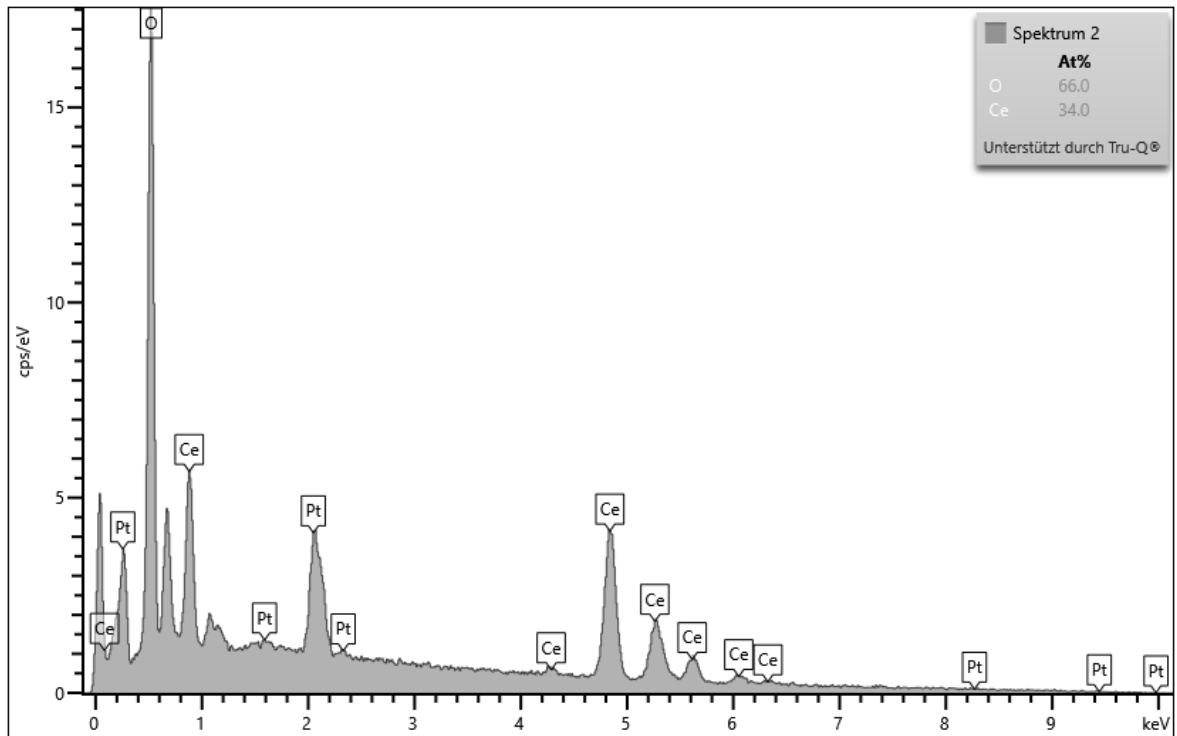


Figure G.3.: EDX of spectrum 2 in Figure G.1. Sample: Particles as before experiments.

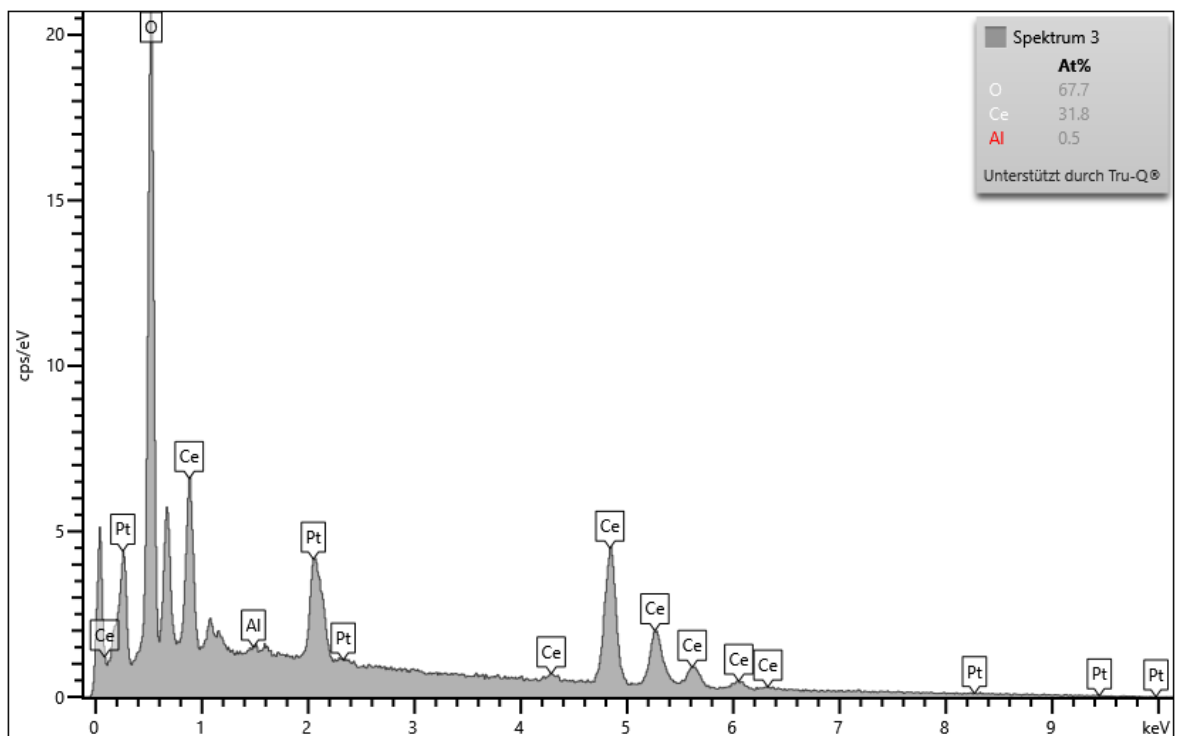


Figure G.4.: EDX of spectrum 3 in Figure G.1. Sample: Particles as before experiments.

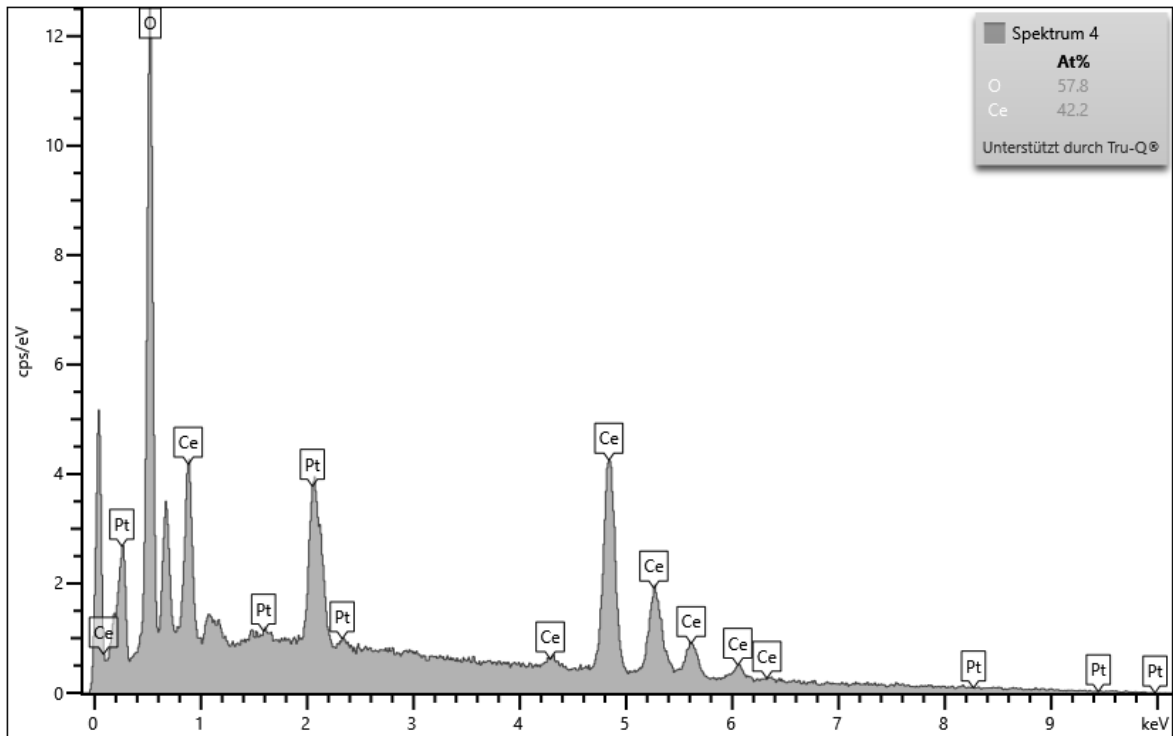


Figure G.5.: EDX of spectrum 4 in Figure G.1. Sample: Particles as before experiments.

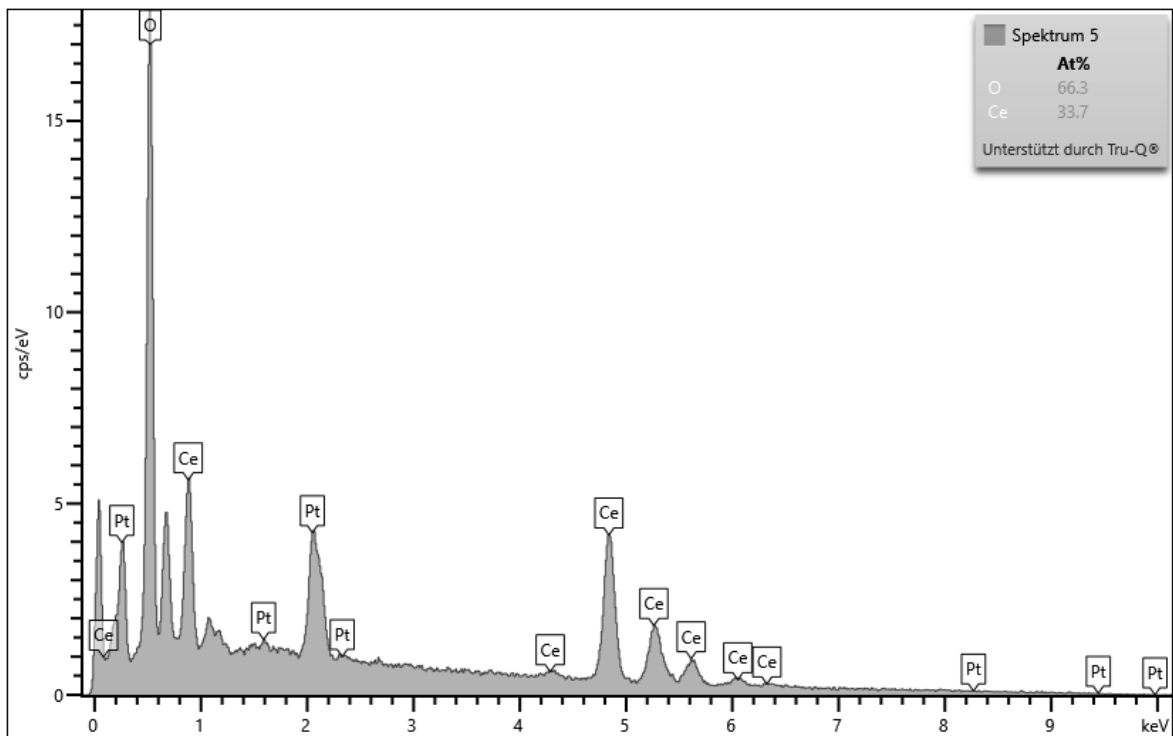


Figure G.6.: EDX of spectrum 5 in Figure G.1. Sample: Particles as before experiments.

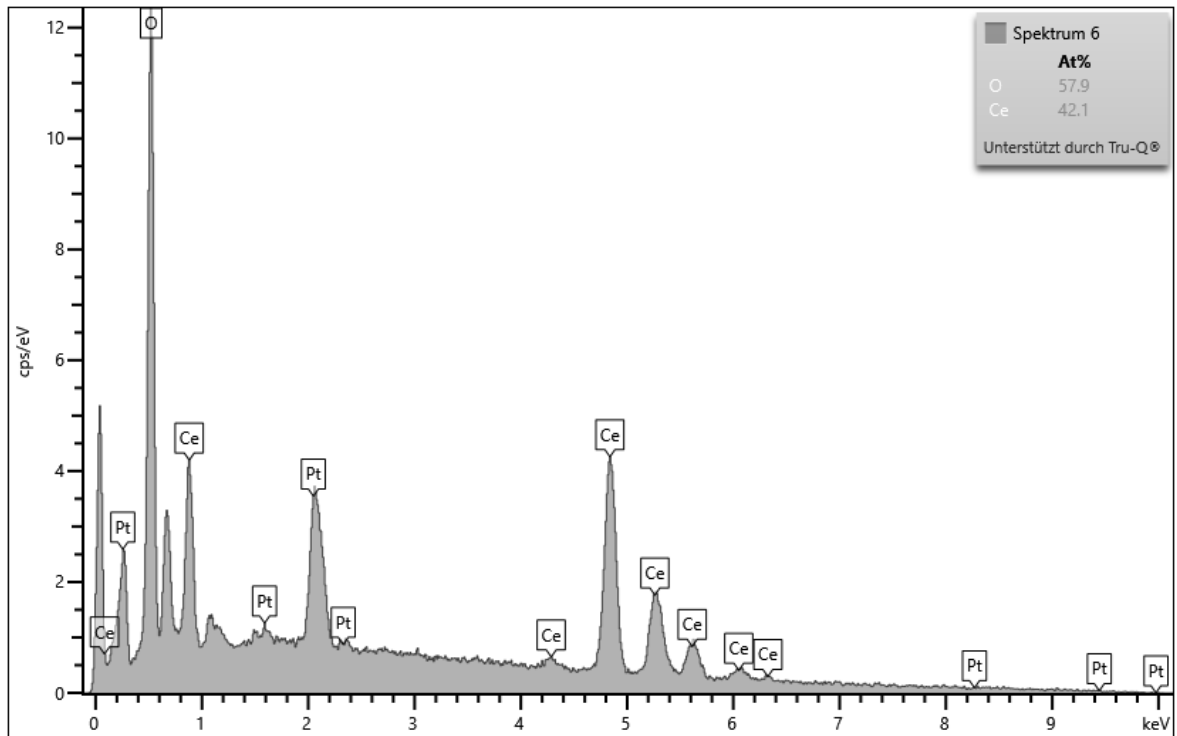


Figure G.7.: EDX of spectrum 6 in Figure G.1. Sample: Particles as before experiments.

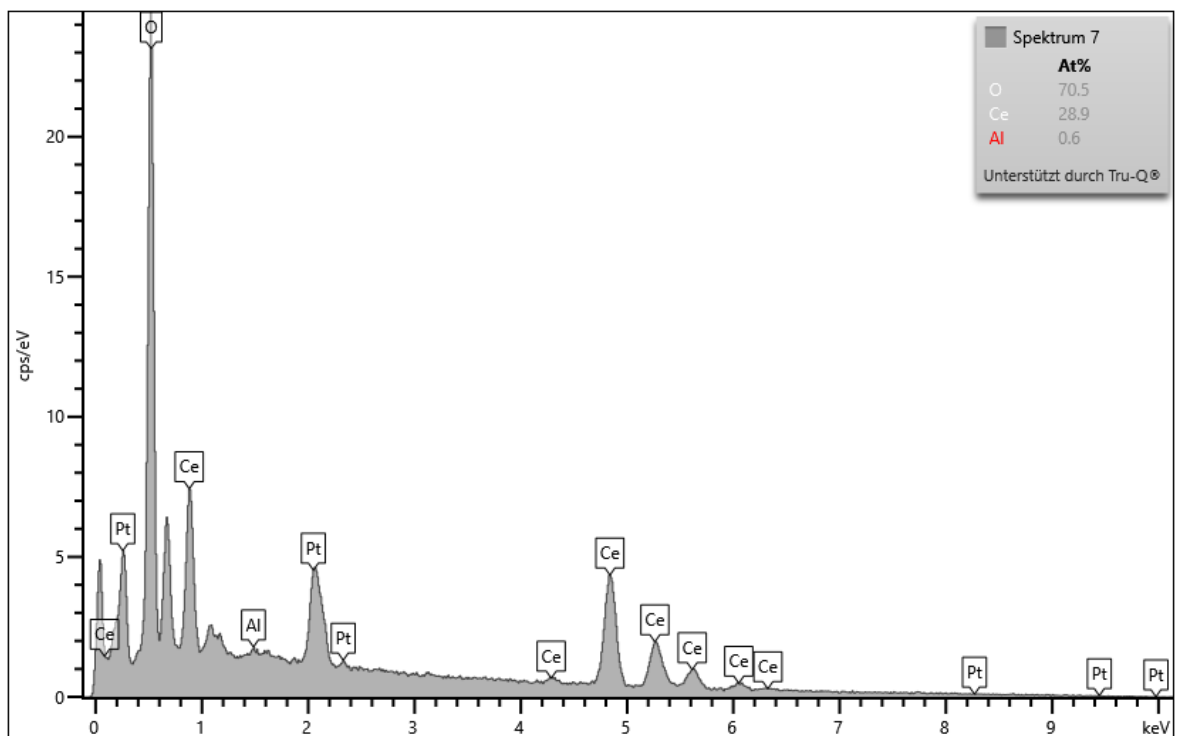


Figure G.8.: EDX of spectrum 7 in Figure G.1. Sample: Particles as before experiments.

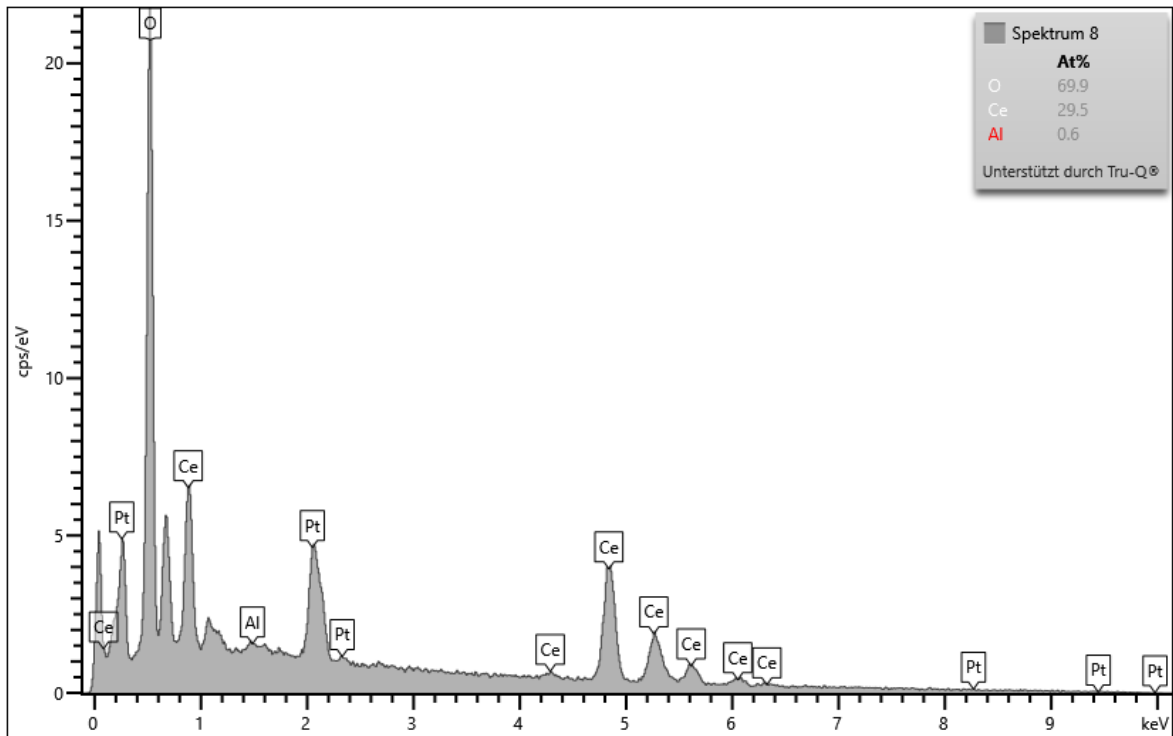


Figure G.9.: EDX of spectrum 8 in Figure G.1. Sample: Particles as before experiments.

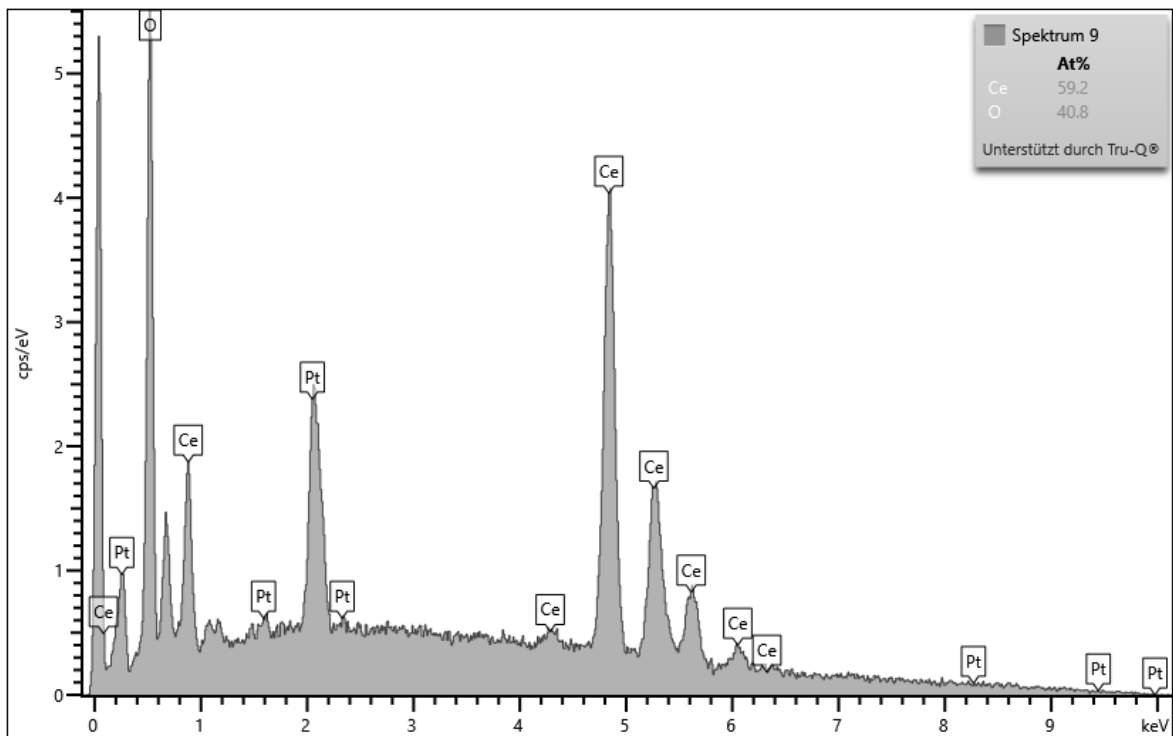


Figure G.10.: EDX of spectrum 9 in Figure G.1. Sample: Particles as before experiments.

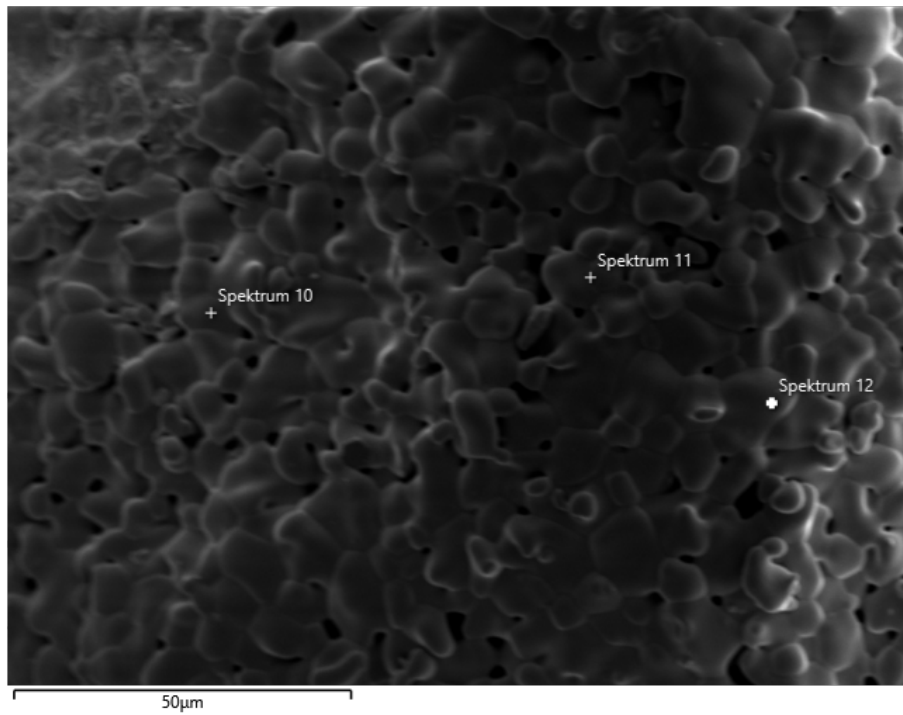


Figure G.11.: Particle surface after one experiment with locations at which EDX spectra were recorded.

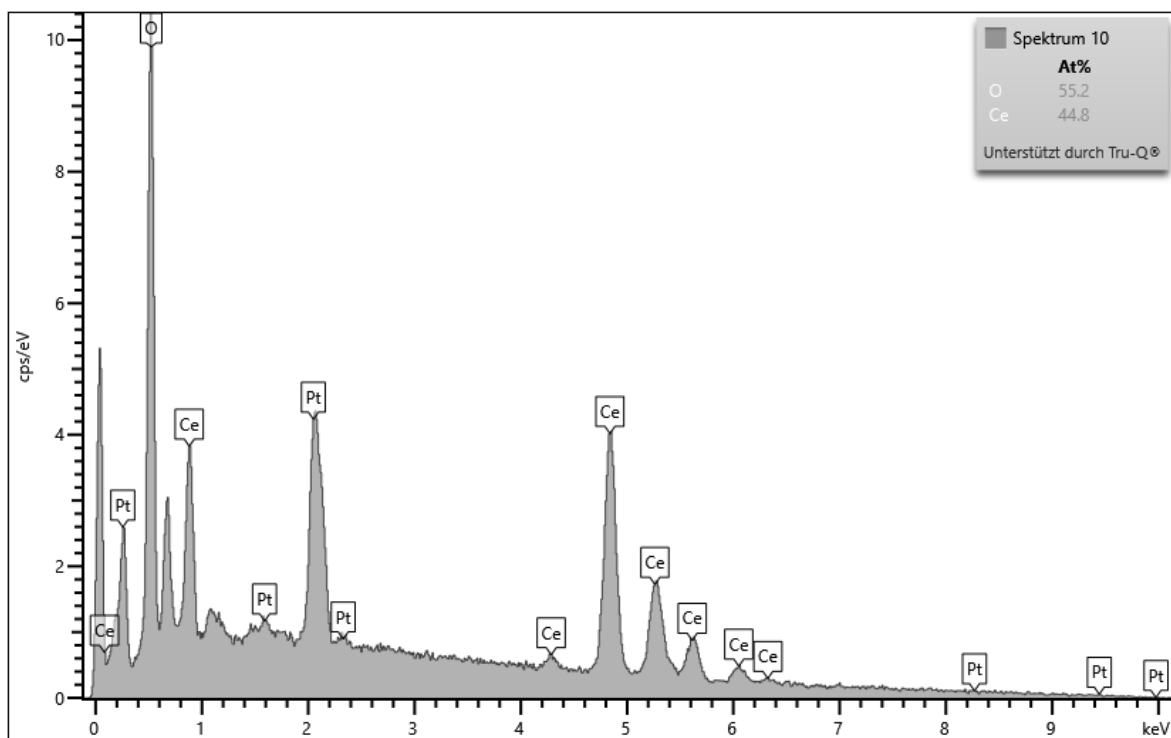


Figure G.12.: EDX of spectrum 10 in Figure G.11. Sample: Particles after one experiment.

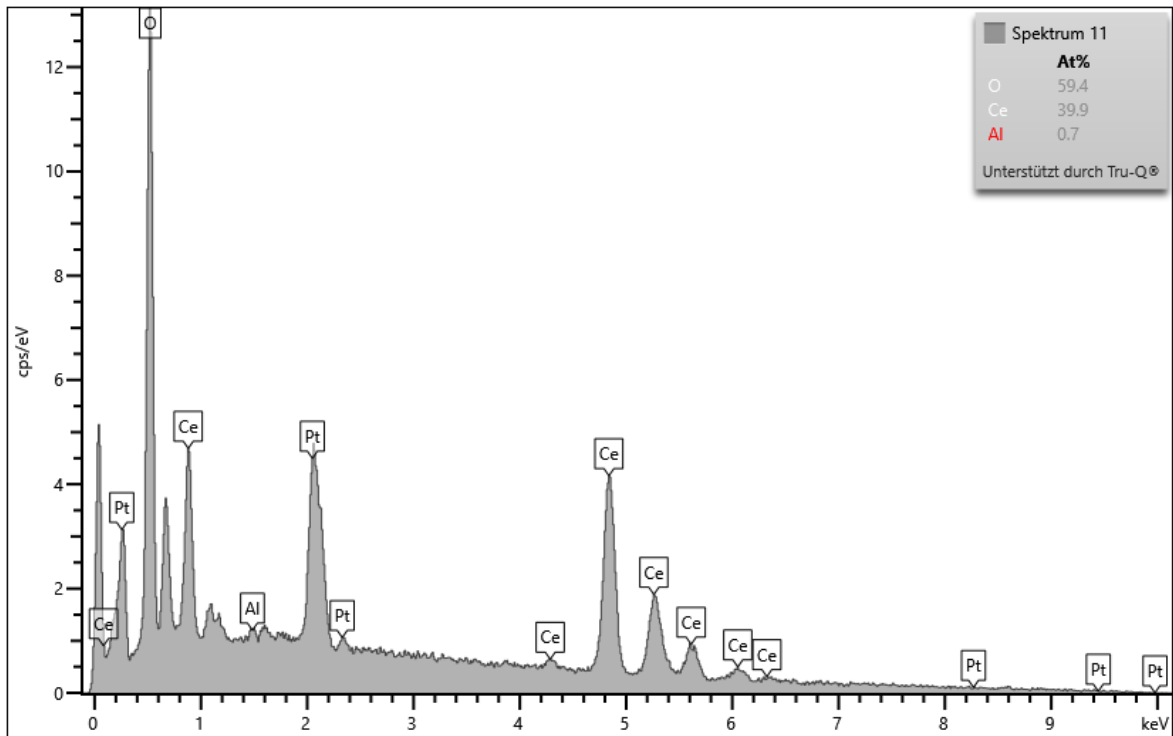


Figure G.13.: EDX of spectrum 11 in Figure G.11. Sample: Particles after one experiment.

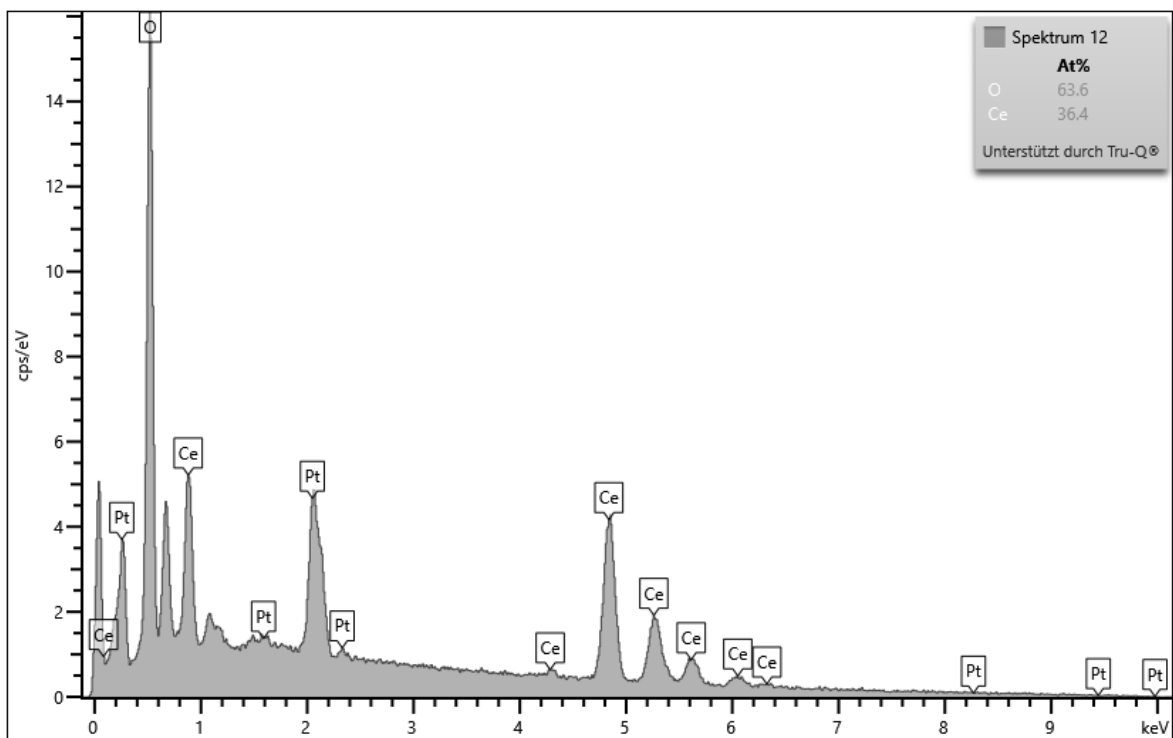


Figure G.14.: EDX of spectrum 12 in Figure G.11. Sample: Particles after one experiment.

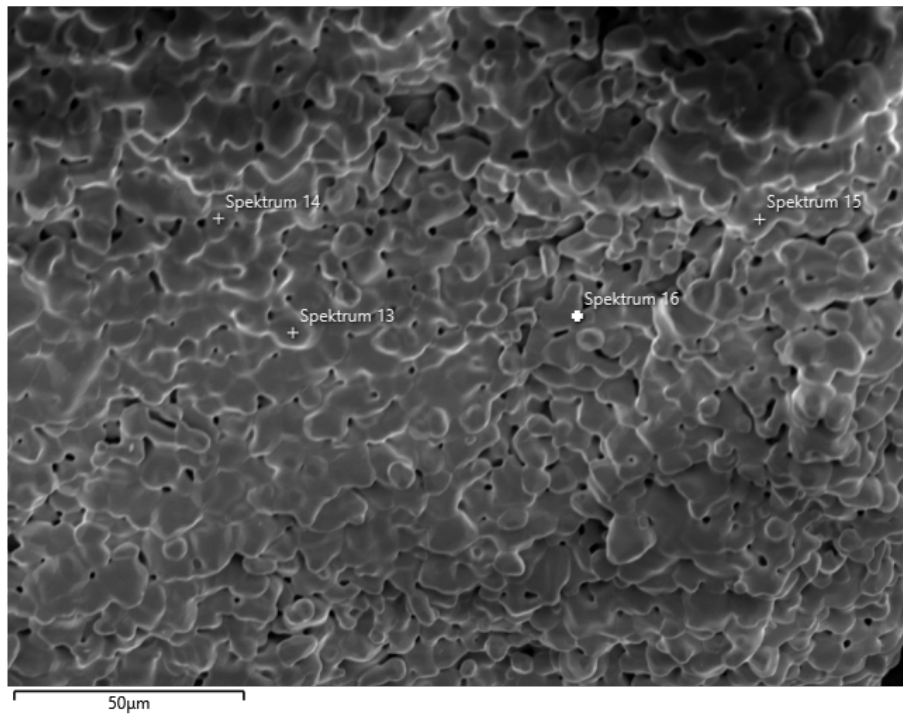


Figure G.15.: Particle surface after eight experiments with locations at which EDX spectra were recorded.

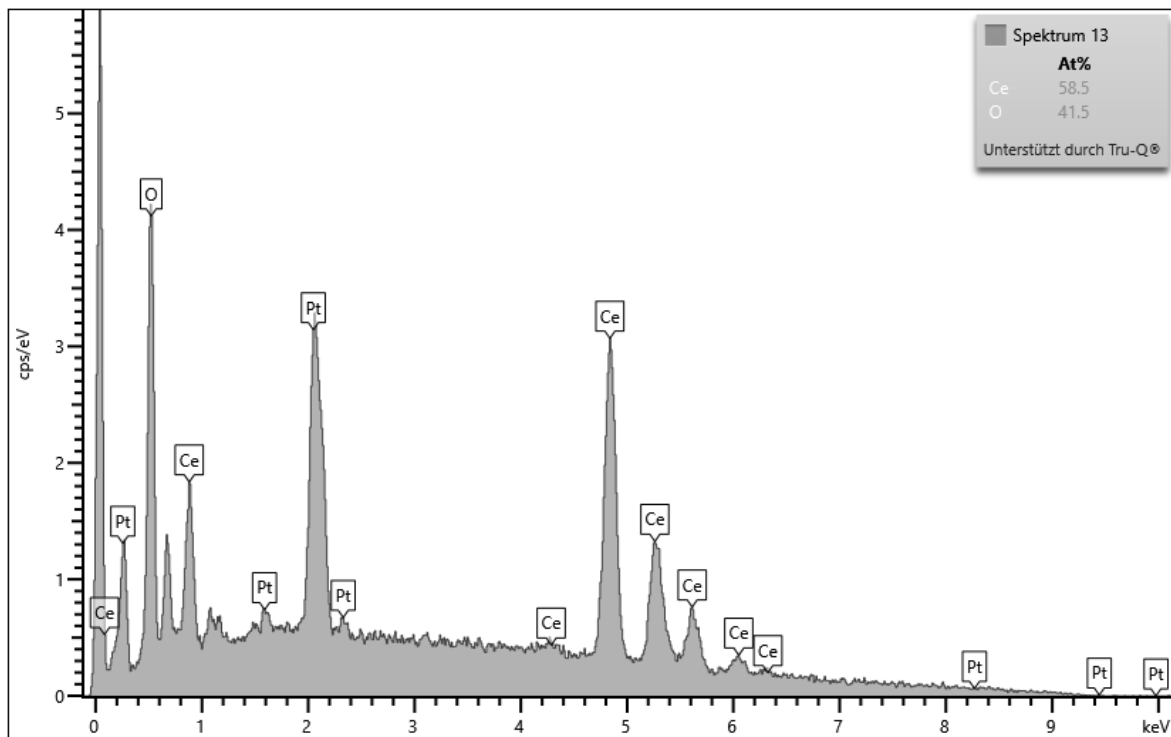


Figure G.16.: EDX of spectrum 13 in Figure G.15. Sample: Particles after eight experiments.

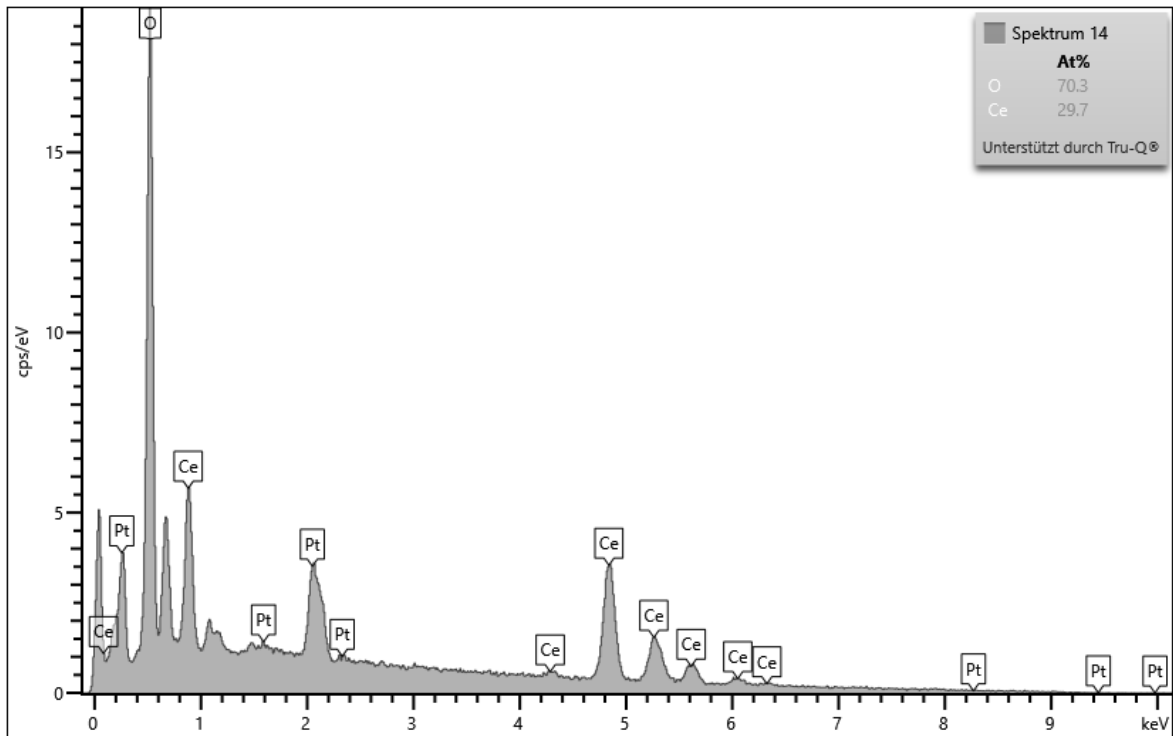


Figure G.17.: EDX of spectrum 14 in Figure G.15. Sample: Particles after eight experiments.

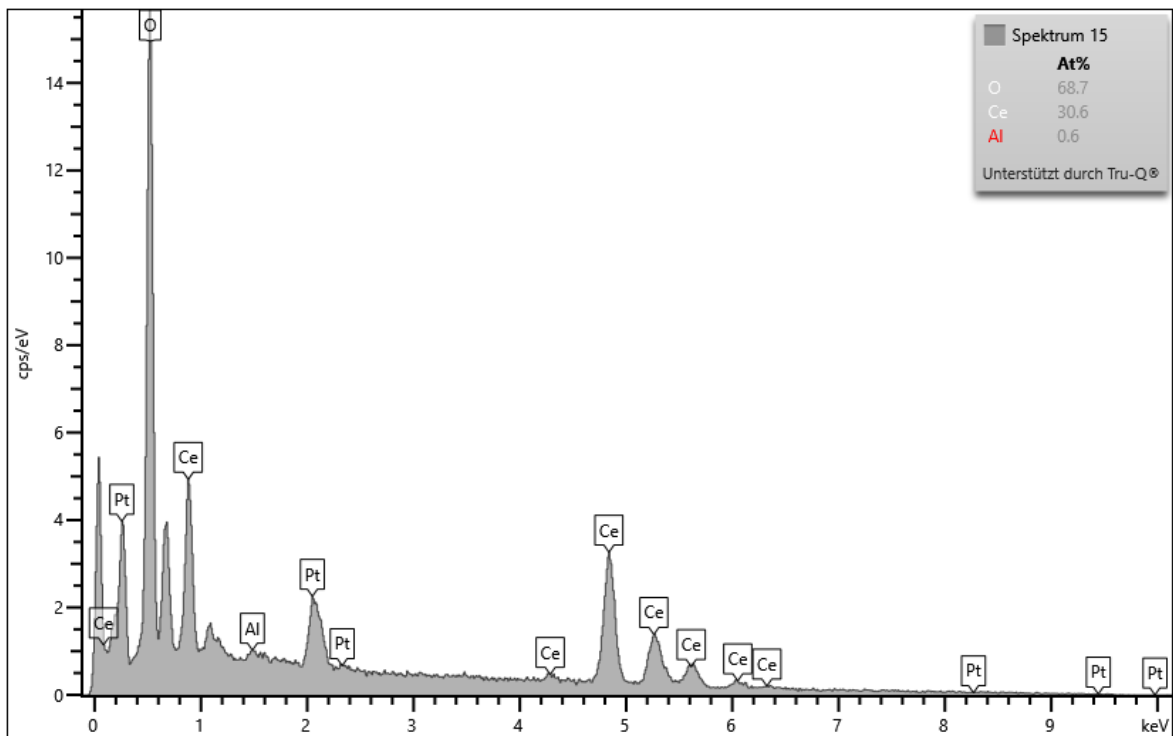


Figure G.18.: EDX of spectrum 15 in Figure G.15. Sample: Particles after eight experiments.

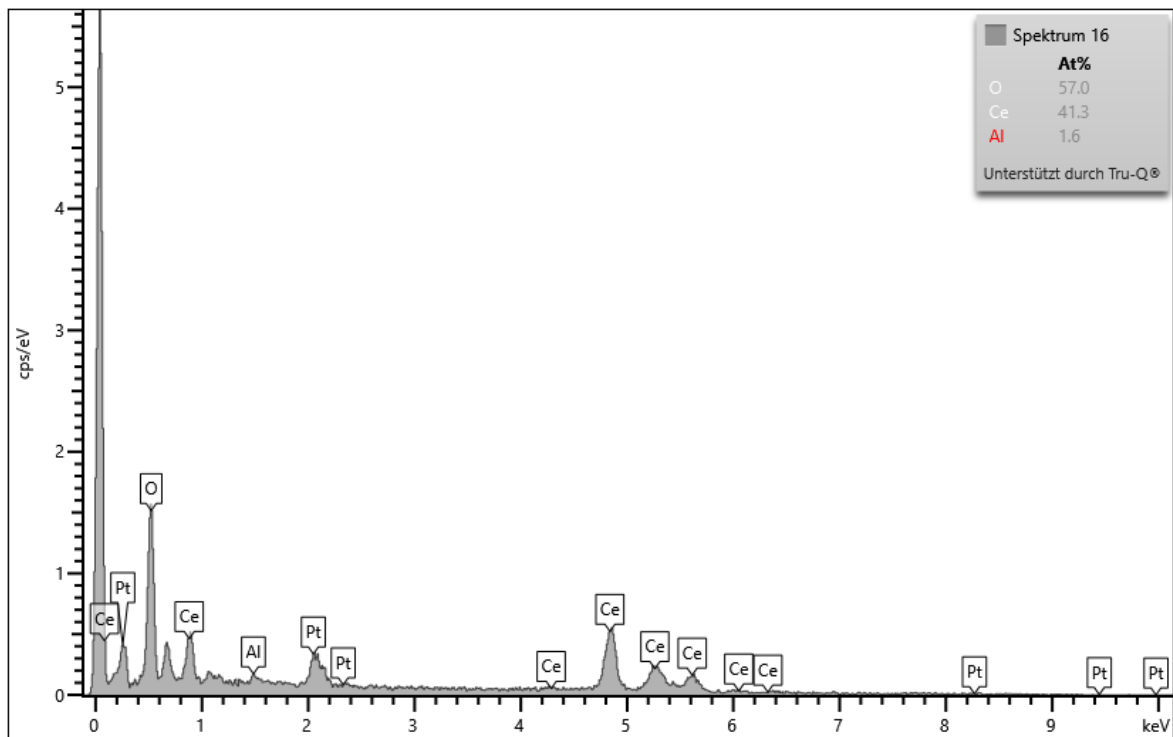


Figure G.19.: EDX of spectrum 16 in Figure G.15. Sample: Particles after eight experiments.

Bibliography

- [1] European Commission, Directorate-General for Mobility and Transport, A Tsamis, E Andrew, H Figg, R Neiva, A Pons, B Baxter, A Humphris-Bach, S Kollamthodi, P Siskos, S Statharas, Y Moysoglou, T Kalokyris, C Stasio, V Holve, M Laoreti, S Mader, and I Skinner. *Evaluation of the White Paper 'Roadmap to a Single European Transport Area - towards a competitive and resource efficient transport system' : final report*. Publications Office, 2021. DOI: 10.2832/157948.
- [2] European Commission, Directorate-General for Mobility and Transport. *White paper on transport : roadmap to a single European transport area : towards a competitive and resource efficient transport system*. Publications Office, 2011. DOI: 10.2832/30955.
- [3] M. Lange, M. Roeb, C. Sattler, and R. Pitz-Paal. „T-S diagram efficiency analysis of two-step thermochemical cycles for solar water splitting under various process conditions“. In: *Energy* 67 (2014), pp. 298–308. ISSN: 0360-5442. DOI: <https://doi.org/10.1016/j.energy.2014.01.112>.
- [4] Stéphane Abanades. „A Review of Oxygen Carrier Materials and Related Thermochemical Redox Processes for Concentrating Solar Thermal Applications“. In: *Materials* 16.9 (2023). ISSN: 1996-1944. DOI: 10.3390/ma16093582.
- [5] Youjun Lu, Liya Zhu, Christos Agrafiotis, Josua Vieten, Martin Roeb, and Christian Sattler. „Solar fuels production: Two-step thermochemical cycles with cerium-based oxides“. In: *Progress in Energy and Combustion Science* 75 (2019), p. 100785. ISSN: 0360-1285. DOI: <https://doi.org/10.1016/j.pecs.2019.100785>.
- [6] Franz Fischer and Hans Tropsch. „Über die Herstellung Synthetischer Ölgemische (Synthol) Durch Aufbau aus Kohlenoxyd und Wasserstoff“. In: *Brennst. Chem* 4 (1923). (German), pp. 276–285.
- [7] Jan Felinks, Stefan Brendelberger, Martin Roeb, Christian Sattler, and Robert Pitz-Paal. „Heat recovery concept for thermochemical processes using a solid heat transfer medium“. In: *Applied Thermal Engineering* 73.1 (2014), pp. 1006–1013. ISSN: 1359-4311. DOI: <https://doi.org/10.1016/j.applthermaleng.2014.08.036>.
- [8] Friedemann Call, Martin Roeb, Martin Schmücker, Christian Sattler, and Robert Pitz-Paal. „Ceria Doped with Zirconium and Lanthanide Oxides to Enhance Solar Thermochemical Production of Fuels“. In: *The Journal of Physical Chemistry C* 119.13 (2015), pp. 6929–6938. DOI: 10.1021/jp508959y.
- [9] Qingqing Jiang, Guilin Zhou, Zongxuan Jiang, and Can Li. „Thermochemical CO₂ splitting reaction with C_xM_{1-x}O_{2-δ} (M=Ti⁴⁺, Sn⁴⁺, Hf⁴⁺, Zr⁴⁺, La³⁺, Y³⁺ and Sm³⁺) solid solutions“. In: *Solar Energy* 99 (2014), pp. 55–66. ISSN: 0038-092X. DOI: <https://doi.org/10.1016/j.solener.2013.10.021>.
- [10] Elysia J. Sheu, Esmail M.A. Mokheimer, and Ahmed F. Ghoniem. „Dry redox reforming hybrid power cycle: Performance analysis and comparison to steam redox reforming“. In: *International Journal of Hydrogen Energy* 40.7 (2015), pp. 2939–2949. ISSN: 0360-3199. DOI: <https://doi.org/10.1016/j.ijhydene.2015.01.018>.

- [11] Elysia J. Sheu and Ahmed F. Ghoniem. „Redox reforming based, integrated solar-natural gas plants: Reforming and thermodynamic cycle efficiency“. In: *International Journal of Hydrogen Energy* 39.27 (2014), pp. 14817–14833. ISSN: 0360-3199. DOI: <https://doi.org/10.1016/j.ijhydene.2014.07.086>.
- [12] Ivan Ermanoski, Nathan P. Siegel, and Ellen B. Stechel. „A New Reactor Concept for Efficient Solar-Thermochemical Fuel Production“. In: *Journal of Solar Energy Engineering* 135.3 (Feb. 2013). 031002. ISSN: 0199-6231. DOI: 10.1115/1.4023356.
- [13] Daniel Marxer, Philipp Furler, Michael Takacs, and Aldo Steinfeld. „Solar thermochemical splitting of CO₂ into separate streams of CO and O₂ with high selectivity, stability, conversion, and efficiency“. In: *Energy Environ. Sci.* 10 (5 2017), pp. 1142–1149. DOI: 10.1039/C6EE03776C.
- [14] J. Lapp, J.H. Davidson, and W. Lipiński. „Efficiency of two-step solar thermochemical non-stoichiometric redox cycles with heat recovery“. In: *Energy* 37.1 (2012). 7th Biennial International Workshop “Advances in Energy Studies”, pp. 591–600. ISSN: 0360-5442. DOI: <https://doi.org/10.1016/j.energy.2011.10.045>.
- [15] Stefan Brendelberger, Philipp Holzemer-Zerhusen, Henrik von Storch, and Christian Sattler. „Performance Assessment of a Heat Recovery System for Monolithic Receiver-Reactors“. In: *Journal of Solar Energy Engineering* 141.2 (Jan. 2019). 021008. ISSN: 0199-6231. DOI: 10.1115/1.4042241.
- [16] Christopher L. Muhich, Samuel Blaser, Marie C. Hoes, and Aldo Steinfeld. „Comparing the solar-to-fuel energy conversion efficiency of ceria and perovskite based thermochemical redox cycles for splitting H₂O and CO₂“. In: *International Journal of Hydrogen Energy* 43.41 (2018), pp. 18814–18831. ISSN: 0360-3199. DOI: <https://doi.org/10.1016/j.ijhydene.2018.08.137>.
- [17] Silvan Siegrist, Henrik von Storch, Martin Roeb, and Christian Sattler. „Moving Brick Receiver-Reactor: A Solar Thermochemical Reactor and Process Design With a Solid-Solid Heat Exchanger and On-Demand Production of Hydrogen and/or Carbon Monoxide“. In: *Journal of Solar Energy Engineering* 141.2 (Jan. 2019). 021009. ISSN: 0199-6231. DOI: 10.1115/1.4042069.
- [18] Tatsuya Kodama and Nobuyuki Gokon. „Thermochemical Cycles for High-Temperature Solar Hydrogen Production“. In: *Chem. Rev.* 107.10 (Oct. 2007), pp. 4048–4077. ISSN: 0009-2665. DOI: 10.1021/cr050188a.
- [19] William C. Chueh, Christoph Falter, Mandy Abbott, Danien Scipio, Philipp Furler, Sossina M. Haile, and Aldo Steinfeld. „High-Flux Solar-Driven Thermochemical Dissociation of CO₂ and H₂O Using Nonstoichiometric Ceria“. In: *Science* 330.6012 (2010), pp. 1797–1801. DOI: 10.1126/science.1197834.
- [20] Philipp Furler, Jonathan Scheffe, Daniel Marxer, Michal Gorbar, Alexander Bonk, Ulrich Vogt, and Aldo Steinfeld. „Thermochemical CO₂ splitting via redox cycling of ceria reticulated foam structures with dual-scale porosities“. In: *Phys. Chem. Chem. Phys.* 16 (22 2014), pp. 10503–10511. DOI: 10.1039/C4CP01172D.
- [21] Martin Roeb, Martina Neises, Nathalie Monnerie, Christian Sattler, and Robert Pitz-Paal. „Technologies and trends in solar power and fuels“. In: *Energy Environ. Sci.* 4 (7 2011), pp. 2503–2511. DOI: 10.1039/C1EE01128F.
- [22] Aldo Steinfeld and Anton Meier. „Solar Fuels and Materials“. In: *Encyclopedia of Energy*. Ed. by Cutler J. Cleveland. New York: Elsevier, 2004, pp. 623–637. ISBN: 978-0-12-176480-7. DOI: <https://doi.org/10.1016/B0-12-176480-X/00322-3>.

- [23] Henrik von Storch, Martin Roeb, Hannes Stadler, Christian Sattler, André Bardow, and Bernhard Hoffschmidt. „On the assessment of renewable industrial processes: Case study for solar co-production of methanol and power“. In: *Applied Energy* 183 (2016), pp. 121–132. ISSN: 0306-2619. DOI: <https://doi.org/10.1016/j.apenergy.2016.08.141>.
- [24] „Section 10 - Solar“. In: *Handbook of Energy*. Ed. by Cutler J. Cleveland and Christopher Morris. Amsterdam: Elsevier, 2013, pp. 405–450. ISBN: 978-0-08-046405-3. DOI: <https://doi.org/10.1016/B978-0-08-046405-3.00010-3>.
- [25] T. Kodama. „High-temperature solar chemistry for converting solar heat to chemical fuels“. In: *Progress in Energy and Combustion Science* 29.6 (2003), pp. 567–597. ISSN: 0360-1285. DOI: [https://doi.org/10.1016/S0360-1285\(03\)00059-5](https://doi.org/10.1016/S0360-1285(03)00059-5).
- [26] Alberto de la Calle and Alicia Bayon. „Annual performance of a thermochemical solar syngas production plant based on non-stoichiometric CeO₂“. In: *International Journal of Hydrogen Energy* 44.3 (2019), pp. 1409–1424. ISSN: 0360-3199. DOI: <https://doi.org/10.1016/j.ijhydene.2018.11.076>.
- [27] Stefan Brendelberger, Andreas Rosenstiel, Anton Lopez-Roman, Cristina Prieto, and Christian Sattler. „Performance analysis of operational strategies for monolithic receiver-reactor arrays in solar thermochemical hydrogen production plants“. In: *International Journal of Hydrogen Energy* 45.49 (2020). Progress in Hydrogen Production and Utilization, pp. 26104–26116. ISSN: 0360-3199. DOI: <https://doi.org/10.1016/j.ijhydene.2020.06.191>.
- [28] Erik Koepf, Stefan Zoller, Salvador Luque, Martin Thelen, Stefan Brendelberger, José González-Aguilar, Manuel Romero, and Aldo Steinfeld. „Liquid fuels from concentrated sunlight: An overview on development and integration of a 50 kW solar thermochemical reactor and high concentration solar field for the SUN-to-LIQUID project“. In: *AIP Conference Proceedings* 2126.1 (2019), p. 180012. DOI: 10.1063/1.5117692.
- [29] Manuel Romero, José González-Aguilar, Andreas Sizmann, Valentin Batteiger, Christoph Falter, Aldo Steinfeld, Stefan Zoller, Stefan Brendelberger, and Dick Liefstink. „Solar-driven thermochemical production of sustainable liquid fuels from H₂O and CO₂ in a heliostat field“. In: *Proceedings of the ISES Solar World Congress*. 2019.
- [30] Meng Tian, Yuehong Su, Hongfei Zheng, Gang Pei, Guiqiang Li, and Saffa Riffat. „A review on the recent research progress in the compound parabolic concentrator (CPC) for solar energy applications“. In: *Renewable and Sustainable Energy Reviews* 82 (2018), pp. 1272–1296. ISSN: 1364-0321. DOI: <https://doi.org/10.1016/j.rser.2017.09.050>.
- [31] Mark Schmitz, Peter Schwarzbözl, Reiner Buck, and Robert Pitz-Paal. „Assessment of the potential improvement due to multiple apertures in central receiver systems with secondary concentrators“. In: *Solar Energy* 80.1 (2006), pp. 111–120. ISSN: 0038-092X. DOI: <https://doi.org/10.1016/j.solener.2005.02.012>.
- [32] J.-P. Säck, S. Breuer, P. Cotelli, A. Houaijia, M. Lange, M. Wullenkord, C. Spenke, M. Roeb, and Chr. Sattler. „High temperature hydrogen production: Design of a 750KW demonstration plant for a two step thermochemical cycle“. In: *Solar Energy* 135 (2016), pp. 232–241. ISSN: 0038-092X. DOI: <https://doi.org/10.1016/j.solener.2016.05.059>.
- [33] Henrik von Storch, Hannes Stadler, Martin Roeb, and Bernhard Hoffschmidt. „Efficiency potential of indirectly heated solar reforming with open volumetric solar receiver“. In: *Applied Thermal Engineering* 87 (2015), pp. 297–304. ISSN: 1359-4311. DOI: <https://doi.org/10.1016/j.applthermaleng.2015.05.026>.

- [34] Henrik von Storch, Martin Roeb, Hannes Stadler, Christian Sattler, and Bernhard Hoffschmidt. „Available online Efficiency potential of indirectly heated solar reforming with different types of solar air receivers“. In: *Applied Thermal Engineering* 92 (2016), pp. 202–209. ISSN: 1359-4311. DOI: <https://doi.org/10.1016/j.applthermaleng.2015.09.065>.
- [35] Sebastian Richter, Stefan Brendelberger, Felix Gersdorf, Tobias Oschmann, and Christian Sattler. „Demonstration Reactor System for the Indirect Solar-Thermochemical Reduction of Redox Particles—The Particle Mix Reactor“. In: *Journal of Energy Resources Technology* 142.5 (Mar. 2020). 050911. ISSN: 0195-0738. DOI: 10.1115/1.4046315.
- [36] Johannes Grobbel, Stefan Brendelberger, Christian Sattler, and Robert Pitz-Paal. „Heat transfer in a directly irradiated ceria particle bed under vacuum conditions“. In: *Solar Energy* 158 (2017), pp. 737–745. ISSN: 0038-092X. DOI: <https://doi.org/10.1016/j.solener.2017.10.022>.
- [37] Elysia J. Sheu and Alexander Mitsos. „Optimization of a hybrid solar-fossil fuel plant: Solar steam reforming of methane in a combined cycle“. In: *Energy* 51 (2013), pp. 193–202. ISSN: 0360-5442. DOI: <https://doi.org/10.1016/j.energy.2013.01.027>.
- [38] A. Steinfeld, P. Kuhn, and J. Karni. „High-temperature solar thermochemistry: Production of iron and synthesis gas by Fe₃O₄-reduction with methane“. In: *Energy* 18.3 (1993), pp. 239–249. ISSN: 0360-5442. DOI: [https://doi.org/10.1016/0360-5442\(93\)90108-P](https://doi.org/10.1016/0360-5442(93)90108-P).
- [39] Edward A. Fletcher and Roger L. Moen. „Hydrogen and Oxygen from Water“. In: *Science* 197.4308 (1977), pp. 1050–1056. DOI: 10.1126/science.197.4308.1050.
- [40] Christoph P. Falter, Andreas Sizmann, and Robert Pitz-Paal. „Modular reactor model for the solar thermochemical production of syngas incorporating counter-flow solid heat exchange“. In: *Solar Energy* 122 (2015), pp. 1296–1308. ISSN: 0038-092X. DOI: <https://doi.org/10.1016/j.solener.2015.10.042>.
- [41] Christoph P. Falter and Robert Pitz-Paal. „A generic solar-thermochemical reactor model with internal heat diffusion for counter-flow solid heat exchange“. In: *Solar Energy* 144 (2017), pp. 569–579. ISSN: 0038-092X. DOI: <https://doi.org/10.1016/j.solener.2017.01.063>.
- [42] S. Hurst. „Production of hydrogen by the steam-iron method“. In: *Oil and Soap* 16.2 (1939), pp. 29–35. DOI: <https://doi.org/10.1007/BF02543209>.
- [43] Viktor Hacker, Robert Fankhauser, Gottfried Faleschini, Heidrun Fuchs, Kurt Friedrich, Michael Muhr, and Karl Kordes. „Hydrogen production by steam-iron process“. In: *Journal of Power Sources* 86.1 (2000), pp. 531–535. ISSN: 0378-7753. DOI: [https://doi.org/10.1016/S0378-7753\(99\)00458-9](https://doi.org/10.1016/S0378-7753(99)00458-9).
- [44] Shiyi Chen, Qiliang Shi, Zhipeng Xue, Xiaoyan Sun, and Wenguo Xiang. „Experimental investigation of chemical-looping hydrogen generation using Al₂O₃ or TiO₂-supported iron oxides in a batch fluidized bed“. In: *International Journal of Hydrogen Energy* 36.15 (2011), pp. 8915–8926. ISSN: 0360-3199. DOI: <https://doi.org/10.1016/j.ijhydene.2011.04.204>.
- [45] James E. Funk. „Thermochemical hydrogen production: past and present“. In: *International Journal of Hydrogen Energy* 26.3 (2001), pp. 185–190. ISSN: 0360-3199. DOI: [https://doi.org/10.1016/S0360-3199\(00\)00062-8](https://doi.org/10.1016/S0360-3199(00)00062-8).

- [46] William C Chueh and Sossina M Haile. „A thermochemical study of ceria: exploiting an old material for new modes of energy conversion and CO₂ mitigation“. In: *Philosophical Transactions of the Royal Society A: Mathematical, Physical and Engineering Sciences* 368.1923 (2010), pp. 3269–3294. DOI: 10.1098/rsta.2010.0114.
- [47] S. Yalçın. „A review of nuclear hydrogen production“. In: *International Journal of Hydrogen Energy* 14.8 (1989). WHEC-VII papers not included in the proceedings, pp. 551–561. ISSN: 0360-3199. DOI: [https://doi.org/10.1016/0360-3199\(89\)90113-4](https://doi.org/10.1016/0360-3199(89)90113-4).
- [48] B. Bulfin, A. J. Lowe, K. A. Keogh, B. E. Murphy, O. Lübben, S. A. Krasnikov, and I. V. Shvets. „Analytical Model of CeO₂ Oxidation and Reduction“. In: *The Journal of Physical Chemistry C* 117.46 (2013), pp. 24129–24137. DOI: 10.1021/jp406578z.
- [49] B. Bulfin, F. Call, J. Vieten, M. Roeb, C. Sattler, and I. V. Shvets. „Oxidation and Reduction Reaction Kinetics of Mixed Cerium Zirconium Oxides“. In: *The Journal of Physical Chemistry C* 120.4 (2016), pp. 2027–2035. DOI: 10.1021/acs.jpcc.5b08729.
- [50] R.J. Panlener, R.N. Blumenthal, and J.E. Garnier. „A thermodynamic study of nonstoichiometric cerium dioxide“. In: *Journal of Physics and Chemistry of Solids* 36.11 (1975), pp. 1213–1222. ISSN: 0022-3697. DOI: [https://doi.org/10.1016/0022-3697\(75\)90192-4](https://doi.org/10.1016/0022-3697(75)90192-4).
- [51] Y. S. Touloukian and E. H. Buyco. „Specific Heat - Nonmetallic Solids“. In: *Thermophysical Properties of Matter - The TPRC Data Series*. Ed. by Y. S. Touloukian and C. Y. Ho. Vol. 5. IFI/Plenum Data Corporation, 1970.
- [52] Jonathan R. Scheffe, David Weibel, and Aldo Steinfeld. „Lanthanum–Strontium–Manganese Perovskites as Redox Materials for Solar Thermochemical Splitting of H₂O and CO₂“. In: *Energy & Fuels* 27.8 (2013), pp. 4250–4257. DOI: 10.1021/ef301923h.
- [53] Kyle M. Allen, Eric N. Coker, Nick Auyeung, and James F. Klausner. „Cobalt Ferrite in YSZ for Use as Reactive Material in Solar Thermochemical Water and Carbon Dioxide Splitting, Part I: Material Characterization“. In: *JOM* 65.12 (2013), pp. 1670–1681. ISSN: 1543-1851. DOI: 10.1007/s11837-013-0704-2.
- [54] M. Neises, M. Roeb, M. Schmücker, C. Sattler, and R. Pitz-Paal. „Kinetic investigations of the hydrogen production step of a thermochemical cycle using mixed iron oxides coated on ceramic substrates“. In: *International Journal of Energy Research* 34.8 (2010). cited By 56, pp. 651–661. DOI: 10.1002/er.1565.
- [55] P. G. Loutzenhiser, M. E. Gálvez, I. Hischer, A. Stamatiou, A. Frei, and A. Steinfeld. „CO₂ Splitting via Two-Step Solar Thermochemical Cycles with Zn/ZnO and FeO/Fe₃O₄ Redox Reactions II: Kinetic Analysis“. In: *Energy & Fuels* 23.5 (2009), pp. 2832–2839. DOI: 10.1021/ef801142b.
- [56] B. Bulfin, L. Hoffmann, L. de Oliveira, N. Knoblauch, F. Call, M. Roeb, C. Sattler, and M. Schmücker. „Statistical thermodynamics of non-stoichiometric ceria and ceria zirconia solid solutions“. In: *Phys. Chem. Chem. Phys.* 18 (33 2016), pp. 23147–23154. DOI: 10.1039/C6CP03158G.
- [57] Alex Le Gal, Stéphane Abanades, Nicolas Bion, Thierry Le Mercier, and Virginie Harlé. „Reactivity of Doped Ceria-Based Mixed Oxides for Solar Thermochemical Hydrogen Generation via Two-Step Water-Splitting Cycles“. In: *Energy & Fuels* 27.10 (2013), pp. 6068–6078. DOI: 10.1021/ef4014373.
- [58] Asim Riaz, Christopher I. Bodger, Jingjing Chen, Adrian Lowe, Takuya Tsuzuki, and Wojciech Lipiński. „Redox Performance of Ceria–Vanadia Mixed-Phase Reticulated Porous Ceramics for Solar Thermochemical Syngas Production“. In: *Energy & Fuels* 35.20 (2021), pp. 16791–16798. DOI: 10.1021/acs.energyfuels.1c01856.

- [59] Peter G. Loutzenhiser, Anton Meier, and Aldo Steinfeld. „Review of the Two-Step H₂O/CO₂-Splitting Solar Thermochemical Cycle Based on Zn/ZnO Redox Reactions“. In: *Materials* 3.11 (2010), pp. 4922–4938. ISSN: 1996-1944. DOI: 10.3390/ma3114922.
- [60] R. Müller and A. Steinfeld. „H₂O-splitting thermochemical cycle based on ZnO/Zn-redox: Quenching the effluents from the ZnO dissociation“. In: *Chemical Engineering Science* 63.1 (2008), pp. 217–227. ISSN: 0009-2509. DOI: <https://doi.org/10.1016/j.ces.2007.09.034>.
- [61] Anthony H. McDaniel, Elizabeth C. Miller, Darwin Arifin, Andrea Ambrosini, Eric N. Coker, Ryan O’Hayre, William C. Chueh, and Jianhua Tong. „Sr- and Mn-doped LaAlO₃- δ for solar thermochemical H₂ and CO production“. In: *Energy Environ. Sci.* 6 (8 2013), pp. 2424–2428. DOI: 10.1039/C3EE41372A.
- [62] Xianglei Liu, Tong Wang, Ke Gao, Xianguang Meng, Qiao Xu, Chao Song, Zhonghui Zhu, Hangbin Zheng, Yong Hao, and Yimin Xuan. „Ca- and Ga-Doped LaMnO₃ for Solar Thermochemical CO₂ Splitting with High Fuel Yield and Cycle Stability“. In: *ACS Applied Energy Materials* 4.9 (2021), pp. 9000–9012. DOI: 10.1021/acsaem.1c01274.
- [63] M. Takacs, S. Ackermann, A. Bonk, M. Neises-von Puttkamer, Ph. Haueter, J. R. Scheffe, U. F. Vogt, and A. Steinfeld. „Splitting CO₂ with a ceria-based redox cycle in a solar-driven thermogravimetric analyzer“. In: *AIChE Journal* 63.4 (2017), pp. 1263–1271. DOI: <https://doi.org/10.1002/aic.15501>.
- [64] Stefan Brendelberger, Martin Roeb, Matthias Lange, and Christian Sattler. „Counter flow sweep gas demand for the ceria redox cycle“. In: *Solar Energy* 122 (2015), pp. 1011–1022. ISSN: 0038-092X. DOI: <https://doi.org/10.1016/j.solener.2015.10.036>.
- [65] Stefan Zoller, Erik Koepf, Dustin Nizamian, Marco Stephan, Adriano Patané, Philipp Haueter, Manuel Romero, José González-Aguilar, Dick Lieftink, Ellart de Wit, Stefan Brendelberger, Andreas Sizmann, and Aldo Steinfeld. „A solar tower fuel plant for the thermochemical production of kerosene from H₂O and CO₂“. In: *Joule* 6.7 (2022), pp. 1606–1616. ISSN: 2542-4351. DOI: <https://doi.org/10.1016/j.joule.2022.06.012>.
- [66] Marie Hoes, Simon Ackermann, David Theiler, Philipp Furler, and Aldo Steinfeld. „Additive-Manufactured Ordered Porous Structures Made of Ceria for Concentrating Solar Applications“. In: *Energy Technology* 7.9 (2019), p. 1900484. DOI: <https://doi.org/10.1002/ente.201900484>.
- [67] Sha Li, Vincent M. Wheeler, Peter B. Kreider, and Wojciech Lipiński. „Thermodynamic Analyses of Fuel Production via Solar-Driven Non-stoichiometric Metal Oxide Redox Cycling. Part 1. Revisiting Flow and Equilibrium Assumptions“. In: *Energy & Fuels* 32.10 (2018), pp. 10838–10847. DOI: 10.1021/acs.energyfuels.8b02081.
- [68] M. Kawabe, H. Ono, T. Sano, M. Tsuji, and Y. Tamaura. „Thermochemical oxygen pump with praseodymium oxides using a temperature-swing at 403–873 K“. In: *Energy* 22.11 (1997), pp. 1041–1049. ISSN: 0360-5442. DOI: [https://doi.org/10.1016/S0360-5442\(97\)00044-3](https://doi.org/10.1016/S0360-5442(97)00044-3).
- [69] Miriam Ezbiri, Kyle M. Allen, Maria E. Gálvez, Ronald Michalsky, and Aldo Steinfeld. „Design Principles of Perovskites for Thermochemical Oxygen Separation“. In: *ChemSusChem* 8.11 (2015), pp. 1966–1971. DOI: <https://doi.org/10.1002/cssc.201500239>.
- [70] Stefan Brendelberger, Henrik von Storch, Brendan Bulfin, and Christian Sattler. „Vacuum pumping options for application in solar thermochemical redox cycles – Assessment of mechanical-, jet- and thermochemical pumping systems“. In: *Solar Energy* 141 (2017), pp. 91–102. ISSN: 0038-092X. DOI: <https://doi.org/10.1016/j.solener.2016.11.023>.

- [71] Stefan Brendelberger, Josua Vieten, Muralimohan Juttu Vidyasagar, Martin Roeb, and Christian Sattler. „Demonstration of thermochemical oxygen pumping for atmosphere control in reduction reactions“. In: *Solar Energy* 170 (2018), pp. 273–279. ISSN: 0038-092X. DOI: <https://doi.org/10.1016/j.solener.2018.05.063>.
- [72] Stefan Brendelberger, Josua Vieten, Martin Roeb, and Christian Sattler. „Thermochemical oxygen pumping for improved hydrogen production in solar redox cycles“. In: *International Journal of Hydrogen Energy* 44.20 (2019). 9th International Conference on Hydrogen Production (ICH2P-2018), pp. 9802–9810. ISSN: 0360-3199. DOI: <https://doi.org/10.1016/j.ijhydene.2018.12.135>.
- [73] Mathias Pein, Christos Agrafiotis, Josua Vieten, Dimitra Giasafaki, Stefan Brendelberger, Martin Roeb, and Christian Sattler. „Redox thermochemistry of Ca-Mn-based perovskites for oxygen atmosphere control in solar-thermochemical processes“. In: *Solar Energy* 198 (2020), pp. 612–622. ISSN: 0038-092X. DOI: <https://doi.org/10.1016/j.solener.2020.01.088>.
- [74] Ivan Ermanoski and Ellen B. Stechel. „Thermally-driven adsorption/desorption cycle for oxygen pumping in thermochemical fuel production“. In: *Solar Energy* 198 (2020), pp. 578–585. ISSN: 0038-092X. DOI: <https://doi.org/10.1016/j.solener.2020.01.050>.
- [75] Mai Xu, Ivan Ermanoski, Ellen B. Stechel, and Shuguang Deng. „Oxygen pumping characteristics of YBaCo₄O_{7+δ} for solar thermochemical cycles“. In: *Chemical Engineering Journal* 389 (2020), p. 124026. ISSN: 1385-8947. DOI: <https://doi.org/10.1016/j.cej.2020.124026>.
- [76] Peter T. Krenzke, Jesse R. Fosheim, and Jane H. Davidson. „Solar fuels via chemical-looping reforming“. In: *Solar Energy* 156 (2017). Advances in Solar Thermochemistry, pp. 48–72. ISSN: 0038-092X. DOI: <https://doi.org/10.1016/j.solener.2017.05.095>.
- [77] Rainer Tamme, Reiner Buck, Michael Epstein, Uriyel Fisher, and Chemi Sugarmen. „Solar Upgrading of Fuels for Generation of Electricity“. In: *Journal of Solar Energy Engineering* 123.2 (Jan. 2001), pp. 160–163. ISSN: 0199-6231. DOI: 10.1115/1.1353177.
- [78] Philipp Holzemer-Zerhusen, Stefan Brendelberger, Henrik von Storch, Martin Roeb, Christian Sattler, and Robert Pitz-Paal. „Efficiency assessment of solar redox reforming in comparison to conventional reforming“. In: *International Journal of Hydrogen Energy* 45.7 (2020), pp. 4137–4151. ISSN: 0360-3199. DOI: <https://doi.org/10.1016/j.ijhydene.2019.12.065>.
- [79] Feng He, James Trainham, Gregory Parsons, John S. Newman, and Fanxing Li. „A hybrid solar-redox scheme for liquid fuel and hydrogen coproduction“. In: *Energy Environ. Sci.* 7 (6 2014), pp. 2033–2042. DOI: 10.1039/C4EE00038B.
- [80] Kent J. Warren, Julie Reim, Kelvin Randhir, Benjamin Greek, Richard Carrillo, David W. Hahn, and Jonathan R. Scheffe. „Theoretical and Experimental Investigation of Solar Methane Reforming through the Nonstoichiometric Ceria Redox Cycle“. In: *Energy Technology* 5.11 (2017), pp. 2138–2149. DOI: <https://doi.org/10.1002/ente.201700083>.
- [81] Hye Heun Jeong, Jung Hun Kwak, Gui Young Han, and Ki June Yoon. „Stepwise production of syngas and hydrogen through methane reforming and water splitting by using a cerium oxide redox system“. In: *International Journal of Hydrogen Energy* 36.23 (2011), pp. 15221–15230. ISSN: 0360-3199. DOI: <https://doi.org/10.1016/j.ijhydene.2011.08.079>.

- [82] Xing Zhu, Yonggang Wei, Hua Wang, and Kongzhai Li. „Ce-Fe oxygen carriers for chemical-looping steam methane reforming“. In: *International Journal of Hydrogen Energy* 38.11 (2013), pp. 4492–4501. ISSN: 0360-3199. DOI: <https://doi.org/10.1016/j.ijhydene.2013.01.115>.
- [83] Mario Zuber, Moritz Patriarca, Simon Ackermann, Philipp Furler, Ricardo Conceição, José Gonzalez-Aguilar, Manuel Romero, and Aldo Steinfeld. „Methane dry reforming via a ceria-based redox cycle in a concentrating solar tower“. In: *Sustainable Energy Fuels* 7 (8 2023), pp. 1804–1817. DOI: 10.1039/D2SE01726A.
- [84] Justin Lapp, Jane H. Davidson, and Wojciech Lipiński. „Heat Transfer Analysis of a Solid-Solid Heat Recuperation System for Solar-Driven Nonstoichiometric Redox Cycles“. In: *Journal of Solar Energy Engineering* 135.3 (Mar. 2013). 031004. ISSN: 0199-6231. DOI: 10.1115/1.4023357.
- [85] Cansheng Yuan, Colby Jarrett, William Chueh, Yoshiaki Kawajiri, and Asegun Henry. „A new solar fuels reactor concept based on a liquid metal heat transfer fluid: Reactor design and efficiency estimation“. In: *Solar Energy* 122 (2015), pp. 547–561. ISSN: 0038-092X. DOI: <https://doi.org/10.1016/j.solener.2015.08.019>.
- [86] Richard B. Diver, James E. Miller, Mark D. Allendorf, Nathan P. Siegel, and Roy E. Hogan. „Solar Thermochemical Water-Splitting Ferrite-Cycle Heat Engines“. In: *Journal of Solar Energy Engineering* 130.4 (Sept. 2008). 041001. ISSN: 0199-6231. DOI: 10.1115/1.2969781.
- [87] Richard B. Diver, James E. Miller, Nathan P. Siegel, and Timothy A. Moss. „Testing of a CR5 Solar Thermochemical Heat Engine Prototype“. In: *Proceedings of the ASME 2010 4th International Conference on Energy Sustainability*. Vol. 2. ASME 2010 4th International Conference on Energy Sustainability. Phoenix, Arizona, USA, May 2010, pp. 97–104. DOI: 10.1115/ES2010-90093.
- [88] Darryl L. James, Nathan P. Siegel, Richard B. Diver, Barry D. Boughton, and Roy E. Hogan. „Numerical Modeling of Solar Thermo-Chemical Water-Splitting Reactor“. In: *Proceedings of the ASME 2006 International Solar Energy Conference*. Solar Energy. Denver, Colorado, USA, July 2006, pp. 221–227. DOI: 10.1115/ISEC2006-99141.
- [89] Luke J. Mayer and Darryl L. James. „Thermal Recuperation Modeling of a Solar Thermochemical Reactor“. In: *Proceedings of the ASME 2011 5th International Conference on Energy Sustainability*. ASME 2011 5th International Conference on Energy Sustainability, Parts A, B, and C. Washington, DC, USA, Aug. 2011, pp. 729–736. DOI: 10.1115/ES2011-54468.
- [90] James E. Miller, Mark A. Allendorf, Andrea Ambrosini, Eric N. Coker, Richard B. Diver, Ivan Ermanoski, Lindsey R. Evans, Roy E. Hogan, and Anthony H. McDaniel. *Development and Assessment of Solar-Thermal Activated Fuel Production: Phase 1 Summary, Sandia Report*. Tech. rep. Albuquerque, New Mexico 87185 and Livermore, California 94550: Sandia National Laboratories, 2012.
- [91] Christoph Falter, Andreas Sizmann, and Robert Pitz-Paal. „Perspectives of advanced thermal management in solar thermochemical syngas production using a counter-flow solid-solid heat exchanger“. In: *AIP Conference Proceedings* 1850.1 (2017), p. 100005. DOI: 10.1063/1.4984462.

- [92] Aniket S. Patankar, Xiao-Yu Wu, Wonjae Choi, Harry L. Tuller, and Ahmed F. Ghoniem. „A Reactor Train System for Efficient Solar Thermochemical Fuel Production“. In: *Proceedings of the ASME 2021 International Mechanical Engineering Congress and Exposition*. Vol. 8B: Energy. ASME International Mechanical Engineering Congress and Exposition. V08BT08A024. Nov. 2021. DOI: 10.1115/IMECE2021-69716.
- [93] Aniket S. Patankar, Xiao-Yu Wu, Wonjae Choi, Harry L. Tuller, and Ahmed F. Ghoniem. „A Reactor Train System for Efficient Solar Thermochemical Fuel Production“. In: *Journal of Solar Energy Engineering* 144.6 (Sept. 2022). 061014. ISSN: 0199-6231. DOI: 10.1115/1.4055298.
- [94] Aniket S. Patankar, Xiao-Yu Wu, Wonjae Choi, Harry L. Tuller, and Ahmed F. Ghoniem. „Efficient Solar Thermochemical Hydrogen Production in a Reactor Train System With Thermochemical Oxygen Removal“. In: *Proceedings of the ASME 2022 International Mechanical Engineering Congress and Exposition*. Vol. 6: Energy. ASME International Mechanical Engineering Congress and Exposition. V006T08A052. Oct. 2022. DOI: 10.1115/IMECE2022-94821.
- [95] Adrian Orozco Ivan Ermanoski. *C2R2: Compact Compound Recirculator/Recuperator for Renewable Energy and Energy Efficient Thermochemical Processing*. Tech. rep. Albuquerque, New Mexico 87185 and Livermore, California 94550: Sandia National Laboratories, 2015.
- [96] Silvan Siegrist and Henrik von Storch. „Solarstrahlungsempfänger, Reaktorsystem mit einem Solarstrahlungsempfänger, Verfahren zum Erwärmen von Feststoffmedium mittels konzentrierter Solarstrahlung sowie Verfahren zum solaren Betrieb einer thermochemischen Reaktion“. (German). German pat. DE102018201319B4. 2019.
- [97] Alon Lidor, Yves Aschwanden, Jamina Häseli, Pit Reckinger, Philipp Haueter, and Aldo Steinfeld. „High-temperature heat recovery from a solar reactor for the thermochemical redox splitting of H₂O and CO₂“. In: *Applied Energy* 329 (2023), p. 120211. ISSN: 0306-2619. DOI: <https://doi.org/10.1016/j.apenergy.2022.120211>.
- [98] Karl Schwartzwalder, Holly Somers, and Arthur V. Somers. „Method of making porous ceramic articles“. U.S. pat. 3 090 094. May 1963.
- [99] Tobias Fey, Ulf Betke, Stefan Rannabauer, and Michael Scheffler. „Reticulated Replica Ceramic Foams: Processing, Functionalization, and Characterization“. In: *Advanced Engineering Materials* 19.10 (2017), p. 1700369. DOI: <https://doi.org/10.1002/adem.201700369>.
- [100] U.F. Vogt, M. Gorbar, P. Dimopoulos-Eggenschwiler, A. Broenstrup, G. Wagner, and P. Colombo. „Improving the properties of ceramic foams by a vacuum infiltration process“. In: *Journal of the European Ceramic Society* 30.15 (2010), pp. 3005–3011. ISSN: 0955-2219. DOI: <https://doi.org/10.1016/j.jeurceramsoc.2010.06.003>.
- [101] Mathias Pein, Luca Matzel, Lamark de Oliveira, Gözde Alkan, Alexander Francke, Peter Mechnich, Christos Agrafiotis, Martin Roeb, and Christian Sattler. „Reticulated Porous Perovskite Structures for Thermochemical Solar Energy Storage“. In: *Advanced Energy Materials* 12.10 (2022), p. 2102882. DOI: <https://doi.org/10.1002/aenm.202102882>.
- [102] Philipp Furler, Jonathan Scheffe, Michal Gorbar, Louis Moes, Ulrich Vogt, and Aldo Steinfeld. „Solar Thermochemical CO₂ Splitting Utilizing a Reticulated Porous Ceria Redox System“. In: *Energy Fuels* 26.11 (Nov. 2012), pp. 7051–7059. ISSN: 0887-0624. DOI: 10.1021/ef3013757.

- [103] Daniel Marxer, Philipp Furler, Jonathan Scheffe, Hans Geerlings, Christoph Falter, Valentin Batteiger, Andreas Sizmann, and Aldo Steinfeld. „Demonstration of the Entire Production Chain to Renewable Kerosene via Solar Thermochemical Splitting of H₂O and CO₂“. In: *Energy Fuels* 29.5 (May 2015), pp. 3241–3250. ISSN: 0887-0624. DOI: 10.1021/acs.energyfuels.5b00351.
- [104] Philipp Furler and Aldo Steinfeld. „Heat transfer and fluid flow analysis of a 4kW solar thermochemical reactor for ceria redox cycling“. In: *Chemical Engineering Science* 137 (2015), pp. 373–383. ISSN: 0009-2509. DOI: <https://doi.org/10.1016/j.ces.2015.05.056>.
- [105] Sergey Sokolov, David Bell, and Andreas Stein. „Preparation and Characterization of Macroporous α -Alumina“. In: *Journal of the American Ceramic Society* 86.9 (2003), pp. 1481–1486. DOI: <https://doi.org/10.1111/j.1151-2916.2003.tb03500.x>.
- [106] D. Zou, S. Ma, R. Guan, M. Park, L. Sun, J. J. Aklonis, and R. Salovey. „Model filled polymers. V. Synthesis of crosslinked monodisperse polymethacrylate beads“. In: *Journal of Polymer Science Part A: Polymer Chemistry* 30.1 (1992), pp. 137–144. DOI: <https://doi.org/10.1002/pola.1992.080300118>.
- [107] Luke J. Venstrom, Nicholas Petkovich, Stephen Rudisill, Andreas Stein, and Jane H. Davidson. „The Effects of Morphology on the Oxidation of Ceria by Water and Carbon Dioxide“. In: *Journal of Solar Energy Engineering* 134.1 (Nov. 2011). 011005. ISSN: 0199-6231. DOI: 10.1115/1.4005119.
- [108] Anita Haeussler and Stéphane Abanades. „Additive manufacturing and two-step redox cycling of ordered porous ceria structures for solar-driven thermochemical fuel production“. In: *Chemical Engineering Science* 246 (2021). HAL Id: hal-03365894, p. 116999. DOI: 10.1016/j.ces.2021.116999.
- [109] Xiaoyan Zhang, Youfei Zhang, Yuju Lu, Shuhao Zhang, and Jinlong Yang. „Hierarchically porous ceria with tunable pore structure from particle-stabilized foams“. In: *Journal of the European Ceramic Society* 40.12 (2020), pp. 4366–4372. ISSN: 0955-2219. DOI: <https://doi.org/10.1016/j.jeurceramsoc.2020.05.034>.
- [110] Basam A. E. Ben-Arfa, Stéphane Abanades, Isabel M. Miranda Salvado, José M. F. Ferreira, and Robert C. Pullar. „Robocasting of 3D printed and sintered ceria scaffold structures with hierarchical porosity for solar thermochemical fuel production from the splitting of CO₂“. In: *Nanoscale* 14 (13 2022), pp. 4994–5001. DOI: 10.1039/D2NR00393G.
- [111] Mogens Mogensen, Nigel M. Sammes, and Geoff A. Tompsett. „Physical, chemical and electrochemical properties of pure and doped ceria“. In: *Solid State Ionics* 129.1 (2000), pp. 63–94. ISSN: 0167-2738. DOI: [https://doi.org/10.1016/S0167-2738\(99\)00318-5](https://doi.org/10.1016/S0167-2738(99)00318-5).
- [112] Stéphane Abanades and Gilles Flamant. „Thermochemical hydrogen production from a two-step solar-driven water-splitting cycle based on cerium oxides“. In: *Solar Energy* 80.12 (2006), pp. 1611–1623. ISSN: 0038-092X. DOI: <https://doi.org/10.1016/j.solener.2005.12.005>.
- [113] Stéphane Abanades, Alex Legal, Anne Cordier, Gilles Peraudeau, Gilles Flamant, and Anne Julbe. „Investigation of reactive cerium-based oxides for H₂ production by thermochemical two-step water-splitting“. In: *Journal of Materials Science* 45.15 (2010), pp. 4163–4173. ISSN: 1573-4803. DOI: 10.1007/s10853-010-4506-4.
- [114] N. Knoblauch, H. Simon, and M. Schmücker. „Chemically induced volume change of CeO_{2- δ} and nonstoichiometric phases“. In: *Solid State Ionics* 301 (2017), pp. 43–52. ISSN: 0167-2738. DOI: <https://doi.org/10.1016/j.ssi.2017.01.003>.

- [115] E.C. Subbarao and H.S. Maiti. „Solid electrolytes with oxygen ion conduction“. In: *Solid State Ionics* 11.4 (1984), pp. 317–338. ISSN: 0167-2738. DOI: [https://doi.org/10.1016/0167-2738\(84\)90024-9](https://doi.org/10.1016/0167-2738(84)90024-9).
- [116] B. Bulfin, F. Call, M. Lange, O. Lübben, C. Sattler, R. Pitz-Paal, and I. V. Shvets. „Thermodynamics of CeO₂ Thermochemical Fuel Production“. In: *Energy & Fuels* 29.2 (2015), pp. 1001–1009. DOI: [10.1021/ef5019912](https://doi.org/10.1021/ef5019912).
- [117] Ihsan Barin. *Thermochemical Data of Pure Substances*. 3rd ed. VCH Verlagsgesellschaft mbH, 1995. ISBN: 3-527-28745-0.
- [118] Peter Atkins and Julio de Paula. *Physical Chemistry*. 9th ed. W. H. Freeman and Company, 2010. ISBN: 1-4292-1812-6.
- [119] Simon Ackermann, Jonathan R. Scheffe, and Aldo Steinfeld. „Diffusion of Oxygen in Ceria at Elevated Temperatures and Its Application to H₂O/CO₂ Splitting Thermochemical Redox Cycles“. In: *The Journal of Physical Chemistry C* 118.10 (2014), pp. 5216–5225. DOI: [10.1021/jp500755t](https://doi.org/10.1021/jp500755t).
- [120] R.N. Blumenthal and R.K. Sharma. „Electronic conductivity in nonstoichiometric cerium dioxide“. In: *Journal of Solid State Chemistry* 13.4 (1975), pp. 360–364. ISSN: 0022-4596. DOI: [https://doi.org/10.1016/0022-4596\(75\)90152-8](https://doi.org/10.1016/0022-4596(75)90152-8).
- [121] M. Stan, Y. T. Zhu, H. Jiang, and D. P. Butt. „Kinetics of oxygen removal from ceria“. In: *Journal of Applied Physics* 95.7 (2004), pp. 3358–3361. DOI: [10.1063/1.1650890](https://doi.org/10.1063/1.1650890).
- [122] M.A. Panhans and R.N. Blumenthal. „A thermodynamic and electrical conductivity study of nonstoichiometric cerium dioxide“. In: *Solid State Ionics* 60.4 (1993), pp. 279–298. ISSN: 0167-2738. DOI: [https://doi.org/10.1016/0167-2738\(93\)90006-0](https://doi.org/10.1016/0167-2738(93)90006-0).
- [123] Nicole Knoblauch, Lars Dörrer, Peter Fielitz, Martin Schmücker, and Günter Borchardt. „Surface controlled reduction kinetics of nominally undoped polycrystalline CeO₂“. In: *Phys. Chem. Chem. Phys.* 17 (8 2015), pp. 5849–5860. DOI: [10.1039/C4CP05742B](https://doi.org/10.1039/C4CP05742B).
- [124] Michiyo Kamiya, Eriko Shimada, Yasuro Ikuma, Manabu Komatsu, and Hajime Haneda. „Intrinsic and Extrinsic Oxygen Diffusion and Surface Exchange Reaction in Cerium Oxide“. In: *Journal of The Electrochemical Society* 147.3 (2000), p. 1222. DOI: [10.1149/1.1393340](https://doi.org/10.1149/1.1393340).
- [125] Matvei Zinkevich, Dejan Djurovic, and Fritz Aldinger. „Thermodynamic modelling of the cerium–oxygen system“. In: *Solid State Ionics* 177.11 (2006), pp. 989–1001. ISSN: 0167-2738. DOI: <https://doi.org/10.1016/j.ssi.2006.02.044>.
- [126] Simon Ackermann, Michael Takacs, Jonathan Scheffe, and Aldo Steinfeld. „Reticulated porous ceria undergoing thermochemical reduction with high-flux irradiation“. In: *International Journal of Heat and Mass Transfer* 107 (2017), pp. 439–449. ISSN: 0017-9310. DOI: <https://doi.org/10.1016/j.ijheatmasstransfer.2016.11.032>.
- [127] A. W. Coats and J. P. Redfern. „Thermogravimetric analysis. A review“. In: *Analyst* 88 (1053 1963), pp. 906–924. DOI: [10.1039/AN9638800906](https://doi.org/10.1039/AN9638800906).
- [128] Kangjae Lee, Nicole Knoblauch, Christos Agrafiotis, Mathias Pein, Martin Roeb, and Christian Sattler. „Oxidation kinetics of La and Yb incorporated Zr-doped ceria for solar thermochemical fuel production in the context of dopant ionic radius and valence“. In: *Open Ceramics* 10 (2022), p. 100269. ISSN: 2666-5395. DOI: <https://doi.org/10.1016/j.oceram.2022.100269>.
- [129] M. M. Markowitz and D. A. Boryta. „Thermogravimetric Study of Magnesium and Aluminum Metal-Gas Reactions“. In: *Analytical Chemistry* 33.7 (1961), pp. 949–951. DOI: [10.1021/ac60175a040](https://doi.org/10.1021/ac60175a040).

- [130] V.K. Thanda, Th. Fend, D. Laaber, A. Lidor, H. von Storch, J.P. Säck, J. Hertel, J. Lampe, S. Menz, G. Piesche, S. Berger, S. Lorentzou, M. Syrigou, Th. Denk, A. Gonzales-Pardo, A. Vidal, M. Roeb, and Ch. Sattler. „Experimental investigation of the applicability of a 250 kW ceria receiver/reactor for solar thermochemical hydrogen generation“. In: *Renewable Energy* 198 (2022), pp. 389–398. ISSN: 0960-1481. DOI: <https://doi.org/10.1016/j.renene.2022.08.010>.
- [131] J. Grote K.-H.;Feldhusen, ed. *Dubbel – Taschenbuch für den Maschinenbau*. 23rd ed. (German). Springer-Verlag, 2012. ISBN: 978-3-642-17305-9. DOI: 10.1007/978-3-642-17306-6.
- [132] Peter Stephan, Stephan Kabelac, Matthias Kind, Holger Martin, Dieter Mewes, and Karlheinz Schaber, eds. *VDI Heat Atlas*. 2nd ed. Springer, Berlin, Heidelberg, 2010. ISBN: 978-3-540-77876-9. DOI: 10.1007/978-3-540-77877-6.
- [133] Michael J Moran, Howard N Shapiro, Daisie D Boettner, and Margaret B Bailey. *Fundamentals of engineering thermodynamics*. 8th ed. Hoboken, N.J.: Wiley, 2014. ISBN: 978-1-118-82044-5.
- [134] Stuart W. Churchill and Humbert H.S. Chu. „Correlating equations for laminar and turbulent free convection from a vertical plate“. In: *International Journal of Heat and Mass Transfer* 18.11 (1975), pp. 1323–1329. ISSN: 0017-9310. DOI: [https://doi.org/10.1016/0017-9310\(75\)90243-4](https://doi.org/10.1016/0017-9310(75)90243-4).
- [135] Stuart W. Churchill and Humbert H.S. Chu. „Correlating equations for laminar and turbulent free convection from a horizontal cylinder“. In: *International Journal of Heat and Mass Transfer* 18.9 (1975), pp. 1049–1053. ISSN: 0017-9310. DOI: [https://doi.org/10.1016/0017-9310\(75\)90222-7](https://doi.org/10.1016/0017-9310(75)90222-7).
- [136] S. W. Churchill and R. Usagi. „A general expression for the correlation of rates of transfer and other phenomena“. In: *AIChE Journal* 18.6 (1972), pp. 1121–1128. DOI: <https://doi.org/10.1002/aic.690180606>.
- [137] Ekbert Hering, Rolf Martin, and Martin Stohrer. *Physik für Ingenieure*. 11th ed. (German). Berlin; Heidelberg: Springer, 2012. ISBN: 978-3-642-22568-0.
- [138] H D Baehr and K Stephan. *Heat and mass-transfer*. 2nd ed. Berlin; New York: Springer, 2006. ISBN: 3-540-63695-1.
- [139] Miguel A.A. Mendes, Prabal Talukdar, Subhashis Ray, and Dimosthenis Trimis. „Detailed and simplified models for evaluation of effective thermal conductivity of open-cell porous foams at high temperatures in presence of thermal radiation“. In: *International Journal of Heat and Mass Transfer* 68 (2014), pp. 612–624. ISSN: 0017-9310. DOI: <https://doi.org/10.1016/j.ijheatmasstransfer.2013.09.071>.
- [140] Michael F. Modest. *Radiative heat transfer*. 3rd ed. Kidlington, Oxford, U.K: Academic Press, 2013. ISBN: 978-0-12-386944-9.
- [141] Simon Ackermann, Jonathan R. Scheffe, Jonas Duss, and Aldo Steinfeld. „Morphological Characterization and Effective Thermal Conductivity of Dual-Scale Reticulated Porous Structures“. In: *Materials* 7.11 (2014), pp. 7173–7195. ISSN: 1996-1944. DOI: 10.3390/ma7117173.
- [142] D. A. G. Bruggeman. „Berechnung verschiedener physikalischer Konstanten von heterogenen Substanzen. I. Dielektrizitätskonstanten und Leitfähigkeiten der Mischkörper aus isotropen Substanzen“. In: *Annalen der Physik* 416.7 (1935). (German), pp. 636–664. DOI: <https://doi.org/10.1002/andp.19354160705>.

- [143] „Oxides and Their Solutions and Mixtures. Part 1. Simple Oxygen Compounds and Their Mixtures“. In: *Thermophysical Properties of High Temperature Solid Materials*. Ed. by Y. S. Touloukian. Vol. 4. New York: Macmillan, 1967.
- [144] M. W. Chase Jr. „NIST-JANAF Thermochemical Tables, Fourth Edition“. In: *J. Phys. Chem. Ref. Data, Monograph 9* (1998), pp. 1–1951. URL: <https://webbook.nist.gov/cgi/cbook.cgi?Source=1998CHA1-1951&Units=SI&Mask=1>.
- [145] P.J. Linstrom and W.G. Mallard, eds. *NIST Chemistry WebBook, NIST Standard Reference Database Number 69*. (retrieved March 18, 2022). Gaithersburg MD, 20899: National Institute of Standards and Technology. DOI: <https://doi.org/10.18434/T4D303>.
- [146] Philipp Holzemer-Zerhusen, Stefan Brendelberger, Martin Roeb, and Christian Sattler. „Oxygen Crossover in Solid–Solid Heat Exchangers for Solar Water and Carbon Dioxide Splitting: A Thermodynamic Analysis“. In: *Journal of Energy Resources Technology* 143.7 (Oct. 2020). 071301. ISSN: 0195-0738. DOI: 10.1115/1.4048772.
- [147] Philipp Holzemer-Zerhusen, Stefan Brendelberger, Martin Roeb, and Christian Sattler. „Oxygen Crossover in Solid-Solid Heat Exchangers for Solar Water and Carbon Dioxide Splitting: A Thermodynamic Analysis“. In: *Proceedings of the ASME 2020 14th International Conference on Energy Sustainability*. ASME 2020 14th International Conference on Energy Sustainability. V001T13A001. Virtual, Online, June 2020. DOI: 10.1115/ES2020-1608.
- [148] Python Software Foundation. *Python 3*. URL: <https://www.python.org/>.
- [149] Python Software Foundation. *The Python Language Reference*. 2022. URL: <https://docs.python.org/3.9/reference/index.html> (visited on 03/17/2022).
- [150] C.W. Bale, E. Béglise, P. Chartrand, S.A. Deckerov, G. Eriksson, A.E. Gheribi, K. Hack, I.-H. Jung, Y.-B. Kang, J. Melançon, A.D. Pelton, S. Petersen, C. Robelin, J. Sangster, P. Spencer, and M.-A. Van Ende. „FactSage thermochemical software and databases, 2010–2016“. In: *Calphad* 54 (2016), pp. 35–53. ISSN: 0364-5916. DOI: <https://doi.org/10.1016/j.calphad.2016.05.002>.
- [151] Chao Xu, Zhifeng Wang, Xin Li, and Feihu Sun. „Energy and exergy analysis of solar power tower plants“. In: *Applied Thermal Engineering* 31.17 (2011). SET 2010 Special Issue, pp. 3904–3913. ISSN: 1359-4311. DOI: <https://doi.org/10.1016/j.applthermaleng.2011.07.038>.
- [152] Richard E. Sonntag Claus Borgnakke. *Fundamentals of engineering thermodynamics*. 7th ed. Hoboken, NJ: John Wiley & Sons, Inc, 2009. ISBN: 978-0-470-04192-5.
- [153] Luca Christian Matzel. *Development of reticulated porous metal oxides for the production of solar fuels*. bachelor thesis (German). 2020. URL: <https://elib.dlr.de/138311/>.
- [154] Douglas C. Giancoli. *Physik*. 4th ed. (German). Pearson Studium, 2019. ISBN: 978-3-86894-363-4.
- [155] Pauli Virtanen, Ralf Gommers, Travis E. Oliphant, Matt Haberland, Tyler Reddy, David Cournapeau, Evgeni Burovski, Pearu Peterson, Warren Weckesser, Jonathan Bright, Stefan J. van der Walt, Matthew Brett, Joshua Wilson, K. Jarrod Millman, Nikolay Mayorov, Andrew R. J. Nelson, Eric Jones, Robert Kern, Eric Larson, C J Carey, İlhan Polat, Yu Feng, Eric W. Moore, Jake VanderPlas, Denis Laxalde, Josef Perktold, Robert Cimrman, Ian Henriksen, E. A. Quintero, Charles R. Harris, Anne M. Archibald, Antônio H. Ribeiro, Fabian Pedregosa, Paul van Mulbregt, and SciPy 1.0 Contributors. „SciPy 1.0: Fundamental Algorithms for Scientific Computing in Python“. In: *Nature Methods* 17 (2020), pp. 261–272. DOI: 10.1038/s41592-019-0686-2.

- [156] Charles R. Harris, K. Jarrod Millman, Stéfan J. van der Walt, Ralf Gommers, Pauli Virtanen, David Cournapeau, Eric Wieser, Julian Taylor, Sebastian Berg, Nathaniel J. Smith, Robert Kern, Matti Picus, Stephan Hoyer, Marten H. van Kerkwijk, Matthew Brett, Allan Haldane, Jaime Fernández del Río, Mark Wiebe, Pearu Peterson, Pierre Gérard-Marchant, Kevin Sheppard, Tyler Reddy, Warren Weckesser, Hameer Abbasi, Christoph Gohlke, and Travis E. Oliphant. „Array programming with NumPy“. In: *Nature* 585.7825 (2020), pp. 357–362. ISSN: 1476-4687. DOI: 10.1038/s41586-020-2649-2.
- [157] Ludwig Fahrmeir, Rita Künstler, Iris Pigeot, and Gerhard Tutz. *Statistik: der Weg zur Datenanalyse*. 7th ed. (German). Springer-Verlag, 2011. ISBN: 978-3-642-01938-8.
- [158] Stefan Brendelberger, Philipp Holzemer-Zerhusen, Estefania Vega Puga, Martin Roeb, and Christian Sattler. „Study of a new receiver-reactor cavity system with multiple mobile redox units for solar thermochemical water splitting“. In: *Solar Energy* 235 (2022), pp. 118–128. ISSN: 0038-092X. DOI: <https://doi.org/10.1016/j.solener.2022.02.013>.
- [159] Stefan Brendelberger and Philipp Holzemer-Zerhusen. „Solarstrahlungsreceiver sowie Reaktorsystem mit Solarstrahlungsreceiver“. (German). German pat. DE102020118651B4. 2022.
- [160] Stefan Brendelberger and Philipp Holzemer-Zerhusen. „Solarabsorbervorrichtung sowie Transportsystem für eine Solarabsorbervorrichtung“. (German). German pat. DE102020118683B4. 2022.
- [161] Rath. *Feuerfeste Vakuumformteile*. datasheet (German). URL: https://www.rath-group.com/fileadmin/content/Rath-Group/Downloads/Broschueren_Produkte/RATH_VacuumFormedShapes_201710_DE.pdf (visited on 07/27/2022).
- [162] Donald G. Archer. „Thermodynamic Properties of Synthetic Sapphire (α -Al₂O₃), Standard Reference Material 720 and the Effect of Temperature-Scale Differences on Thermodynamic Properties“. In: *Journal of Physical and Chemical Reference Data* 22.6 (1993), pp. 1441–1453. DOI: 10.1063/1.555931.
- [163] S. Zoller, E. Koepf, P. Roos, and A. Steinfeld. „Heat Transfer Model of a 50 kW Solar Receiver-Reactor for Thermochemical Redox Cycling Using Cerium Dioxide“. In: *Journal of Solar Energy Engineering* 141.2 (Jan. 2019). 021014. ISSN: 0199-6231. DOI: 10.1115/1.4042059.
- [164] I. Riess, M. Ricken, and J. Nolting. „On the specific heat of nonstoichiometric ceria“. In: *Journal of Solid State Chemistry* 57.3 (1985), pp. 314–322. ISSN: 0022-4596. DOI: [https://doi.org/10.1016/0022-4596\(85\)90193-8](https://doi.org/10.1016/0022-4596(85)90193-8).